HYDROLOGICAL MODELING WITH GR MODELS USING REMOTE SENSING DATA

MASTER'S THESIS

Mamadi TRAORE

July 2024

HYDROLOGICAL MODELING WITH GR MODELS USING REMOTE SENSING DATA

Mamadi TRAORE

Master's Thesis

Department of Civil Engineering

Programme in Hydraulics

Supervisor: Assoc. Prof. Dr. Ali Arda ŞORMAN

Eskişehir

Eskişehir Technical University

Institute of Graduate Programs

July 2024

FINAL APPROVAL FOR THESIS

This thesis titled HYDROLOGICAL MODELING WITH GR MODELS USING REMOTE SENSING DATA has been prepared and submitted by Mamadi TRAORE in partial fulfillment of the requirements in "Eskişehir Technical University Directive on Graduate Education and Examination" for the Degree of Master's in Civil Engineering Department has been examined and approved on 24/07/2024.

Committee Members		**Title, Name and Surname**	**Signature**
Member	:	Assoc. Prof. Dr. Ali Arda ŞORMAN	
Member	:	Assoc. Prof. Dr. Gökçen UYSAL	
Member	:	Assoc. Prof. Dr. H. İbrahim BURGAN	

Prof. Dr. Semra KURAMA
Director of the Institute of Graduate Programs

24/07/2024

SUPERVISOR APPROVAL

Master's student Mamadi TRAORE, whom I supervise, has completed this thesis titled HYDROLOGICAL MODELING WITH GR MODELS USING REMOTE SENSING DATA. According to my inspections, the work is scientifically and ethically appropriate for the student to the thesis defense exam.

Supervisor
Assoc. Prof. Dr. Ali Arda ŞORMAN

ABSTRACT

HYDROLOGICAL MODELING WITH GR MODELS USING REMOTE SENSING DATA

Mamadi TRAORE

Department of Civil Engineering

Programme in Hydraulics

Eskişehir Technical University, Institute of Graduate Programs, July 2024

Supervisor: Assoc. Prof. Dr. Ali Arda ŞORMAN

Water scarcity is a critical issue that needs attention to achieve sustainability. Remote sensing technology has advanced in recent decades, providing important data on hydrological variables for effective water resource management. This study analyzed two regions with different hydroclimatic conditions: Türkiye, with a temperate climate where snowmelt significantly contributes to streamflow, and Guinea, with a humid tropical climate characterized by monsoon rains. Rainfall-runoff modeling was performed at daily, monthly, and annual time steps using the split-sample test method and single objective calibration. Three algorithms—Calibration Michel, DEoptim, and hydroPSO—were used at the daily time step to effectively explore the parameter space. Satisfactory results were achieved for both regions at all time steps, although the standard CemaNeige for snow accounting and GR1A in the Guinean watershed were less satisfactory. A multi-objective calibration was then conducted to further refine the daily models by considering hysteresis between snow accumulation and melting phases in snowy basins and soil moisture in others. This approach aimed to enhance model accuracy and robustness by incorporating multiple hydrological variables, providing a comprehensive understanding of the water balance in these regions. By considering hysteresis in the CemaNeige snow module, snow cover dynamics were accurately simulated without compromising discharge performance. Additionally, when both soil moisture and discharge were considered in the GR4J model, simulations of soil moisture closely matched SMAP data during the rainy season, especially with increased weighting on soil moisture.

Keywords: Remote sensing, Snow, Soil moisture, GR models, Hydrological modeling.

ÖZET

GR MODELLERİNDE UYDU GÖRÜNTÜLERİ KULLANARAK HİDROLOJİK MODELLEME

Mamadi TRAORE

İnşaat Mühendisliği Anabilim Dalı

Hidrolik Bilim Dalı

Eskişehir Teknik Üniversitesi, Lisansüstü Eğitim Enstitüsü, Temmuz 2024

Danışman: Doç. Dr. Ali Arda ŞORMAN

Su kıtlığı, sürdürülebilirliğe ulaşmak için dikkat edilmesi gereken kritik bir sorundur. Uzaktan algılama teknolojisi son on yıllarda ilerlemiş ve su kaynaklarının etkili yönetimi için önemli hidrolojik değişkenler hakkında veri sağlamıştır. Bu çalışmada, farklı hidroklimatik koşullara sahip iki bölge analiz edilmiştir: Kar erimesinin akışa önemli ölçüde katkıda bulunduğu ılıman iklimi ile Türkiye ve muson yağmurlarıyla karakterize edilen nemli tropikal iklime sahip Gine. Yağış-akış modellemesi, split-sample test yöntemi ve tek hedefli kalibrasyon kullanılarak günlük, aylık ve yıllık zaman dilimlerinde gerçekleştirilmiştir. Parametre uzayını etkin bir şekilde keşfetmek için günlük zaman diliminde Calibration Michel, DEoptim ve hydroPSO olmak üzere üç algoritma kullanılmıştır. Her iki bölge için de tüm zaman dilimlerinde tatmin edici sonuçlar elde edilmiştir, ancak kar hesaplaması için standart CemaNeige ve Gine havzasında GR1A daha az tatmin edici olmuştur. Ardından, kar birikimi ve erime fazları arasındaki histerezisi ve diğer bölgelerdeki toprak nemini dikkate alarak günlük modelleri daha da iyileştirmek için çok amaçlı kalibrasyon yapılmıştır. Bu yaklaşım, birden fazla hidrolojik değişkeni dahil ederek model doğruluğunu ve sağlamlığını artırmayı ve bu bölgelerdeki su dengesi hakkında kapsamlı bir anlayış sağlamayı amaçlamıştır. CemaNeige kar modülünde histerezis dikkate alındığında, akış performansını bozmadan kar örtüsü dinamikleri doğru bir şekilde simüle edilmiştir. Ayrıca, GR4J modelinde hem toprak nemi hem de akış dikkate alındığında, simülasyonlar yağışlı sezonda SMAP verileriyle yakından eşleşmiş, özellikle toprak nemine verilen ağırlık arttıkça bu uyum daha da belirginleşmiştir.

Anahtar Sözcükler: Uzaktan algılama, Kar, Toprak nemi, GR modelleri, Hidrolojik modelleme.

ACKNOWLEDGEMENTS

Embarking on the initial stages of an international journey, far away from one's family and immersed in an unfamiliar language, can pose various challenges. However, these challenges can be significantly eased when one is fortunate enough to encounter welcoming and guiding individuals. This work would not have been possible without the invaluable assistance of many, and I would like to extend my sincerest gratitude to every one of them.

Above all, I would like to express my heartfelt appreciation to my esteemed supervisor, Assoc. Prof. Dr. Ali Arda ŞORMAN, for his practical guidance, unwavering support, and limitless patience, all of which have played a great role throughout my study journey. I am deeply grateful for his mentorship and the significant impact he has had on both my academic and personal growth.

I would also like to extend my sincere thanks to my committee members, Assoc. Prof. Dr. Gökçen UYSAL and Assoc. Prof. Dr. Halil İbrahim BURGAN, for their insightful feedback, and valuable suggestions, which have greatly improved my research.

I am sincerely grateful to Dr. Mory TRAORE, who fostered my passion for hydrological sciences and provided me with hydrometeorological data from the Guinean basins for my research. Additionally, my sincere gratitude to Prof. Aynur Şensoy ŞORMAN, for her exceptional teaching and invaluable guidance.

Special thanks to my colleague Ayça EYLEN for her dedicated time and our enriching discussions on hydrological modeling. I am also deeply indebted to Fode CAMARA and Hamed HAFIZI for their assistance during the early stages of my journey with R programming. I also want to thank my friend Mohamed CONDE for his continuous support.

I would like to extend my gratitude to Guillaume THIREL for his insightful feedback on my mails. My sincere thanks to Mr. Fara Anselme KAMANO for his support.

A heartfelt thanks to my family, especially my brothers Sory TRAORE and Mamadou TRAORE, for their love and encouragement throughout this process.

Last but certainly not least, I am grateful to the Presidency for Turks Abroad and Related Communities (YTB) for their generous financial support and the scholarship that made this research possible.

Mamadi TRAORE

24/07/2024

STATEMENT OF COMPLIANCE WITH ETHICAL PRINCIPLES AND RULES

I hereby truthfully declare that this thesis is an original work prepared by me; that I have behaved in accordance with the scientific ethical principles and rules throughout the stages of preparation, data collection, analysis and presentation of my work; that I have cited the sources of all the data and information that could be obtained within the scope of this study, and included these sources in the references section; and that this study has been scanned for plagiarism with "scientific plagiarism detection program" used by Eskişehir Technical University, and that "it does not have any plagiarism" whatsoever. I also declare that, if a case contrary to my declaration is detected in my work at any time, I hereby express my consent to all the ethical and legal consequences that are involved.

Mamadi TRAORE

CONTENTS

LIST OF TABLES

Page

LIST OF FIGURES

Page

GLOSSARY OF SYMBOLS AND ABBREVIATIONS

AGİ	:	Stream Gauging Station (Akım Gözlem İstasyonu)
CEMAGREF	:	National Center for the Study and Experimentation of Agricultural Machinery
CGF	:	Cloud Gap Filled
CM	:	Calibration Michel
DEoptim	:	Differential Evolutive Optimization Algorithm
DNH	:	National Hydraulic Directorate
DSİ	:	State Hydraulics Waorks (Devlet Su İsleri)
DNM	:	National Meteorological Directorate
Dv%	:	Deviation of runoff Volume in percent
GR1A	:	Rural Engineering 1 parameter Annual
GR2M	:	Rural Engineering 2 parameters Monthly
GR4J	:	Rural Engineering 4 parameters Daily
hydroPSO	:	Particle Swarm Optimization
IRSTEA	:	National Research Institute of Science and Technology for Agriculture and Environment
Kf	:	Degree-day factor
KGE	:	Kling-Gupta Efficiency
MGM	:	State Meteorological Services (Meteoroloji Genel Müdürlüğü)
MODIS	:	Moderate Resolution Imaging Spectroradiometer
NSE	:	Nash-Sutcliffe Efficiency
r	:	Pearson correlation coefficient
R^2	:	Determination coefficient
RMSE	:	Root Mean Square Error
SCA	:	Snow Cover Area
SMAP	:	Soil Moisture Active Passive
SWE	:	Snow Water Equivalent
UH1	:	One-sided Unit Hydrograph
wSM	:	Soil Moisture weight
wSN	:	Snow Cover Area weight

1. INTRODUCTION

1.1. Background

The history of water and human civilization are deeply intertwined. From the earliest days, the quest for reliable water sources has driven human activity and settlement. The first great civilizations, such as those in Mesopotamia, Egypt, and the Indus Valley, emerged along the banks of major rivers, providing essential water for agriculture, transportation, and daily life (Mouelhi, 2003). These rivers were not only lifelines but also the foundation upon which complex societies were built. However, it soon became evident that water, while essential for life, could also be a source of catastrophic events. Floods, droughts, and other water-related disasters have caused significant destruction of property and loss of life throughout history. Recognizing both the vital importance and the potential dangers of water, early societies began to invest in understanding the processes that govern the movement and distribution of water in nature. This investment led to the development of early hydrological knowledge, focusing on the physical and climatic factors that influence water behavior. Ancient engineers and scientists made significant strides in managing water resources and constructing irrigation systems, canals, and reservoirs to control water flow and mitigate the impacts of floods and droughts. Over time, this foundational understanding has evolved into the sophisticated field of hydrology we know today, encompassing the study of water cycles, weather patterns, and the intricate interactions between water and the environment. Hydrological models are the key tools that are used to achieve this understanding.

Therefore, to understand and predict the behavior of water in various environmental settings in a scale of a watershed, hydrological models are used. These models have been classified in various ways, reflecting different approaches to understanding and predicting water processes. Some common classifications include deterministic versus stochastic, empirical versus physical-based with conceptual models falling in between, lumped versus distributed, and event versus continuous models.

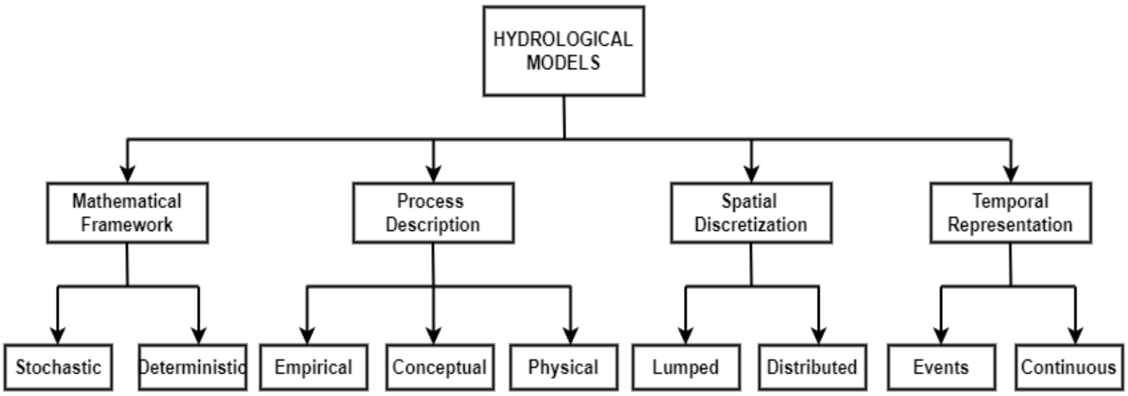

Figure 1.1. *Hydrological models classification*

Deterministic models are based on predefined equations and parameters, providing a specific output for a given set of inputs. They are predictable and reproducible, making them valuable for studying specific scenarios under controlled conditions (Maidment, 1993). In contrast, stochastic models incorporate randomness and probabilistic elements to consider the inherent variability and uncertainty in hydrological processes. They are useful for assessing risks and understanding the range of potential outcomes under different conditions (Singh, 1995).

Empirical models, also known as statistical or data-driven models, use observed data to establish relationships between inputs and outputs without necessarily understanding the underlying physical processes (Ponce & Hawkins, 1996). GR1A can be cited as an example. These models can make quick and straightforward predictions, but their performance may be limited when conditions fall outside the range of observed data. On the other hand, physical-based models aim to simulate the physical processes that govern the hydrological cycle in great detail (Arnold et al., 1998). They employ fundamental principles of physics, such as the conservation of mass, momentum, and energy, to describe the movement and distribution of water. Examples include the SWAT (Soil and Water Assessment Tool) and MIKE SHE models. While physical-based models offer a high level of accuracy, their complexity and data requirements can pose challenges during implementation and calibration. In the intersection of these two types of models, there is conceptual models. They are simplified representations of the hydrological cycle, designed to mimic real-world processes (Perrin et al., 2003). They utilize equations and reservoirs to describe different components of the water cycle, including precipitation, evaporation, infiltration, and runoff. By finding a balance between complexity and simplicity, conceptual models are widely used in both research and operational hydrology. Examples of such models include the HBV (Hydrologiska Byråns Vattenbalansavdelning) model and the GR4J (Génie Rural à 4 paramètres Journalier) model. To ensure accuracy, conceptual models must be calibrated using historical data to fine-tune their parameters. Once calibrated, these models can provide reliable predictions under various conditions.

Lumped models simplify the catchment area by treating it as a single or a few interconnected units, assuming uniformity within each unit. They are fairly straightforward and require less data, which makes them beneficial for large-scale areas or regions with limited data availability. On the other hand, distributed models divide the catchment into multiple small units, each having its own parameters and inputs. This approach enables a more detailed spatial representation and comprehension of hydrological processes at smaller scales, but it also adds complexity and increases the data requirements of the model (Beven & Kirkby, 1979).

Finally, event models are used to simulate short-term hydrological events like storms or floods. They aim to predict how a watershed will respond to a specific rainfall event with a high level of detail and precision. In contrast, continuous models simulate the long-term behavior of hydrological processes over extended periods. They capture the ongoing interactions between precipitation, evaporation, soil moisture, and streamflow. Continuous models are valuable for gaining insight into and managing water resources, assessing the effects of land use changes, and planning for sustainable water supply and demand (Feldman, 2000).

Among many hydrological models, rainfall-runoff models are the most used in hydrological practices and are the most crucial part of the water resources management procedure. The choice of model for the study depends on specific objectives, data availability, and the desired level of detail. For the sake of data availability and the purpose of our study, conceptual-lumped models are used.

1.2. Study Importance

In recent times, more than a fifth of the world's basins have witnessed significant changes in their surface water area. These changes include both rapid increases, which are indicative of flooding, as well as rapid declines, which suggest drying up of lakes, reservoirs, wetlands, floodplains, and seasonal water bodies (UN-Water, 2021).

Furthermore, it is worth noting that only 0.5% of Earth's water is usable and available freshwater, and this supply is being dangerously impacted by climate change. In fact, over the past two decades, terrestrial water storage, which encompasses soil moisture, snow, and ice, has been decreasing at a rate of 1 cm per year, posing significant challenges to water security (WMO, 2021). Addressing issues related to watershed management, particularly the development of bridges and dams and predicting the consequences of flooding, requires a complete understanding of low water levels and flood dynamics. Problems can arise at any point in the river system, making it essential for hydrologists to have accurate data for model parameterization. However, direct flow measurements are not always available at the specific hydrographic points of interest. More often, hydrologists have access to precipitation data, which is generally more abundant and better spatially distributed than runoff data. This is the reason that naturally leads to an interest in rainfall-runoff models which make it possible to reconstitute or complete runoff series from existing rainfall series. They also make it possible to predict the flow rates of a watercourse from simulated rainfall. Simulation can be done at different time steps. Hence, to accurately simulate rainfall-runoff models that closely resemble physical phenomena, it is ideal to use the finest possible time step. This ensures that all the processes involved in converting rain to flow are considered with utmost precision. However, in certain cases, this approach can be cumbersome and unnecessary. When it comes to managing dams for resource regulation purposes, there is no need to study them on a daily basis. A monthly or even annual time step is sufficient, especially for large reservoirs, as it allows for a broader perspective without getting lost in the details (Mouelhi, 2003).

Sometimes, the objectives of hydrological studies extend beyond simulating runoff to include variables such as snow cover and soil moisture (e.g. Parajka & Blöschl, 2008; Riboust et al., 2019; Li et al., 2018; Nan & Tian, 2024). In these cases, remote sensing data plays a pivotal role by providing crucial information that enhances the accuracy, scope, and reliability of models.

Remote sensing offers a broad, consistent, and real-time source of data for various hydrological variables, which are often difficult to measure directly on the ground due to logistical, financial, or environmental constraints. This technology enables the monitoring of large and inaccessible areas, making it indispensable for comprehensive water resource management, especially in regions where ground-based data is sparse or unavailable.

In mountainous regions, snow cover data from remote sensing is particularly valuable. Snowmelt is a critical component of the hydrological cycle, significantly contributing to river flows and groundwater recharge. Satellite-based snow cover data provide accurate and timely information on the extent, distribution, and dynamics of snowpacks. This information is essential for predicting snowmelt runoff, which in turn helps in forecasting streamflow, managing reservoirs, and mitigating flood risks. Without remote sensing, monitoring snow cover in remote and high-altitude regions would be challenging, leading to less accurate hydrological models and water resource management plans. Additionally, these data help understand and manage the impacts of climate change in mountainous regions, where changes in snowfall patterns, snow cover duration, and snowmelt timing due to global warming can significantly alter water availability.

Soil moisture is another valuable variable in hydrological modeling, influencing processes such as infiltration, evapotranspiration, and runoff generation. When ground-based soil moisture data are unavailable, remote sensing provides an invaluable alternative. Satellites equipped with microwave sensors, like those in the Soil Moisture Active Passive (SMAP) mission, offer reliable soil moisture measurements at various depths and spatial resolutions. These data improve the accuracy of hydrological models, especially in agricultural areas, arid and semi-arid regions, and during drought conditions. Furthermore, integrating remote sensing data into hydrological models supports emergency response and disaster management. Accurate soil moisture data contributes to more precise flood forecasting and landslide risk assessment, enabling quicker decision-making and more effective disaster preparedness and response efforts.

This study uses remote sensing-based variables to accurately model two mountainous watersheds in Türkiye, where snowmelt affects streamflow, and three watersheds in Guinea, where soil moisture is critical for agriculture.

1.3. Study Objectives

Water resource management is a critical global challenge that requires precise and comprehensive hydrological modeling. Rainfall-runoff models are essential tools for effective watershed management. They enable the prediction of flow rates and assist in designing and placing infrastructure, such as bridges and dams. These models also help anticipate the consequences of flooding, which allows for better planning and mitigation strategies. By integrating precipitation data into hydrological models, we can enhance our understanding and management of water resources. This, in turn, contributes to more resilient and sustainable watershed management practices.

Hydrological modeling at different time scales, such as daily, monthly, and annual, provides a detailed understanding of the temporal dynamics of water resources. Daily modeling captures short-term variations and extreme events, while monthly modeling reveals seasonal patterns and water availability. Annual modeling, on the other hand, offers insights into long-term trends and the overall water balance. Addressing these varying time scales is crucial for comprehensive water resource management, flood prediction, and agricultural planning.

Remote sensing technology has revolutionized the field by providing valuable data on key hydrological variables. In regions with diverse hydroclimatic conditions, such as Türkiye's temperate mountainous areas and Guinea's humid tropical regions. Incorporating remote sensing data into hydrological models can significantly enhance prediction accuracy and reliability. This study focuses on leveraging remote sensing data to improve hydrological modeling in these various climatic conditions.

In this study, the objectives aimed to achieve are:

- **Evaluating Temporal Dynamics:** Conduct rainfall-runoff modeling at daily, monthly, and annual time steps to understand short-term variations, seasonal patterns, and long-term trends in hydrological processes, enhancing the overall understanding and management of water resources.
- **Applying Multiple Algorithms:** Calibrate daily model with Calibration Michel, DEoptim, and hydroPSO to effectively explore the parameter space and allow for assessment of the model's parsimony and equifinality.
- **Integrating Remote Sensing Data:** Utilize MODIS Cloud Gap Filled (CGF) snow cover data and SMAP SPL4SMGP soil moisture data obtained from remote sensing technologies to enhance the accuracy of hydrological models in two Turkish mountainous basins and three Guinean watersheds.
- **Assessing Streamflow Pattern:** Assess the impact of including remote sensing data on discharge patterns through multi-criteria optimization, focusing on the contributions of snowmelt to streamflow in Turkish

mountainous basins and soil moisture dynamics in Guinean watersheds, to enhance water resource management.

1.4. Thesis Organization

This thesis is organized into five main parts. The Introduction (Chapter 1) provides background information, emphasizes the importance of the study, and states the objectives. GR Models and Functioning (Chapter 2) explains the GR hydrological models, introduces criteria for evaluating the models, and discusses algorithms for optimizing the objective function. Study Areas (Chapter 3) provides detailed descriptions of the Çukurkışla, Kayabaşı, Niger, Milo, and Sokotoro watersheds, as well as the hydro-meteorological and remote sensing data used. Hydrological Modeling Results (Chapter 4) presents findings from both single-objective and multi-objective calibrations, assessing the performance of different algorithms in simulating hydrological processes. Finally, Conclusion and Recommendations (Chapter 5) summarizes the key findings, highlights practical implications for water resource management, and suggests directions for future research to improve hydrological modeling practices.

2. GR MODELS AND FUNCTIONING

2.1. GR Models

For a long time, researchers have been engaged in a process of understanding the water cycle by looking into the interactions that exist between precipitation and runoff. To understand these interactions, hydrological models are created. They allow hydrologists to decode the mystery of the complex water cycle process. Thus, they have become essential and indispensable tools in a wide range of fields, encompassing urban planning, construction of hydraulic infrastructure, flood prevention, and forecasting, climate change investigations, assessment of anthropogenic influences, analysis of the impacts of natural disasters, and even the reconstruction of ancient climates, and so forth. Among many hydrological models, rainfall-runoff models are the most used in hydrological practices and are the most crucial part of the water resources management procedure. Rainfall-runoff modeling is a part of the Hydrological Sciences. In the early 1980s, CEMAGREF (Centre National du Machinisme Agricole du Génie Rural, des Eaux et des Forêts) the former institute of IRSTEA began developing hydrological models named **G**énie **R**ural (Rural Engineering) – **GR** (Michel, 1983). They were developed with the objective of efficiency and robustness, leading to parsimonious structures and requiring few input data, and easily available, namely Precipitation (P), temperature (T), and discharge (Q) (Perrin et al., 2003). Although these models are sometimes associated with conceptual models because of their reservoir structure, they are empirical models because their structures were built based on large datasets and gradually discovering the structure that allowed reproduction of the best behavior of these models. During its development, new ideas gradually emerged to make it possible to obtain reliable and robust models (Mathevet, 2005). To perform the tests, many data samples were collected from watersheds with a wide variety of characteristics and a wide variety of climatic and hydrological conditions (Perrin C. , 2000). A total of 429 basins, 307 in France, 82 in the United States, 26 in Australia, 10 in Ivory Coast and 4 in Brazil, were examined and used to develop GR models (Mouelhi, 2003).

The GR4J model is the most commonly used in the GR series, including the GR1A, GR2M, GR6J, GR3H, and others. Literary reviews often involve comparing the performance criteria of the different GR models with other rainfall-runoff models. This was done in a study of the water resources in southeast Australia, where the GR4J model was applied to 232 gauged and ungauged basins to estimate daily runoff in the region (Vaze et al. 2011). Additionally, a performance evaluation of the GR4J and AWBM rainfall-runoff models was conducted in Australia. In other studies, the SURM and GR4J models were evaluated for the Nazloo River in northwest Iran and the Ouémé in the Save region of Benin. The second study compared the GR4J conceptual model with the semi-distributed GEOSFM model.

J. Vaze, et al. (2011) conducted a comparative study of six rainfall-runoff models in 232 basins to determine the most suitable model for south-eastern Australia. This region, which covers about 1.4 million km^2 and is home to half of Australia's population, has a climate that varies from temperate to arid. Out of the six daily rainfall-runoff models (AWBM, IHACRES, Sacramento, SIMHYD, SMARG, and GR4J), the Sacramento and GR4J models provided the best regionalization results, with a slight advantage over the other four models (a difference in NSE values of about 0.05) (Vaze, et al., 2011). Multiple studies conducted in Benin, Senegal, Iran, Morocco, and Indonesia have shown that the GR4J model consistently produces better results compared to other models. The success of the GR4J model can be attributed to its small number of optimizable parameters, specifically four. In Benin, the GeoSFM model, which is a semi-distributed model, yielded less significant results when considering the size of the basin and the number of meteorological stations available (AGUE, 2014). Similarly, in Iran, while the best-calibrated model was the GR4J model with a best value of 0.62 for the NSE as objective function, the best set of parameters in the calibration process for the SURM model resulted in an NSE value of 0.4 (Rezaie et al., 2014). In Senegal, Traoré, et al. (2014) conducted a study on the Koulountou basin using the GR4J and GR2M models. They found that the Nash criteria for both models were greater than 0.70, and that allowed them to successfully simulate the flow in the Koulountou watershed at the Missirah Gounass gauge. Furthermore, Mouelhi et al. (2013) compared the performance of the GR4J, GR2M, and GR1A models using data from 407 watersheds. Their study revealed that the daily time-step model outperformed the monthly and annual time-step models. Bouanani et al. (2012) studied the Oued Sikkak watershed using the GR1A and GR2M models in Algeria. They obtained satisfactory Nash criteria of 96% and 86.5% for both models, respectively. In Morocco, a comparison was made between the GR4J model and the SWAT model over a calibration period of 17 years. The GR4J model demonstrated its superiority, while the SWAT model failed to meet the satisfactory Nash criterion.

However, the GR4J model showed comparable performance to the SWAT model over a one-year period (Simonneaux et al. n.d). Similarly, in Indonesia, the GR4J model outperformed the NRECA model with calibration and validation Nash-Sutcliffe coefficients of 0.75 and 0.73, respectively (Harlan et al., 2010).

Overall, the GR4J model consistently outperforms other models in various regions, making it a reliable choice for hydrological modeling.

2.1.1. Annual time step model: GR1A

2.1.1.1. Model description

The GR1A model is an empirical hydrological model that operates at an annual time step. It is designed to convert precipitation into streamflow at the watershed scale. The name of the model comes from the French acronym "**G**énie **R**ural à un (**1**) paramètre **A**nnuel". The model was initially developed at CEMAGREF in France during the 1990s, and multiple versions were created. However, the version presented here is the latest one developed by Mouelhi et al. (2006a). The main objective of the model's development was to create a robust and reliable model that can transform rainfall into flow, thereby improving our understanding and management of water resources (Perrin et al., 2010).

2.1.1.2. Model structure

The structure of GR1A is elegantly easy to understand as it consists of a single equation with one free optimizable parameter. The equation demonstrates that the annual flow of a given year is proportional to the rainfall of that year with a runoff coefficient. This coefficient depends on the rainfall of the previous year and the year being considered, as well as the average annual evapotranspiration. It allows the model to acknowledge the influence of climatic factors on hydrological processes and consider the water balance over time by incorporating the effects of climate and antecedent conditions on the flow generation process. Mouelhi (2003), after a systematic search, found that the most effective approach to considering the system's previous state was to limit solely the precipitation of the year before the current year.

Naming the runoff of a given year Q_k, the rainfall of that year as P_k, the rainfall of the year preceding that year as P_{k-1}, and the average annual potential evapotranspiration as E, then the model formula which derives from Turc (1955) formula is given as follows:

$$Q_k = P_k \left\{ 1 - \frac{1}{\left[1 + \left(\frac{0.7P_k + 0.3P_{k-1}}{X \cdot E}\right)^2\right]^{0.5}} \right\} \tag{2.1}$$

where X is the unique parameter of the model to be optimized.

2.1.1.3. Model parameter

There is only one dimensionless, optimizable parameter in GR1A, called X. This parameter acts as a modulating coefficient of potential evapotranspiration and a measure of how basin dynamics affect non-atmospheric exchanges like interactions with nearby basins or deep aquifers. Thus, it represents the rate of exchange between the study's target watershed and its neighboring watersheds, which is always positive and can be less or greater than 1. When it is less than 1, the basin gains water, whereas when it is greater than 1, the basin loses water. The median of X is 0.7, based on a large sample of watersheds. A 90% confidence interval is given as [0.13; 3.5] (Perrin et al. 2007). The simplicity and versatility of the GR1A model contributes to its effectiveness in capturing the intricate dynamics of water flow in diverse hydrological contexts. Mouelhi et al. (2013) conducted a study on how GR(s) models can be applied to improve the simulation of yearly runoff. Their findings indicate that using a model specifically designed for the annual time-step is more effective in simulating annual flow, as opposed to using a model intended for a finer time-step, such as daily, and then aggregating the results.

2.1.2. Monthly time step model: GR2M

2.1.2.1. Model description

The GR2M hydrological model, which stands for “Le modèle du **G**énie **R**ural à **2** paramètres **M**ensuel” in French, is a global conceptual model with two parameters and was initiated at CEMAGREF in the late 1980s, with application objectives in the field of water resources and low water levels. Like all GR models, GR2M is simple to use and requires a few input data to simulate the runoff response of a catchment area in monthly steps, namely precipitation and potential evapotranspiration. Since its first version, it has had several versions, including those of Kabouya, (1990), Kabouya & Michel (1991), Makhlouf, (1994), Makhlouf & Michel, (1994), Mouelhi (2003) and Mouelhi and al.

(2006b). The most recent structure has been developed using a “step by step” approach or “stepwise approach”. It was a question of testing a multitude of interconnected components and retaining only the combination leading to a better performance (Mouelhi et al. 2006b). For the sake of this work, the version of Mouelhi et al. (2006b), which seems to be the most effective, is selected and presented. Empirically, and further to a comparative study with eight other structures of global conceptual rainfall-runoff models, the GR2M model seems to be the most performant (Mouelhi et al. 2013)

2.1.2.2. Model structure

The structure of the GR2M model is composed of two reservoirs: a production store characterized by its content S that fluctuates after an event of rainfall or evapotranspiration with the maximum capacity X1 and a routing store characterized by its content R that controls the transfer function with a capacity of 60 mm (Figure 2.1). The production store accounts for processes such as infiltration, evaporation, interception, and soil moisture storage. As the inputs are precipitation and potential evapotranspiration which behave differently on the production of runoff, two possibilities can occur in the soil reservoir: feeding or removing an amount of water. Therefore, a part of rainfall that reaches S by infiltration updates its level to S1 then evapotranspiration updates it again to S2. The other part of the precipitation or specific rainfall that flows on surface P1 joins the percolated water (P2) from the production store to form running precipitation (P3) that enters the routing phase and updates the routing store level to R1. Watersheds interact with their surroundings through lateral water exchanges, causing the reservoir to either gain or lose water, and that is considered by GR2M through its second parameter X2. Finally, the routing reservoir provides the river water discharge Q. All formulas are recapitulated in Figure 2.2.

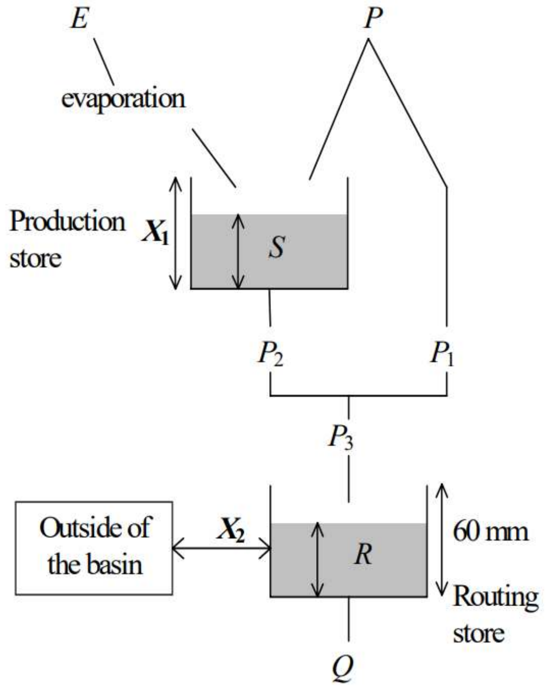

Figure 2.1. *Structure of GR2M rainfall-runoff model (Perrin et al. 2007)*

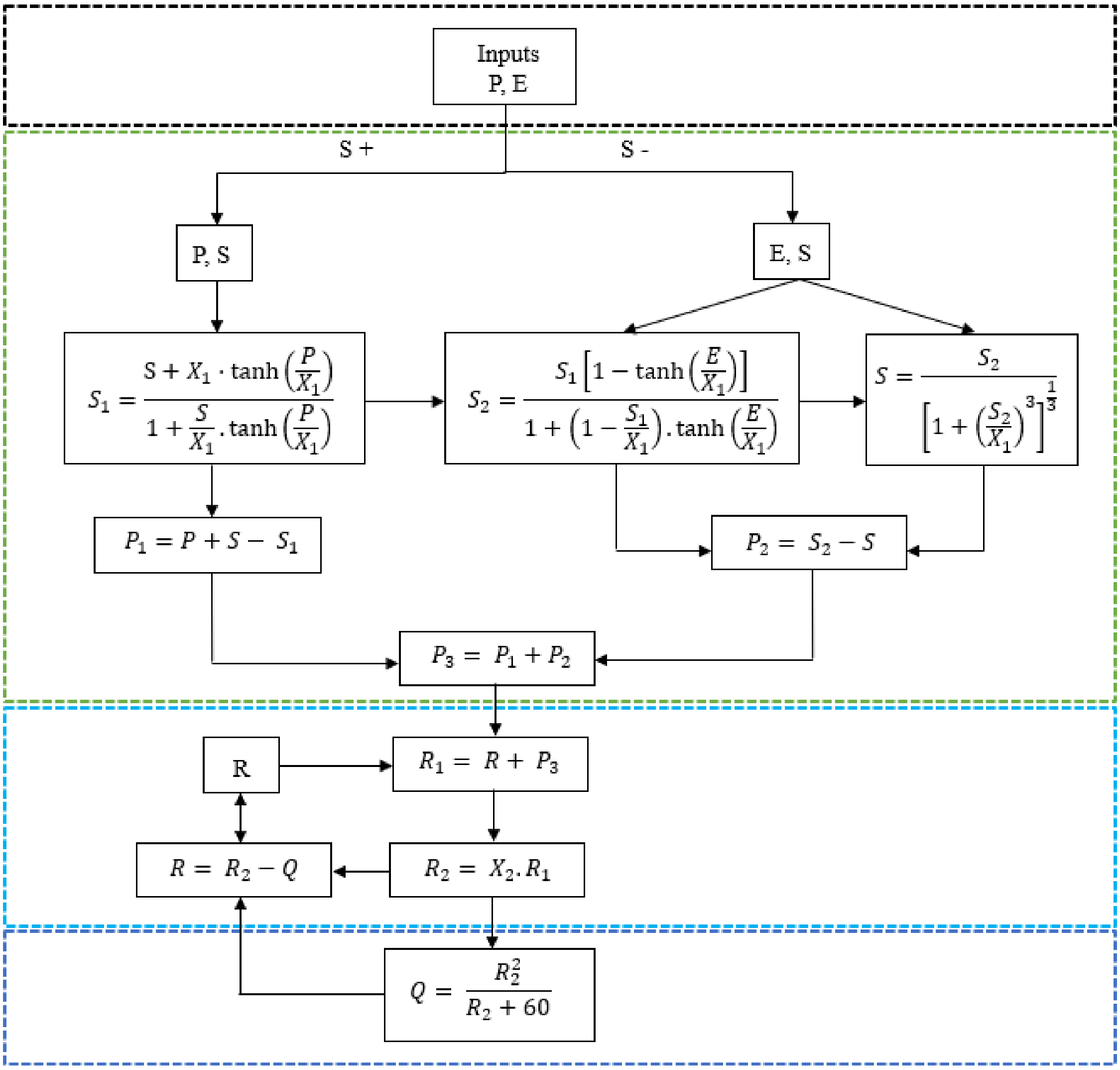

Figure 2.2. *GR2M formulas flowchart*

2.1.2.3. Model parameters

The GR2M model has two free optimizable parameters namely X1 and X2. X1 in millimeters is the maximum capacity of the production store and it controls the production function. When the inflow to the production store exceeds its maximum capacity, any additional water is either spilled or routed out of the store, ensuring that the storage does not exceed its optimal limit. On the other hand, positive and dimensionless, X2 represents the rate of exchange between the system and its surrounding environment like nearby basins or deep aquifers. Its value can be less or greater than 1. When it is less than 1, the basin gains water, otherwise it loses water. On a large sample of watersheds (Perrin et al. 2003), the values of the parameters obtained are given in Table 2.1.

Table 2.1. *Parameters of GR2M and values of median model parameters and approximate 90% confidence intervals (Mouelhi, 2003)*

Parameters	Median	90% confidence intervals
X1: Production Store maximum capacity (mm)	380	140 – 2640
X2 Exchange coefficient (-)	0.92	0.21 – 1.31

2.1.3. Daily time step model: GR4J

2.1.3.1. Model description

The GR4J hydrological model, stands for "Le modèle du **G**énie **R**ural à **4** paramètres **J**ournalier" in French, is a widely used daily rainfall–runoff model in hydrology. Developed in France at the Nationale Research Institute of Science and Technology for Environment and Agriculture (IRSTEA) is a lumped conceptual rainfall-runoff model and is the last modified version of the GR3J model developed by Edijatno & Michel (1989). Its current version was introduced by Perrin et al. (2003) which is simple to use and requires few input data to simulate the runoff response of a catchment area, namely precipitation and potential evapotranspiration. Precipitation in the daily time scale in millimeters (mm) as input can be observed rainfall or forecasted rainfall data at the scale of a specific catchment found by any interpolation method and daily potential evapotranspiration in millimeters (mm) can be estimated by the Oudin formula using daily average temperature or any other common methods including the Penman-Monteith equation or Hargreaves-Samani method. GR4J model simplifies the complexities of hydrological processes, making it an attractive choice for researchers and hydrologists applying it in different sorts of studies for water resources management purposes, predicting river discharge, forecasting flood and drought periods, evaluating the impact of climate change on streamflow, and so forth.

2.1.3.2. Model structure

GR4J's functionality involves partitioning net precipitation (Pn), calculated by subtracting potential evapotranspiration (E) from precipitation (P), into two separate portions (Ps and $Pn - Ps$). The portion Ps finds refuge in the Production Store, one of the two model's reservoirs which is characterized by the maximum capacity of the soil moisture accounting (X1). It percolates gradually over time, while vegetation utilizes a part of this portion for evapotranspiration. The percolated water ($Prec$) from the

Production store joins the second part of net precipitation to form running precipitation (Pr) that enters the routing phase. In this phase, 10% of Pr is directed to the outlet (Qd) via a two-sided unit hydrograph, whilst the one-sided unit hydrograph routes the remaining 90% before being stored in the Routing storage which is the second reservoir of the model characterized by its maximum capacity (X3). The eventually stored water in the Routing store is gradually released by Qr and joins Qd, together to form the total streamflow or the model output (Q), (Figure 2.3).

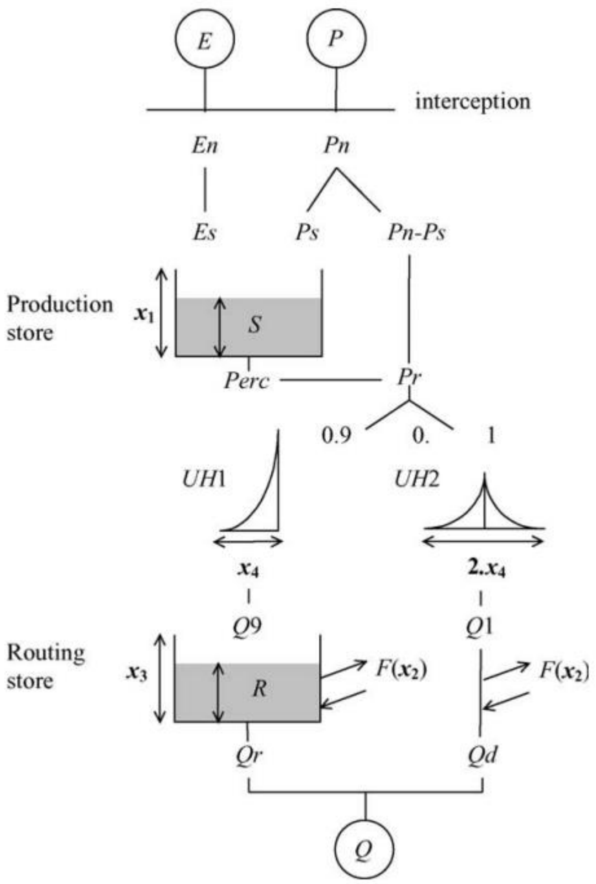

Figure 2.3. *Structure of GR4J rainfall-runoff model (Perrin et al., 2003)*

As mentioned above, GR4J combines a production store, a routing reservoir, as well as two unit hydrographs. So, it consists of two functions: the production function and the routing function.

- ***Production function***

The production store accounts for processes such as infiltration, evaporation, interception, and soil moisture storage. As the inputs are precipitation and potential evapotranspiration which behave differently on the production of runoff, two possibilities can occur in the reservoir: feeding or removing an amount of water. The value of net precipitation must be greater or equal to zero otherwise the net potential evapotranspiration (En) is calculated by subtracting precipitation from potential evapotranspiration. The first case corresponds to the positive value of net precipitation. In that case, the production store is fed by specific rainfall (Ps). That leads to an increase in soil water content level (SM) but cannot be more than its maximum capacity (X1). In case Ps is too much, the reservoir spills out the surplus. If the first condition is not verified, then specific potential evapotranspiration (Es) is removed from the reservoir and that leads to a decrease in soil water content level. The production store provides two types of flow: quick flow on the surface and slow flow from percolation.

- ***Transfer function***

The routing reservoir represents the flow routing and delay processes within the watershed. It allows for the modeling of the runoff's temporal distribution and travel times. The fund running rain (Pr) enters in the routing phase through units hydrographs and routing store as mentioned above. Here, it is needed to find the base time of the unit hydrograph which is the fourth model’s parameter (X4) in day. The value of X4 must be more than half of the day and is equal to the base time of the one-sided unit hydrograph UH1 while it doubles for the second unit hydrograph UH2. The unit hydrograph temporally distributes the volumes of water coming from the production reservoir. The larger the parameter, the more the hydrograph will extend over time and therefore the more the response of the rainfall, returned in the form of flow, will be smoothed over time.

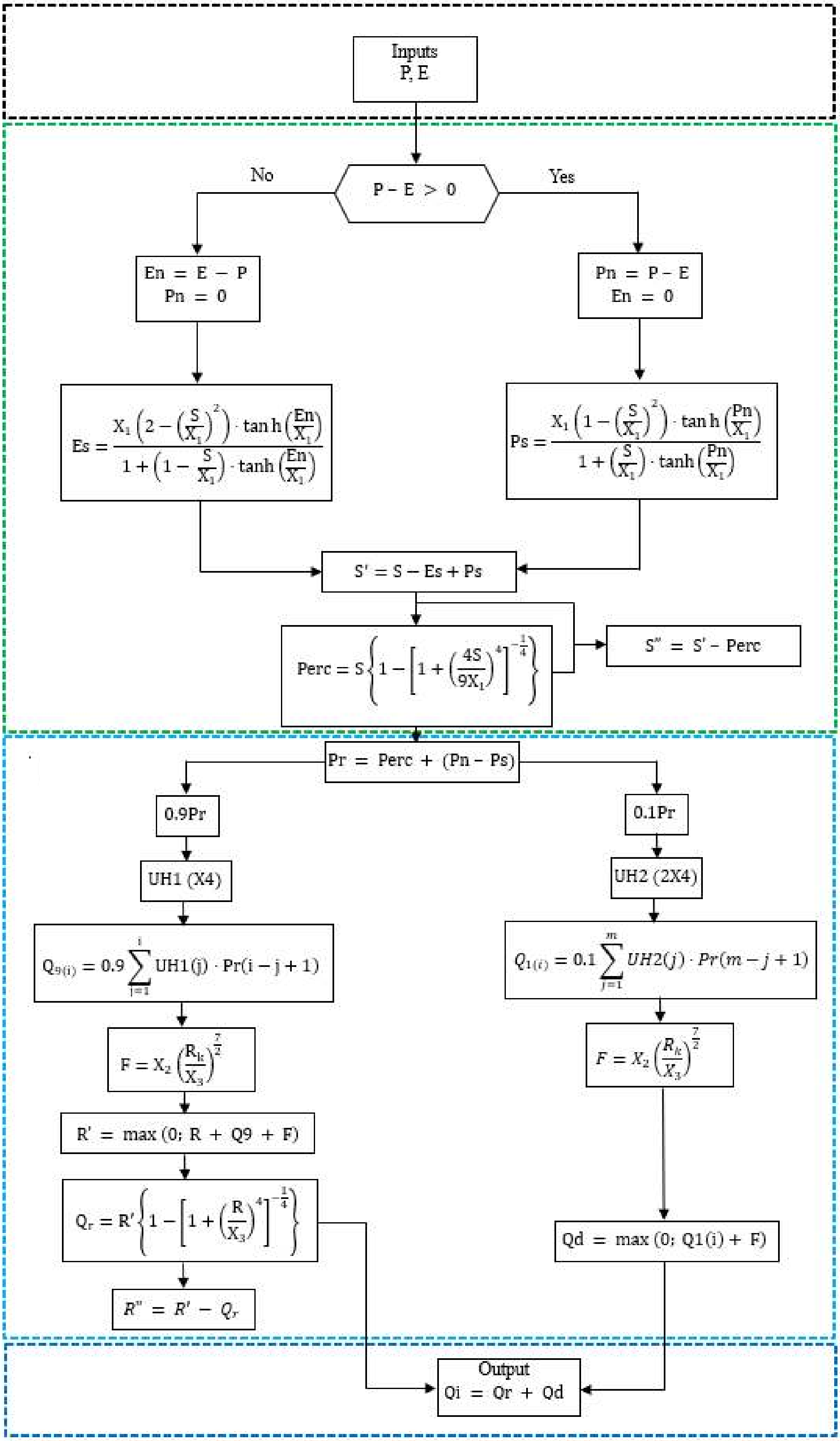

Figure 2.4. *The GR4J formulas flowchart*

2.1.3.3. Model parameters

As mentioned, the GR4J model requires the calibration of four parameters (X1, X2, X3, and X4) to adapt to the specific characteristics of the catchment being modeled. These parameters are linked, and their relationships are explained using integrated equations over a time step. They are typically calibrated using historical precipitation, potential evapotranspiration, and streamflow data. X1 and X3 are model key parameters. However, each of them plays a specific role in simulating the hydrological processes within a catchment. X1 represents the maximum water storage capacity of the soil or production store. It indicates the amount of water the soil can hold before it contributes to runoff. When the soil is not saturated, precipitation fills the production store up to its capacity (X1). This parameter plays a significant role in soil moisture dynamics and infiltration rates. A higher X1 value indicates that the soil can store more water, resulting in less immediate runoff and a gradual release of water through subsurface flow. The amount of water stored in the production store directly affects actual evapotranspiration. Once the production store is filled, the water becomes available for evapotranspiration.

X2 represents the net exchange rate of water between the catchment being modeled and its surrounding catchments or deeper groundwater. It can be positive (indicating a net gain of water from the surroundings) or negative (indicating a net loss of water to the surroundings). X2 adjusts the overall water balance of the catchment by accounting for lateral flows that are not directly measured or observed in precipitation and streamflow data. A higher positive X2 indicates that the catchment is gaining more water from the surrounding areas or deeper groundwater sources, which can increase baseflow and result in higher streamflow levels during dry periods or between rainfall events. With more water gradually being added to the catchment, peak flows following precipitation events might be slightly reduced because the increased baseflow decreases the relative contribution of direct runoff to the total streamflow. On the other hand, a higher negative X2 indicates that the catchment is losing more water to the surrounding areas or deeper groundwater, leading to a reduction in baseflow. This reduction makes the streamflow more reliant on direct runoff from precipitation events, resulting in increased flow variability with higher peaks during storms and lower flows during dry periods. Since the catchment is continuously losing water, it may become less saturated. When precipitation occurs, the reduced antecedent moisture conditions can lead to higher peak flows as the soil's capacity to absorb water is less affected by ongoing losses. Delaigue et al. (2023) illustrated very well flow simulation sensitivity to X2 by varying it from -2 to 2.

X3 represents the maximum storage capacity of the routing store. It affects how runoff is directed and slowed down as it moves through the river network, influencing the shape and timing of the hydrograph. A higher X3 means more water can be stored and released slowly, resulting in a more attenuated (flattened and delayed) hydrograph. On the other hand, lower X3 values lead to quicker runoff responses with sharper hydrograph peaks. X3 also regulates high flows and reduces the risk of flooding by temporarily storing excess water during heavy precipitation and gradually releasing it.

X4 represents the base time of the unit hydrograph, which reflects the speed at which the catchment responds to rainfall. It can be understood as the time it takes for water to travel from the point of precipitation to the catchment outlet. X4 determines when the runoff response to precipitation occurs and affects the time lag between rainfall and streamflow, as well as the duration of the distributed runoff. Higher X4 values cause a delay in the flow peak and become more attenuated because the runoff response to rainfall is spread over a longer period. This means that the peak flow occurs later compared to scenarios with lower X4 values. This can be seen in Delaigue et al. (2023) where flow simulation sensitivity to X4 by varying it from 1 to 3 with 0.5 increment was illustrated.

Table 2.2. *Parameters of GR4J and values of median model parameters and approximate 80% confidence intervals (Perrin et al. 2003)*

Parameters	**Median**	**80% confidence intervals**
X1: Production Store maximum capacity (mm)	350	100 – 1200
X2: Exchange coefficient (mm)	0	-5 – 3
X3: Routing store maximum capacity (mm)	90	20 – 300
X4: Base time of UH1 (day)	1.7	1.1 – 2.9

2.1.4. Snow melt accounting module: CemaNeige

2.1.4.1. Model description

Incorporating a snowmelt module into a rainfall-runoff model enhances its ability to capture the complex interactions between snow, temperature, and precipitation, making it a more comprehensive and accurate tool for modeling and managing water resources in regions with snowfall. CemaNeige is one of them developed by Valéry (2010) at

IRSTEA. It was adopted based on systematic testing to evaluate a large number of ideas from the literature and a large sample of 380 basins in four countries (Canada, France, Sweden, and Switzerland). Its standard version adopted by Valéry et al. (2014b) has two parameters developed specifically for hydrological modeling and is based on a degree-day type approach (Valéry, 2010). It makes it possible to simulate the accumulation and melting of snow in a watershed by taking into account altitudinal and spatial variations to provide a detailed representation of hydrological processes linked to snow. The main purpose of CemaNeige was to improve the modeling of flows at the outlet of the catchment areas by taking into account the contribution of snow. A poor estimate of the quantity of accumulated snow then leads to a less good estimate of the flows during the onset of snowmelt, and this can lead to a significant underestimation of the flood if this snowmelt phenomenon is combined with an extreme precipitation event (Gosset, 2014). It is most often coupled with the GR4J rainfall-runoff model but can be adapted to any global or semi-distributed hydrological model or adapted to finer time steps.

2.1.4.2. Model structure and functioning

The standard version of CemaNeige (Valéry et al., 2014b) has two optimizable parameters and needs daily precipitation and average daily temperature data at the scale of the basin as inputs. However, different areas of a basin can receive different amounts of snow due to the spatial variability of snow. To capture this spatial variability, the basin is divided into distinct altitudinal zones with equal surface areas. Valéry (2010) showed that the discretization of basins in five equal area altitudinal zones, whose limits are determined from the hypsometry of the basin, is sufficient and more than five zones does not improve model performances. This zoning allows for a more detailed consideration of orographic gradients and ensures that the snowpack's evolution is distinct at different altitudes. Temperature, in particular, is known to decrease with altitude, and precipitation tends to be higher at higher elevations. To take these facts into account, the process of CemaNeige can be presented as follows:

- ***Input data extrapolation***

Firstly, precipitation and temperature data are extrapolated to each altitudinal zone from input data.

Precipitation $P(t, zone_i)$ for the altitudinal zone being considered is extrapolated using an exponential function given by the following equation:

$$P(t, zone_i) = P_{basin}(t) + \exp[\beta_{alt} * (Z_{zone_i} - Z_{med\_basin})] \quad (2.2)$$

where $P_{basin}\,(mm.j^1)$ is the input precipitation, $\beta_{alt}\,(m^{-1})$ precipitation altitudinal gradient taking equal to 4.1 $10^{-4}\,m^{-1}$ (Valéry et al. 2010), $Z_{zone_i}\,(m)$ altitude median of the zone being considered, and $Z_{med\_basin}\,(m)$ basin altitude median.

Temperature $T(t, zone_i)$ for the altitudinal zone being considered is extrapolated using a linear function given by the following equation:

$$T_m(t, zone_i) = T_{basin}(t) + \theta_{alt} * (Z_{zone_i} - Z_{med_{basin}}) \quad (2.3)$$

Where $T_{basin}\,(°C)$ is the input temperature, $\theta_{alt}\,(°C.m^{-1})$ is the temperature altitudinal gradient, $Z_{zone_i}\,(m)$ altitude median of the zone being considered, and $Z_{med\_basin}\,(m)$ basin altitude median.

- ***Rain-snow partition***

The snow fraction $\%Snow(t, zone_i)$ in precipitation is determined by linear functions based on the daily average temperature for each zone by using two different methods which depend on the altitude. The first (2.4) comes from Hydrotel (Turcotte et al., 2007) and the second (2.5) from (USACE, 1956).

$$\%Snow(t, zone_i) = 1 - \frac{T_{max}(t, zone_i)}{T_{max}(t, zone_i) - T_{min}(t, zone_i)}\ ; if\ Z_{zone_i} \leq 1500\ m \quad (2.4)$$

$$\begin{cases} \%Snow(t, zone_i) = 0\ ;\ if\ T_m(t, zone_i) \geq 3\ °C \\ \%Snow(t, zone_i) = 1\ ;\ if\ T_m(t, zone_i) \leq -1\ °C\ ; \qquad if\ Z_{zone_i} > 1500\ m \\ \%Snow(t, zone_i) = \dfrac{3 - T_m(t, zone_i)}{4}\ ;\ if\ -1 < T_m(t, zone_i) < 3\ °C \end{cases} \quad (2.5)$$

- ***Snowpack storage***

Within each altitude range, a conceptual reservoir (snow stock) is used to store snow (Figure 2.5). This reservoir represents the snowpack, exclusively fed by the solid fraction of precipitation $P_{sol}(t, zone_i)$ while an amount of melting snow $F(t, zone_i)$ is removed from it in the one-day time interval Δt. The reservoir initially may have inside an amount of snow water equivalent $SWE(t-1, zone_i)$ which represents the previous day's SWE before day t. Then, the day t SWE, which is not limited in volume is given by (Equation 2.6)

$$SWE(t, zone_i) = SWE(t-1, zone_i) + P_{sol}(t, zone_i) - F(t, zone_i) * \Delta t \quad (2.6)$$

- ***Snow thermal state and melting***

The reservoir representing the snowpack has a thermal state that delays the onset of melting and is modulated by the first optimizable parameter (cT). The cold content of the snowpack (eTG) depends on the previous day's eTG and the temperature of the day being considered. The thermal state of the snow cover can be influenced by several factors, including the density of the snow, its water content, and its thermal conductivity. Its value cannot be greater than 0 °C, from which temperature melting starts and is given by the following equation:

$$eTG(t, zone_i) = \min\left(\boldsymbol{cT} eTG(t-1, zone_i) + (1 - \boldsymbol{cT}) * T_m(t, zone_i), 0\right) \quad (2.7)$$

The melting process is regulated at the surface of the snow cover area (SCA). The extent of snow cover on the watershed surface significantly influences the rate of melting. Melting occurs when the altitudinal zone's average air temperature $T_m(t, zone_i)$ is above 0˚C and the snowpack thermal state reaches 0˚C, then the potential melt $F_{pot}(t, zone_i)$, which is based on the degree-day factor K_f (the second optimizable parameter of the model in $mm.°C^{-1}.d^{-1}$) will be positive and will indicate the amount of melted water.

$$F_{pot}(t, zone_i) = \boldsymbol{K_f} * T_m(t, zone_i)\ ;$$
$$if\ eTG(t, zone_i)\ \&\ T_m(t, zone_i) \quad (2.8)$$

Then, the actual melt F_{melt} ($mm.d^{-1}$) from the snow cover area (SCA) depends on the potential melt and snow cover area (Equation 2.9):

$$F_{melt}(t, zone_i) = [0.9SCA(t, zone_i + 0.1)]F_{pot}(t, zone_i) \quad (2.9)$$

The snow cover Area (SCA) is crucial in determining the actual snowmelt instead of potential melting. When the SCA is at 100%, the actual melting will be identical to the potential melting. However, as the SCA decreases, the effective melting rate slows down to a minimum of 10% of the potential melting. F_{melt} is added to the liquid precipitation to constitute the precipitation input of the hydrological model.

The snow cover area and snow water equivalent are linked and SCA is given by:

$$SCA(t, zone_i) = \min\left(\frac{SWE(t, zone_i)}{T_{h,melt}}, 1\right) \quad (2.10)$$

Where $T_{h,melt}$ is the snow stock melting threshold, set at 90% of the annual average snow accumulation in the watershed (Valéry et al. 2014b).

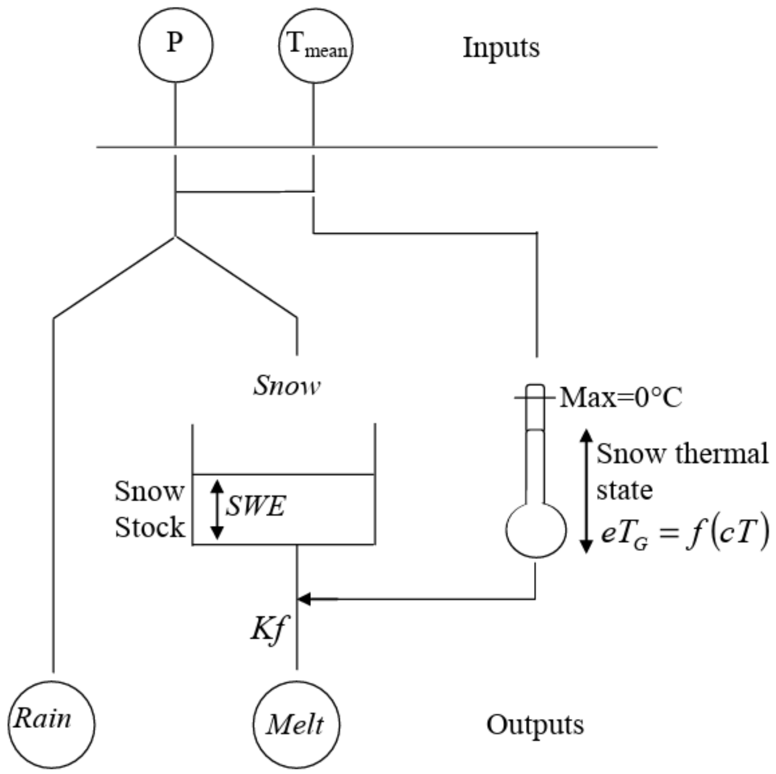

Figure 2.5. *Diagram of CemaNeige snow accounting module (Valéry et al. 2014b)*

2.1.4.3. Model parameters

As mentioned, standard CemaNeige (Valéry et al. 2014b) has two parameters: weighting coefficient and degree-day factor. The thermal state of the mantle weighting coefficient cT or $CNX1$ plays a significant role in determining the inertia or resistance of the snow cover to variations in air temperature. This coefficient represents how quickly or slowly the snow cover responds to changes in air temperature. The value of $CNX1$ typically ranges between 0 and 1. A higher value indicates that the snow cover has more inertia and will change its temperature more slowly in response to changes in air temperature. Conversely, a lower value means that the snow cover will change temperature more quickly. When it is equal to 0, that means the snow cover has no inertia and immediately adopts the air temperature. On the other hand, if it is equal to 1, that indicates the snow cover has infinite inertia and its temperature does not change at all with air temperature variations. The degree-day factor also called melting factor K_f or $CNX2$ is a key parameter in degree-day snowmelt models, representing the rate at which snow melts in response to temperature variations, usually expressed in terms of the number of millimeters of snow depth that melts per degree-day ($mm.°C^{-1}.d^{-1}$ or $mm.°K^{-1}.d^{-1}$). $CNX2$ value can significantly be influenced by local climate, elevation, and snow conditions. Warmer climates or wetter snow conditions might require higher Kf values, while colder climates or drier snow might require lower values. Thus, the World Meteorological Organization proposed a range of melting factors between 2 $mm.°C^{-1}.d^{-1}$ and 5 $mm.°C^{-1}.d^{-1}$ (WMO, 1986). However, a higher value is accepted in some studies (e.g. Morid, et al. (2000)). For instance, Valéry, (2010) suggested kf value between 0 and 20 $mm.°C^{-1}.d^{-1}$.

On a large sample of watersheds, Valéry (2010) obtained the values given in Table 2.3 with 80% confidence intervals.

Table 2.3. *Parameters of CemaNeige and values of median model parameters and approximate 80% confidence intervals (Valéry, 2010)*

Parameters	**Median**	**80% confidence intervals**
CNX1: Weighting coefficient (-)	0.39	0 – 1
CNX2 Degree-day factor ($mm.°C^{-1}.d^{-1}$)	2.45	0 – 20

2.1.5. Snow melt accounting module: CemaNeige with hysteresis

2.1.5.1. Hysteresis and it purpose in CemaNeige

Hysteresis refers to the dependence of the state of a system not only on its current inputs but also on its history. This means that the system's response to an external stimulus depends not just on the current value of that stimulus but also on the path it has taken to reach the current state. In snow hydrology, especially in snow cover dynamics, hysteresis acknowledges that the relationship between Snow Cover Area (SCA) and Snow Water Equivalent (SWE) can vary depending on the previous accumulation and ablation processes. However, traditional snowmelt models often struggle to simulate the complex relationship between SWE and SCA. This is the case of the standard CemaNeige that formulates the SCA-SWE relation based on equation (2.10). For instance, Le Moine et al. (2007) tested on 687 French watersheds including 89 mountain basins the calibration of the model with the evaluation criterion F = ½*NSE(Q) + ½*NSE(SCA) using equation (2.10) and the MODIS observations in SCA. Their results show that the CemaNeige model is not capable of simulating realistic SCA values because of the fixed value of $T_{h,melt}$ taking equal to 90% of mean annual solid precipitation. $T_{h,melt}$ tends to underestimate SCA, therefore, SCA value merely reaches 100% which is in contrast to MODIS data. When the threshold was set to a lower value, SCA performance improved in accumulation but a delay in snow melting was observed.

Based on this observation, a hysteresis that allows simulating a fast increase of the SCA at the accumulation period and a smooth decrease at the ablation period was suggested (Riboust et al., 2019). The study was carried out on 277 French mountain watersheds whose outlet is located above 300 m. The results of this study demonstrated that the original CemaNeige model gives highly satisfactory runoff simulations when it is combined with a rainfall-runoff model, but also its internal snow cover area variable cannot capture the MODIS SCA data. Introducing a hysteresis in CemaNeige made it possible to go beyond the restrictions of the original model by improving the performance of the SCA simulation, without deteriorating the runoff performance. It was admitted after several analyses that the most advantageous compromise for the model's evaluation criterion was a 75% weighting of the flow criterion and an identical weighting of each of the elevation zones with 5% weighting on the SCA criterion (Riboust et al., 2019). Furthermore, considering only the highest elevation zones to calibrate the model was not sufficiently informative and gave unsatisfactory results of SCA validation compared to the other calibration methods. Riboust et al. (2019) tested different SWE-SCA hystereses from the literature (Linear Hysteresis, Modified Linear Hysteresis, MATSIRO Hysteresis, and Swenson Hysteresis), but Modified Linear Hysteresis formulation with a melting threshold depending on annual solid precipitation presented the best results and was retained then was implemented in the airGR package in R environment (Coron et al., 2017; Coron, et al., 2023). Therefore, we will present only this one.

2.1.5.2. Modified linear hysteresis

The modified linear hysteresis is based on the principle of linear hysteresis that was implemented in the Catchment Land Surface Model (CLSM) by Magand et al. (2014). The approach of linear hysteresis assumes that the system's response is proportional to its past state or history, which can be represented using linear relationships between variables. Its modified version purpose by Riboust et al. (2019) brought the dependency between the melting threshold and the total mean annual snowfall ($\overline{P_{sol_{annual}}}$). Hysteresis between SCA and SWE encompasses two phases: Accumulation and Ablation. During accumulation, $\Delta SWE(t, zone_i) \geq 0$, SCA increases quickly to reach its maximum value

(SCA = 1, means that considered altitudinal zone is completely snow-covered) and maintains this value for a while (blue line on Figure 2.6b). When SCA reaches 1 firstly, there is a part of accumulated snow that melts and corresponds to a value of SWE that is accumulation threshold ($T_{h,acc}$), a new parameter. During melting, $\Delta SWE(t, zone_i) < 0$, the SCA value decreases only if the accumulated SWE is lower than the calibrated melt threshold ($T_{h,melt}$) otherwise the local maximal threshold ($T_{h,max}$) takes the maximal SWE value before the beginning of the melt (SWE_{melt}). The local maximum threshold ($T_{h,max}$) determines the point at which the SCA starts to decrease (inflexion point) as the accumulated SWE reaches a certain level and the slope of the melting curve (red line in Figure 2.6b). During winter, if the SWE never exceeds $T_{h,melt}$, or in the case where there is an accumulation of snow after the start of the melting (yellow line in Figure 2.6b), the local maximum threshold takes the maximum value of the snow water equivalent before the onset of melting. All these processes are mathematically written as follows:

$$\begin{cases} SCA(t, zone_i) = \min\left(\dfrac{SWE(t, zone_i)}{T_{h,max}}\ ,\ 1\right);\ if\ \Delta SWE(t, zone_i) < 0 \\ SWE_{melt}(t, zone_i) = SWE(t-1, zone_i)\ ;if\ SCA(t-1, zone_i) = 1 \end{cases} \quad (2.12)$$

$$T_{h,max} = \begin{cases} T_{h,melt};if\ SWE_{melt}(t, zone_i)\ >\ T_{h,melt} \\ SWE_{melt}(t, zone_i)\ ;if\ SWE_{melt}(t, zone_i)\ <\ T_{h,melt} \end{cases} \quad (2.13)$$

$$T_{h,melt} = \overline{P_{sol_{annual}}}.R_{sp} \quad (2.14)$$

Where R_{sp} is a parameter between 0 and 1.

Riboust et al. (2019) formulated a linear function that depends on an accumulation threshold $T_{h,acc}$ based on the dependency of the snow cover curve on the SWE in the case of snow accumulation (Equations 2.15 & 2.16).

$$\Delta SWE(t, zone_i) =\ P_{sol}(t, zone_i) - F_{melt}(t, zone_i) \quad (2.15)$$

$$SCA(t, zone_i) = min\left(SCA(t-1, zone_i) + \frac{P_{sol}(t, zone_i)}{T_{h,acc}}, 1\right);$$
$$if\ \Delta SWE(t, zone_i) \geq 0 \quad (2.16)$$

This parametrization of snowmelt dynamics introduces flexibility and realism by incorporating local thresholds and conditional behavior based on accumulated snow water equivalent (SWE). It allows for better simulation of snow cover evolution, especially in regions where snow accumulation and melting processes are complex and variable. Previously, SCA-SWE relationship was regulated in CemaNeige (Valéry et al. 2014b) by a fixed threshold $T_{h,melt}$ taking equal to 90% of mean annual solid precipitation (Figure 2.6a)

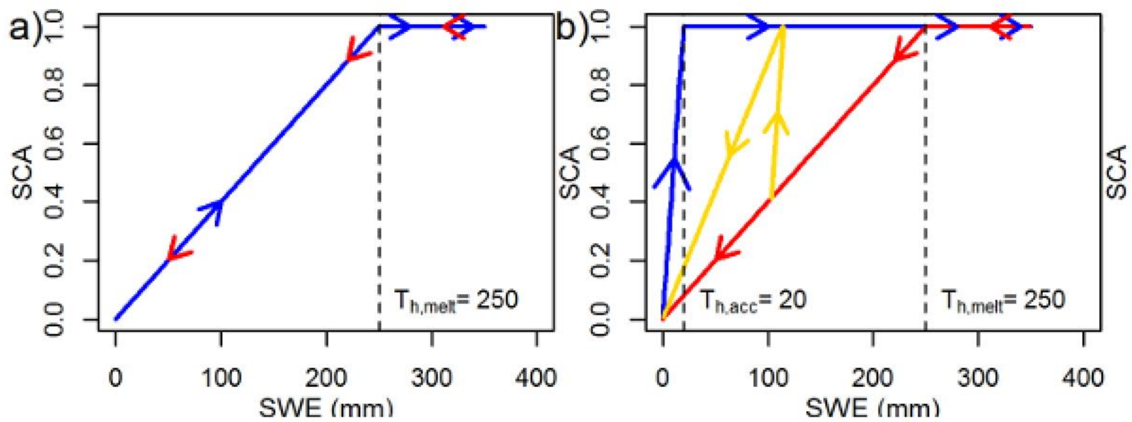

Figure 2.6. *Linear relationship between SCA and SWE (blue: accumulation, red: melting, yellow: transition between accumulation and melting). a) Snow accumulation and melting in Valéry et al. 2014. b) Snow accumulation and melting with linear hysteresis proposed by Riboust et al. (2019)*

2.1.5.3. Model parameters

In the version of CemaNeige with hysteresis introduced by Riboust et al. (2019), two additional parameters are incorporated alongside the original parameters from the version by Valéry et al. (2014a, b). These new parameters are the solid precipitation coefficient (R_{sp}) and the accumulation threshold ($T_{h,acc}$). R_{sp} or CNHX1 is a regulating coefficient of the average annual solid precipitation that influences snow cover area determination. It ranges between 0 and 1, where 0 represents no influence of solid precipitation and 1 represents full influence. Optimizing R_{sp} provides a better representation of local precipitation characteristics and flexibility to adapt the model to different regions and climates. This is not the case in the standard version, where R_{sp} is set to 0.9. $T_{h,acc}$ is the second optimizable parameter introduced in the model. It represents a threshold value used in the formulation of the snow cover curve during the accumulation phase. This parameter allows for optimization to better capture snow accumulation dynamics and hysteresis effects. In his doctoral thesis, Riboust, (2018) found that the flow performance is minimally sensitive to $T_{h,acc}$, while the snow cover area (SCA) simulation is significantly influenced by it. Out of 277 watersheds studied, the median $T_{h,acc}$ value was 11 mm. To reduce model equifinality (multiple parameters sets producing similar results) and calibration time, Riboust suggested setting $T_{h,acc}$ at 10 mm.`

2.2. Testing Model Performance

After checking data availability, the first step in hydrological modeling is to select the model structure and estimate the model parameters with precision in order to simulate the hydrological systems' behavior successfully. As most parameters are unknown and cannot be measured or somehow calculated in advance, model calibration is required. Modelers are called to define a criterion, often based on minimizing the difference between observed and simulated data (objective function). Therefore, it implies trying various combinations of model parameters to find one that minimizes (or maximizes, depending on the objective function) to effectively optimize the model's ability to represent the hydrological system being studied. Literature provides many objective functions that can be used in rainfall-runoff models. We called Y_i^{Obs} the i^{th} observation value being evaluated; Y_i^{Sim} the i^{th} simulated value; Y_{mean}^{Obs} the mean of observed data; Y_{mean}^{Sim} the mean of simulated data; σ^{Obs} the observed data standard deviation ; σ^{Sim} the simulates data standard deviation; and n the total number of observations. On the following lines, some calibration criteria are presented.

2.2.1. Nash-Sutcliffe efficiency: NSE

Nash & Sutcliffe, (1970) developed an efficiency criterion named after them and is a commonly used metric in hydrological modeling to evaluate the goodness of fit between observed and simulated data. It is given as follows:

$$NSE = 1 - \frac{\sum_{i=1}^{\eta}\left(Y_i^{0bs} - Y_i^{Sim}\right)^2}{\sum_{i=1}^{n}\left(Y_i^{0bs} - Y_{mean}^{Obs}\right)^2} \tag{2.17}$$

$$logNSE(Q) = 1 - \frac{\sum_{i=1}^{\eta}\left(\log\left(Q_i^{0bs}\right) - \log\left(Q_i^{Sim}\right)\right)^2}{\sum_{i=1}^{n}\left(\log\left(Q_i^{0bs}\right) - \log\left(Q_{mean}^{Obs}\right)\right)^2} \tag{2.18}$$

NSE ranges from $-\infty$ to 1.0, with 1.0 being the best possible value for the observed and simulated data. An NSE value close to 1.0 means that the model's simulations closely reflect the observed data, and they fit the 1:1 line well. Conversely, an NSE close to $-\infty$

implies that the model performs worse than a simple mean of the observed data (Moriasi, et al., 2007). The key limitation of NSE is the fact that it squares the differences between observed and simulated values leading to larger discrepancies and can lead to overestimation of errors for high values while underestimating errors for lower values. This can lead to misleading results, especially during critical hydrological events (Legates & McCabe, 1999). To overcome this fact, some researchers combined NSE with its logarithmic value to capture peak and low flows (e.g. Duethmann et al, (2014), Parajka & Blöschl, (2008), Nan & Tian, (2024)) instead of NSE they use other metrics such as the Root Mean Square Error (RMSE), Kling-Gupta Efficiency (KGE), or Percent Bias (PBIAS) (e.g. Troin et al, (2015); Yi et al. (2018); Li et al, (2018); Uysal et al, (2024)) to provide a more comprehensive assessment of model performance.

2.2.2. Kling-Gupta efficiency: KGE

Kling-Gupta efficiency is a metric proposed by Gupta et al. (2009) and is composed of three components (Equation 2.18): Pearson correlation (r), bias ratio (β), and variability ratio (α). In their work, Kling et al. (2012) proposed a revised version of KGE named modified Kling-Gupta Efficiency (KGE') in which the bias and variability rates are not cross-correlated and the variability ratio is (γ) (Equation 2.19). The two versions are written as follows:

$$KGE = 1 - \sqrt{(r-1)^2 + (\beta-1)^2 + (\alpha-1)^2} \tag{2.19}$$

$$KGE' = 1 - \sqrt{(r-1)^2 + (\beta-1)^2 + (\gamma-1)^2} \tag{2.20}$$

where:

$$r = \frac{\sum\left(Y_i^{Obs} - Y_{mean}^{Obs}\right)\left(Y_i^{Sim} - Y_{mean}^{Sim}\right)}{\sqrt{\sum\left(Y_i^{Obs} - Y_{mean}^{Obs}\right)^2 . \left(Y_i^{Sim} - Y_{mean}^{Sim}\right)^2}} \tag{2.21}$$

$$\beta = \frac{Y_{mean}^{Sim}}{Y_{mean}^{Obs}} \tag{2.22}$$

$$\alpha = \frac{\sigma^{Sim}}{\sigma^{Obs}} \tag{2.23}$$

$$\gamma = \frac{\sigma^{Sim} / Y_{mean}^{Obs}}{\sigma^{Obs} / Y_{mean}^{Sim}} \tag{2.24}$$

The KGE value ranges from −∞ to 1, and its interpretation varies among researchers. Some authors interpret a negative KGE value as indicating poor or "bad" model performance, suggesting that the mean of the observed values provides better estimates than the model simulations (Schönfelder et al., 2017; Andersson et al., 2017). However, others argue against attaching such a straightforward interpretation to negative KGE values. A positive KGE signifies that the model simulations are in agreement with the observed data, capturing the key characteristics of the hydrological system being modeled; the closer it is to 1 the better it is.

2.2.3. Pearson's correlation coefficient r and r^2

In 1895, Bravais Pearson came up with the mathematical formula (Kim, et al., 2021)) named after him which is one of the most commonly used methods for assessing the relationship between numerical variables (Equation 2.20). It assigns a value between -1 and 1, where: 1 represents a perfect positive correlation, and −1 represents a perfect negative correlation. When it is positive, that indicates that as one variable increases, the other variable also increases linearly. Conversely, its negative value would show an inverse relationship. Finally, when it is 0 that indicates no linear correlation between the two variables. Although it is widely used due to its simplicity and ease of interpretation, a good correlation does not always imply causation and other considerations like p-value are often required to establish causality.

R-squared correlation, also known as the coefficient of determination (r^2), is the squared of Pearson correlation which is a crucial metric in regression analysis.

$$r^2 = \left(\frac{\sum_{i=1}^{n} \left(Y_i^{Obs} - Y_{mean}^{Obs}\right)\left(Y_i^{Sim} - Y_{mean}^{Sim}\right)}{\sqrt{\sum_{i=1}^{n} \left(Y_i^{Obs} - Y_{mean}^{Obs}\right)^2} \sqrt{\sum_{i=1}^{n} \left(Y_i^{Sim} - Y_{mean}^{Sim}\right)^2}} \right)^2 \tag{2.25}$$

The range of r^2 lies between 0 and 1 and measures how well the regression model captures the variability observed in the dependent variable. A value of 0 indicates that the regression model fails to explain any variability in the dependent variable and 1 suggests that the regression model perfectly explains all variability in the dependent variable. However, a higher value of r^2 does not necessarily mean that the model is a good fit or that it is the best model. It simply indicates that the model explains a large proportion of the variability in the dependent variable.

2.2.4. Root mean squared error: $RMSE$

Root mean squared error (RMSE) quantifies the average magnitude of the residuals, which are the differences between observed and predicted values (Equation 2.25). It serves as a consolidated metric to quantify the overall error magnitude of a predictive model. RMSE is calculated by taking the square root of the average of the squared differences between observed and predicted values and is written:

$$RMSE = \sqrt{\frac{\sum_{i=1}^{n}(Y_i^{Obs} - Y_i^{Sim})^2}{n}} \tag{2.26}$$

The RMSE value can range from 0 to ∞ and its intuitive interpretation makes it a widely adopted metric for evaluating model accuracy. Its lower values signify better model performance and higher predictive accuracy. Therefore, when it is equal to 0, that means the model made no errors. However, RMSE does not provide insights into the direction of the errors (overestimation and underestimation), and it may not always capture the full picture of model performance. Hence it should be used in conjunction with other evaluation metrics and considerations to provide a comprehensive assessment of model performance.

2.2.5. Deviation of runoff volume: D_v

The Deviation of Runoff Volumes (D_v) or percentage bias ($PBIAS$), established by the World Meteorological Organization (WMO) in 1986, quantifies the disparity between modeled and observed runoff volumes. It quantifies the difference between modeled and observed runoff volumes, offering insights into the model's accuracy in simulating hydrological processes, and is given as follows:

$$D_v = 100\left[\frac{\sum_{i=1}^{n}\left(Y_i^{Sim} - Y_i^{Obs}\right)}{\sum_{i=1}^{n}\left(Y_i^{0bs}\right)}\right] \tag{2.27}$$

D_v can take both values (positive and negative) and provide a straightforward and intuitive measure of bias in model simulations. Zero is the optimal value of D_v that indicates no bias and accurate model simulation. Low-magnitude values reflect accurate model simulation with minimal bias. Besides, positive values indicate that biases are overestimated while negative values may lead to underestimation of bias, meaning the model tends to predict values that are smaller than observed. PBIAS values for streamflow tend to vary more, among different autocalibration methods, during dry years than during wet years. This fact should be considered when attempting to do a split-sample evaluation, one for calibration and one for validation (Moriasi et al. 2007).

2.3. Calibration Optimization Algorithms

Calibration, as mentioned in Section 2.2, involves adjusting model parameters to achieve the best fit between observed and simulated data. This process is complex and challenging because hydrological models usually have multiple parameters that require simultaneous calibration. Thus, manual calibration or trial-and-error methods can be time-consuming, inefficient, and often lead to suboptimal solutions. Therefore, optimization algorithms are crucial in this regard. They efficiently search complex parameter spaces, minimize errors between observed and simulated data, and ensure robust and accurate parameter estimation during hydrological model calibration. Many algorithms are available in the literature from global to local; deterministic to metaheuristic via stochastic but only those used in our work are presented here.

2.3.1. Steepest descent algorithm (step-by-step method) in GR models

The step-by-step optimization algorithm is an iterative method that refines an initial solution to find the best possible outcome. It consists of four main steps: initialization, iteration, criterion acceptance, and criterion stopping.

Initialization involves selecting an initial solution and defining a stopping criterion, which can be a maximum number of iterations or a minimum desired improvement. During the iteration stage, the current solution is evaluated, and a new solution is generated by making a small modification to the current solution. This modification can include adding, removing, or modifying an element of the solution. The new solution is then evaluated. The acceptance criterion compares the new solution with the current one. If the new solution is better (according to a defined criterion, such as an objective function to be minimized), it replaces the current solution; otherwise, the current solution is kept. Finally, the stopping criterion is checked to see if the predefined condition has been met (for example, the maximum number of iterations or a lack of significant improvement). If the condition is not met, the algorithm returns to the iteration stage; otherwise, it stops.

The step-by-step optimization methods are commonly employed for combinatorial optimization problems where finding an optimal solution in one step is challenging.

The PAP_GR step-by-step optimization algorithm in GR was initially proposed by Michel (1989) and further developed by Edijatno (1991) for GR models. It is a local algorithm that can start from multiple points. Mathevet (2005) enhanced this approach by introducing a method to eliminate vectors of unlikely parameters through a global search, aiming to find a starting point closer to the optimum. By coupling these two algorithms, Magnand demonstrated that they work effectively and efficiently together, contributing to more accurate and robust optimization of hydrological models. Consequently, this led to two steps of search: global search and local search.

2.3.1.1. Global search step

During the global search phase, the parameters space is thoroughly explored by using distribution quantiles. These quantiles, specifically the 16.66, 50, and 83.33 percentiles, are assigned to each parameter interval. By testing all possible combinations using these quantiles, a total of $3^{n_{param}}$ combinations (where n_{param} is the number of model parameters) are considered. This exhaustive search is crucial in finding promising starting points for the subsequent local optimization step. It guarantees that the algorithm initiates its fine-tuning process from a region that is likely to contain optimal solutions. The whole process of seed point generation (Mathevet 2005) is given below (Figure 2.7).

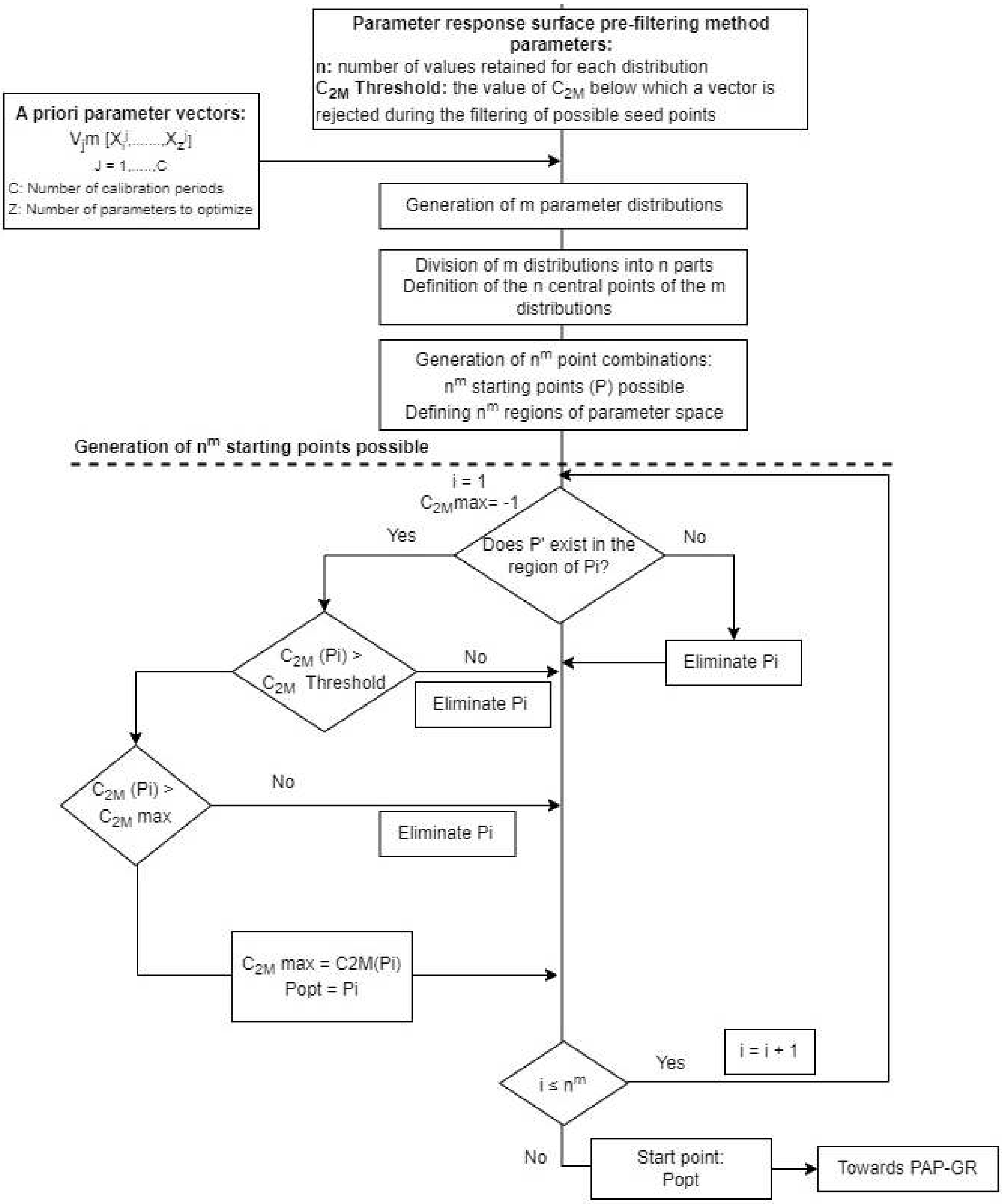

Figure 2.7. *Flow diagram of global search algorithm of seed generation (Mathevet 2005)*

2.3.1.2. Local search step

The second step employs a gradient-based calibration algorithm. Parameters are adjusted one by one with a variable step size, depending on the optimization's progress. If performance consistently improves over several iterations (indicating a consistent direction of optimization), the step size increases to speed up calibration. Conversely, if no improvement is observed, the step size decreases. The algorithm terminates when the step size falls below a certain threshold, indicating convergence and stable model performance (Riboust, 2018).

The whole process of stable model performance generation (Mathevet 2005) is given below (Figure 2.8)

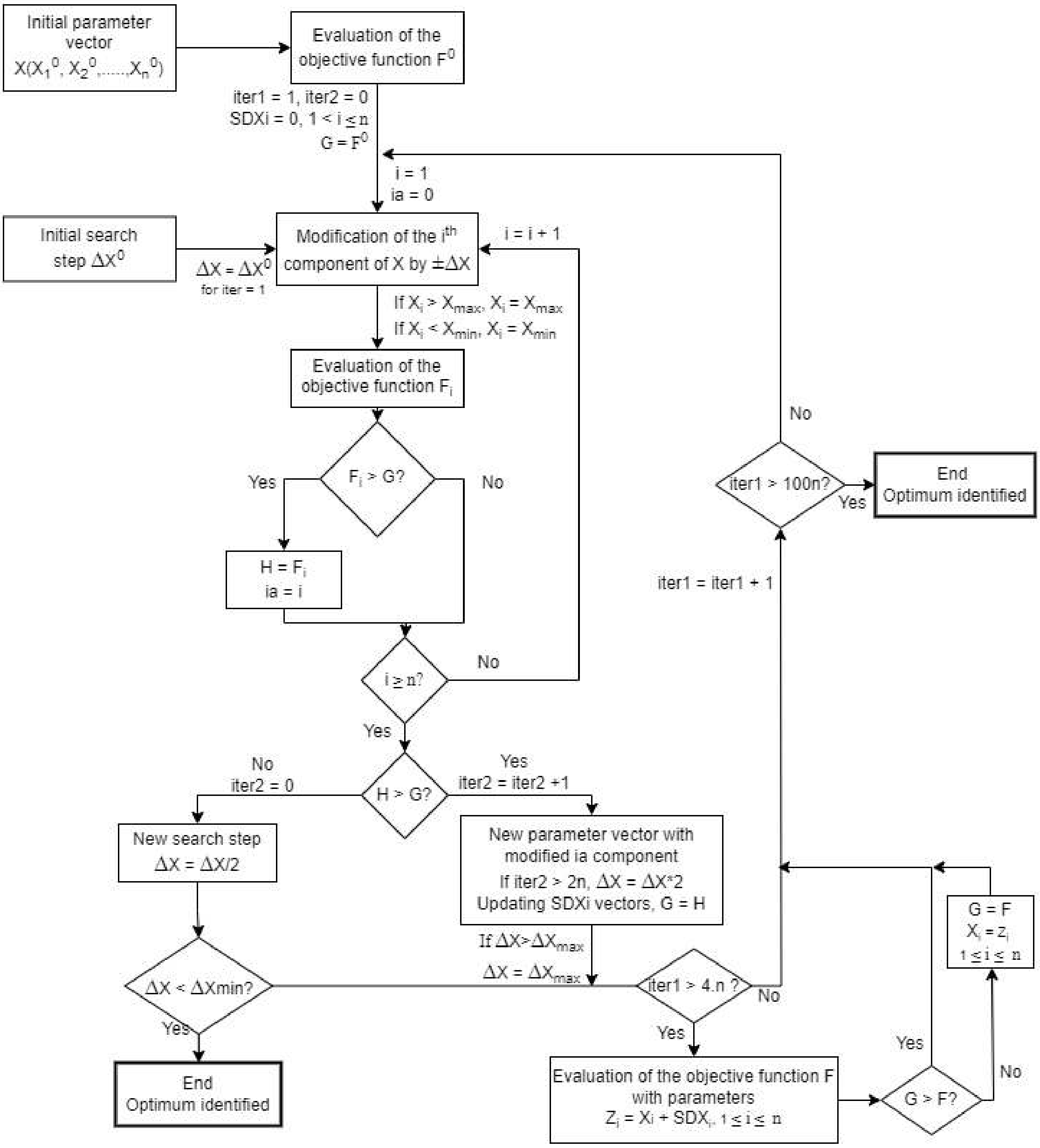

Figure 2.8. *Flow diagram of global search step by step calibration algorithm stable model parameters generation (Michel, 1989 & Edijatno, 1991 in Mathevet, 2005)*

In the airGR package (https://cran.r-project.org/web/packages/airGR), the optimization algorithm underwent a name change in the 1.0.1 release. Initially known as

"Calibration_HBAN," it was renamed to "Calibration_Michel" in honor of its creator, Michel (NEWS (r-project.org)).

2.3.2. Differential Evolutive optimization algorithm

Differential Evolution (DE) is a stochastic, population-based heuristic search strategy for continuous domains which is a branch of evolutionary programming, developed by Storn & Price in 1995 (Karcı, 2017). It is particularly useful for solving nonlinear, non-differentiable, and complex optimization problems. The whole logic behind this powerful algorithm is divided into five steps: Initialization, mutation, crossover, selection and stopping criterion (condition).

Initialization involves generating an initial population of candidate solutions for each solution (i.e., the model's parameters). These candidate solutions are represented as vectors in the search space, with each vector component corresponding to a variable in the problem. In the mutation phase, a mutation operation is applied to each solution in the population, creating new solutions by combining multiple existing ones. Subsequently, crossover is performed between the mutated and original solutions to produce a child solution. One common approach for crossover is using binomial crossover, where each component of the child solution is selected from either the mutated or original solution, with a crossover probability denoted as CR. The selection phase involves comparing the child solution with the original solution. If the child solution is better, then the original solution is replaced by the child solution in the population. This process of mutation, crossover, and selection repeats until a stopping criterion or condition is met. For instance, the stopping criterion could be a maximum number of iterations, a tolerance for solution improvement, or a maximum execution duration. A comprehensive flow diagram is given in Figure 2.19

DEoptim (Ardia & Mullen, 2010) is the implementation of DE global optimization algorithm in the R language for statistical computing.

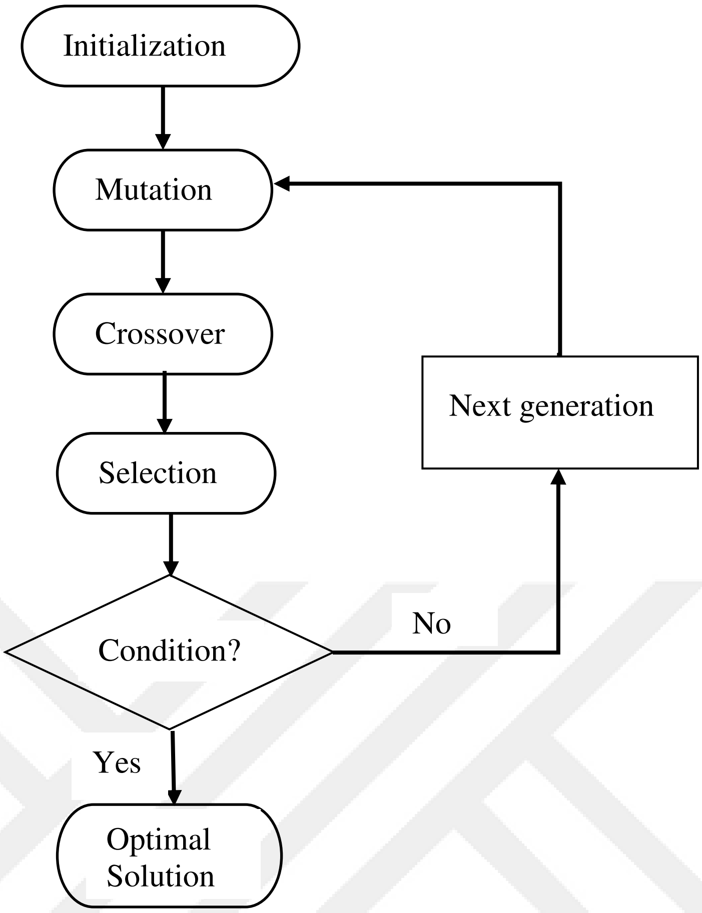

Figure 2.9. *Flow diagram of Differential Evolutive (DE) optimization algorithm*

2.3.3. Particles swarm optimization algorithm

Particles Swarm Optimization (PSO) is a population-based optimization algorithm inspired by the social behavior of birds flocking or fish schooling. It was developed by Kennedy & Eberhart (1995). It was developed to optimize continuous functions and is widely used in various application fields. The basic idea of PSO is to evolve a swarm of particles in the search space to find the best possible solution. Each particle represents a potential solution to the optimization problem and is characterized by its position and velocity in the search space.

Initialization involves generating an initial population of particles (i.e., the model's parameters), each associated with a random initial position in the search space and a random initial velocity. Then, the current position in the search space of each particle is calculated based on the objective function to evaluate the quality of each particle. The local best position for each particle is determined by considering the best quality it has encountered so far, known as the personal best position (pBest). If its current quality is better than its personal best, then its personal best is updated; otherwise, its current quality is maintained. Among all the personal best positions (pBest) of particles, the best personal quality is selected as the global best position (gBest). Once the global best position is selected, the speed and position of each particle are updated based on its current speed, current position, personal best position (pBest), and global best position (gBest) of the group. If the stopping criterion is reached, the algorithm stops, or the process is repeated until this criterion is reached. The stopping criterion can be a maximum number of iterations, a tolerance for improvement of the solution, or a maximum execution time (Figure 2.10)

hydroPSO is a global optimization R package implementing a state-of-the-art version of the PSO algorithm, with a special focus on the calibration of environmental models (Zambrano-Bigiarini & Rojas, 2013). hydroPSO is a model-independent tool that allows users to easily integrate any computer simulation model with the calibration engine (PSO). It communicates with the model using the model's input and output files, eliminating the need to have access to the model's source code. Essentially, hydroPSO only requires information about the specific model parameters that need to be calibrated and where to write them. hydroPSO package is made of two main functions: $hydromod()$ which is used to returns a goodness-of-fit value and $hydroPSO()$ having as arguments fn, $lower$, $upper$, $method$, $control$ and $model.FUN$. fn uses hydromod for objective function. $Lower$ and $upper$ define the lower and upper boundary of model parameters. There is more than one method available, one of them is "$spso2011$". $control$ is a list of control parameters which defines all conditions. $model.FUN$ is optional and is used only if fn is set to $hydromod$. For more information one could check out this link https://github.com/hzambran/hydroPSO.

It is important to note that the 'hydroPSO' package is no longer available on CRAN but there is a way to link it from $github$ and use it, if one wanted.

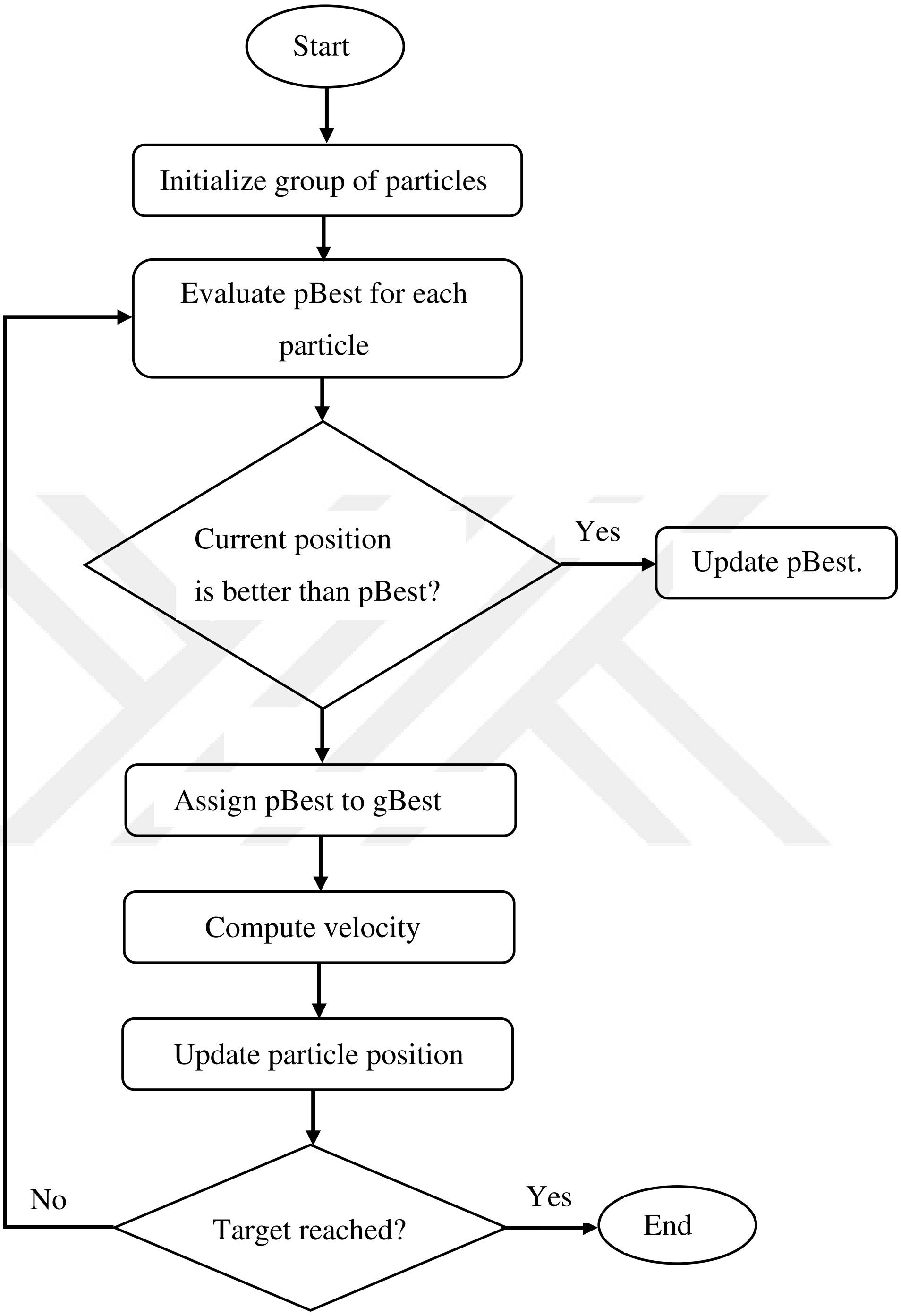

Figure 2.10. *Flow diagram of Particles Swarm Optimization (PSO) algorithm*

3. MATERIALS AND METHOD

3.1. Study Areas

3.1.1. Türkiye

Located between 35° 54' 9" to 42° 1' 37" N and 25° 54' 33" to 44° 34' 27" E, Türkiye is a transcontinental country with a small part in southeastern Europe (Eastern Thrace) and the majority situated on the Anatolian Peninsula in Western Asia. It is bordered by Greece, Bulgaria, and the Marmara Sea to the northwest, the Black Sea to the north, Georgia to the northeast, Armenia, Azerbaijan, and Iran to the east, Iraq, Syria, and the Mediterranean Sea to the south, and the Aegean Sea to the west. Its total area is 783,562 km^2 and it has a coastline length of 8,333 km.

Türkiye has diverse climatic regions due to its varied topography mainly made up of two mountain ranges in the south and north with a central plateau. Running parallel to the southern coast, the Taurus Mountains act as a natural barrier between the Mediterranean coastal region and the central Anatolian plateau. This mountain range is characterized by rugged terrain and substantially impacts the climate and precipitation patterns in the surrounding areas. The Pontic Mountains also contribute to the country's diverse topography in the northern part and along the Black Sea. The proximity to the Black Sea influences the climate in this region, bringing about higher precipitation and contributing to the lush green landscapes. The Anatolian Plateau is a vast elevated region positioned between the Taurus Mountains and the Pontic Mountains and constitutes the heartland of Türkiye and has a more arid and continental climate compared to the coastal areas. The plateau is essential for agriculture and has been a historically significant region due to its central location in the country. Coastal areas generally have a Mediterranean climate, while inland areas experience more continental climates. The eastern part of the country has a more mountainous and harsher climate (Figure 3.1). The average annual precipitation, around 574 mm, is lower than the average value for the entire Earth. The water year starts on the 1st of October of the previous year and finishes on the 30th of September.

As part of this thesis, two Turkish watersheds were selected: one in the southern part of the country, characterized by a Mediterranean climate, and the other in the eastern part, characterized by continental climatic conditions. The first presents varied reliefs, seasonal precipitation and land use dominated by intensive agriculture and urbanization.

The second is marked by mountainous terrain, less abundant rainfall, and an increased importance of pastoral breeding. These geographical and climatic divergences between the two watersheds induce varied impacts on hydrological and environmental aspects, thus underlining the choice of these two in order to highlight the robustness of the GR models in the Turkish context. Below, a concise presentation of these two watersheds is undertaken.

Figure 3.1. *Türkiye physical map* mapsofworld.com

3.1.1.1. Çukurkışla watershed

The Göksu Basin, which lies in the eastern part of the Middle Taurus orogenic belt within the boundaries of the Adana section of the Mediterranean region, extends in the northeast-southwest direction, is located between 37° 33' - 38° 40' north latitudes and 35° 35’ - 36° 41’ east longitudes (Karaosmanoglu, 2021). Çukurkışla (Figure 3.2) constitutes a sub-basin of the Göksu watershed, itself located in the Seyhan hydrological network, one of the 26 main hydrological basins of Türkiye, whose flow ends into the Mediterranean Sea. The Stream Gauging Station (AGİ: Akım Gözlem İstasyonu) is the Çukurkışla Station identified under the reference E18A024 which is managed by State Hydraulics Works (DSİ: Devlet Su İşleri). The area drains by this station is 1524.36 km^2.

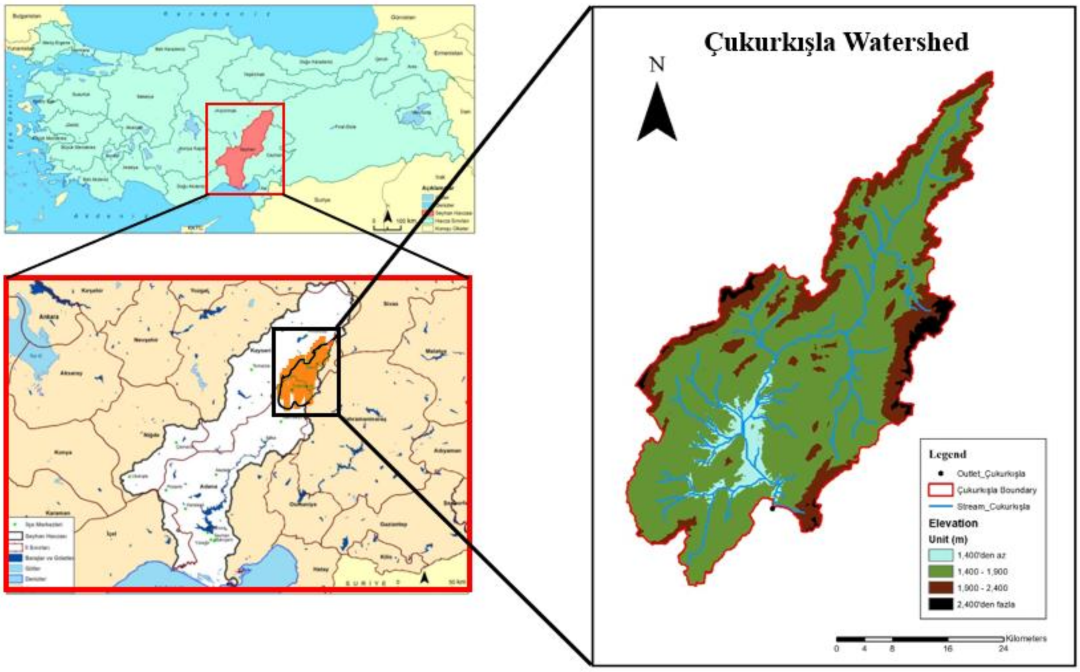

Figure 3.2. *Localization of Çukurkışla watershed in Türkiye*

The morphometric characteristics were extracted from the Digital Elevation Model (DEM) by using geographic information system technics. These allow us to see that the most common altitudes are between 1,299m and 1,800m representing 70% of the total area of the Çukurkışla watershed. The altitudes over 2,400m represent less than 3% of the total area. The mean and maximum elevations are 1,716m and 2954m respectively (Figure 3.3-a). Çukurkışla watershed is characterized by relatively steep slopes upstream in the northwestern and the southeastern parts, then, the slope decreases downstream. The extreme slope, which is the slope above 50%, occupies 10% of the basin's total area and the gentle slope (0 – 10%) occupies 26.75% of the area (Table 3.2). The mean slope is 23.65% (Figure 3.3-b). The aspect of a slope affects the amount of solar radiation it receives and therefore influences evapotranspiration and snowmelt. In the northern hemisphere, south-facing slopes receive more direct sunlight than north-facing slopes. In Çukurkışla the aspect of the east-south and west-north slopes are 30,23% and 27.19% of its area (Figure 3.3-c). According to the Copernicus Global Land Service (CGLS) 2015 global Land Cover product at 100 m spatial resolution, Çukurkışla land cover is dominated by herbaceous vegetation (65,58%), cropland (21.41%) and all types of forests occupy only (8.61%) that can be seen in (Figure 3.3-d). All types of land cover of this classification are given in Table 3.1.

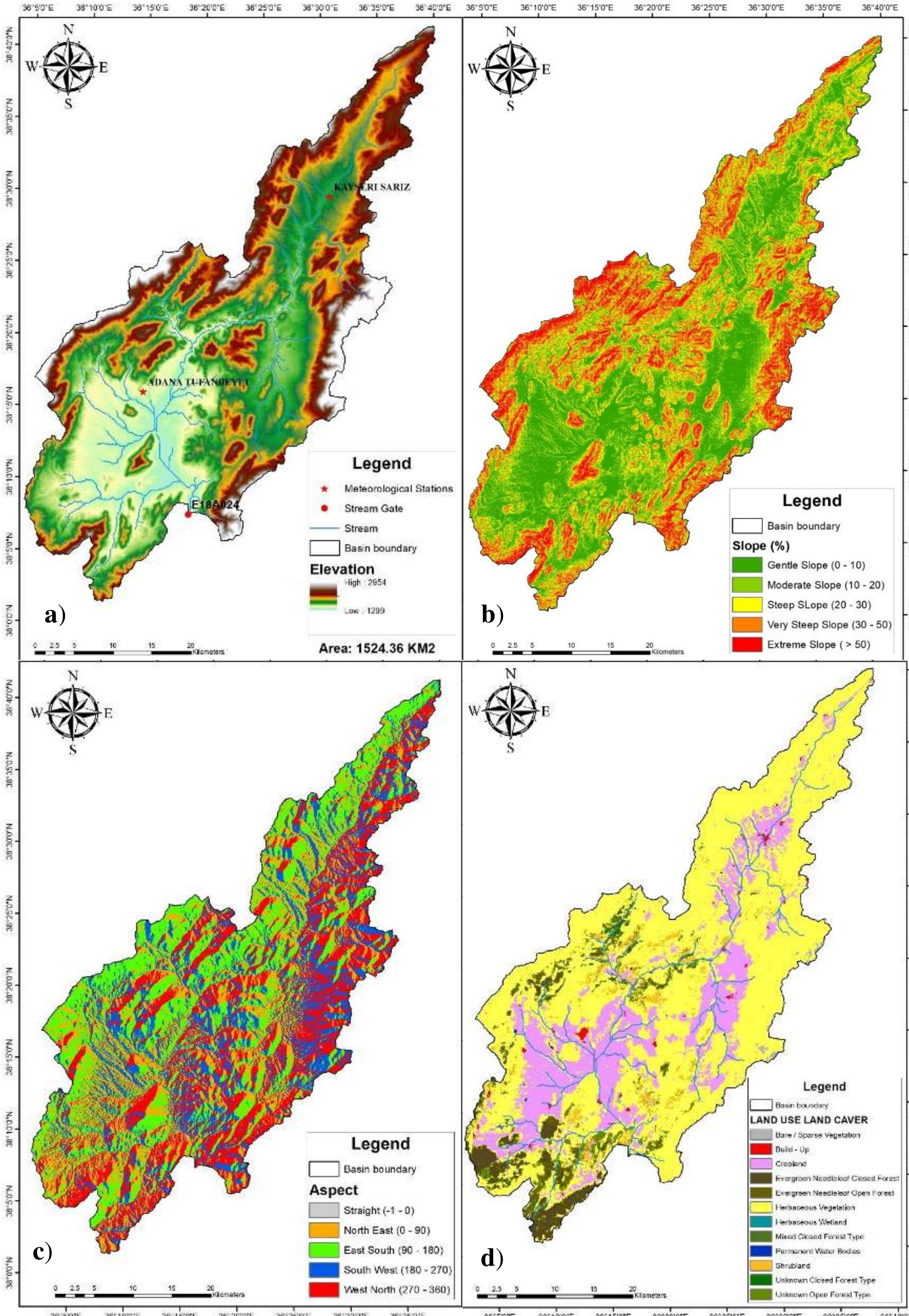

Figure 3.3. *Çukurkışla basin physical characteristics maps from geospatial data: a) Digital Elevation Model map; b) Slope map;* ***c****) Aspect map; and d) Land cover map (CGLS 2015)*

Table 3.1. *Çukurkışla watershed land cover type classification*

Label	Area (Km^2)	Area (%)
Shrubland	53.85	3.53
Herbaceous Vegetation	999.62	65.58
Cropland	326.42	21.41
Build-Up	7.87	0.52
Bare / Sparse Vegetation	4.41	0.29
Permanent Water Bodies	0.88	0.058
Herbaceous Wetland	0.02	0.001
Evergreen Needleleaf Closed Forest	39.32	2.58
Mixed Closed Forest Type	0.04	0.003
Unknown Closed Forest Type	2.10	0.14
Evergreen Needleleaf Open Forest	34.24	2.25
Unknown Open Forest Type	55.60	3.65

Quantitative measurements allow geomorphologists to objectively compare different landforms and to calculate less straightforward parameters that may be useful for identifying a particular characteristic of an area (Keller & Pinter, 1996). To characterize the relief of the basin, we plotted the altitude distribution curve, also called the hypsometric curve. This distribution is obtained by using the DEM of the watershed in the ArcGIS software using the "reclassify" tool, which generates the surfaces whose altitude is lower than a given altitude (Table 3.2). The result obtained from this classification was entered in MS Excel to construct the hypsometric curve (Figure 3.4-a). The same work was done to plot the slope distribution curve (figure 3.4-b), and its distribution is given in Table 3.2.

Table 3.2. *Altitude and slope distribution of basin areas of Çukurkışla watershed*

Altitude (m)	Area (km^2)	Area (%)	Slope (%)	Area (km^2)	Area (%)
2954	0	0	206.4792	0	0
2600	17.07	1.12	120	0.29	0.02
2400	44.36	2.91	70	31.48	2.07
2200	93.44	6.13	50	152.94	10.03
2000	207.77	13.63	40	297.37	19.51
1800	464.02	30.44	30	493.83	32.40
1600	857.45	59.25	20	744.87	48.86
1400	1443.11	94.67	10	1116.75	73.25
1299	1524.36	100.00	0	1524.36	100

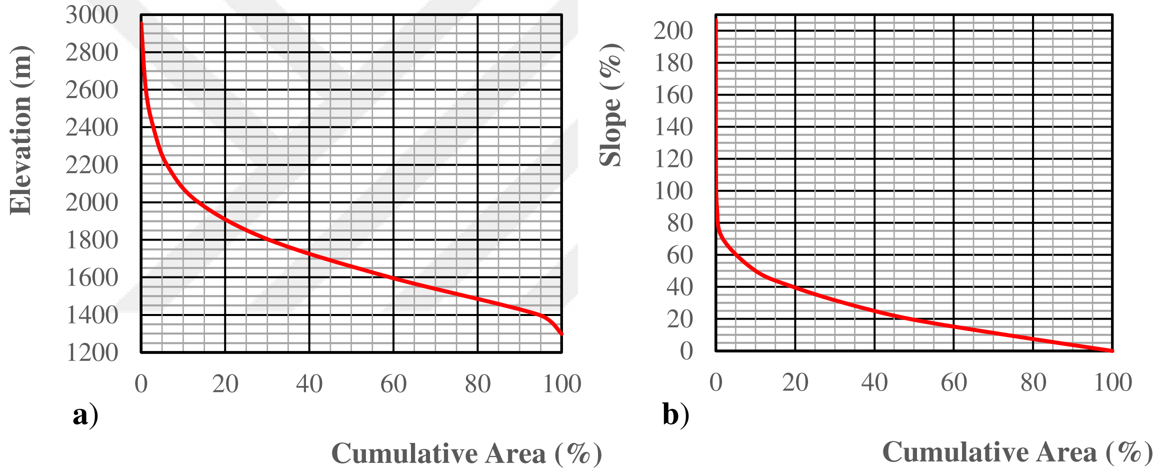

Figure 3.4. *Çukurkışla distribution curves. a) hypsometric curve, b) slope distribution curve*

Çukurkışla is a basin where snowmelt contributes significantly to spring and summer runoff. Thus, to consider the effect of snow on hydrological modeling, the snow module CemaNeige snow which works by dividing the basin into elevation zones of equal area (Table 3.3; Figure 3.5-a) was considered. Furthermore, to run CemaNeige in airGR, the basin hypsometric data (altitude in meters) is needed from 0 to 100% by step 1% (i.e. 101 increasing values).

Based on F. Karaosmanoğlu, (2021) studies at the scale of the Göksu watershed, Soil types of the Çukurkışla basin are as follows: colluvial soils, non-calcareous brown soils, non-calcareous brown forest soils, bare rocks, and - alluvial soils (Figure 3.5-b).

Table 3.3. *Çukurkışla watershed into five equal elevation area zones*

Zone	Elevation range (m)	Average elevation (m)	Area (Km^2)
1	1299 - 1477	1412.26	306.21
2	1482 - 1590	1536.49	303.37
3	1596 - 1727	1660.80	302.94
4	1734 - 1912	1811.82	304.59
5	1924 - 2954	2176.03	307.25

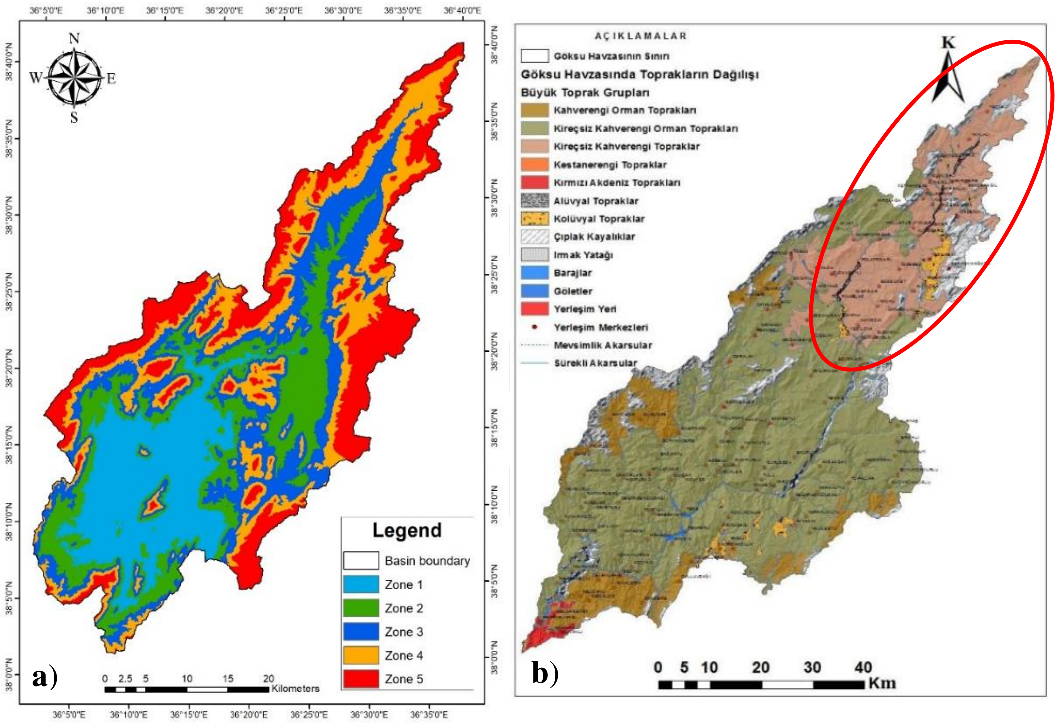

Figure 3.5. *Five elevation zones and soil types in Çukurkışla. a) Çukurkışla watershed in 5 equal area zones; b) Göksu watershed soil type classification map (Karaosmanoğlu, 2021) where Çukurkışla is highlighted in a red ellipse*

3.1.1.2. Kayabaşı watershed

The Aras basin in northeastern Türkiye is one of the 26 main hydrological basins of the country. The Aras River, after which the basin is named, from Bingöl mountain flows through northeastern Türkiye, forming part of the border between Türkiye and Armenia, before continuing towards Iran and Azerbaijan, where it joins the Kura River to flow into the Caspian Sea. Kayabaşı (Figure 3.6), situated in Upper Aras in Erzurum and Kars provinces, is located between 39° 52' - 39° 18' north latitudes and 41° 10' - 41°

55' east longitudes and has a flow observation station identified under the reference D24A096 which drains area of 2727.36 km^2.

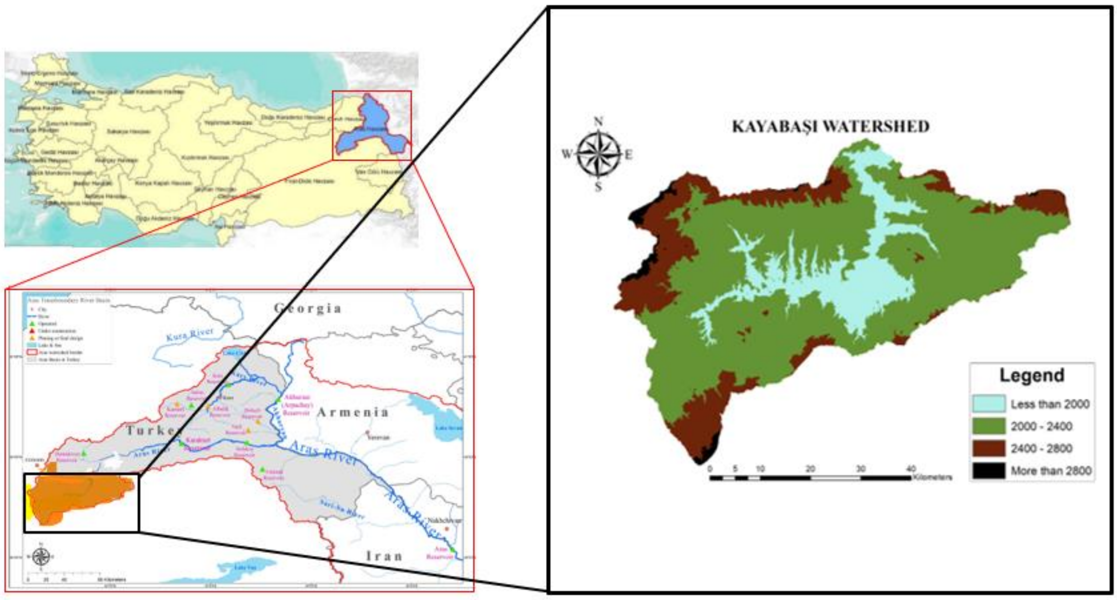

Figure 3.6. *Localization of Kayabaşı watershed in Türkiye*

The morphometric characteristics were extracted from the Digital Elevation Model (DEM) using geographic information system technics. These allow us to see that the basin altitudes are between 1,679 m and 3,155 m which is above 1167m the country's average altitude, therefore mountainous. The altitudes below 2,400m represent 80% of the total area and more than 5% is above 2800m. The mean elevation is 2,214m (Figure 3.7-a). Kayabaşı watershed is characterized by relatively steep slopes upstream in the northern part, then, the slope decreases downstream. The extreme slope, which is the slope above 50%, occupies 2.37% of the basin's total area and the gentle slope (0 – 10%) occupies 34.26% of the area (Table 3.5). The mean slope is 16.77% (Figure 3.8-b). In Kayabaşı, the slope aspect of the four directions is almost identical and all above 20% of its area (Figure 3.7-c). According to the Copernicus Global Land Service (CGLS) 2015 global Land Cover product at 100 m spatial resolution, Kayabaşı land cover is dominated by herbaceous vegetation (95,61%), cropland (3.93%), and all types of forests occupy less than 1% that can be seen in (Figure 3.7-d). All types of land cover of this classification are given in Table 3.4.

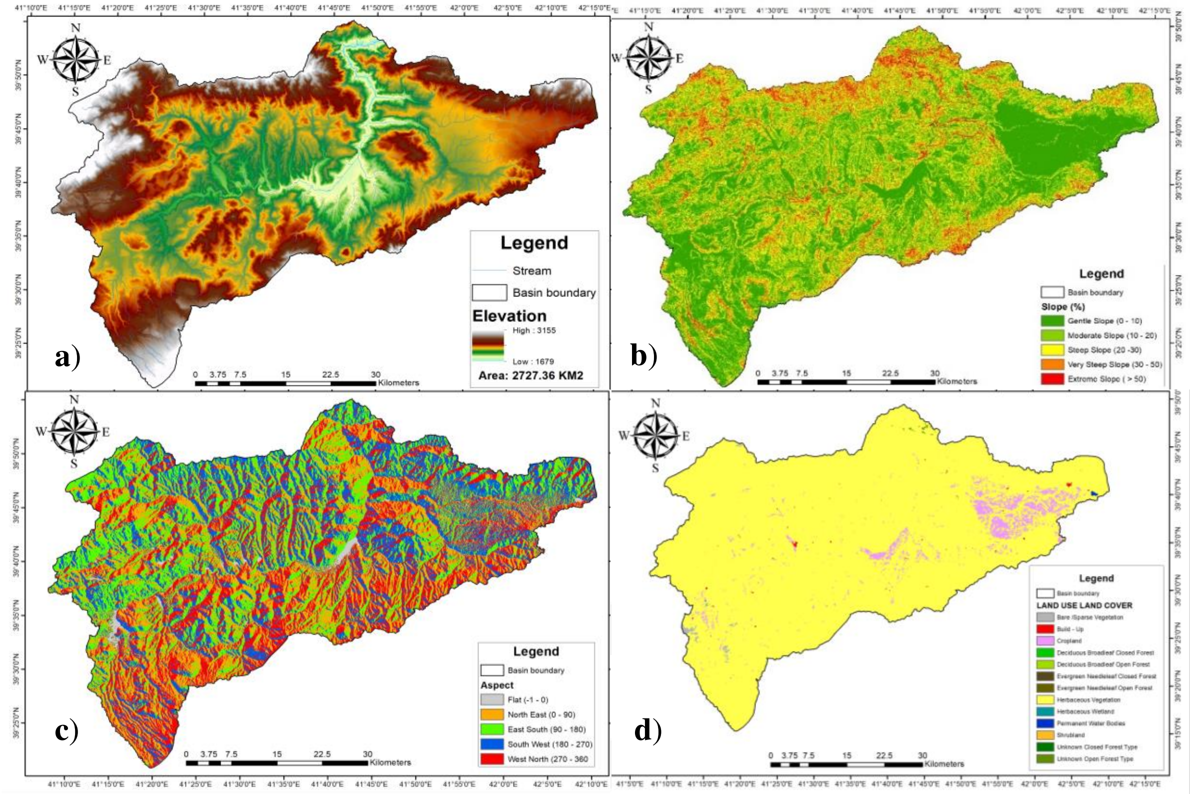

Figure 3.7. *Kayabaşı watershed physical characteristics maps from geospatial data: a) Digital Elevation Model map; b) Slope map;* **c***) Aspect map; and d) Land cover map (CGLS 2015)*

Table 3.4. *Kayabaşı watershed land cover type classification*

Label	Area (Km^2)	Area (%)
Shrubland	2.81	0.001
Herbaceous Vegetation	260765.48	95.611
Cropland	10711.75	3.928
Build-Up	294.53	0.108
Bare / Sparse Vegetation	736.32	0.270
Permanent Water Bodies	85.36	0.031
Herbaceous Wetland	18.76	0.007
Evergreen Needleleaf Closed Forest	3.75	0.001
Deciduous Broadleaf Closed Forest	5.63	0.002
Unknown Closed Forest Type	11.26	0.004
Evergreen Needleleaf Open Forest	2.81	0.001
Deciduous Broadleaf Open Forest	8.44	0.003
Unknown Open Forest Type	89.11	0.033

The hypsometric and slope distribution curves are given in Figures 3.8-a; 3.8-b respectively, and their distribution are given in Table 3.5.

Table 3.5. *Altitude and slope distribution of basin areas of Kayabaşı watershed*

Altitude (m)	Area (km^2)	Area (%)	Slope (%)	Area (km^2)	Area (%)
3155	0	0	246.62	0	0
2604.2	272.736	10	150	0.03	0.001
2406.4	545.472	20	120	0.15	0.006
2273.6	818.208	30	90	1.60	0.06
2220.3	1090.944	40	70	9.81	0.36
2178.4	1363.68	50	50	64.69	2.37
2131.6	1636.416	60	40	167.14	6.13
2087.2	1909.152	70	30	412.81	15.14
2040	2181.888	80	20	930.43	34.11

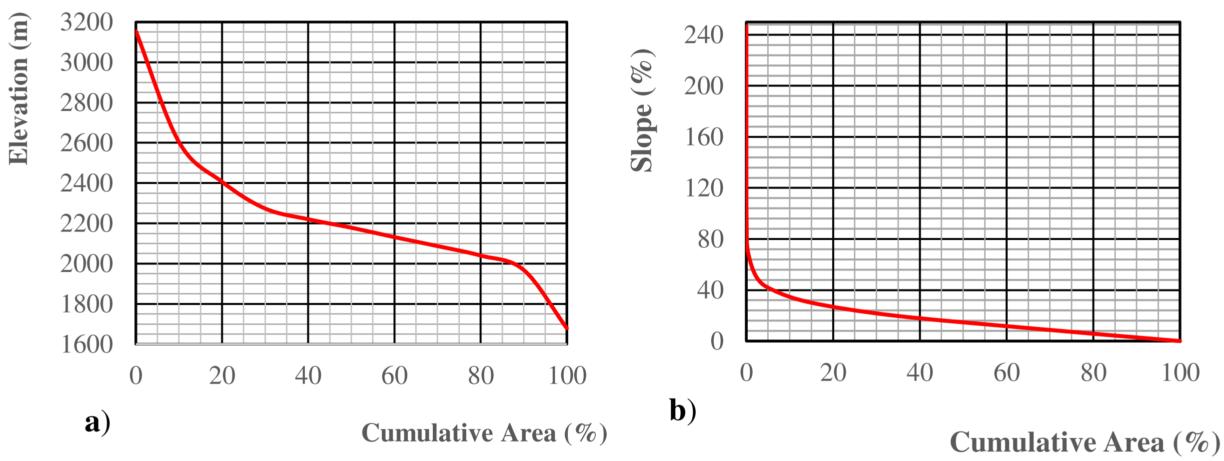

Figure 3.8. *Kayabaşı watershed distribution curves: a) hypsometric curve; b) slope distribution curve*

Kayabaşı is a watershed where snowmelt contributes significantly to spring and summer runoff. Thus, to consider the effect of snow on hydrological modeling, the snow module CemaNeige which works by dividing the basin into elevation zones of equal area (Figure 3.9) was considered. Furthermore, to run CemaNeige in airGR, the basin hypsometric data (altitude in m) is needed from 0 to 100% by step 1% (i.e. 101 increasing values).

Table 3.6. *Kayabaşı watershed into five equal elevation area zones*

Zone	Elevation range (m)	Average elevation (m)	Area (Km^2)
1	1679 – 2035	1917.66	546.62
2	2040 – 2127	2083.55	548.14
3	2131 – 2227	2177.50	545.26
4	2230 – 2398	2284.15	544.04
5	2406 – 3155	2681.95	543.30

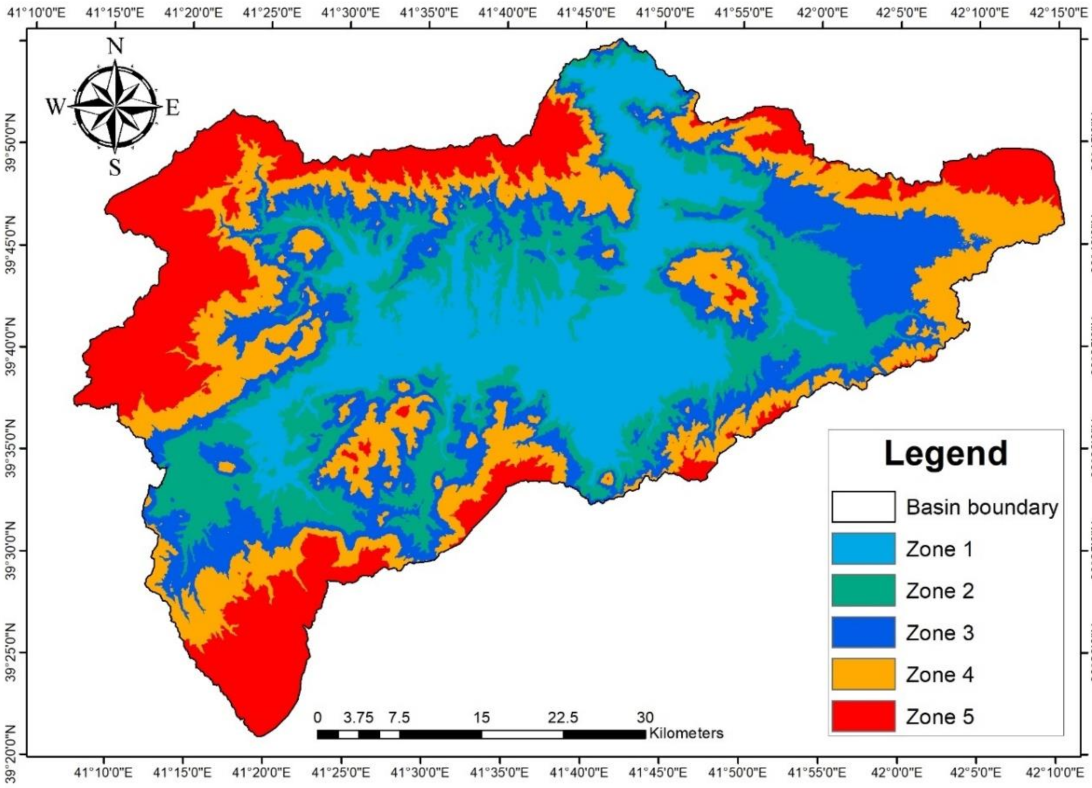

Figure 3.9. *Kayabaşı watershed in five equal elevation zones*

3.1.2. Guinea

Located between 07° 05' to 12° 51' north latitude and 07° 30' to 15° 10' west longitude and covering an area of 245,857 km^2, Guinea is a coastal country in West Africa commonly referred to as the *"water tower of West Africa"*. It has a coastline of 300 kilometers on the Atlantic Ocean and is bordered by Guinea-Bissau to the northwest, Senegal to the north, Mali to the north and northeast, Ivory Coast to the east and southeast, and Liberia and Sierra Leone to the south. The geography of Guinea is characterized by a diverse landscape. It includes coastal plains along the Atlantic Ocean, rolling savanna in the north, and mountainous regions in the central and southeastern parts of the country. These geographical conditions make Guinea a country with four distinct natural regions, each characterized by different relief, vegetation, and climatic conditions. Maritime Guinea, covering the coastal strip, features mangrove formations, plains, and plateaus, receiving over 1,500mm of rain annually, with peaks reaching 4,000mm in Conakry. Middle Guinea (Fouta Djallon) is the most mountainous region, with elevations reaching over 1,500m above sea level and rainfall varying from 1,300mm in the north to over 2,000mm in the south, crucial for Guinea's river systems. Upper Guinea, characterized by relatively flat terrain and abundant alluvial plains, experiences rainfall between 1,200 and 1,600mm annually. Forest Guinea, with rugged terrain and Mount Nimba rising to 1,752m, enjoys abundant forest cover and a prolonged rainy season lasting up to nine months, with an average annual rainfall of approximately 2,500mm. These regions collectively contribute to Guinea's diverse landscape, biodiversity, and climatic conditions (Figure 3.10).

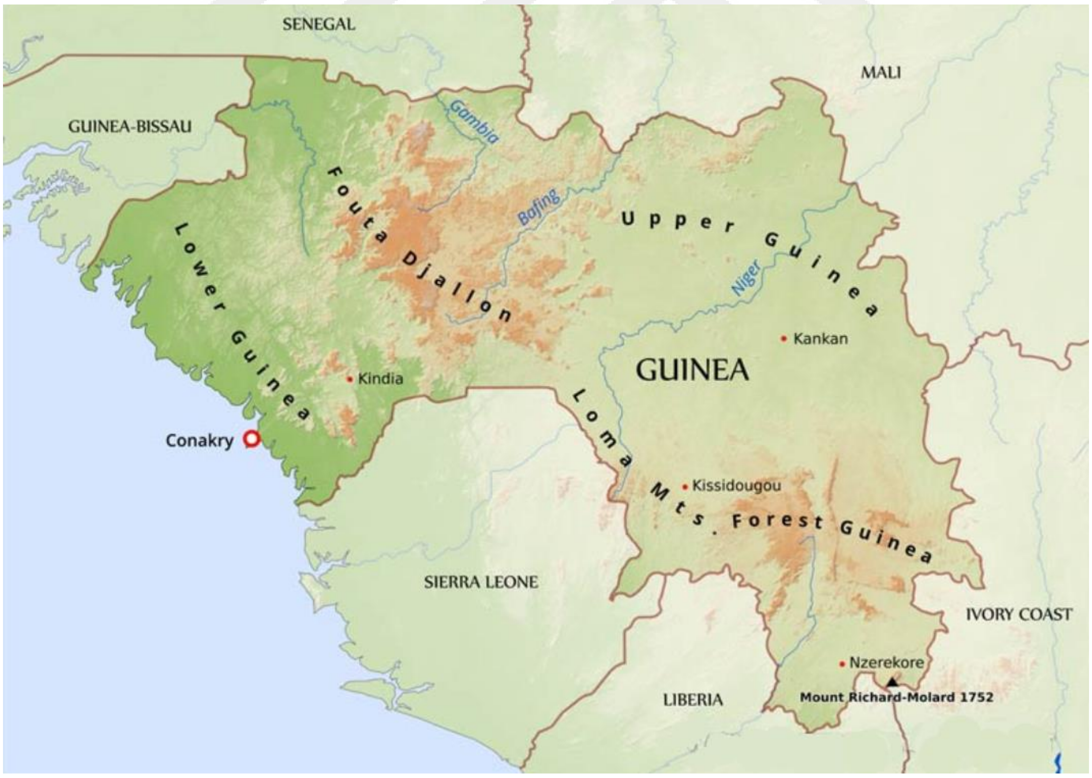

Figure 3.10. *Guinea physical map* free world map

Guinea is home to 1161 rivers grouped into 23 watersheds, including 14 international rivers, among them the Niger River, which flows along its northeastern border, and the Senegal River, which forms part of its northern border. As part of this thesis, two sub-basins of Niger, notably the Niger à Kouroussa Watershed and the Milo à Kankan Watershed on Guinean territory, and a sub-basin of Bafing (Senegal), namely Sokotoro, have been the subject of the study. Below, a concise presentation of these three watersheds is undertaken.

3.1.2.1. Niger à Kouroussa watershed

The Niger River, one of the 14 transboundary rivers originating in Guinea, spans within Guinea's boundary approximately between 08°45'30" to 12°01'30" N and 07°51'30" to 11°30'50" W and occupies 38.5% of the country's total area (e.g. 94,763.78km2). The Niger à Kouroussa (Figure 3.11) is a sub-basin of the Upper Niger basin and has a flow observation station in Kouroussa identified under the reference 117 150 0120 which drains an area of 16,649.18 km2.

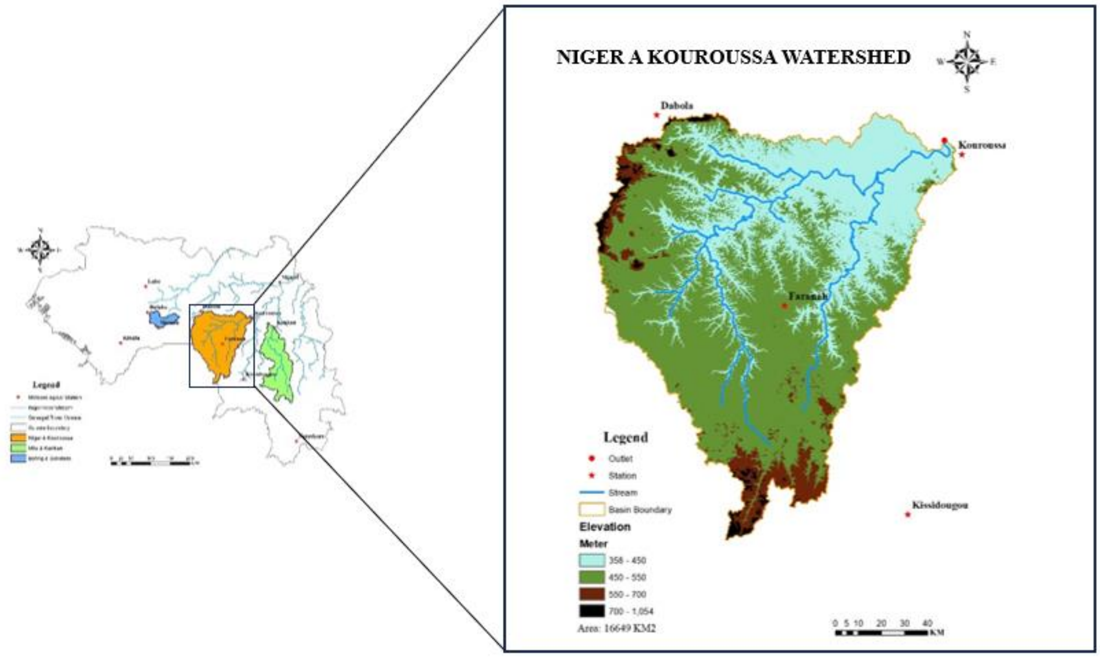

Figure 3.11. *Localization of Niger à Kouroussa watershed in Guinea*

The analysis of the basin’s Digital Elevation Model (DEM) reveals that 90% of the basin's total area is under 550m altitude and its elevation varies between 358m and 1054m. The altitudes over 800m represent 0.5% of the total area which makes the basin relatively flat with a mean elevation of 475.87m (Figure 3.12-a). Niger à Kouroussa watershed is characterized by relatively steep slopes upstream in the northwestern and southern parts. The basin is dominated by gentle and moderate slopes downstream (Figure 3.12-b). The mean slope is 6.40% and the slope distribution is given in Table 3.8. The aspect of a slope affects the amount of solar radiation it receives and therefore influences evapotranspiration. In Niger à Kouroussa the slope aspect of the four directions is almost identic and all above 20% of its area and flat occupies 5.72% of the area (Figure 3.12-c). According to the Copernicus Global Land Service (CGLS) 2015 global Land Cover product at 100 m spatial resolution, Niger à Kouroussa land cover (Figure 3.12-d) reveals that the basin area has not undergone any major change in its vegetation cover. Thus, the watershed is then almost in a natural state, and deciduous broadleaf open forest occupies half of its total area (Table 3.7).

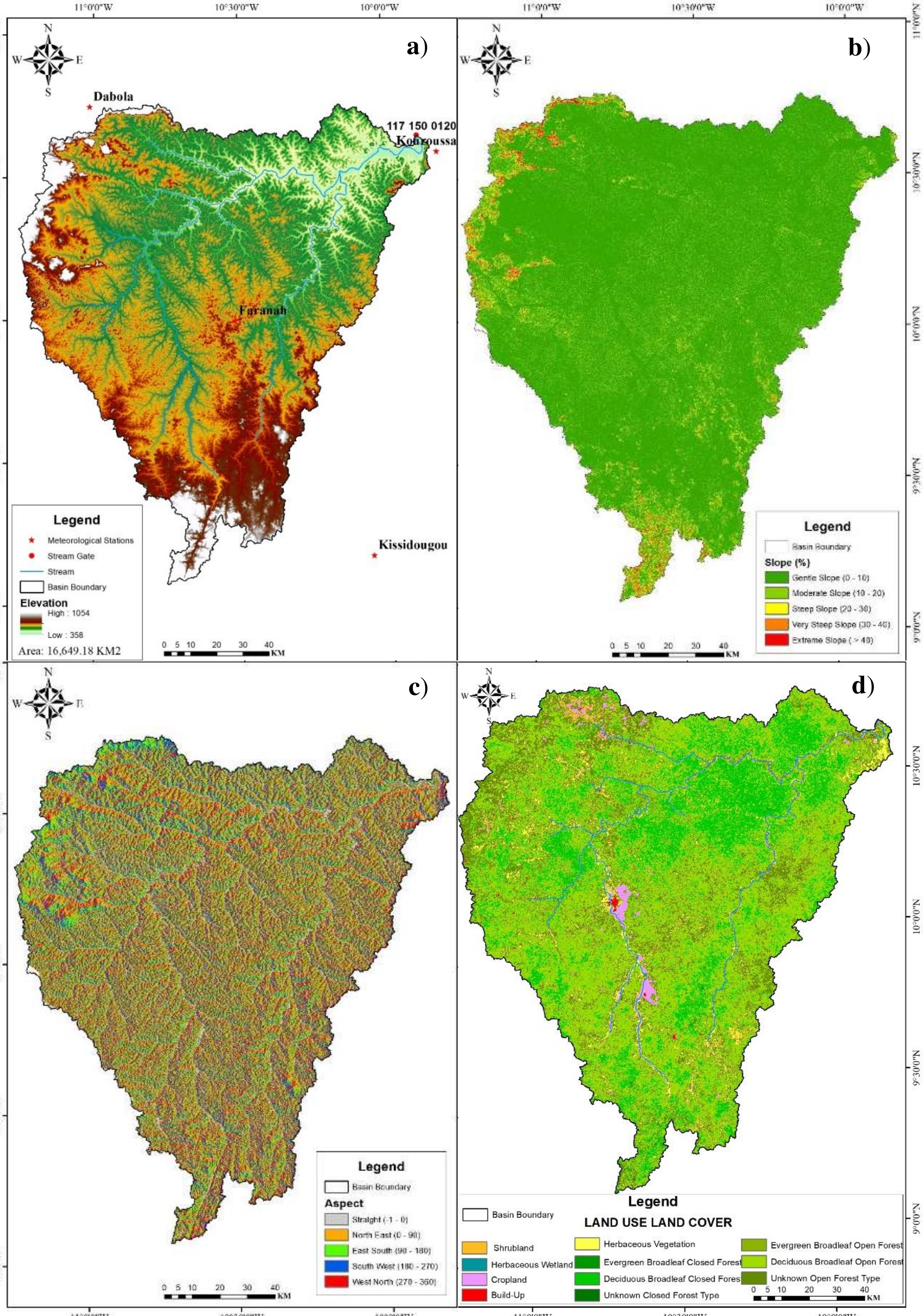

Figure 3.12. *Niger à Kouroussa basin physical characteristics maps from geospatial data: a) Digital Elevation Model map; b) Slope map;* ***c****) Aspect map; and d) Land cover map (CGLS 2015)*

Table 3.7. *Niger à Kouroussa watershed land cover type classification*

Label	**Area (Km^2)**	**Area (%)**
Shrubland	281.26	1.69
Herbaceous Vegetation	748.12	4.49
Cropland	198.08	1.19
Build-Up	34.35	0.21
Herbaceous Wetland	31.21	0.19
Evergreen Broadleaf Closed Forest	32.93	0.20
Deciduous Broadleaf Closed Forest	3449.81	20.72
Unknown Closed Forest Type	48.45	0.29
Evergreen Broadleaf Open Forest	10.42	0.06
Deciduous Broadleaf Open Forest	8485.54	50.97
Unknown Closed Open Type	3329.00	19.99

The hypsometric and slope distribution curves are given in Figures 3.13-a; 3.13-b respectively, and their distribution are given in Table 3.8.

Table 3.8. *Altitude and slope distribution of basin areas of Niger à Kouroussa watershed*

Altitude (m)	**Area (km^2)**	**Area (%)**	**Slope (%)**	**Area (km^2)**	**Area (%)**
1054	0	0	330.36	0	0
1000	2.72	0.02	50	42.62	0.26
900	18.75	0.11	40	106.26	0.64
800	81.63	0.49	35	163.85	0.98
700	307.65	1.85	30	251.56	1.51
600	822.05	4.94	25	385.54	2.32
550	1398.05	8.40	20	626.06	3.76
500	3456.00	20.76	15	1215.80	7.30
450	10578.02	63.54	10	3281.70	19.71
400	15998.96	96.09	5	9352.35	56.17
358	16648.18	100.00	0	16649.18	100.00

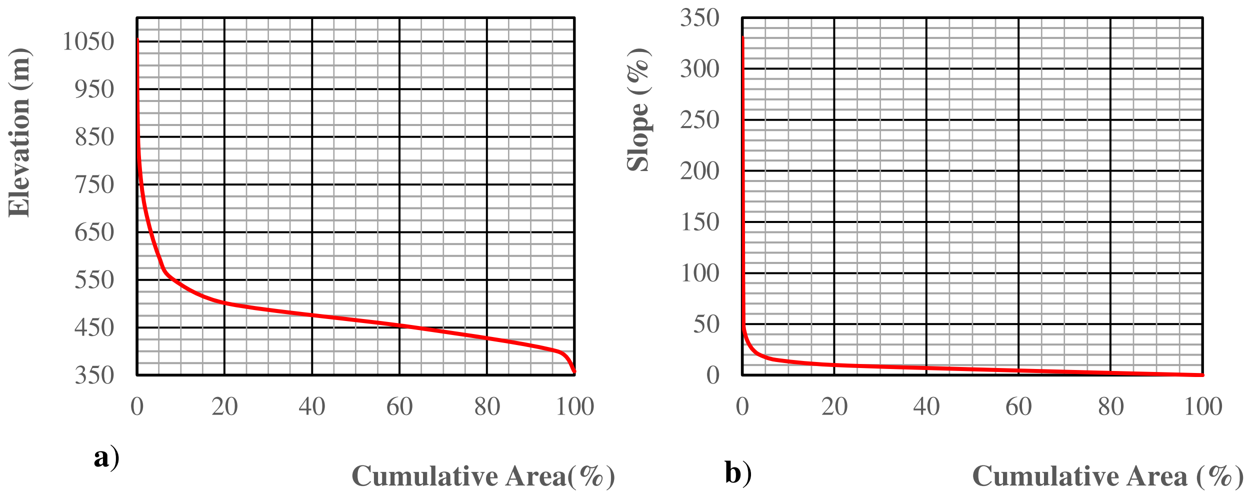

Figure 3.13. *Niger à Kouroussa basin distribution curves: a) hypsometric curve; b) slope distribution curve*

3.1.2.2. Milo à Kankan watershed

The Milo is the second tributary on the right bank of the Niger River in the Guinean part after the Niandan. Originating in the highlands southern region of Guinea and flowing northwards, it passes through Kankan before merging with the Niger River (Djoliba) approximately ten kilometers upstream of Siguiri. The stream gate at Kankan on Milo which is identified under the reference 117 150 1705 formed the watershed of Milo à Kankan (Figure 3.14) with an area of 9,484 km2.

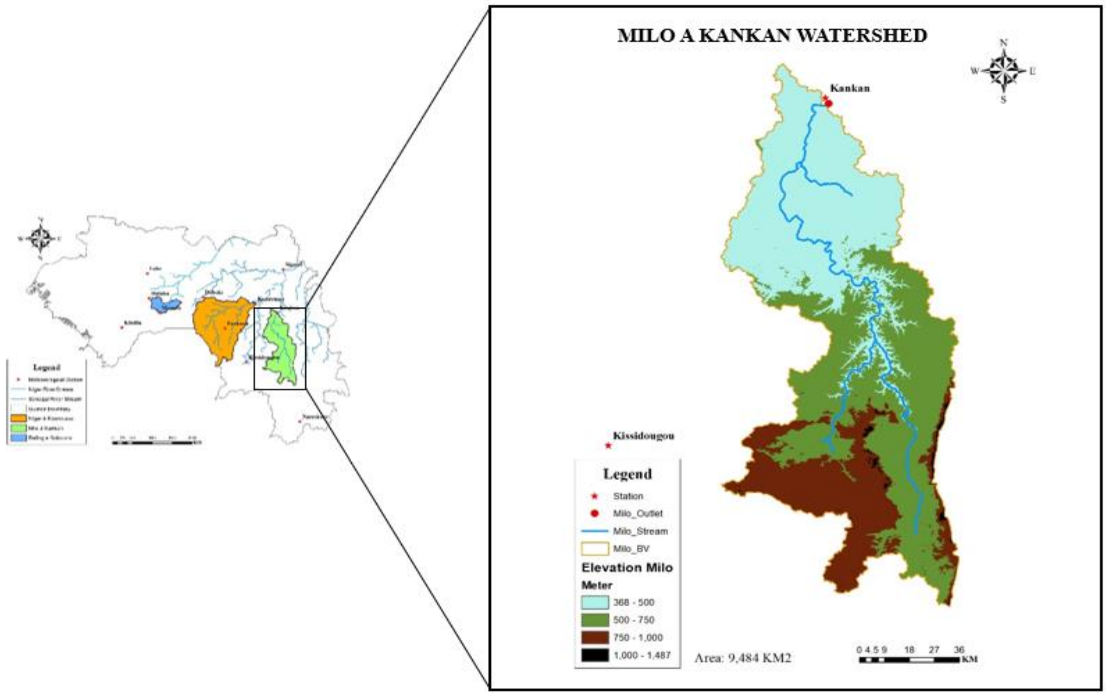

Figure 3.14. *Localization of Milo à Kankan watershed in Guinea*

The analysis of the basin's Digital Elevation Model (DEM) reveals that 60% of the basin's total area is under 650m altitude and its elevation varies between 368m and 1487m. The altitudes over 900m represent 3.67% of the total area which makes the basin relatively higher than Niger à Kouroussa with a mean elevation of 579.90m (Figure 3.15-a). Milo à Kankan watershed is characterized by relatively steep slopes upstream and decreases downstream (Figure 3.15-b). The mean slope is 7.81% and the slope distribution is given in Table 3.10. In Milo à Kankan, the slope aspect of the four directions is almost identical and all about 23% of its area, and flat occupies 5.50% of the area (Figure 3.15-c). According to the Copernicus Global Land Service (CGLS) 2015 global Land Cover product at 100 m spatial resolution, Milo à Kankan land cover (Figure 3.15-d) reveals that the basin has not undergone any major change in its vegetation cover. Thus, the watershed is then almost in a natural state, and deciduous broadleaf open forest occupies 44.86% of its total area (Table 3.9).

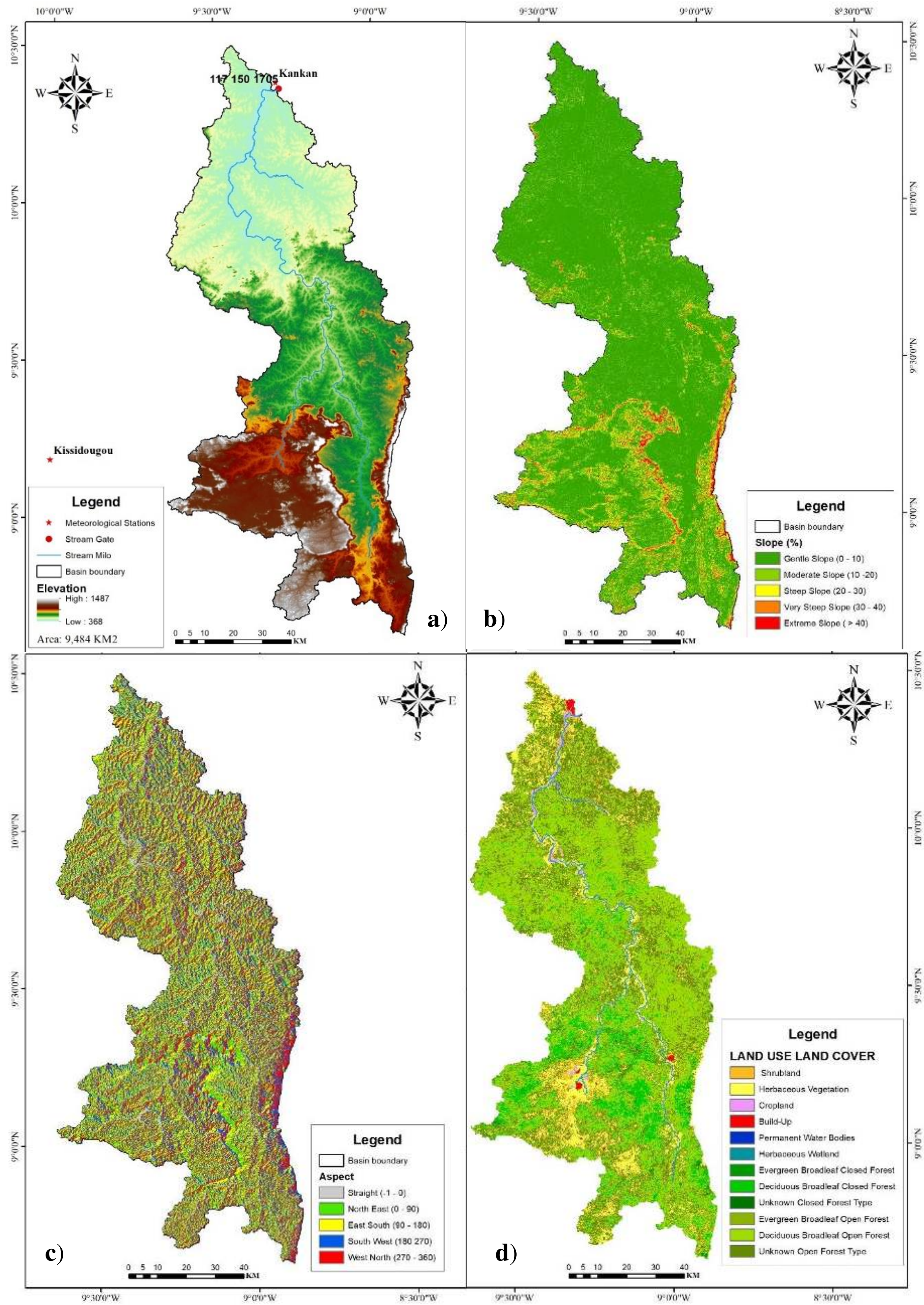

Figure 3.15. *Milo à Kankan basin physical characteristics maps from geospatial data: a) Digital Elevation Model map; b) Slope map;* ***c****) Aspect map; and d) Land cover map (CGLS 2015)*

Table 3.9. *Milo à Kankan watershed land cover type classification*

Label	Area (Km^2)	Area (%)
Shrubland	508.41	5.36
Herbaceous Vegetation	1000.80	10.55
Cropland	58.53	0.62
Build-Up	34.17	0.36
Permanent Water Bodies	0.20	0.002
Herbaceous Wetland	29.38	0.31
Evergreen Broadleaf Closed Forest	47.84	0.50
Deciduous Broadleaf Closed Forest	829.24	8.74
Unknown Closed Forest Type	45.56	0.48
Evergreen Broadleaf Open Forest	14.47	0.15
Deciduous Broadleaf Open Forest	4254.62	44.86
Unknown Open Forest Type	2660.77	28.06

The hypsometric and slope distribution curves are given in Figures 3.16-a; 3.16-b respectively, and their distribution are given in Table 3.10.

Table 3.10. *Altitude and slope distribution of basin areas of Milo à Kankan watershed*

Altitude (m)	Area (km^2)	Area (%)	Slope (%)	Area (km^2)	Area (%)
1054	0	0	330.36	0	0
1000	2.72	0.02	50	42.62	0.26
900	18.75	0.11	40	106.26	0.64
800	81.63	0.49	35	163.85	0.98
700	307.65	1.85	30	251.56	1.51
600	822.05	4.94	25	385.54	2.32
550	1398.05	8.40	20	626.06	3.76
500	3456.00	20.76	15	1215.80	7.30
450	10578.02	63.54	10	3281.70	19.71
400	15998.96	96.09	5	9352.35	56.17
358	16648.18	100.00	0	16649.18	100.00

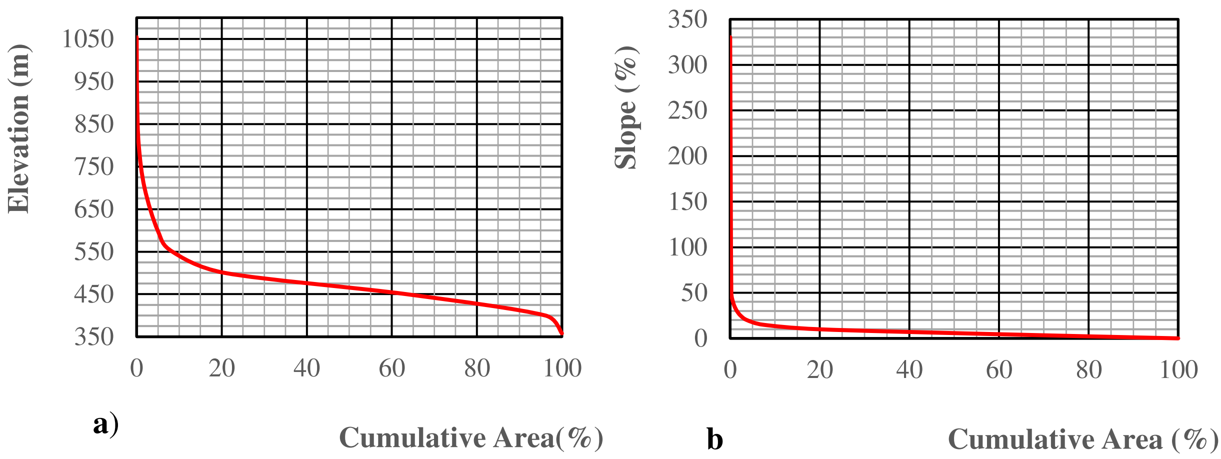

Figure 3.16. *Milo à Kankan basin distribution: a) hypsometric curve; b) slope distribution curve*

3.1.2.3. Bafing à Sokotoro watershed

The Senegal River is the second largest shared basin in West Africa after the Niger River (Bodian, Dezetter, & Dacosta, 2012) and drains a basin of 300,000 km2, straddling four countries which are, from upstream to downstream, Guinea, Mali, Senegal, and Mauritania. It is made up of several tributaries, the main ones being the Bafing, the Bakoye, and the Falémé. These three tributaries have their sources in Guinea and form the upper basin (Nonguierma & Niang, 2006). Originating in the highlands of the Fouta Djallon, the Bafing in Guinean territory is located approximately between 10°25'50" to 12°15'30" N and 09°41'10" to 12°23'20" W and covers an area of 20,695.91 km2. The Bafing à Sokotoro (Figure 3.17) is an upper sub-basin of the Bafing basin and has a stream gate at Sokotoro station identified under the reference 117 260 0125 which drains an area of 1,849.88 km2.

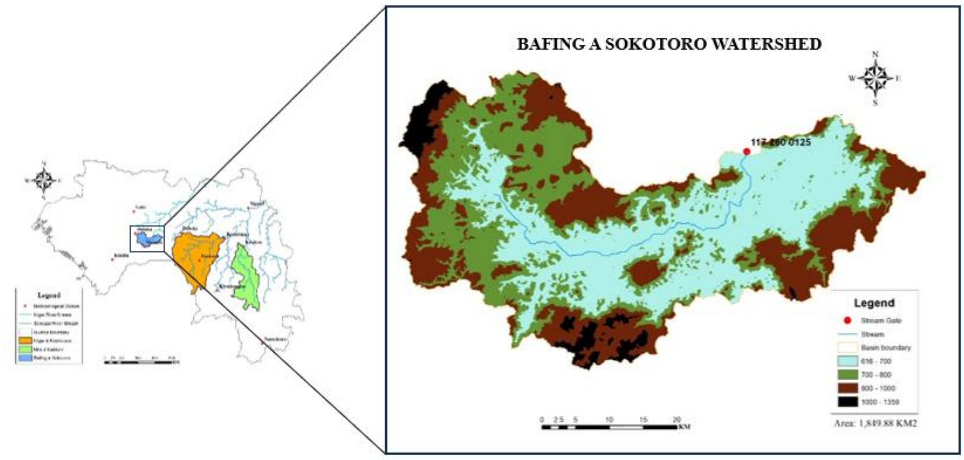

Figure 3.17. *Localization of Bafing à Sokotoro watershed in Guinea*

The analysis of the basin’s Digital Elevation Model (DEM) reveals that 4.17% of the basin's total area is above 1000m altitude and its elevation varies between 616m and 1359m. The altitudes below 900m represent 86.75% of the total area, making Sokotoro a mountainous basin with a mean elevation of 767m (Figure 3.18-a). Sokotoro watershed is characterized by a range of mountains on both banks with relatively steep slopes upstream and decreases downstream (Figure 3.18-b). The mean slope is 12.75% and the slope distribution is given in Table 3.12. As Sokotoro is a mountainous basin, there is a slight disparity between the aspect slopes; for instance, east-south occupies 26.34% while other slope aspects are around 22% of the area (Figure 3.18-c). According to the Copernicus Global Land Service (CGLS) 2015 global Land Cover product at 100 m spatial resolution, Bafing à Sokotoro land cover (Figure 3.18-d) reveals that 79.95% of the basin is covered by all types of forests and only 13.49% and 2.64% are occupied by herbaceous vegetation and cropland respectively (Table 3.11).

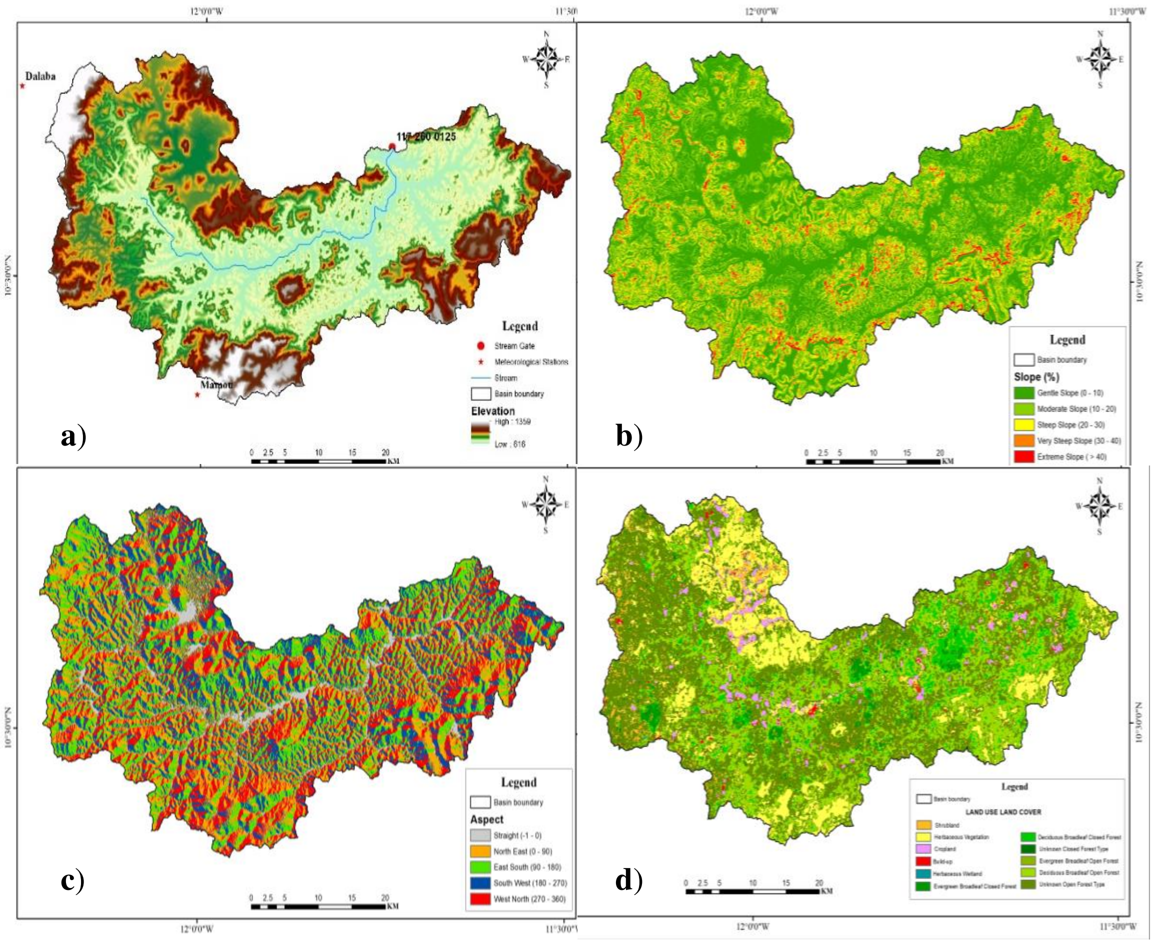

Figure 3.18. *Bafing à Sokotoro basin physical characteristics maps from geospatial data: a) Digital Elevation Model map; b) Slope map; c) Aspect map; and d) Land cover map (CGLS 2015)*

Table 3.11. *Bafing à Sokotoro watershed land cover type classification*

Label	Area (Km^2)	Area (%)
Shrubland	62.16	3.36
Herbaceous Vegetation	249.54	13.49
Cropland	48.86	2.64
Build-Up	9.95	0.54
Herbaceous Wetland	0.48	0.03
Evergreen Broadleaf Closed Forest	22.37	1.21
Deciduous Broadleaf Closed Forest	116.71	6.31
Unknown Closed Forest Type	21.08	1.14
Evergreen Broadleaf Open Forest	6.83	0.37
Deciduous Broadleaf Open Forest	498.67	26.96
Unknown Open Forest Type	813.23	43.96

The hypsometric and slope distribution curves are given in Figures 3.19-a; 3.19-b respectively, and their distribution are given in Table 3.12.

Table 3.12. *Altitude and slope distribution of basin areas of Bafing à Sokotoro watershed*

Altitude (m)	Area (km^2)	Area (%)	Slope (%)	Area (km^2)	Area (%)
1359	0	0	296.37	0	0
1200	8.94	0.48	50	11.74	0.63
1100	23.87	1.29	40	36.73	1.99
1000	77.08	4.17	35	66.55	3.60
900	245.16	13.25	30	121.63	6.58
850	392.41	21.21	25	217.88	11.78
800	585.90	31.67	20	388.55	21.00
750	876.26	47.37	15	659.02	35.63
700	1151.93	62.27	10	1041.88	56.32
650	1677.48	90.68	5	1464.46	79.17
616	1849.88	100.00	0	1849.88	100.00

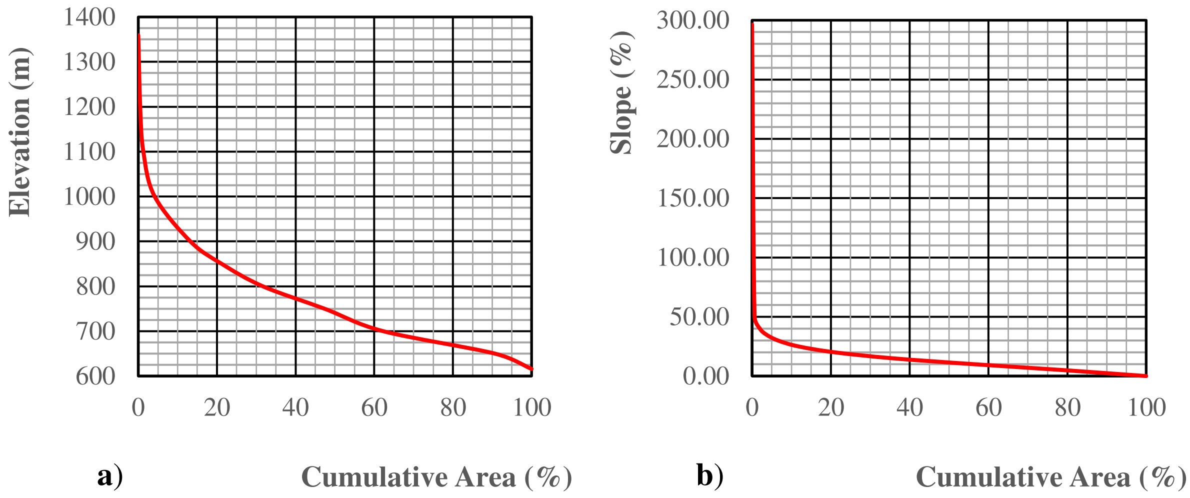

Figure 3.19. *Sokotoro basin distribution curves: a) hypsometric curve; b) slope distribution curve*

3.2. Hydro-meteorological Data

3.2.1. Türkiye hydro-meteorological data

Türkiye has a robust water resources management system supported by an extensive network of meteorological and hydrometric stations. These stations, managed respectively by the State Meteorological Services (MGM stands for Meteoroloji Genel Müdürlüğü) and State Hydraulics Works (DSİ stands for Devlet Su İşleri), provide essential data on weather conditions, precipitation, river discharge, and water quality across Turkish basins. Precipitation and temperature data for Turkish basins were obtained from MGM and flow data were obtained from DSI.

3.2.1.1. Çukurkışla watershed

Çukurkışla meteorological data including daily precipitation (P) and daily average air temperature (T) comes from two meteorological stations within the basin, namely Kayseri Sarız and Adana Tufanbeyli at the altitude of 1400m and 1599m respectively. The data from these two stations covers a period from October 01st, 1999 to September 30th, 2019. To meet the objective of the hydrological modeling, we first started controlling the data quality and constructing the Thiessen polygon in ArcMap software to highlight the covering area of these two stations. It was found that Adana Tufanbeyli covers 65% of the basin's total area and Kayseri Sarız occupies the remaining 35%. Considering some gaps in the temperature data at the Tufanbeyli station, only temperature data from Sarız station, which continues over the entire period, was used.

The average interannual precipitation is 501.37 mm with a standard deviation of 108.10 mm. The annual regime is very irregular from one year to the next; the 2009 hydrological year corresponds to the wettest year with an average annual precipitation height of 668.69 mm, and the driest year is that of 2017 with 306.88 mm (Figure 3.20). The variations in monthly average precipitation show that the biggest amount of precipitation (14.20%) is received in January and the lowest amount in July with only 1.35%. Relying on the data availability from 2000 to 2019, Çukurkışla annual average air temperature is 8.35°C. January is the coldest month with an average air temperature of -4.3°C while August is the hottest month with an average of 20.23°C (Figure 3.21). Çukurkışla hydrometric data was also provided at daily time steps in tandem with meteorological data. The interannual average of past flows amounts to 7.94 m^3/s, the maximum occurs in 2019 with 12.93 m^3/s, and the lowest runoff value (2.92 m^3/s) was recorded in 2014, which does not correspond to the driest year of the period (Figure 3.20). The variation in monthly average discharge shows that the biggest amount of flow is recorded in March and April with 20.61% and 21.63% respectively, and the lowest amount in August with only 3.15%. Over the whole available discharge, from 2000 to 2019 water years, the maximum daily discharge was recorded on March 4th, 2004 with 122.18 m^3/s, and the minimum daily on August 2nd, 2014, with only 0.39 m^3/s.

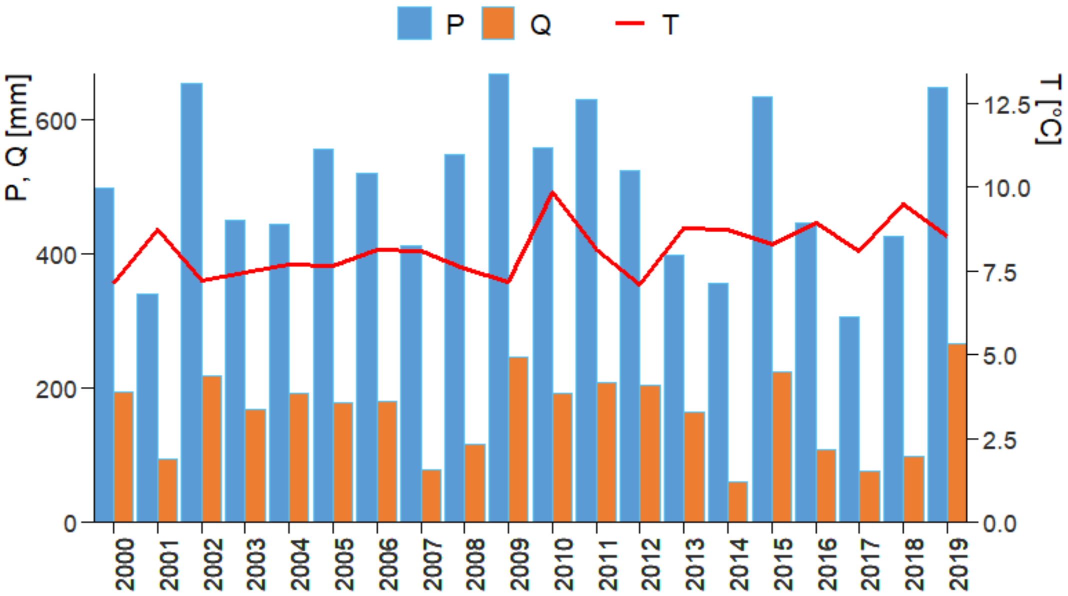

Figure 3.20. *Çukurkışla watershed hydro-meteorologic data*

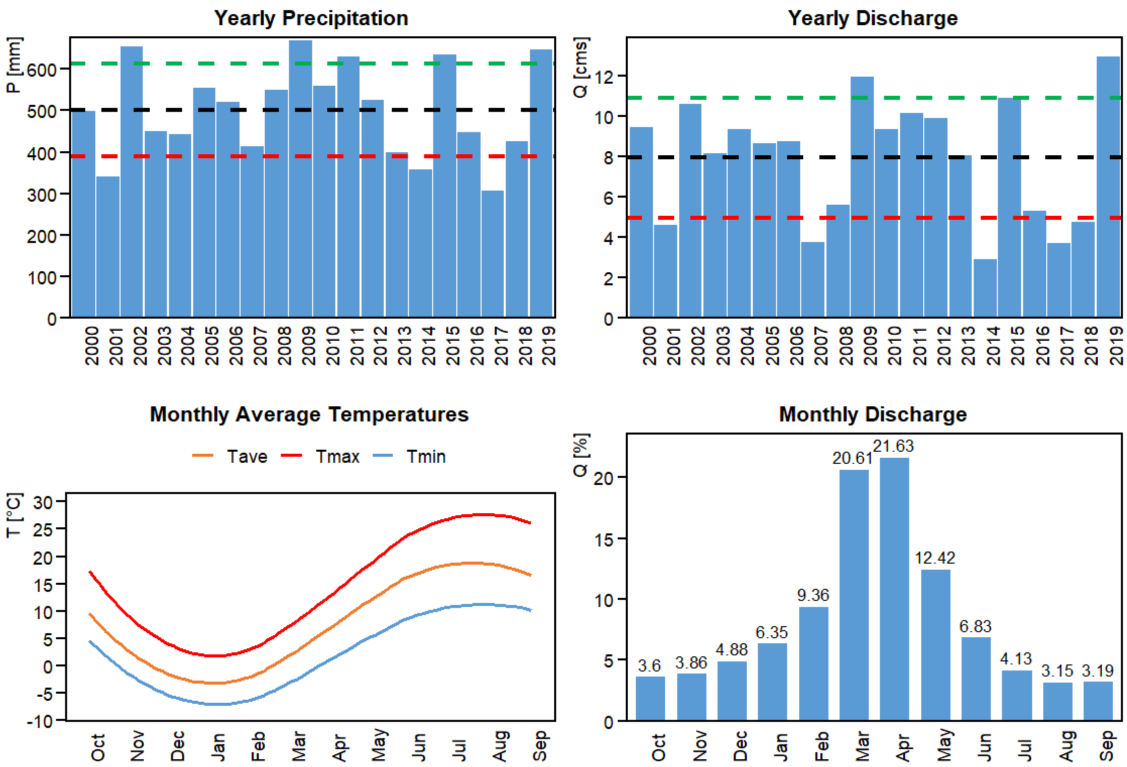

Figure 3.21. *Çukurkışla watershed annual and monthly hydro-meteorologic data (red, black, and green dashed lines are average minus standard deviation, average and average plus standard deviation respectively). Below red line represents drought periods and above green line wet periods*

Potential evapotranspiration (PET) plays a crucial role in hydrological modeling as it represents the maximum amount of water that could be evaporated and transpired by vegetation under ideal conditions and is an input for many rainfall-runoff models. Its value, which is not directly provided, should be calculated based on a formula from the literature. The choice of the formula depends on the available climatic factors such as temperature, humidity, wind speed, and solar radiation. In our case, the Oudin et al. (2005) formula was used which is implemented in the airGR R package. It is easy to use, accurate, and needs a few input data namely daily air temperature and the station latitude in degree or radian. The result of the Oudin formula shows that the average annual PET for the Çukurkışla watershed is 691.07 mm/year, and the highest value was recorded in 2010 (750.38 mm) and the lowest in 2009 (642.69 mm) with a standard deviation of 26.41 mm. July is the month in which the amount of water that evaporates is the highest (19.10%) and in January its lowest value (0.76%) is reached (Figure 3.22).

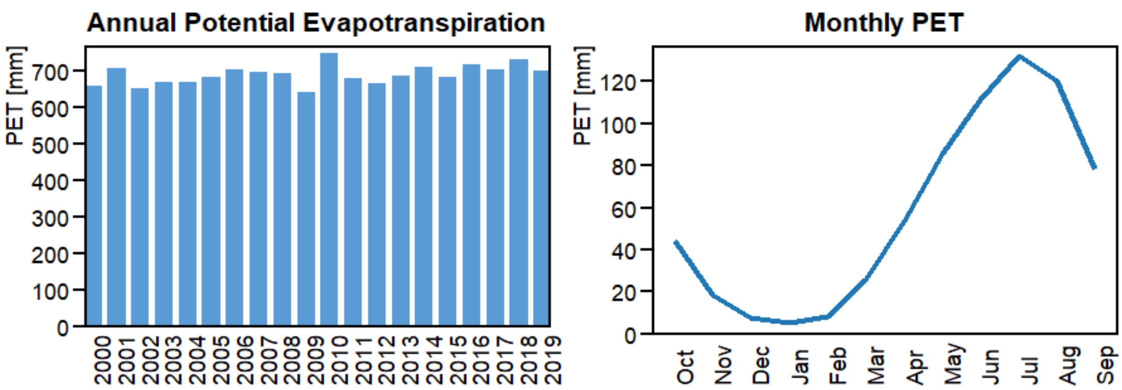

Figure 3.22. *Çukurkışla watershed potential evapotranspiration data calculated using Oudin (2005)*

3.2.1.2. Kayabaşı watershed

Kayabaşı meteorological data including daily precipitation (P) and daily average air temperature (T) comes from five meteorological stations within the basin, namely Palandöken Dağı, Tekman, Karayazı, Hacıömer and Yılanlı Köyü and eight from outside (Havalimanı, Ilıca, Horasan, Hınıs, Varto, Karlıova, Çat, and Köprüköy). The combination of data from these stations allows us to create a meteorologic dataset that covers a period from October 01st, 2006 to September 30th, 2019. The average interannual precipitation is 498.71 mm with a standard deviation of 96.46 mm. The annual regime is very irregular from one year to the next; the 2010 hydrological year corresponds to the wettest year with an average annual precipitation height of 666.78 mm, and the driest year is that of 2014 with 322.59 mm (Figure 3.23). The variations in monthly average precipitation show that the biggest amount of precipitation (14.19%) is received in May and the lowest amount in August with only 3.73%. Relying on the available data from 2007 to 2019, Kayabaşı annual average air temperature is 6.05°C. January is the coldest month with an average air temperature of -8.73°C while July and August are the hottest month with an average of 19.49°C and 19.39°C respectively (Figure 3.24). Kayabaşı hydrometric data was also provided at daily time steps with the 2007 water year was missing. The interannual average of past flows amounts to 20.87 m^3/s, the maximum occurred in 2010 with 34.09 m^3/s, and the lowest runoff value (10.72 m^3/s) was recorded in 2014, which corresponds to the driest year of the period (Figure 3.23). The variation in monthly average discharge shows that the biggest amount of flow is recorded in April and May with 28.12% and 26.31% respectively, and the lowest amount in September with only 2.37%. Over the whole available discharge, from 2008 to 2019 water years, the maximum daily discharge was recorded on March 16th, 2010 with 329 m^3/s, and the minimum daily on February 9th to 12th, 2012 with only 2.82 m^3/s.

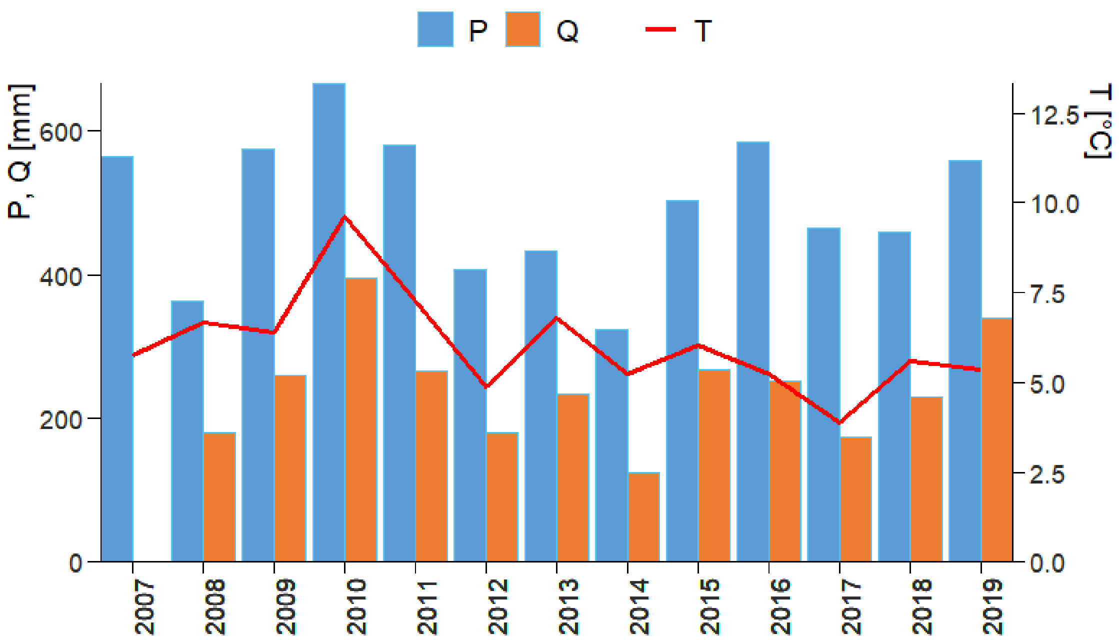

Figure 3.23. *Kayabaşı watershed hydro-meteorologic data*

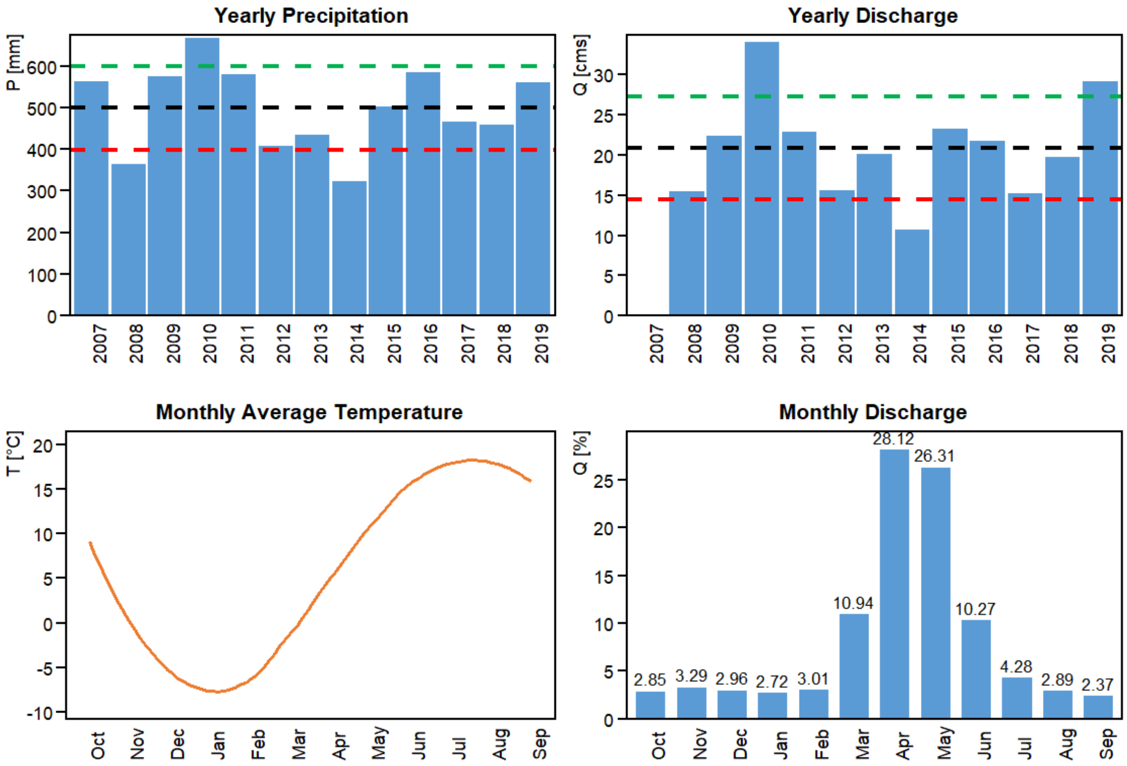

Figure 3.24. *Kayabaşı watershed annual and monthly hydro-meteorologic data (red, black, and green dashed lines are average minus standard deviation, average and average plus standard deviation respectively). Below red line represents drought periods and above green line wet periods*

The result of the Oudin formula shows that the average annual PET for the Kayabaşı watershed is 628.90 mm/year, and the highest value was recorded in 2010 (735.92 mm) and the lowest in 2018 (571.83 mm) with a standard deviation of 46.57 mm. July is the month in which the amount of water that evaporates is the highest (20.42%) and in January its lowest value (0.29%) is reached (Figure 3.25).

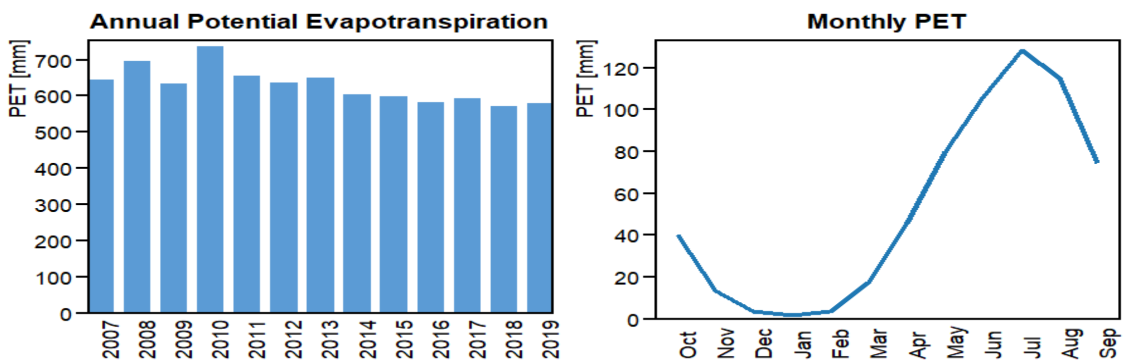

Figure 3.25. *Kayabaşı watershed potential evapotranspiration data calculated using Oudin (2005)*

3.2.2. Guinea basins hydro-meteorological data

Access to comprehensive hydro-meteorological data is crucial for effective water resources management. However, knowledge of water resources and their seasonal variations is limited in Guinea, with fragmented hydrological data series. The flow data available at the National Hydraulic Directorate (DNH) of Guinea are often incomplete, discontinuous, and short-duration, hindering their use for reliable hydrological analysis (Kane & Diallo, 2005 in A. Bodian et al. 2012). Furthermore, in 2008 the total number of meteorological stations owned by Guinea was 45 composed of 12 Syncope stations (Faranah, Kankan, Kissidougou, Mamou, etc.), 24 climatological stations (Dalaba, Dabola, Kouroussa, etc.). These meteorological stations are managed by the National Meteorological Directorate (DNM). The precipitation and temperature data used here were obtained from DNM and flow data were obtained from DNH. Both data had some gaps (Tables 3.13 and 3.14) and missing parts were completed by using the Linear Regression Analysis method

Table 3.13. *Percentage of missing data at meteorological stations*

Stations	Period	Precipitation (%)	Tmin (%)	Tmax (%)
Dabola	1994 – 2015	11.08	20.13	13.28
Dalaba	1990 – 2018	4.63	30.84*	24.51*
Faranah	1981 – 2017	0.61	5.86	21.48
Kankan	1981 – 2019	1.53	11.48	8.65
Kindia	1990 – 2019	0.56	0.60	0.70
Kissidougou	1981 – 2009	1.47	8.57	5.73
Kouroussa	1997 – 2010	6.74	5.83	7.07
Mamou	1981 – 2013	0.51	1.16	0.66
Labé	1981 – 2021	0.41	5.54	0.46
N’zérékoré	1981 – 2021	0.21	0.34	8.21
Siguiri	1990 – 2013	6.08	12.71	26.51

Table 3.14. *Percentage of missing data at meteorological stations*

Stream gauging Station	Period	Missing data (%)
Milo à Kankan	1991 – 2021	6.26
Niger à Kouroussa	1991 – 2021	4.03
Bafing à Sokotoro	2001 – 2021	5.82

3.2.2.1. Niger à Kouroussa watershed

Niger à Kouroussa meteorological data including daily precipitation (P) and daily average air temperature (T) comes from one meteorological station within the basin, namely Faranah and three from outside (Dabola, Kissidougou and Kouroussa). The combination of data from these stations allows us to create a meteorologic dataset that covers a period from April 01st, 1991 to March 31st, 2017. The average interannual precipitation is 1,577.17 mm with a standard deviation of 110.64 mm. The annual regime fluctuates from one year to the next; the 2014 hydrological year corresponds to the wettest year with an average annual precipitation height of 1,763.92 mm, and the driest year is 2002 with 1,337.04 mm (Figure 3.26). The variations in monthly average precipitation show that the biggest amount of precipitation (20.65%) is received in August and the lowest amount in January with only 0.18%. Relying on data availability from 1991 to 2016, The Niger à Kouroussa watershed's annual average air temperature is 25.95°C. The monthly temperature variation is not as much as pronounced; however, April is the hottest month with an average air temperature of 29.31°C while December is the coldest month with an average of 23.47°C (Figure 3.27). The hydrometric data of the Niger à Kouroussa was also provided at daily time steps from April 1st, 1991 to March 31st, 2017 with the 2003 water year missing. The interannual average of past flows amounts to 170.02 m^3/s, the minimum occurred in 1991 with 91.04 m^3/s, and the highest runoff value (244.18 m^3/s) was recorded in 2000, which corresponds to the coldest year of the period (Figure 3.26). The variation in monthly average discharge shows that the biggest amount of flow is recorded in September with 29.97%, and the lowest amount in May with only 0.25%. Over the whole available discharge, from 1991 to 2016 water years, the maximum daily discharge was recorded on September 30th, 2000 with 1192 m^3/s and the minimum daily on May 1, 1992 with only 0.041 m^3/s.

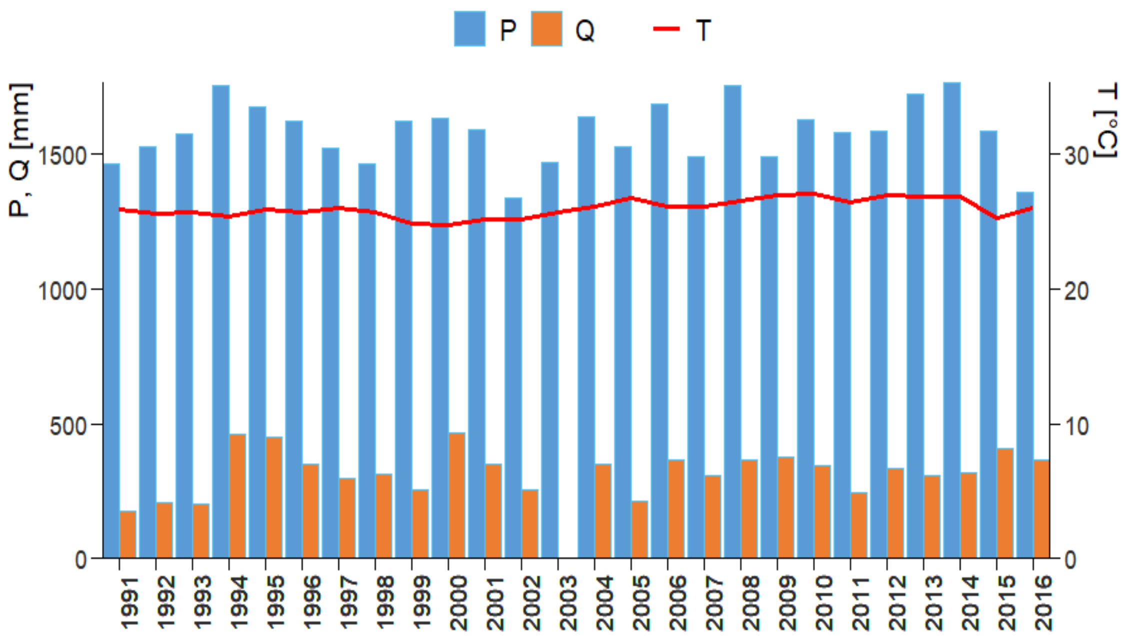

Figure 3.26. *Niger à Kouroussa watershed hydro-meteorologic data*

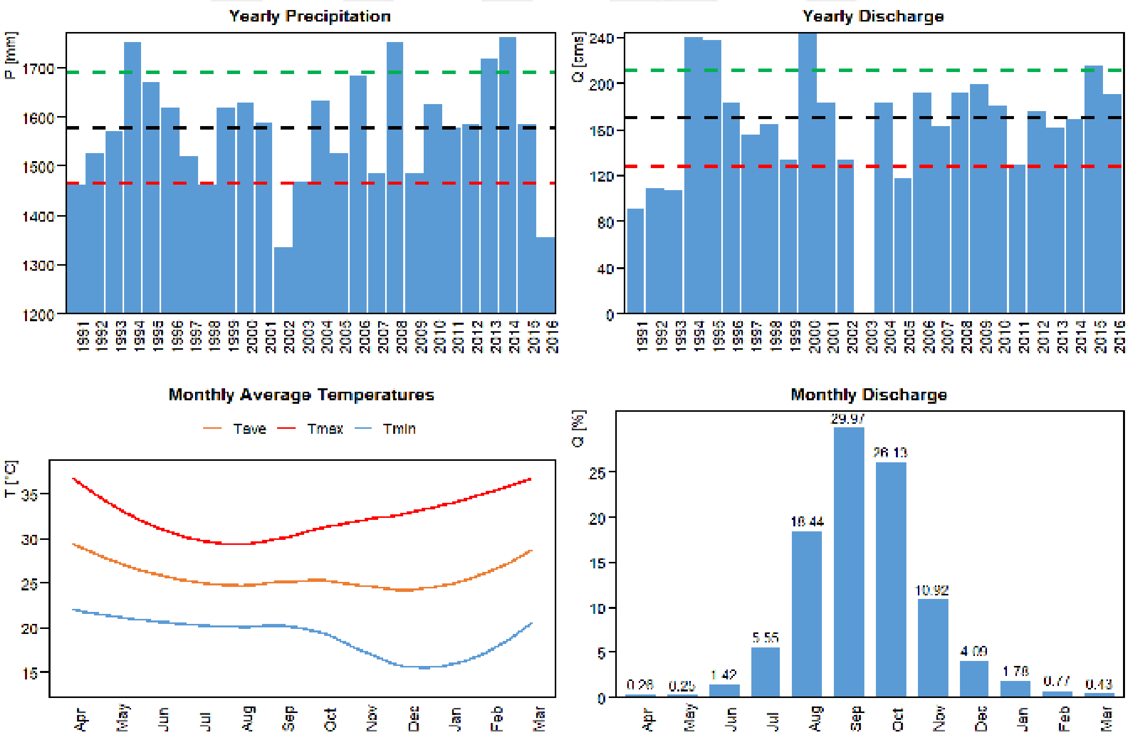

Figure 3.27. *Niger à Kouroussa watershed annual and monthly hydro-meteorologic data (red, black, and green dashed lines are average minus standard deviation, average and average plus standard deviation respectively). Below red line represents drought periods and above green line wet periods*

The result of the Oudin formula shows that the average annual PET for the Niger à Kouroussa watershed is 1677.49 mm/year and the highest value was recorded in 2014 (1755.88 mm) and the lowest in 1999 (1616.53 mm) with a standard deviation of 32.21 mm. April is the month in which the amount of water that evaporates is the highest (9.65%) and in December its lowest value (6.84%) is reached (Figure 3.28).

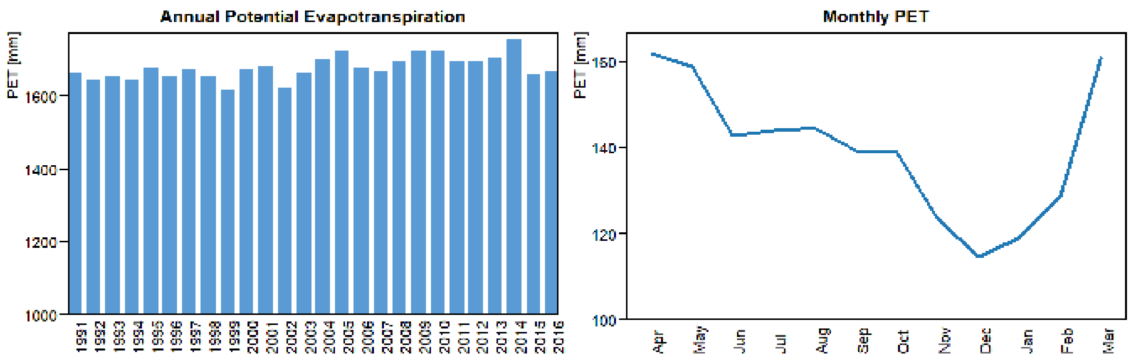

Figure 3.28. *Niger à Kouroussa basin potential evapotranspiration data calculated using Oudin (2005)*

3.2.2.2. Milo à Kankan watershed

Milo à Kankan meteorological data including daily precipitation (P) and daily average air temperature (T) comes from two meteorological stations, namely Kankan and Kissidougou (Figure 3.15). The combination of data from these stations allows us to create a meteorologic dataset that covers a period from April 01, 1991 to March 31, 2017. The average interannual precipitation is 1,614.85 mm with a standard deviation of 251.26 mm. The annual regime fluctuates from one year to the next; the 1994 hydrological year corresponds to the wettest year with an average annual precipitation height of 2,106.17 mm, and the driest year is that of 2011 with 1,142.60 mm (Figure 3.29). The variations in monthly average precipitation show that the biggest amount of precipitation (21.38%) is received in August and the lowest amount in December with only 0.22%. Relying on data availability from 1991 to 2016, The Milo à Kankan watershed's annual average air temperature is 25.47°C. The monthly temperature variation is not as much as pronounced; however, April is the hottest month with an average air temperature of 28.11°C while January is the coldest month with an average of 23.15°C (Figure 3.30). The hydrometric data of the Milo à Kankan was also provided at daily time steps from April 1st, 1991 to March 31st, 2017 with 2011 and 2012 water years missing. The interannual average of past flows amounts to 140.93 m^3/s, the minimum occurred in 2016 with 80.24 m^3/s, and the highest runoff value (194.38 m^3/s) was recorded in 1996 (Figure 3.39). The variation in monthly average discharge shows that the biggest amount of flow is recorded in September with 32.18%, and the lowest amount in February with only 0.11%. Over the whole available discharge, from 1991 to 2016 water years, the maximum daily discharge was recorded on September 30th, 2000 with 938.70 m^3/s and the minimum is close to zero for some days of May.

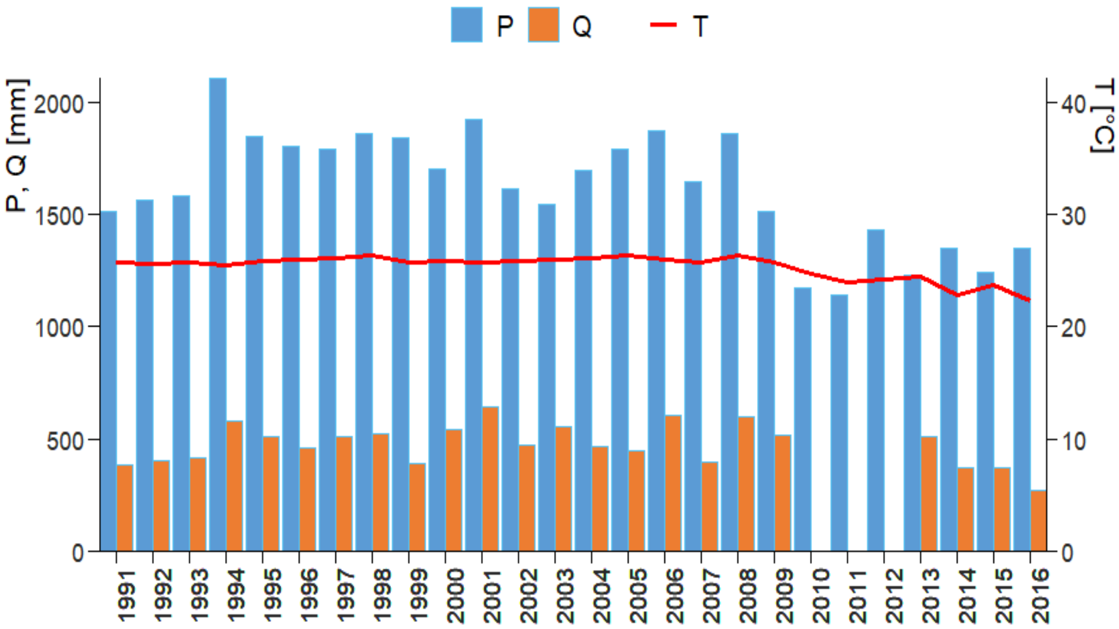

Figure 3.29. *Milo à Kankan watershed hydro-meteorologic data*

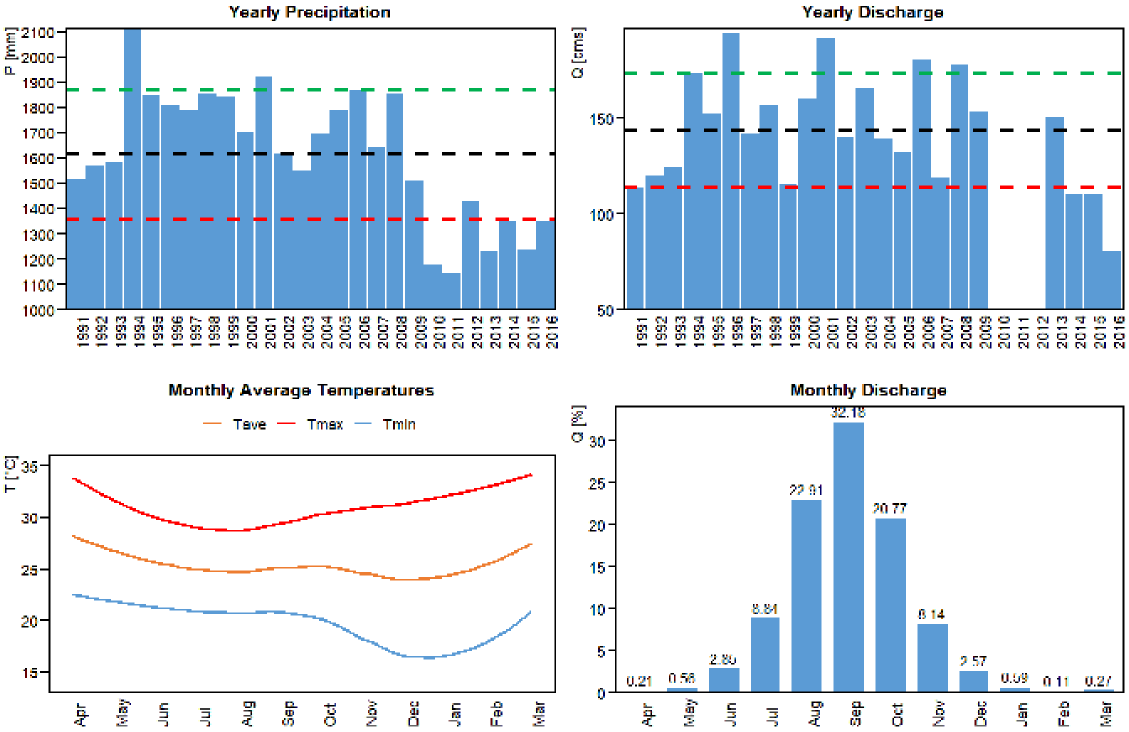

Figure 3.30. *Milo à Kankan watershed annual and monthly hydro-meteorologic data (red, black, and green dashed lines are average minus standard deviation, average and average plus standard deviation respectively). Below red line represents drought periods and above green line wet periods*

The result of the Oudin formula shows that the average annual PET for the Milo watershed is 1,636.99 mm/year and the highest value was recorded in 1998 (1,693.01 mm) and the lowest in 2016 (1,475.40 mm) with a standard deviation of 56.92 mm. March is the month in which the amount of water that evaporates is the highest (9.54%) and in December its lowest value (6.80%) is reached (Figure 3.31).

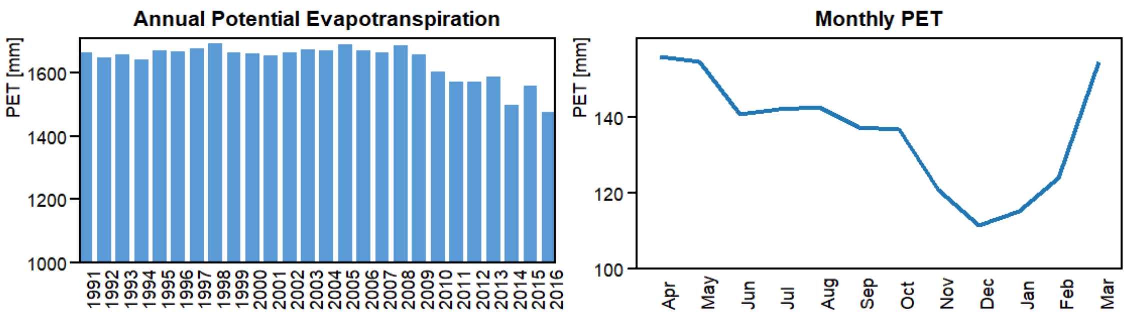

Figure 3.31. *Milo à Kankan watershed potential evapotranspiration data calculated using Oudin (2005)*

3.2.2.3. Bafing à Sokotoro watershed

Sokotoro watershed meteorological data including daily precipitation (P) and daily average air temperature (T) comes from two meteorological stations, namely Dalaba and Mamou (Figure 3.18). The combination of data from these stations allows us to create a meteorologic dataset that covers a period from April 01st, 2001 to March 31st, 2019. The average interannual precipitation is 1,870.83 mm with a standard deviation of 180.41 mm. The annual regime fluctuates from one year to the next; the 2012 hydrological year corresponds to the wettest year with an average annual precipitation height of 2,117.40 mm, and the driest year is that of 2002 with 1,456.30 mm (Figure 3.32). The variations in monthly average precipitation show that the biggest amount of precipitation (25.17%) is received in August and the lowest amount in January with only 0.10%. Relying on data availability from 2001 to 2018, Sokotoro watershed's annual average air temperature is 23.50°C. The monthly temperature variation is not as much as pronounced; however, April is the hottest month with an average air temperature of 25.96°C while August is the coldest month with an average of 21.92°C (Figure 3.33). The hydrometric data of the Sokotoro watershed was also provided at daily time steps from April 1st, 2001 to March 31st, 2019. The interannual average of past flows amounts to 32.45 m^3/s, the minimum occurred in 2004 with 24.99 m^3/s, and the highest runoff value (41.52 m^3/s) was recorded in 2012 (Figure 3.32). The variation in monthly average discharge shows that the biggest amount of flow is recorded in September with 29.34%, and the lowest amount in April with only 0.12%. Over the whole available discharge, from 2001 to 2018 water years, the maximum daily discharge was recorded on August 16th, 2008 with 211.10 m^3/s and the minimum daily on May 20th, 2002 with only 0.006 m^3/s.

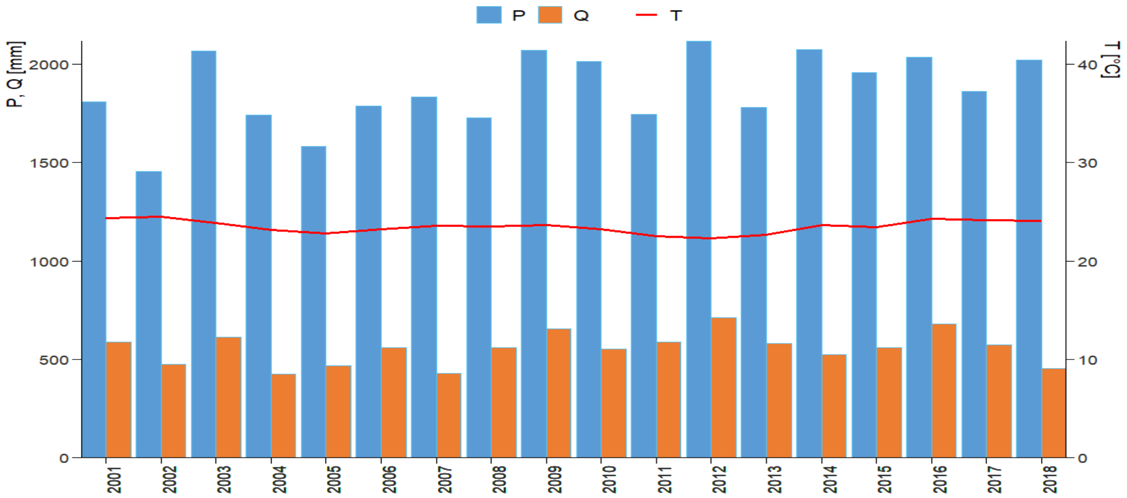

Figure 3.32. *Bafing à Sokotoro watershed hydro-meteorologic data*

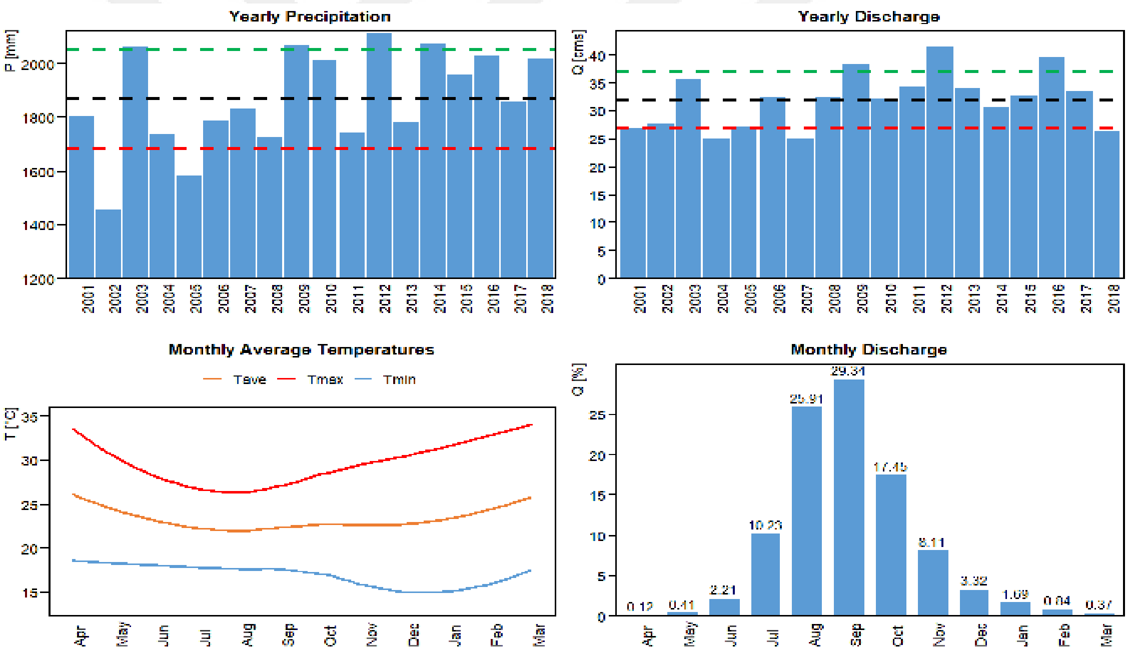

Figure 3.33. *Bafing à Sokotoro watershed annual and monthly hydro-meteorologic data (red, black, and green dashed lines are average minus standard deviation, average and average plus standard deviation respectively). Below red line represents drought periods and above green line wet periods*

The result of the Oudin formula shows that the average annual PET for the Sokotoro is 1,536.98 mm/year and the highest value was recorded in 2002 (1,588.60 mm) and the lowest in 2012 (1,469.24 mm) with a standard deviation of 34.32 mm. March is the month in which the amount of water that evaporates is the highest (9.53%) and in December its lowest value (7.13%) is reached (Figure 3.34).

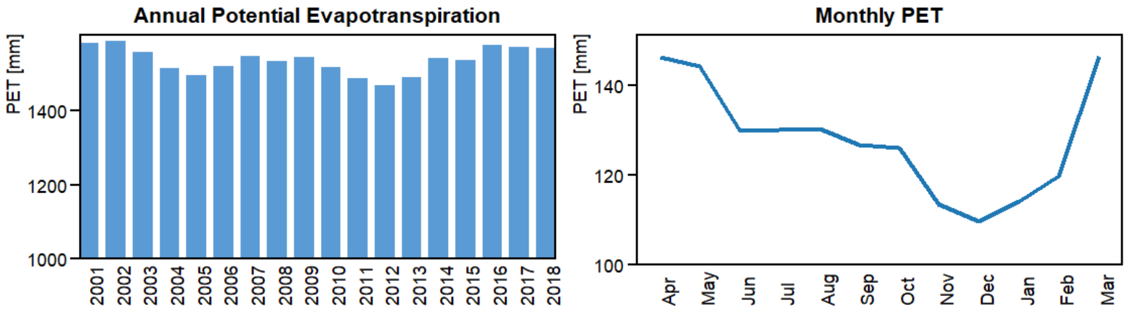

Figure 3.34. *Bafing à Sokotoro basin potential evapotranspiration data calculated using Oudin (2005)*

3.3. Remote Sensing Data

Remote Sensing (RS) technology has made significant advancements in recent decades, providing valuable information on hydrological variables that are essential for effective water resource management. Through remote sensing, we can observe and monitor a wide range of factors such as precipitation, temperature, soil moisture, snow cover area, and so forth over large areas. Additionally, remote sensing offers improved accuracy in estimating conceptual hydrologic models' parameters, as Tong et al. (2022) highlighted. Many products with different resolutions could provide these hydrologic variables. However, to meet the purpose of this study, we limited ourselves to two products. Snow cover area (SCA) data from October 01st, 2000 to September 30th, 2019 for Çukurkışla and from October 1st, 2007 to September 30th, 2019 for Kayabaşı. These SCA data were extracted from MOD10A1F which is provided free of charge by the National Snow and Ice Data Center (NSIDC DAAC https://nsidc.org/data/modis/data). Soil moisture (SM) data from April 01st, 2015 to Mars 31st, 2017 for Niger and Milo and from April 01st, 2015 to Mars 31st, 2019 for Sokotoro. These SM data were extracted from SMAP SPL4SMGP which is provided free of charge by the National Snow and Ice Data Center (NSIDC DAAC https://nsidc.org/data/smap/data). A succinct information about these two products is given below.

3.3.1. MODIS snow cover area cloud gap filled data

MOD10A1F is a daily cloud-free snow cover product derived from MOD10A1 which is NASA's Moderate-resolution Imaging Spectroradiometer (MODIS) sensor product. Specifically, it refers to a particular data set within the MODIS/ Terra Snow Cover Daily snow cover product suite. The MOD10A1F product provides information on snow cover extent and snow cover fraction at a spatial resolution of 500 meters. It is generated by processing MODIS data using algorithms designed to detect the presence of snow on the Earth's surface. MOD10A1 grid cells that are cloud cover are filled by using clear-sky views of the surface from previous days.

Other methods are also used in MODIS snow cover area treatment. One of them is to use Terra (MOD10A1) and Aqua (MYD10A1) concomitantly (e.g. Riboust et al. 2019, Ruelland, 2024). However, MOD10A1F is practiced and ready for use, so it was chosen.

The Türkiye MOD10A1F data in GeoTIFF format was downloaded and processed using the R programming language. The Çukurkışla and Kayabaşı SCA data were then extracted from the Türkiye MOD10A1F data. For more information on Türkiye MOD10A1F SCA data, interested readers can refer to Eylen (2024). The winters of four years with varying snowfall rates were selected and presented in Figures 3.35 and 3.37 for Çukurkışla and Kayabaşı, respectively. Additionally, a few days were chosen to highlight the variation in snow cover from the beginning to the end of winter (Figures 3.36 and 3.38). Finally, to obtain the numerical data of the SCA for the five zones, the basins were divided into five zones of equal surface area and extraction was performed using R (Figure 3.39). Figure 3.39 indicates that snow cover takes longer to develop in the Kayabaşı basin compared to the Çukurkışla basin. This suggests that snow is more prevalent in Kayabaşı, likely due to its higher altitude and specific geographical location.

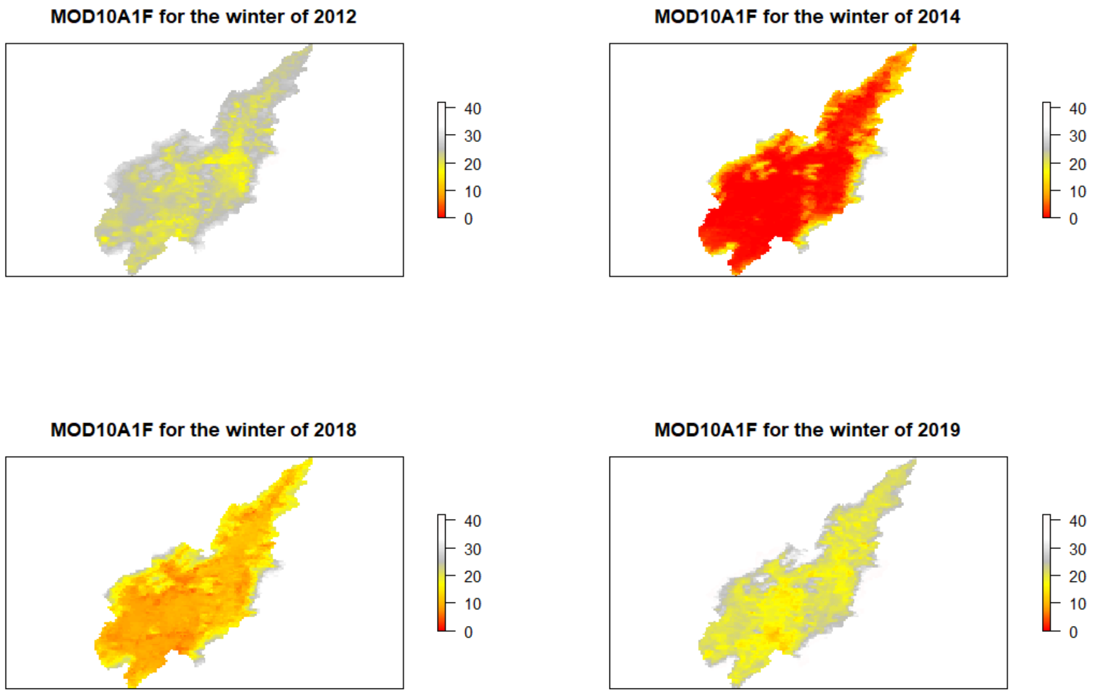

Figure 3.35. *Çukurkışla watershed winter (November to February) snow cover area from MOD10A1F highlighting snow cover area change through years*

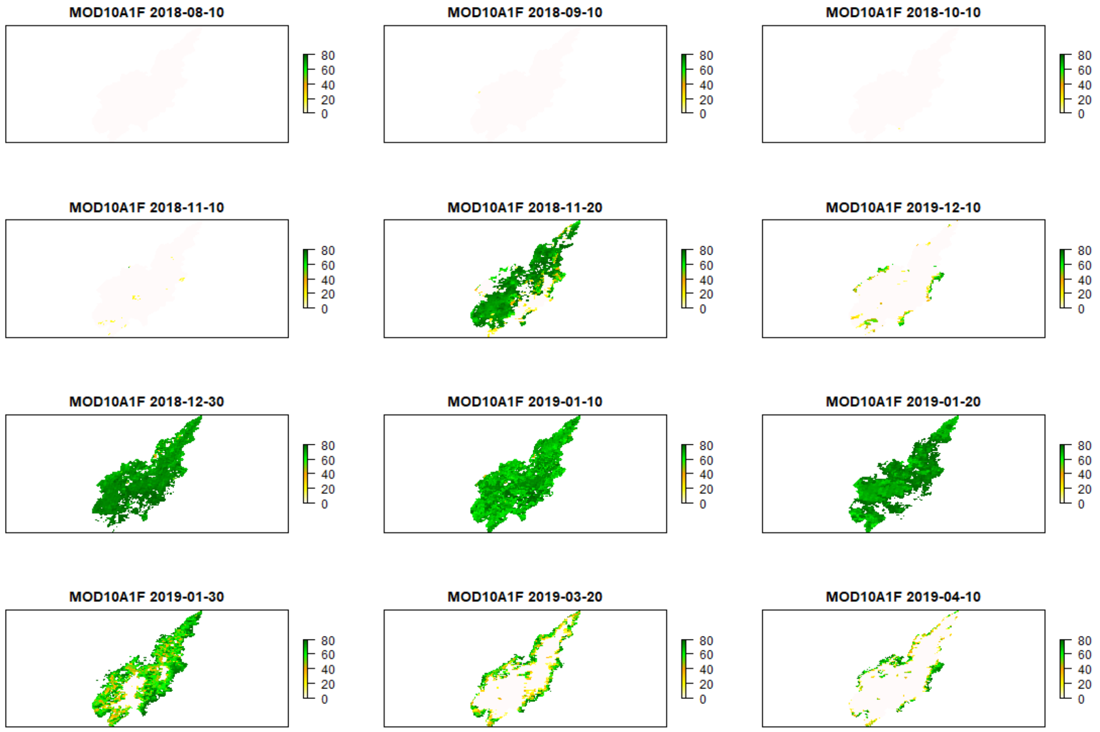

Figure 3.36. *Çukurkışla watershed daily snow cover area from MOD10A1F highlighting snow cover area change through months*

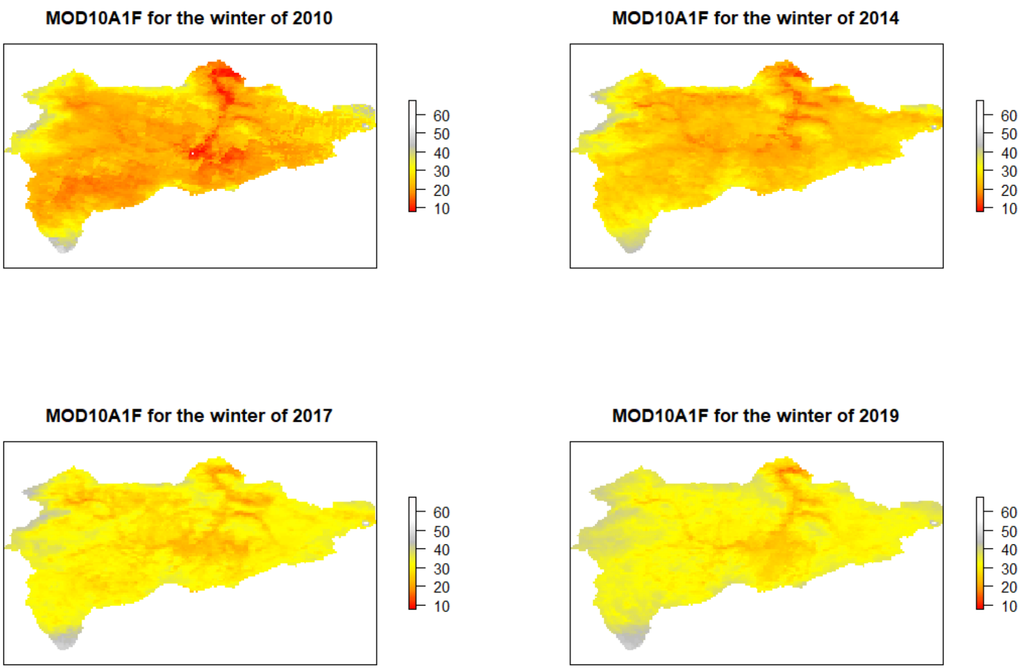

Figure 3.37. *Kayabaşı watershed winter (November to February) snow cover area from MOD10A1F highlighting snow cover area change through years*

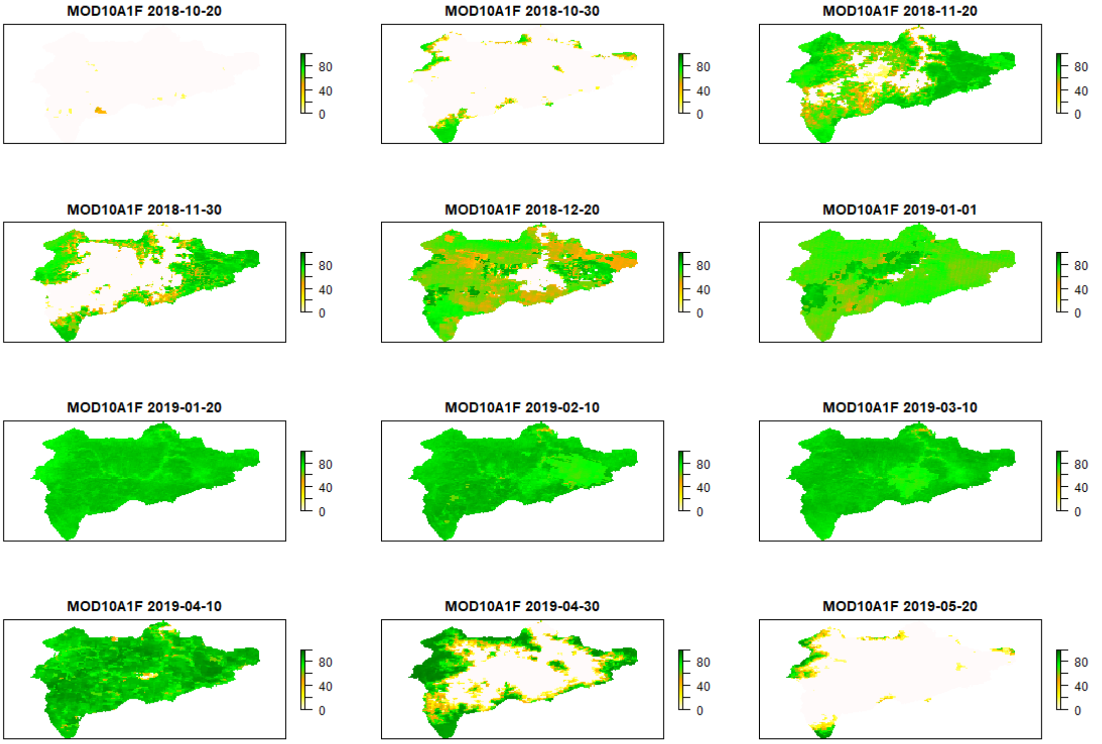

Figure 3.38. *Kayabaşı watershed daily snow cover area from MOD10A1F highlighting snow cover area change through months*

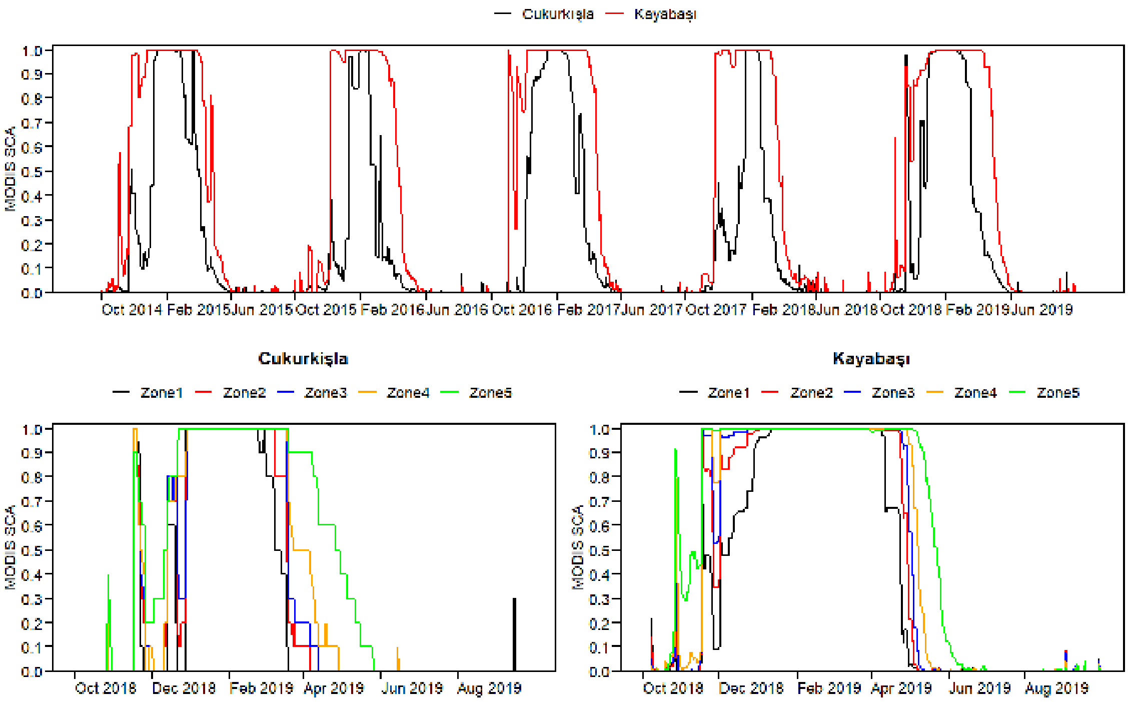

Figure 3.39. *Çukurkışla and Kayabaşı watersheds snow cover area data (above lumped data and below basins discretized in five altitudinal equal areas data)*

3.3.2. SMAP root wet zone level 4 data

SMAP SPL4SMGP is a product derived from NASA's SMAP mission. It stands for "Soil Moisture Analysis Products, Level-4 Surface and Root Zone Soil Moisture Gridded Products". SPL4SMGP provides global gridded data on surface and root zone soil moisture. The SMAP satellite mission collects the data, which uses active and passive microwave sensors to measure soil moisture content. The surface soil moisture depth is 0 – 5 cm while the root zone soil moisture is 0 – 100 cm and two different aspects of soil moisture measurement exist: the volumetric soil moisture content within the root zone (m3/m3) and the relative wetness of the root zone soil (dimensionless fraction: ranges from 0 to 1 or percentage 0% to 100%).

The model' soil moisture is the relative measure of the soil moisture content since it is found by dividing the soil water content level (S) to it maximum capacity (X1). Therefore, soil moisture of root zone wetness is the most appropriate choice for calibrating a hydrological model.

SMAP L4 Global 3-hourly 9 km EASE-Grid Surface and Root Zone Soil Moisture Geophysical Data V007 has a spatial resolution of 9 km and a temporal resolution of 3 hours, containing all soil moisture data at global cylindrical (EASE-Grid 2.0) projection. The soil moisture of root zone wetness data was downloaded in GeoTIFF format and watersheds were extracted from this dataset. To obtain daily soil moisture values, the data were aggregated by averaging the eight raster datasets representing each day. This process was performed using the R language to generate numerical soil moisture values which are used in model calibration. For visualizing monthly variations in soil moisture at the basin scale, a few months were selected (see Figures 3.40,.41 and 3.42 for Niger, Milo and Sokotoro respectively) and it was observed that the land cover (National Park of upper Niger in the northwest of Niger) and the natural region (Forest Guinea in the south of Milo) contribute to high soil moisture, especially on dry season. The resulting daily digital data from the hourly data processing for the three watersheds are shown in Figure 3.43.

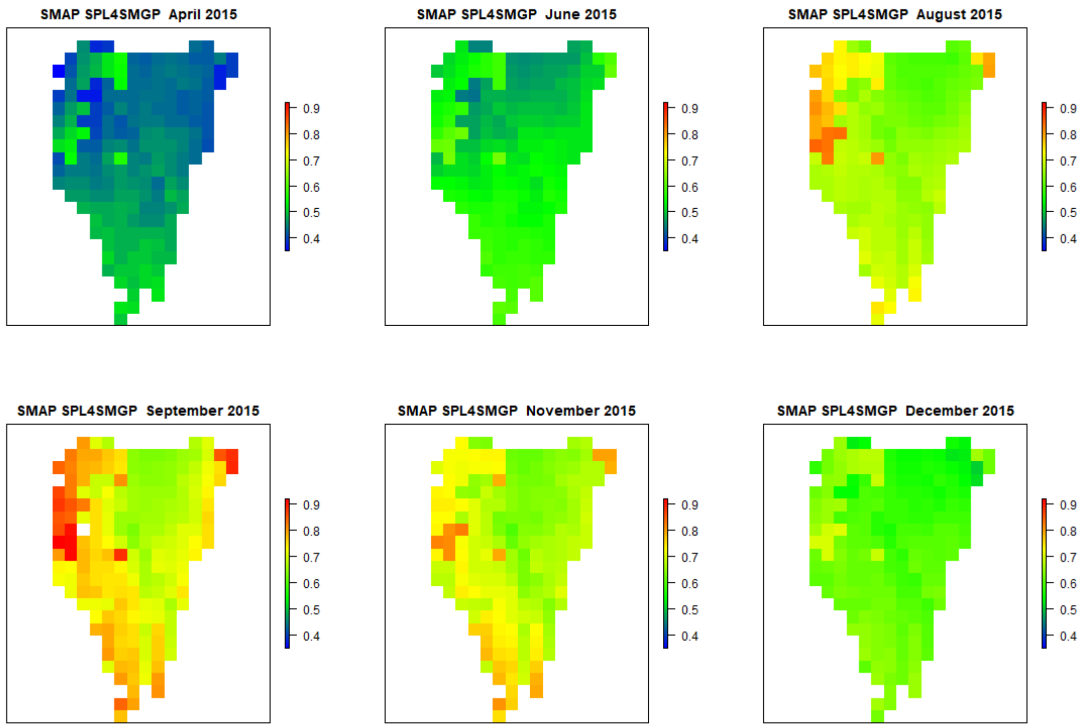

Figure 3.40. *Niger à Kouroussa watershed monthly soil moisture data from SMAP SPL4SMGP highlighting soil moisture changes through months*

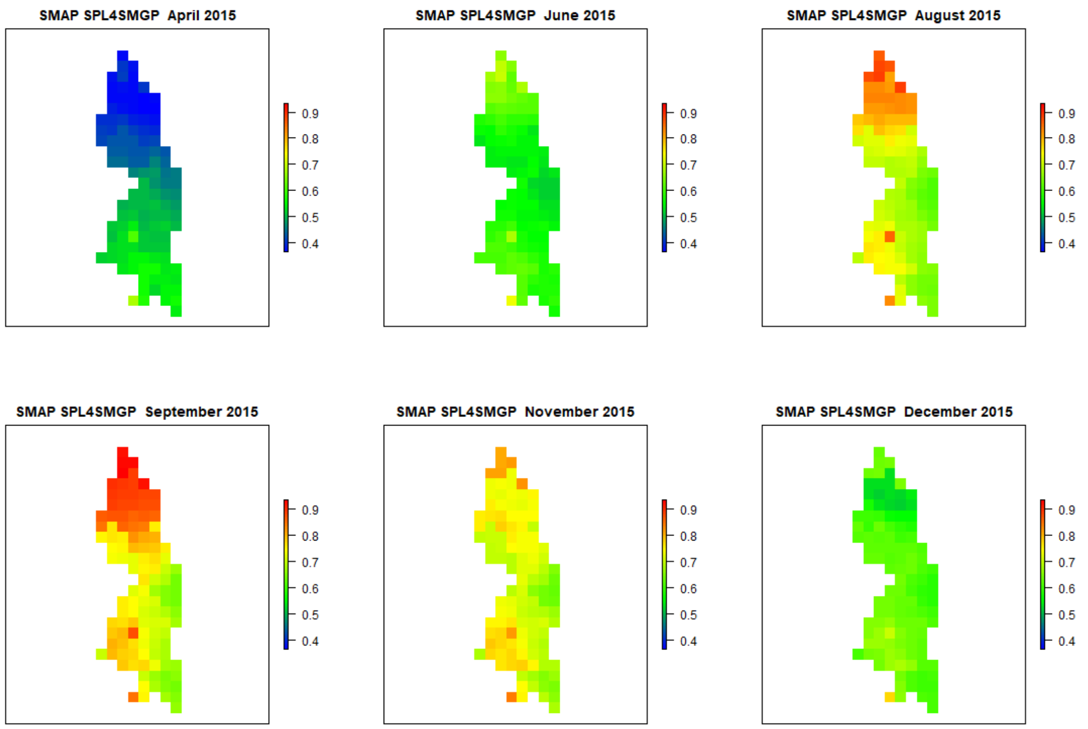

Figure 3.41. *Milo à Kankan watershed monthly soil moisture data from SMAP SPL4SMGP highlighting soil moisture changes through months*

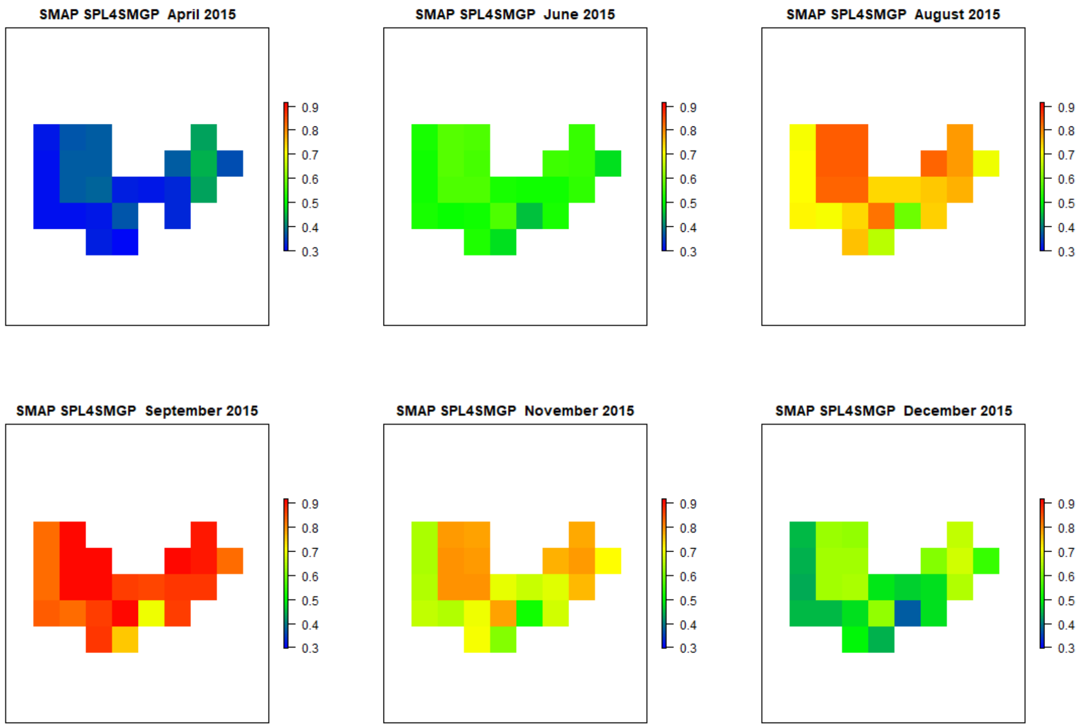

Figure 3.42. *Bafing à Sokotoro watershed monthly soil moisture data from SMAP SPL4SMGP highlighting soil moisture changes through months*

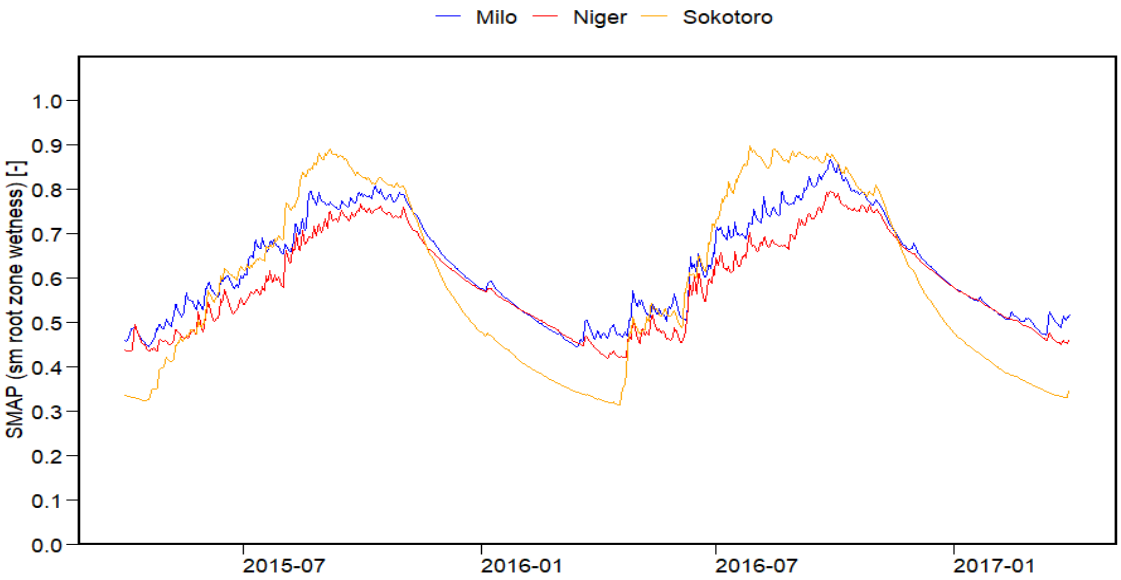

Figure 3.43. *Guinean basins soil moisture data*

3.4. Methodology

In rainfall-runoff modeling, where flow data at the watershed outlet is utilized, the calibration process involves adjusting parameters based on how well the model reproduces observed flow patterns over a historical period. This classic method is widely employed due to its simplicity and effectiveness. However, it is important to note that hydrological modeling is not limited to flow data alone. Other variables, such as snow accumulation and melt, soil moisture, and groundwater levels, can also be modeled either individually or in combination with flow data, resulting in multi-objective calibration approaches. Each variable presents its own challenges and requires its own set of parameters to be calibrated. For instance, modeling snow accumulation and melting might involve parameters related to temperature thresholds, precipitation phase change, and snowpack dynamics. Soil moisture modeling could involve parameters related to infiltration rates, soil properties, and vegetation cover. Integrating these variables into a multi-objective calibration framework adds complexity but can provide a more comprehensive understanding of the hydrological system and improve model performance under various conditions. Ultimately, the choice of variables and calibration approach depends on the specific goals of the modeling study and the available data.

Considering the diverse meteorological conditions across the studied countries, our approach encompassed hydrological modeling at various temporal resolutions across different watersheds. Initially, we conducted daily time-step modeling for the two Turkish watersheds by integrating the GR4J model (Perrin et al. 2003) with the CemaNeige snow module (Valéry et al. 2014b) to capture snow processes. In contrast, for the three watersheds in Guinea, which are located in a tropical region where snow dynamics are absent, we solely employed the GR4J model to reflect the prevailing hydrological conditions. Subsequently, at monthly and annual time steps, we utilized the GR2M and GR1A models across all five watersheds to encompass broader temporal scales. This process allows for a comprehensive understanding of each watershed behavior in both countries.

For multi-objective calibration purposes, we refined the modeling for the two Turkish watersheds at daily intervals by incorporating MODIS SCA data alongside flow data, specifically focusing on addressing hysteresis between snow accumulation and melting (Riboust et al., 2019). Conversely, for the Guinean watersheds, our calibration strategy involved integrating discharge with soil moisture data from SMAP (e.g. Koster et al. 2018, Yi et al 2018). Table 3.15 gives a succinct view of all mentioned above.

Table 3.15. *List of models used in Türkiye and Guinea with single and multiples objectives calibrations*

Method	Türkiye	Guinea
Single Objective Calibration based on flow	GR4J_CN GR2M GR1A	GR4J GR2M GR1A
Multi Objective Calibration	GR4J_CN with hysteresis (Q and SCA)	GR4J (Q and SM)

In hydrological modeling, multi-algorithm optimization (Adeyeri et al., 2020) approach is done by applying multiple optimization algorithms to calibrate a model and find the optimal set of parameters that minimize the difference between observed and simulated data. Each algorithm independently searches the parameter space to find the best-fit parameters based on the objective function, which could be a measure of fit between observed and simulated hydrological data. It allows for increasing the likelihood of finding the global optimum or a high-quality solution, as different algorithms may have different strengths and weaknesses in exploring the parameter space and avoiding local optima.

In this study, this technique was applied to models for leveraging the diversity of optimization algorithms to explore the parameter space more effectively. For this, in single objective optimization, three algorithms were used namely hydroPSO (Zambrano and Rojas, 2013), DEoptim (Mullen, et al., 2011), and Calibration (Michel (1989); Magand (2005)), which was denoted as CM in this study. On the other hand, the multi-objective optimization was done with CM and DE (Figure 3.44).

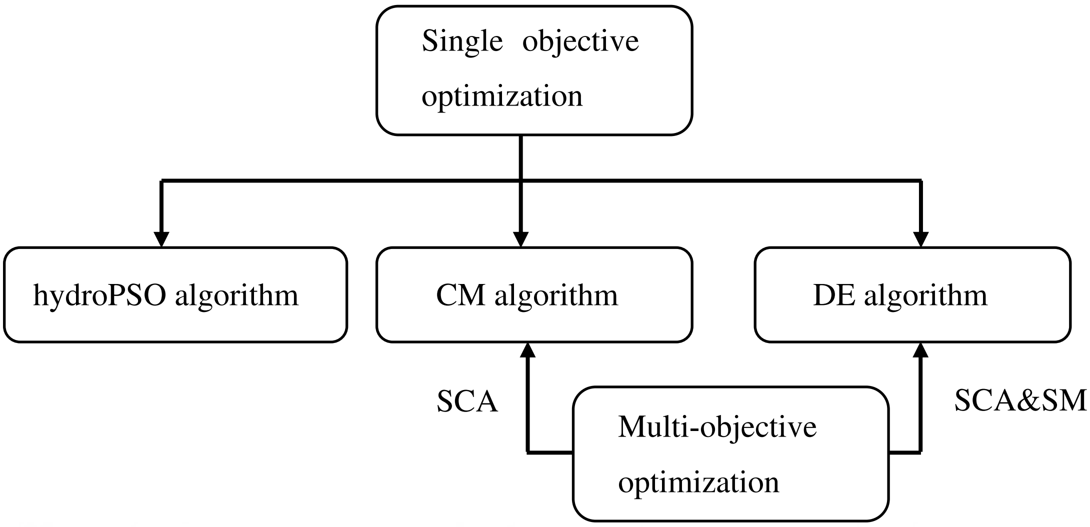

Figure 3.44. *Use of algorithms for single and multi-objective optimizations*

3.4.1. Single objective optimization using runoff data

Firstly, it consisted of modeling Çukurkışla and Kayabaşı watersheds in Türkiye and Niger, Milo and Sokotoro watersheds in Guinea using a single objective function to simulate streamflow data. For all basins, available data were presented in Sections 3.2.1 and 3.2.2. According to available data, we divided them into two parts: on part one (P1) calibration with one year as warm-up was carried out and on the part two (P2) validation was performed. Then P2 was used for calibration and P1 for validation (Figure 3.45). This process is known as split sample test which was proposed by Klemeš (1986). Table 3.16 gives calibration periods for each basin.

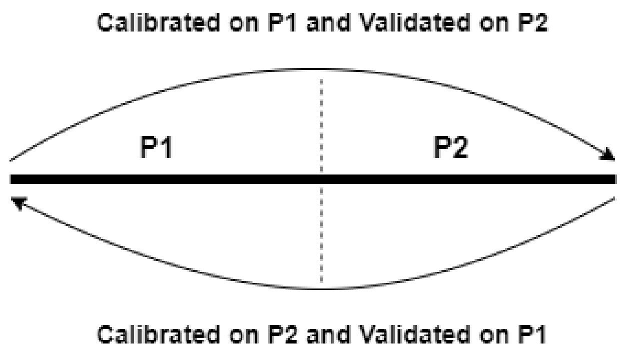

Figure 3.45. *Split-sample test method diagram for calibration and validation*

Table 3.16. *Calibration periods that were used for split-sample test*

Country	Basin name	P1 warm-up	P1	P2 warm-up	P2
Türkiye	Çukurkışla	2000	2001 – 2008	2008	2009 – 2019
	Kayabaşı	2007	2008– 2013	2013	2014 - 2019
Guinea	Niger	1991	1992 – 2002	2003	2004 – 2016
	Milo	1991	1992 – 1999	1999	2000 – 2009
	Sokotoro	2002	2003 – 2010	2010	2011 – 2018

Objective function that we selected to be optimize was the modified Kling Gupta efficiency given in Section 2.2.2 formula 2.19. It was chosen because it offers the advantage of providing a more comprehensive and well-rounded evaluation of hydrological models' performance. It takes into consideration correlation, bias, and the variability ratio. This approach allows for the correction of biases in relation to the volume of water in the hydrological balance and many studies recommended it (e.g. Magand, 2014). Besides of modified KGE, some other efficiencies were used to evaluate more accurately models' performance (e.g. Andrade et al., 2024). They are Nash-Sutcliffe efficiency (NSE) (Section 2.2.1, equation 2.18), Root mean square error (RMSE) (Section 2.2.4, equation 2.25) and deviation of runoff volumes (D_v) (Section 2.2.5, equation 2.26).

3.4.2. Multi objective optimization calibration

The increasing accessibility of satellite data and advancements in computing technology have sparked a growing interest in multi-objective calibration among researchers. In this same perspective, MODIS SCA data from Turkish watersheds and SMAP SM data from Guinean watersheds were used in the second part of this study. In what follows, we started with a brief review of how SCA and SM are utilized in multi-objective calibration by some researchers before diving into our methodology.

3.4.2.1. Runoff and snow cover area

Riboust et al. (2019) conducted a study that aimed to calibrate the CemaNeige snow model using both Snow Cover Area (SCA) and runoff observations, unlike typical conceptual degree-day snow models calibrated solely with runoff data. By revising the CemaNeige SCA formulation to address SCA-Snow Water Equivalent (SWE) hysteresis, the authors conducted their analysis on 277 French mountainous watersheds using

MODIS snow cover data from the NSIDC. Results indicated that calibrating CemaNeige with SCA data alone led to a reduction in runoff simulation performance but improved SCA simulation. Introducing hysteresis improved SCA simulation without compromising runoff performance. The study identified the most effective compromise (weighting: 75% emphasis on runoff and 5% for each zone on SCA) for model evaluation criteria and concluded that the hysteresis-inclusive model showed slightly better performance and greater robustness compared to the original model. However, independently calibrating the snow module using only SCA data yielded mixed results, particularly when applied in sequential calibration or estimating ungauged catchments.

Ruelland (2024) explored how combining snow data with streamflow records can enhance hydrological models in mountain catchments. By calibrating a snow and ice model alongside a rainfall-runoff model, the study showed that integrating snow observations, especially in-situ snow water equivalent (SWE) measurements, improves model accuracy. The optimal approach involved calibrating snow and runoff parameters simultaneously, with a 25% weight on snow data. This method enhanced snow simulations without compromising runoff predictions, though it did not significantly reduce parameter uncertainty or improve climate robustness.

Parajka and Blöschl (2008) investigated the impact of integrating MODIS snow cover data into hydrological models across 148 catchments in Austria. The aim of their study was to assess how MODIS data can enhance snow and runoff model performance. Some searchers previously suggested that incorporating MODIS data can improve snow cover simulations without majorly affecting runoff predictions. The authors conducted a thorough analysis using a larger catchment sample to derive broader conclusions. They calibrated the hydrologic model using both runoff and snow cover data and compared the results with traditional calibration methods. Their findings revealed that assimilating MODIS snow cover observations improved snow coverage simulations compared to ground measurements. They also included a sensitivity analysis to assess the impact of thresholds on snow model performance and validated snowmelt simulations against various MODIS snow cover data sets. Overall, their research underscores the potential advantages of utilizing MODIS snow cover data to validate and calibrate conceptual hydrological models, thereby enhancing hydrological simulations.

Ruelland (2023) examined the complexity necessary in temperature-index models to effectively simulate snow cover and runoff in mountainous areas. The study utilized a dataset from 17 catchments in the French Alps and Pyrenees, calibrating the SIAR model with streamflow, MODIS snow cover data, and local snow water equivalent (SWE) measurements from 2004 to 2016. The findings revealed that a simplified, one-parameter SIAR model proved to be just as effective as more intricate versions, thus avoiding excessive parameterization and equifinality issues. Moreover, the SIAR model, particularly when employing equal-area elevation bands, offered precise simulations of snow and runoff while maintaining computational efficiency, ultimately outperforming the CemaNeige snow routine.

Thirel et al. (2013) examined how incorporating Snow Cover Area (SCA) data from the MODIS sensor into the LISFLOOD model can enhance the prediction of snowmelt-related floods and improve the European Flood Awareness System (EFAS). The study focused on the Morava basin, a tributary of the Danube, over a three-year period. Daily MODIS SCA data at a 500-meter resolution were used, and the data assimilation was performed using the particle filter method at different frequencies. Synthetic experiments initially confirmed the effectiveness of the assimilation schemes, resulting in improvements in both modeled SCA and discharge. Furthermore, when the MODIS SCA data were assimilated, there was a noticeable enhancement in SCA accuracy, and the Nash-Sutcliffe efficiency of the resulting discharge showed improved streamflow simulations in many cases.

In their study, Nemri & Kinnard, (2020) compared four calibration strategies for the GR4J hydrological model coupled with the CemaNeige snow model, to improve snow water equivalent (SWE) simulation and reduce parameter uncertainty. Their findings indicated that incorporating snow survey observations into the model significantly enhanced the simulation of SWE without substantially degrading the streamflow simulations. Despite these improvements, the study also revealed a substantial presence of equifinal parameters, suggesting structural non-identifiability within the model.

Many other researchers had applied multi-objective calibration by using either MODIS SCA or other satellites products for snow alongside of discharge to enhance models' accuracy (e.g. Peker & Şorman, 2021; Duethmann et al., 2014; Sleziak et al., 2020; Thorton et al., 2021; Taia, et al., 2023; Şorman, et al., 2019).

Given that the MODIS SCA data covers the entire temporal span of the available data for the two Turkish watersheds, a multi-objective calibration was performed over the calibration period for each basin. Initially, SCA data were prepared for each basin's five equal area zones. Objective functions were then defined for both flow and snow (SCA), with a variable weighting (w_{sn}) ranging from 0 to 20% in increments of 1% for each zone. The chosen objective function was the modified Kling-Gupta Efficiency (KGE') for both flow and SCA like Riboust et al. (2019) did. Consequently, the multi-objective function was formulated as follows:

$$ME_{sn} = (1 - w_{sn}) \cdot KGE'(Q) + w_{sn} \cdot \sum_{i}^{5} KGE'(SCA_i) \qquad (3.1)$$

Where ME_{sn} is the multi objective criterion, KGE'(Q) modified Kling Gupta Efficiency on discharge (Q), KGE'(SCA) modified Kling Gupta Efficiency on each altitudinal zone i and w_{sn} the variable weight on both discharge and snow.

3.4.2.2. Runoff and soil moisture

In their study, Bajracharya et al. (2023) made enhancements to the HYPE model for the Nelson Churchill River Basin. They did this by increasing the number of soil layers from three to seven, which helped improve the accuracy of subsurface thermodynamics and water transfer simulations. To ensure the fidelity of the model for both soil moisture and streamflow, they used multi-objective optimization (MOO) techniques and incorporated soil moisture data from the years 2013 to 2017. The results of their refined model were quite promising. It showed a significant improvement in soil moisture simulations, with a KGE value increasing from 0.21 to 0.66. Importantly, this improvement did not come at the expense of streamflow performance. Additionally, the refined model demonstrated better evapotranspiration simulations, suggesting its potential for permafrost identification and climate change analysis.

Li et al. (2018) compared a joint calibration scheme that utilized both streamflow measurements and remote sensing-derived soil moisture with a calibration that solely relied on streamflow data. They conducted tests on three different modeling setups: a lumped model, a semi-distributed model with a single gauge, and a semi-distributed model with multiple gauges. The results indicated that the joint calibration led to a slight decline in streamflow predictions during the calibration process but improved the predictions during validation. Furthermore, the joint calibration exhibited significant enhancements at ungauged sites, particularly in upstream and tributary sub-catchments, thanks to the inclusion of spatial information from the soil moisture data.

Nan & Tian (2024) conducted a study to examine the impact of calibrating the tracer-aided hydrological model THREW-T in two mountainous basins on the Tibetan Plateau. The researchers used soil moisture and isotope data in their investigation. The results showed that calibrating the model with soil moisture data did not improve the simulation of streamflow during the validation period. However, when the model was calibrated with isotope data, it successfully improved the simulation of both streamflow and the spatiotemporal variation of soil moisture. Additionally, isotope calibration provided the most reasonable estimation of runoff source apportionment and significantly reduced uncertainty.

Rajib et al. (2016) conducted a study in Indiana, USA to evaluate the effectiveness of using spatially distributed surface and root zone soil moisture estimates to calibrate the Soil and Water Assessment Tool (SWAT) in agricultural watersheds. They employed a multi-objective calibration approach, using remotely sensed surface soil moisture data and observed streamflow. Although this approach improved the simulation of surface soil moisture, it had limited impact on other hydrologic components such as streamflow and evapotranspiration. However, when they incorporated root zone soil moisture data from field sensors, the simulation of both root zone moisture content and streamflow significantly improved. The study emphasized the reduction in parameter uncertainty and sensitivity related to subsurface processes, but also noted difficulties in accurately representing vertical soil moisture stratification in SWAT. They recommend further research using different soil moisture data products to validate these findings.

In a separate study, Eini et al. (2023) investigated the integration of satellite-based soil moisture data from the Climate Change Initiative Soil Moisture dataset (CCI SM) into the calibration of the SWAT+ model for the Odra River Basin, which spans Poland, the Czech Republic, and Germany. They compared a single-objective calibration approach using only river discharge data with a multi-objective calibration approach that included both river discharge and soil moisture data. The multi-objective approach improved the Kling-Gupta efficiency (KGE) for discharge from 0.60 to 0.67 and achieved satisfactory accuracy in simulating soil moisture. Furthermore, it enhanced the accuracy of crop yield simulation. The study highlights the advantages of using satellite-based soil moisture data to improve the accuracy and consistency of agro-hydrological modeling.

In their 2019 study, Xiong and Zeng conducted research in the Qujiang and Ganjiang basins in southern China. They developed a model that adjusted the weighting of the SMAP soil moisture product in the objective function. Their findings indicated that incorporating different soil moisture weights in the objective function led to a minor improvement in soil moisture and flow modeling. However, it was only through flow modeling that they achieved the best flow performance.

Many other researchers had applied multi-objective calibration by using satellites soil moisture (e.g. Kubáň, et al., 2022; Parajka et al., 2009; Tong et al., 2022, Liu, et al., 2024).

Given that the SMAP SM data does not cover the entire temporal span of the available data for the three Guinean watersheds, a multi-objective calibration was performed on a limited period. For Niger and Milo watersheds, only two water years data are available, thus, one year is used for calibration and the other for validation, while Sokotoro had two years for calibration and two years for validation (Table 3.17).

Table 3.17. *Calibration and validation periods for multi-objective optimization in Guinean watersheds*

Basin name	Calibration warm-up	Calibration	Validation
Niger	04/01/2014 – 03/31/2015	04/01/2015 – 03/31/2016	04/01/2016 – 03/31/2017
Milo	04/01/2015 – 03/31/2016	04/01/2016 – 03/31/2017	04/01/2015 – 03/31/2016
Sokotoro	04/01/2014 – 03/31/2015	04/01/2015 – 03/31/2017	04/01/2017 – 03/31/2019

Initially, SM data for each basin were prepared, then the objective functions were defined for both flow (Q) and soil moisture (SM), with a variable weighting (w_{sm}) ranging from 0 to 1 in increments of 5%. The chosen objective function for flow was the combined Nash-Sutcliffe efficiency (NSE) and its logarithmic (logNSE) for discharge and the Pearson correlation coefficient (r) for soil moisture given in Section 2.2.3 equation 2.24. Consequently, the multi-objective function was formulated as follows:

$$ME_{sm} = (1 - w_{sm}) \cdot \frac{NSE(Q) + logNSE(Q)}{2} + w_{sm} \cdot r(SM) \qquad (3.2)$$

Where ME_{sm} is the multi objective criterion, NSE(Q) Nash-Sutcliffe efficiency and logNSE(Q) is the logarithmic Nash- Sutcliffe efficiency on discharge (Q), r(SM) Pearson correlation coefficient on soil moisture and w_{sm} the variable weight on both discharge and soil moisture.

4. RESULTS AND ANALYSIS

This section, divided into two subsections, presents the modeling results. The first subsection provides rainfall-runoff modeling results at different time steps (daily, monthly, and annual). In this part, the split sample test is applied and three algorithms (Calibration Michel, Differential Evolutive, and hydroPSO) are used to calibrate the GR4J coupled with the CemaNeige snow module for Turkish basins, followed by the GR4J in the three Guinean basins. The results of GR2M and GR1A for the five watersheds are also presented. The second subsection focuses on the results of the multi-objective calibration. It begins with the two Turkish watersheds, where both runoff and snow cover area (SCA) are considered, followed by the results for the Guinean watersheds, where flow and soil moisture (SM) are considered.

4.1. Rainfall Runoff Modeling at Different Time Scales

4.1.1. Daily time scale results

4.1.1.1. GR4J with CemaNeige for Turkish watersheds

- ***Çukurkışla watershed***

Calibration was performed using three different optimization techniques: Calibration Michel (CM), DEoptim and hydroPSO. The parameters of the GR4J model coupled with CemaNeige for the Çukurkışla watershed are presented in Table 4.1.

Table 4.1. *Parameters of GR4J coupled with CemaNeige calibrated using Calibration Michel, DEoptim and hydroPSO on the Çukurkışla watershed for both calibration periods*

Parameter	Calibration Michel (CM)		DEoptim		hydroPSO	
	2001 – 2008	**2009 - 2019**	**2001 – 2008**	**2009 - 2019**	**2001 – 2008**	**2009 - 2019**
X1 (mm)	737.946	848.109	1075.457	1195.749	719.837	890.797
X2 (mm)	1.522	1.715	0.952	1.089	1.542	1.812
X3 (mm)	45.802	46.944	21.685	22.827	44.069	49.469
X4 (d)	1.168	1.131	1.256	1.207	1.219	1.247
CNX1 (-)	0.002	0.020	0.364	0.010	0.443	0.355
CNX2 (mm/°C/d)	57.467	96.599	37.716	95.549	66.173	55.807

Every technique yielded slightly different parameter values. However, Calibration Michel (CM) and hydroPSO produced approximately the same values for parameters X1 and X3, while DEoptim (DE) resulted in distinct values for these two parameters. CM and hydroPSO tend to minimize the value of X1, leading to a considerably larger maximum routing capacity. In contrast, DEoptim maximized X1 and produced a smaller value for X3. The calibration over two periods indicated that the Çukurkışla basin receives water from its surrounding environment. However, DEoptim assigned a smaller value to this water influx compared to the other two algorithms. For the fourth parameter of GR4J, all three algorithms yielded nearly identical values, although CM tended to produce a slightly smaller value.

For the first parameter of CemaNeige, all three algorithms affected the snowpack sensitivity to daily temperature variations differently. CM tended to increase sensitivity, while hydroPSO and DE provided high thermal inertia. However, the P2 calibration from DE led to low thermal inertia. Despite these differences, all three algorithms produced CNX2 values that exceed physical limits. As a result, CemaNeige was not practical for use in the Çukurkışla watershed.

In regard to each technique yielded slightly different values for the parameters, that led to a variation in model performance. The performance metrics for both the calibration and validation phases are summarized in Table 4.2.

Table 4.2. *GR4J coupled with CemaNeige performance metrics with modified KGE as objective function on Çukurkışla watershed for calibration and validation periods using split sample test for each algorithm*

Algorithm	Period	Calibration				Validation			
		KGE	NSE	RMSE	Dv	KGE	NSE	RMSE	Dv%
CM	P1	0.881	0.761	0.222	0.236	0.813	0.7379	0.2322	5.4498
	P2	0.885	0.768	0.244	0.205	0.810	0.7307	0.2629	-4.3809
DEoptim	P1	0.816	0.626	0.310	1.810	0.768	0.5870	0.3255	-4.9921
	P2	0.803	0.605	0.285	-0.608	0.769	0.6112	0.2828	6.9242
hydroPSO	P1	0.866	0.736	0.233	3.191	0.757	0.731	0.235	13.718
	P2	0.876	0.749	0.254	0.360	0.770	0.674	0.289	-2.491

Calibration Michel provided the highest value for the objective function (modified KGE) over the two calibration periods, followed closely by hydroPSO. The split-sample test method yielded satisfactory results, as the model's performance and its parameters were almost identical for each algorithm.

Figures 4.1 to 4.4 show the calibration and validation graphical results. The top panel displays snowpack during the calibration and validation periods. All three algorithms showed similar seasonal patterns in snowpack accumulation and melting, with peaks in winter and early spring and a decline through summer and fall. HydroPSO and CM predicted higher snowpack peaks compared to DE. The second panel shows observed runoff and simulated runoff. All algorithms captured the timing and magnitude of peak flow events well, although hydroPSO predicted slightly higher peak runoff in P1 Calibration, and DE predicted higher peaks in P2 Calibration. The bottom left panel illustrates the monthly average runoff for observed and simulated discharge. All algorithms followed the observed seasonal cycle, with some deviations in peak magnitudes. DE, with a higher X1 value, showed delayed rising and falling limbs, indicating more gradual water release. HydroPSO consistently predicted higher monthly average runoff during peak months, except in P2 Calibration, where DE hydrograph was the highest. During non-peak months, CM and hydroPSO more accurately matched observed data. The bottom middle panel presents flow duration curves, showing the relationship between flow and its non-exceedance probability. All three algorithms closely matched observed flow distributions, though they slightly underestimated low flows, especially in P1 Calibration and P2 Validation. HydroPSO tended to slightly overestimate high flows. Finally, the bottom right panel is a scatter plot comparing observed and simulated flows. The alignment between simulated and observed flows indicated satisfactory model performance, with similar R^2 values for all three algorithms (e.g., P1 Cal: CM: 0.7764, DE: 0.6448, hydroPSO: 0.7803). However, there is more dispersion, particularly for higher flows, and DE shows the lowest R^2 values.

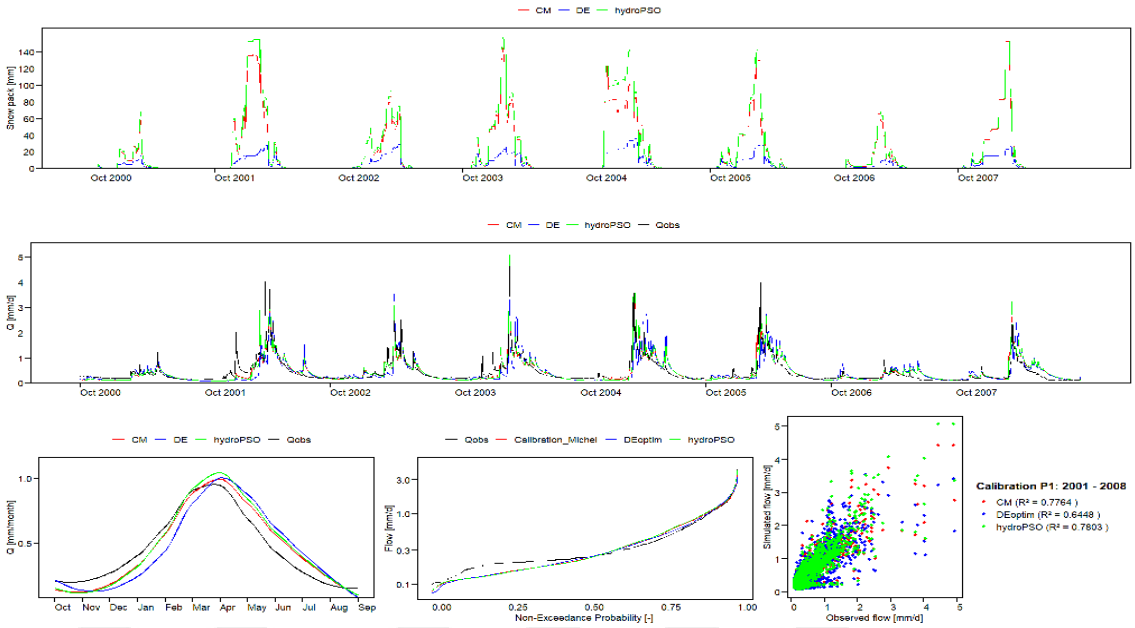

Figure 4.1. *Çukurkışla watershed P1 Calibration with Calibration Michel, DEoptim and hydroPSO algorithms results.*

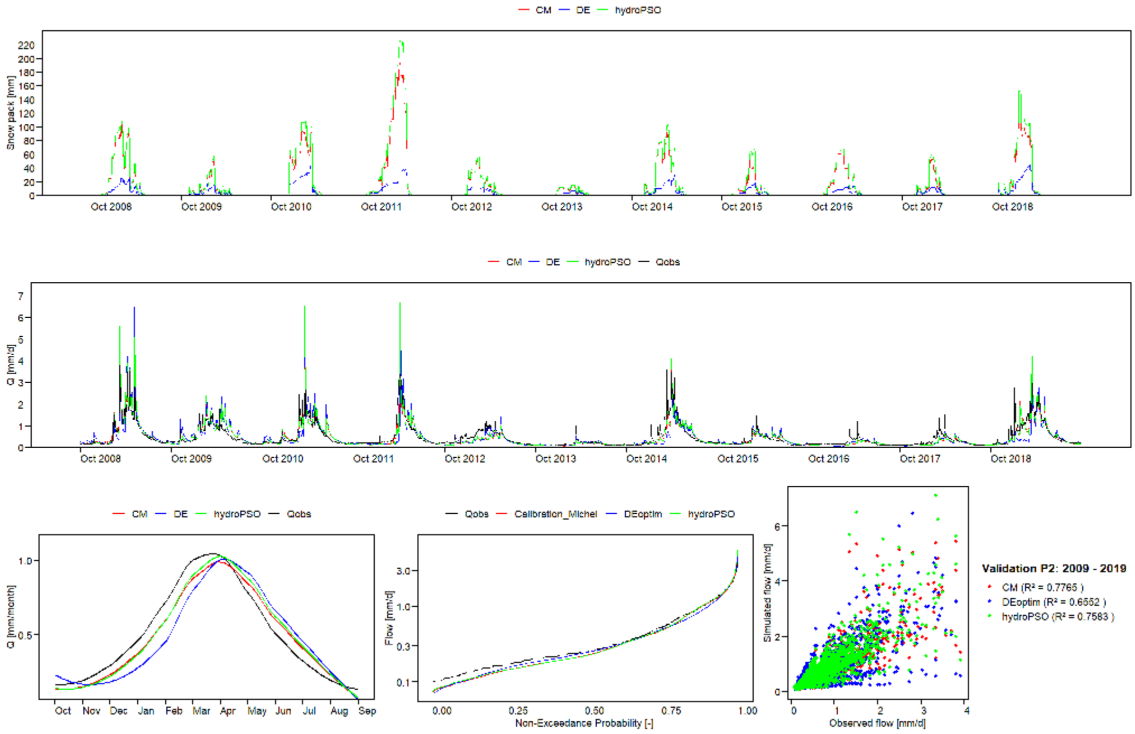

Figure 4.2. *Çukurkışla watershed P2 Validation with Calibration Michel, DEoptim and hydroPSO algorithms results.*

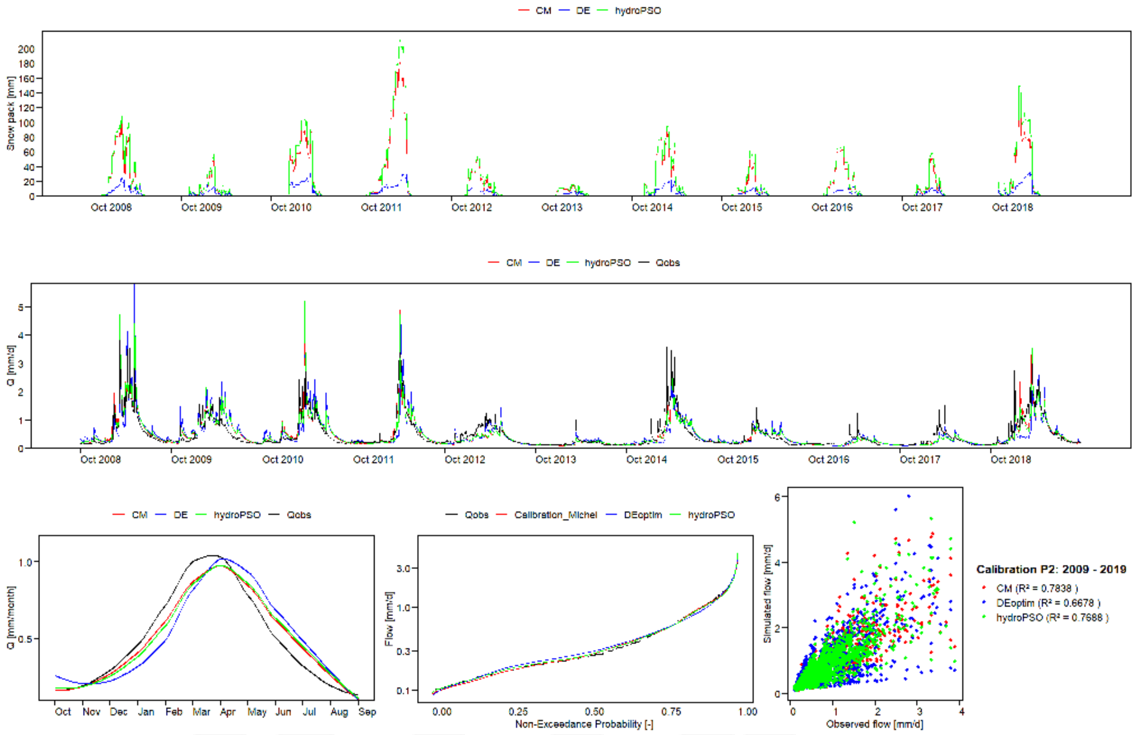

Figure 4.3. *Çukurkışla watershed P2 Calibration with Calibration Michel, DEoptim and hydroPSO algorithms results.*

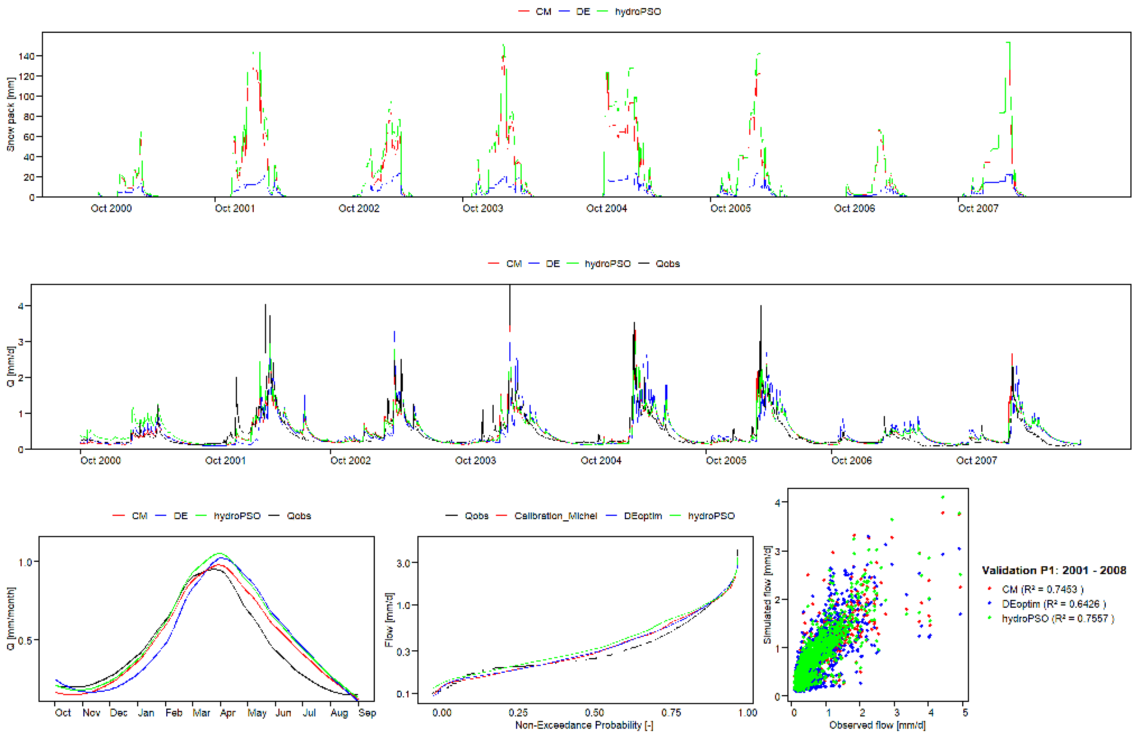

Figure 4.4. *Çukurkışla watershed P1 Validation with Calibration Michel, DEoptim and hydroPSO algorithms results.*

- ***Kayabaşı watershed***

The parameters of the GR4J model coupled with CemaNeige for the Kayabaşı watershed are presented in Table 4.3.

Table 4.3. *Parameters of GR4J coupled with CemaNeige calibrated using Calibration Michel, DEoptim and hydroPSO on the Kayabaşı watershed for both calibration periods*

Parameter	Calibration Michel (CM)		DEoptim		hydroPSO	
	2008 – 2013	2014 - 2019	2008 – 2013	2014 - 2019	2008 – 2013	2014 - 2019
X1 (mm)	52.079	343.779	317.370	400.927	281.583	423.934
X2 (mm)	2.760	3.268	2.377	2.370	2.508	2.163
X3 (mm)	306.485	83.086	43.164	45.609	46.306	37.849
X4 (d)	1.020	1.086	1.233	1.426	1.137	1.424
CNX1 (-)	0.010	0.042	0.786	0.030	0.322	0.623
CNX2 (mm/°C/d)	3.758	15.826	5.702	11.284	4.878	10.659

Table 4.3 reveals that the optimization algorithms produced slightly different model's parameter values. For instance, model X1 and X3 form the CM algorithm during the P1 Calibration was totally different from what were given by DEoptim and hydroPSO. The CM algorithm resulted in a lower maximum capacity of the production store (52.079 mm) in P1, suggesting limited soil water retention, which in turn led to a higher maximum capacity of the routing store (306.485 mm). Besides CM in P1 Calibration, the GR4J with CemaNeige parameters from all three algorithms followed similar trends. The two calibration periods indicated that the Kayabaşı basin receives water from its surroundings (positive X2). In P2 Calibration, CM assigned a higher X2 value (3.268 mm), outside the 80% confidence intervals from Perrin et al. (2003), while all other values fell within this range. For the fourth GR4J parameter, all algorithms produced nearly identical values, with CM yielding slightly smaller values, a trend also observed in the Çukurkışla watershed.

The CemaNeige parameters varied among algorithms, affecting snowpack sensitivity to daily temperature differently. CM increased sensitivity due to a smaller CNX1 value, while hydroPSO and DE provided higher thermal inertia, making the snowpack less sensitive to daily air temperature changes. However, DE's P2 calibration resulted in low inertia. The second CemaNeige parameter (CNX2: degree day factor) from all algorithms fell within Valéry's suggested range of 0 to 20 mm/°C/d, with P1 Calibration yielding more reasonable values compared to P2, where each technique produced values exceeding 10 mm/°C/d. This discrepancy may relate to changes in land cover or meteorological conditions between the calibration periods. Overall, CemaNeige performed better in the Kayabaşı watershed than in the Çukurkışla basin.

The slightly different parameter values from each technique led to variations in model performance. Table 4.4 summarizes the performance metrics for both the calibration and validation phases.

Table 4.4. *GR4J coupled with CemaNeige performance metrics with modified KGE as objective function on Kayabaşı watershed for calibration and validation periods using split sample test for each algorithm*

Algorithm	Period	Calibration				Validation			
		KGE	NSE	RMSE	Dv%	KGE	NSE	RMSE	Dv%
CM	P1	0.810	0.626	0.582	-0.230	0.711	0.589	0.610	-11.14
	P2	0.847	0.691	0.516	0.901	0.743	0.436	0.698	9.178
DEoptim	P1	0.811	0.642	0.570	-2.672	0.724	0.605	0.598	-10.70
	P2	0.850	0.703	0.506	0.743	0.775	0.516	0.646	8.122
hydroPSO	P1	0.803	0.609	0.596	1.873	0.733	0.628	0.580	-0.638
	P2	0.850	0.701	0.508	1.540	0.762	0.498	0.658	12.811

In the P2 Calibration, all three algorithms produced higher values for the objective function (modified KGE) compared to P1 Calibration. CM yielded slightly lower metrics than DEoptim and hydroPSO (Table 4.2). The split-sample test method showed that the model's performance and parameters were consistent across each algorithm, indicating reliable results.

Figures 4.5, 4.6, 4.7, and 4.8 present the calibration and validation results for each algorithm. The snowpack and discharge outputs were similar across all three algorithms, with CM and DE overlapping in both P1 and P2 calibration and validation, while hydroPSO showed slight differences. Notably, hydroPSO's snowpack ended earlier than CM and DE in P1 Calibration and P2 Validation, but this trend reversed in P2 Calibration and P1 Validation. The second panels display observed runoff and simulated runoff. The GR4J coupled with CemaNeige simulated discharge using different algorithms followed observed runoff trends, capturing peak flow events' timing and magnitude. However, there were instances where low runoff (e.g., 2009 in P1 Calibration) and high runoff (e.g., 2012 in P1 Calibration, 2017 in P2 Calibration) were not accurately captured. The bottom left panels show monthly average runoff for observed and simulated discharge. The models generally underestimated flow, except in P2 Validation. The curves for all three algorithms followed the observed seasonal cycle, with hydroPSO consistently producing higher monthly average runoff during peak months compared to CM and DE. All algorithms closely followed the observed data during non-peak months, enhancing accuracy but an equifinality in P1 calibration. The bottom middle panels present the flow duration curves, illustrating the relationship between flow and its non-exceedance probability. GR4J with CemaNeige simulated flows through three algorithms were close to the observed flow, demonstrating it was reliable in the context of Kayabaşı. However, it slightly overestimated low flows' frequency, with hydroPSO showing a more pronounced overestimation. HydroPSO also slightly overestimated high flows compared to the observed data. The scatter plot in the bottom right panel compares observed flows with simulated flows for the three algorithms, showing reasonable alignment and indicating satisfactory model performance. The R^2 values were similar across algorithms (e.g., P2 Cal: CM: 0.7183, DE: 0.7241, hydroPSO: 0.7249), suggesting comparable predictive accuracy. However, the points for the three algorithms were more dispersed for higher flow values, and P1 was more dispersed than P2, with CM showing the lowest R^2 in P1 validation (0.5953).

The GR4J model, integrated with CemaNeige, effectively simulated hydrological processes in the Turkish watersheds of Çukurkışla and Kayabaşı. Calibration using hydroPSO slightly overestimated extreme flows, while CM and DE algorithms aligned well with observed data. Çukurkışla exhibited higher performance metrics than Kayabaşı, although Kayabaşı's parameters were more physically representative due to the greater influence of snow. This underscores the importance of incorporating snow dynamics in model calibration to achieve a more accurate representation of hydrological processes. Detailed results are discussed in section 4.2.1.

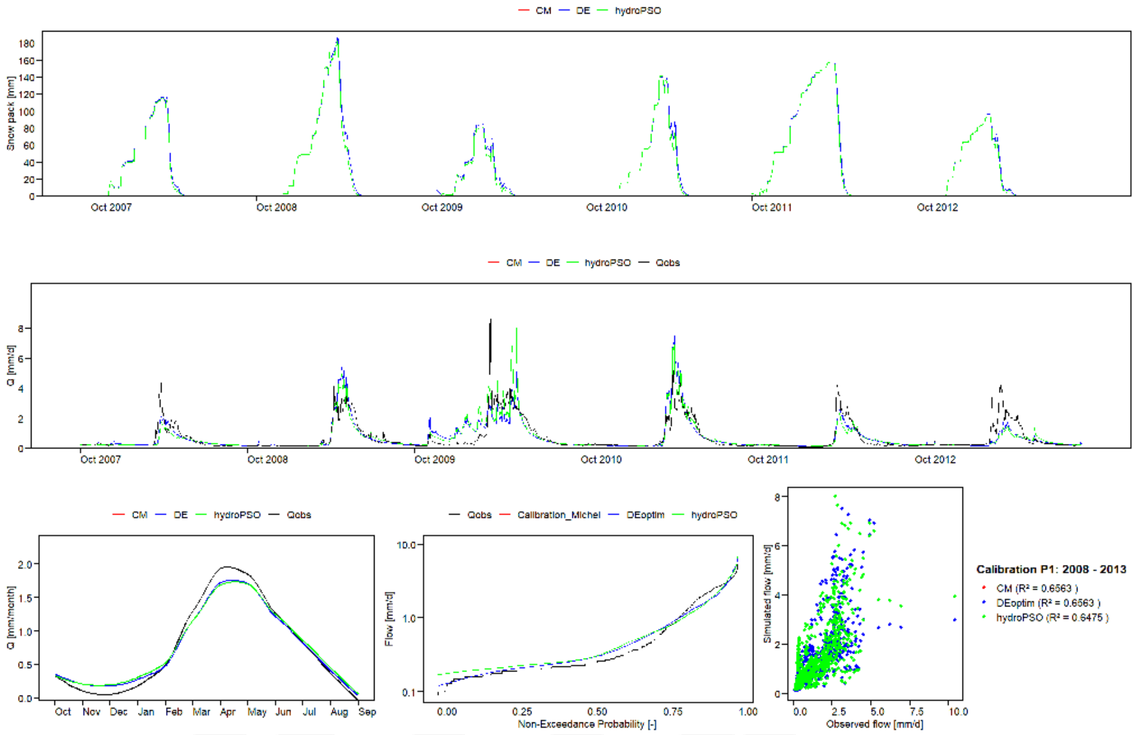

Figure 4.5. *Kayabaşı watershed P1 Calibration with Calibration Michel, DEoptim and hydroPSO algorithms results.*

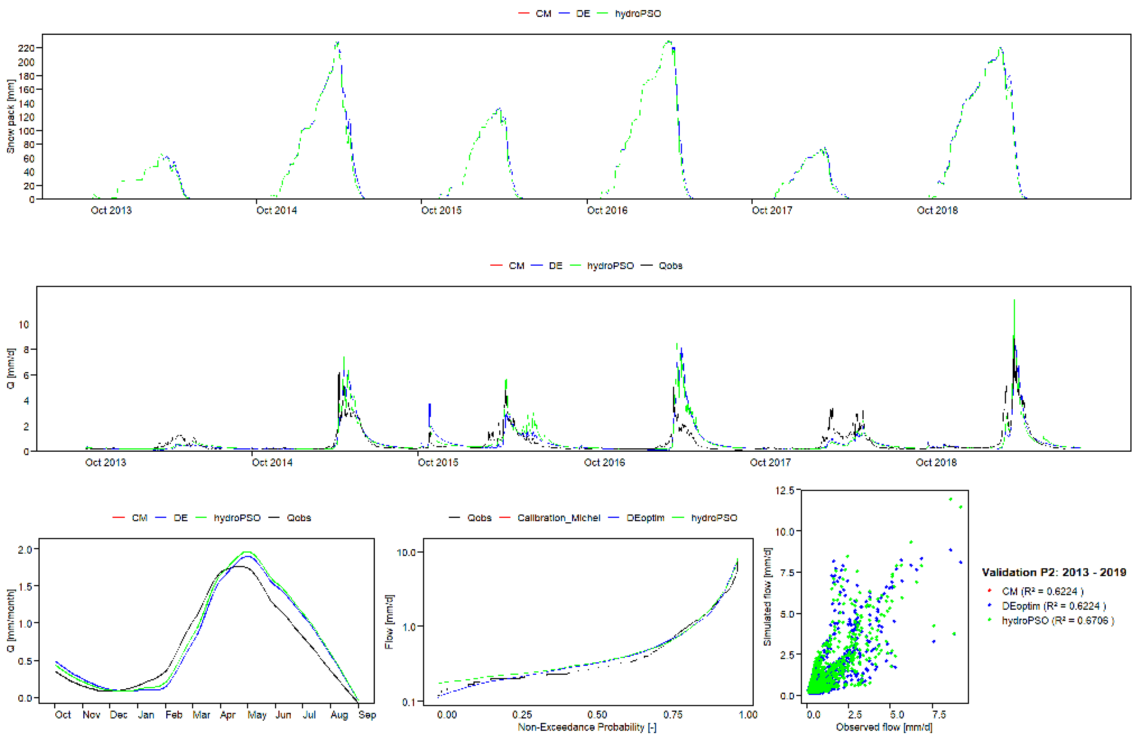

Figure 4.6. *Kayabaşı watershed P2 Validation with Calibration Michel, DEoptim and hydroPSO algorithms results.*

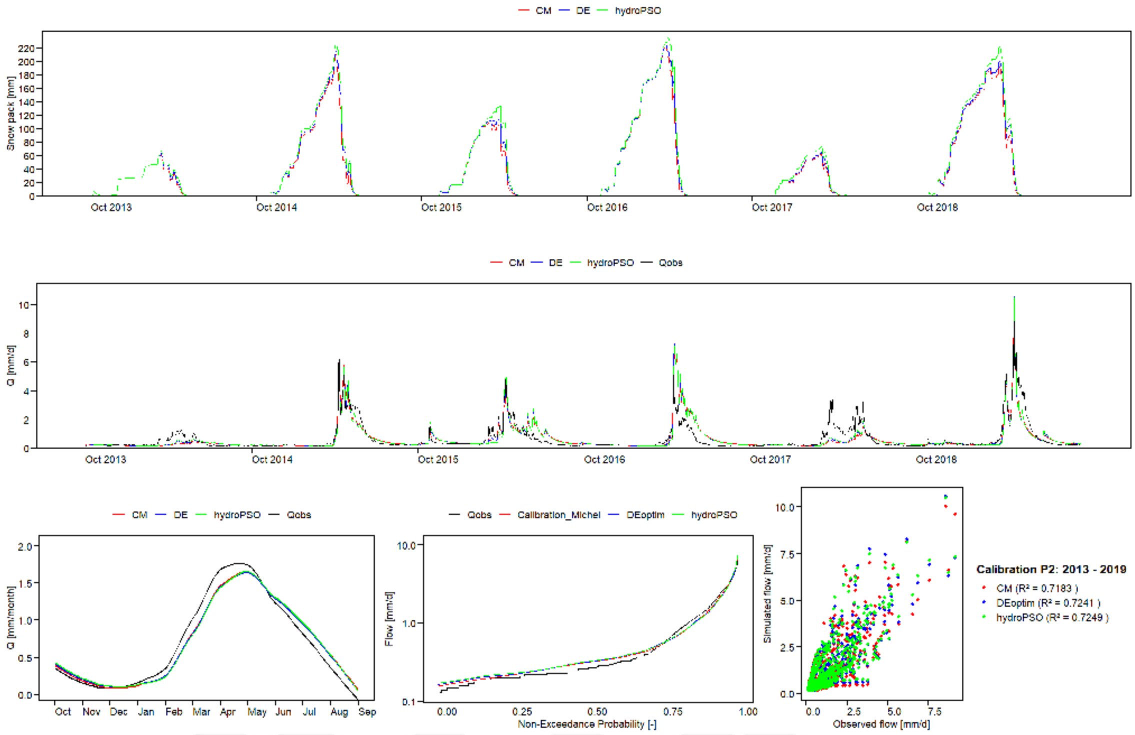

Figure 4.7. *Kayabaşı watershed P2 Calibration with Calibration Michel, DEoptim and hydroPSO algorithms results.*

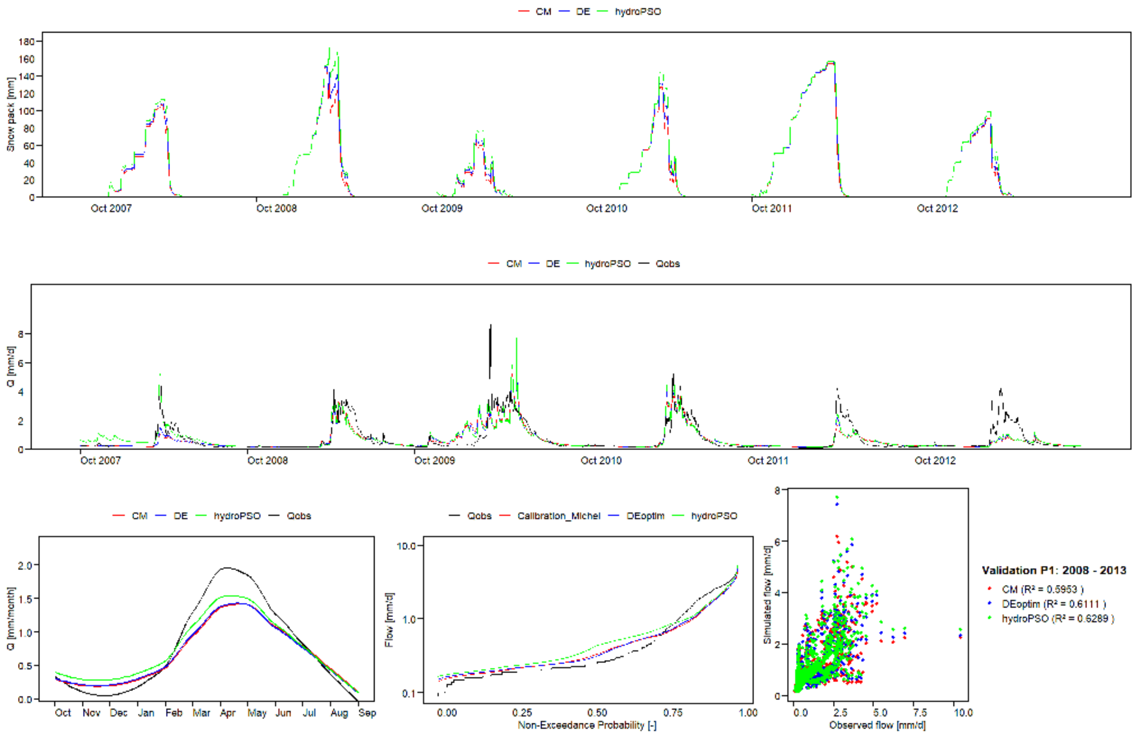

Figure 4.8. *Kayabaşı watershed P1 Validation with Calibration Michel, DEoptim and hydroPSO algorithms results.*

4.1.1.2. GR4J for Guinean watersheds

- ***Niger à Kouroussa watershed***

Calibration was performed using three different optimization techniques: Calibration Michel (CM), DEoptim and hydroPSO. The parameters of the GR4J model for the Niger à Kouroussa watershed are presented in Table 4.5.

Table 4.5. *Parameters of GR4J calibrated using Calibration Michel, DEoptim and hydroPSO on the Niger à Kouroussa watershed for both calibration periods*

Parameter	Calibration Michel (CM)		DEoptim		hydroPSO	
	1992 – 2002	2004 - 2016	1992 – 2002	2004 - 2016	1992 – 2002	2004 - 2016
X1 (mm)	820.571	1128.793	809.304	1165.589	800.529	1154.851
X2 (mm)	-0.685	-0.576	-0.730	-0.478	-0.762	-0.493
X3 (mm)	116.746	157.983	122.195	139.341	123.465	141.782
X4 (d)	6.600	5.816	6.509	6.777	6.484	6.723

The GR4J parameters for the Niger watershed analysis revealed notable differences among the three algorithms. During the P1 calibration period, hydroPSO estimated a slightly lower production store capacity (X1) at 800.529 mm, compared to CM's 820.571 mm and DE's 809.304 mm. This trend changed in the P2 calibration period, where CM estimated 1128.793 mm. For the groundwater exchange coefficient (X2), hydroPSO showed higher groundwater loss with values of -0.762 mm in P1 and -0.493 mm in P2, compared to CM and DE. Additionally, hydroPSO indicated a higher routing store capacity (X3) of 123.465 mm in P1, while CM provided the highest value of 157.983 mm in P2, due to its lower X1 value. Lastly, hydroPSO modeled a faster response time (X4) with a slightly lower value than the other algorithms during P1, whereas CM modeled a faster response time in P2.

These varying parameter values led to differences in model performance, which are summarized in Table 4.6 for both calibration and validation phases.

Table 4.6. *GR4J performance metrics with modified KGE as objective function on Niger à Kouroussa watershed for calibration and validation periods using split sample test for each algorithm*

Algorithm	Period	Calibration				Validation			
		KGE	**NSE**	**RMSE**	**Dv**	**KGE**	**NSE**	**RMSE**	**Dv**
CM	P1	0.9015	0.8045	0.5546	0.0613	0.8202	0.8005	0.5602	-6.681
	P2	0.8561	0.7105	0.6416	0.7184	0.7850	0.5892	0.7643	8.6924
DEoptim	P1	0.9016	0.8041	0.5552	0.2590	0.8187	0.8022	0.5576	-6.791
	P2	0.8589	0.7175	0.6338	0.4997	0.7845	0.5886	0.7649	8.9360
hydroPSO	P1	0.9016	0.8032	0.5564	0.3347	0.8013	0.7744	0.5958	-1.885
	P2	0.8590	0.7168	0.6346	0.6183	0.7824	0.5853	0.7679	9.0182

The model performance metrics indicated that all three algorithms performed well during both the calibration and validation periods, showing high values for KGE and NSE, reflecting good overall model accuracy. In the P1 calibration period, all algorithms had similar KGE values, ranging from 0.9015 to 0.9016. However, hydroPSO had a slightly lower NSE (0.8032) compared to CM (0.8045) and DEoptim (0.8041). The RMSE values were also close among the algorithms, indicating similar error magnitudes in flow prediction. Overall, the P1 calibration was slightly better than the P2 calibration. In the P2 validation, the KGE values decreased slightly, see Table 4.6. HydroPSO showed a slightly higher RMSE and lower NSE compared to the other algorithms, particularly in the validation period, indicating more variability in its predictions. Additionally, the volume bias (Dv%) demonstrated different trends, with CM and DEoptim generally underestimating flows (negative), while hydroPSO tended to overestimate flows (positive). Overall, GR4J calibration using CM and DEoptim maintained higher accuracy and consistency across both periods, while hydroPSO displayed more variability in its performance metrics.

Figures 4.9 and 4.10 present the GR4J model's calibration and validation results for each algorithm. All algorithms effectively captured seasonal patterns and major flood events. However, hydroPSO tended to overestimate peak flows, while CM and DE showed closer alignment with observed data, especially during non-peak months and low flow conditions. The flow duration curves indicated close matches to observed data, with slight deviations by hydroPSO at the high and low ends. Scatter plots revealed good agreement across all algorithms, though hydroPSO exhibited more scatter for higher flows.

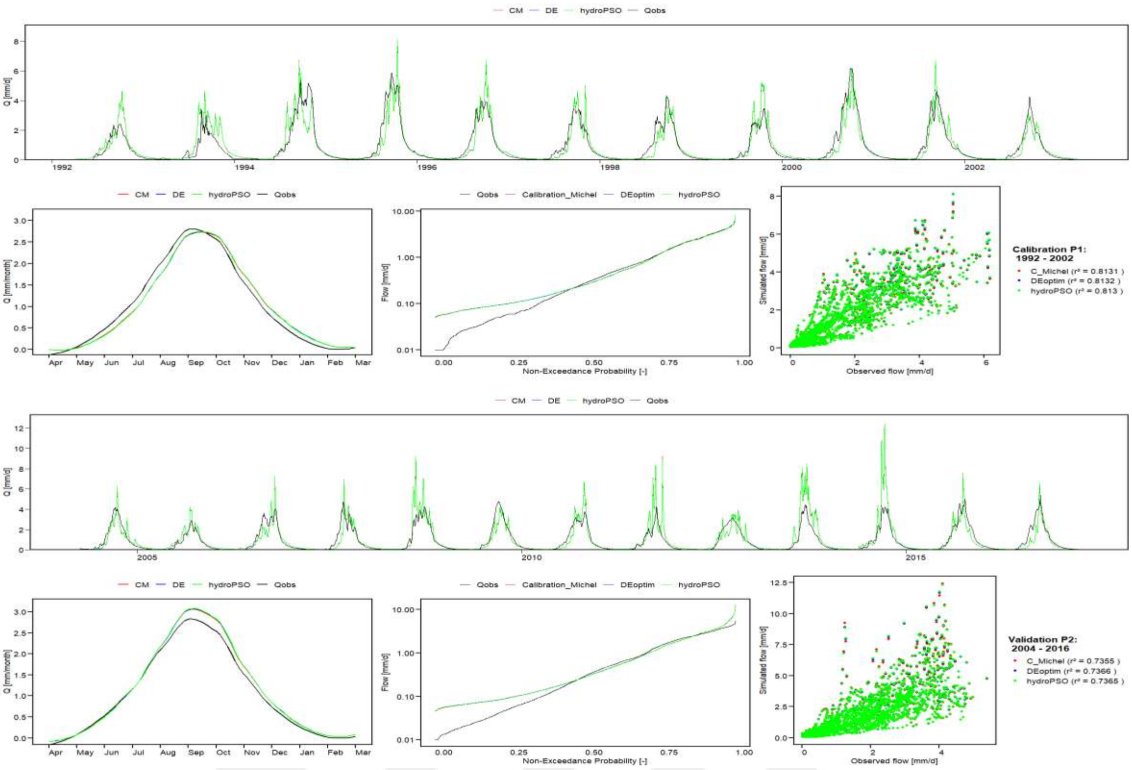

Figure 4.9. *Niger à Kouroussa watershed P1 Calibration – P2 Validation with Calibration Michel, DEoptim and hydroPSO algorithms results.*

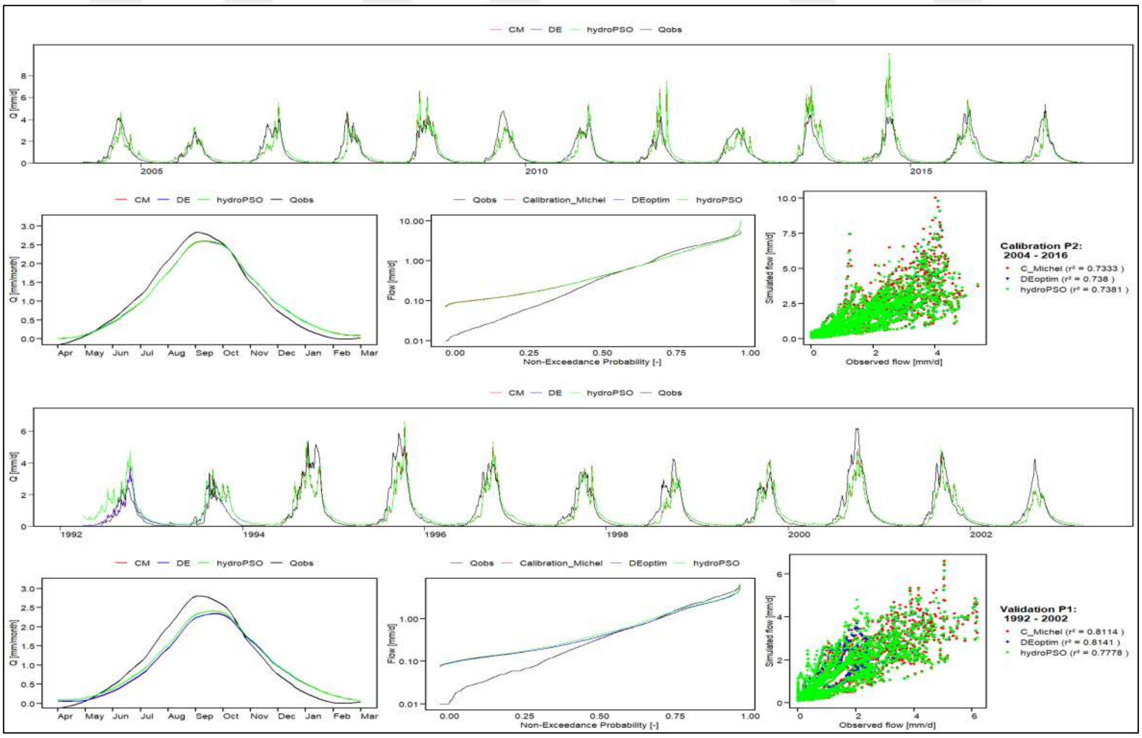

Figure 4.10. *Niger à Kouroussa watershed P2 Calibration – P1 Validation with Calibration Michel, DEoptim and hydroPSO algorithms results.*

- ***Milo à Kankan watershed***

The parameters of the GR4J model for the Milo à Kankan watershed are presented in Table 4.7.

Table 4.7. *Parameters of GR4J calibrated using Calibration Michel, DEoptim and hydroPSO on the Milo à Kankan watershed for both calibration periods*

Parameter	Calibration Michel (CM)		DEoptim		hydroPSO	
	P1	P2	P1	P2	P1	P2
X1 (mm)	923.321	757.482	934.794	734.579	954.969	753.586
X2 (mm)	-0.630	0.998	-0.613	0.963	-0.621	1.020
X3 (mm)	168.290	192.481	164.792	202.727	176.549	194.653
X4 (d)	2.538	2.432	2.565	2.430	2.506	2.441

The GR4J model parameters for the Milo à Kankan watershed displayed notable differences between the two calibration periods (P1: 1992-1999 and P2: 2000-2009) across the three algorithms. Parameter X1, which represents the maximum soil moisture storage capacity, showed a significant decrease from P1 to P2 for all algorithms, indicating a reduced soil moisture capacity in the later period. For example, X1 decreased from 923.321 mm to 757.482 mm for CM, from 934.794 mm to 734.579 mm for DEoptim, and from 954.969 mm to 753.586 mm for hydroPSO. Parameter X2, related to groundwater exchange, shifted from negative in P1 to positive in P2, suggesting a transition from groundwater extraction to recharge, with hydroPSO showing the highest positive value in P2 (1.020 mm). Parameter X3, which denoted the maximum capacity of the routing reservoir, increased from P1 to P2 for all algorithms, indicating a higher storage capacity needed in the routing reservoir to account for flow dynamics, with the largest increase observed in DEoptim (from 164.792 mm to 202.727 mm). Lastly, X4, representing the time base of the unit hydrograph, remained relatively stable across both periods for all algorithms, with only minor decreases in the P2 period, suggesting consistent responsiveness of the watershed to rainfall events.

Since each technique yielded slightly different parameter values, this led to variations in model performance. The performance metrics for both the calibration and validation phases are summarized in Table 4.8.

Table 4.8. *GR4J performance metrics with modified KGE as objective function on Milo à Kankan watershed for calibration and validation periods using split sample test for each algorithm*

Algorithm	Period	Calibration				Validation			
		KGE	NSE	RMSE	Dv%	KGE	NSE	RMSE	Dv%
CM	P1	0.8844	0.7667	0.8829	0.5769	0.7519	0.6687	1.0520	22.428
	P2	0.8664	0.7294	1.0240	0.5838	0.7693	0.7169	1.0472	-18.09
DEoptim	P1	0.8843	0.7673	0.8817	0.3687	0.7504	0.6648	1.0581	22.624
	P2	0.8664	0.7284	1.0257	0.7972	0.7678	0.7161	1.0488	-18.27
hydroPSO	P1	0.8733	0.7440	0.9248	0.6520	0.7096	0.6354	1.1036	26.921
	P2	0.8664	0.7289	1.0249	0.8572	0.7655	0.7133	1.0540	-18.55

The performance metrics for the GR4J model applied to the Milo à Kankan watershed using three optimization algorithms revealed insights into their calibration (P1, P2) and validation efficacy. Across all algorithms, the Kling-Gupta Efficiency (KGE) and Nash-Sutcliffe Efficiency (NSE) were higher during calibration periods compared to validation, indicating better model fit during calibration. Specifically, CM exhibits a KGE of 0.8844 and NSE of 0.7667 in P1, slightly decreasing to 0.8664 and 0.7294 in P2, and further dropping to 0.7519 and 0.6687 during validation (P1). DEoptim and hydroPSO showed a similar trend (see Table 4.8). The Root Mean Square Error (RMSE) increased from calibration to validation, which indicates higher prediction errors during validation, with hydroPSO showing the highest RMSE in validation (1.1036). Additionally, runoff deviation volumes (Dv%) fluctuated, with significant overestimation and in P1 validation for all algorithms, notably higher in hydroPSO (26.921%), and significant underestimation in P2 validation for all algorithms.

Figures 4.11 and 4.12 display the GR4J model's calibration and validation results for three algorithms. All algorithms captured seasonal patterns and major flood events effectively, but hydroPSO overestimated peak flows, noticeable in the time series and monthly average runoff plots. The algorithms aligned well with observed data, especially in low to mid-flow conditions. Flow duration curves showed close matches to observed data, though hydroPSO deviated slightly at high and low ends. Scatter plots indicated good agreement across all algorithms, with hydroPSO showing more scatter for higher flows. All included, all methods performed well at the Milo à Kankan watershed.

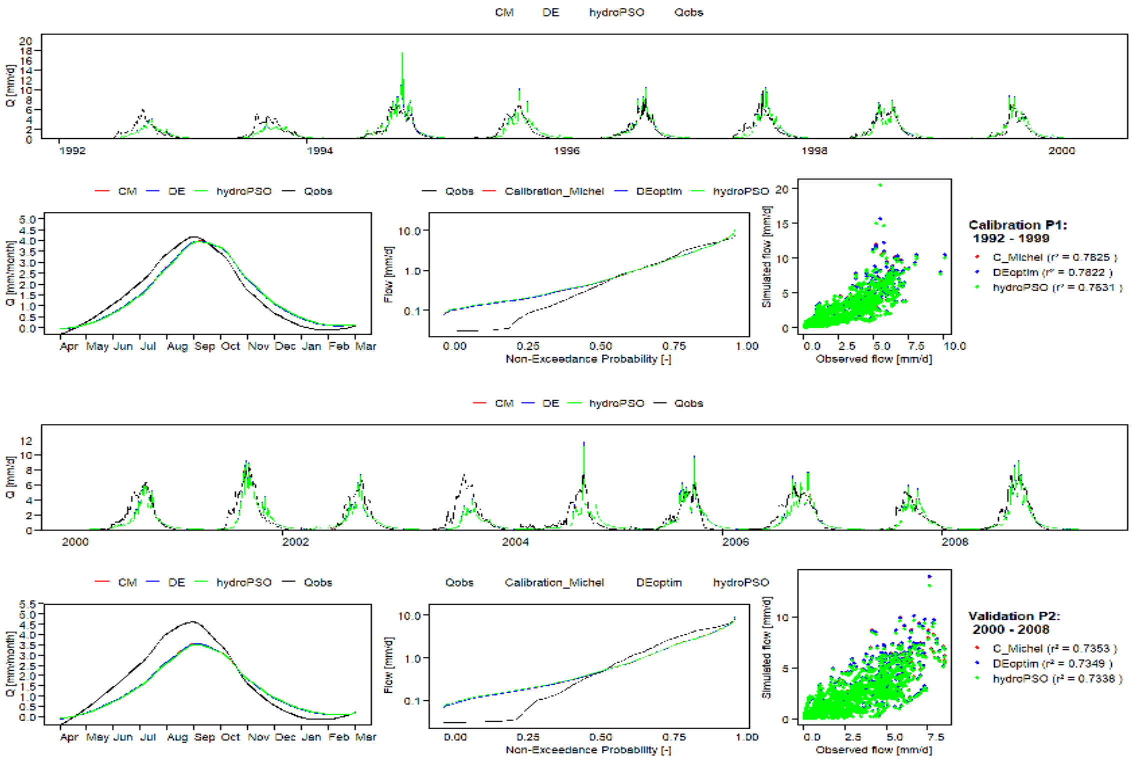

Figure 4.11. *Milo à Kankan watershed P1 Calibration – P2 Validation with Calibration Michel, DEoptim and hydroPSO algorithms results.*

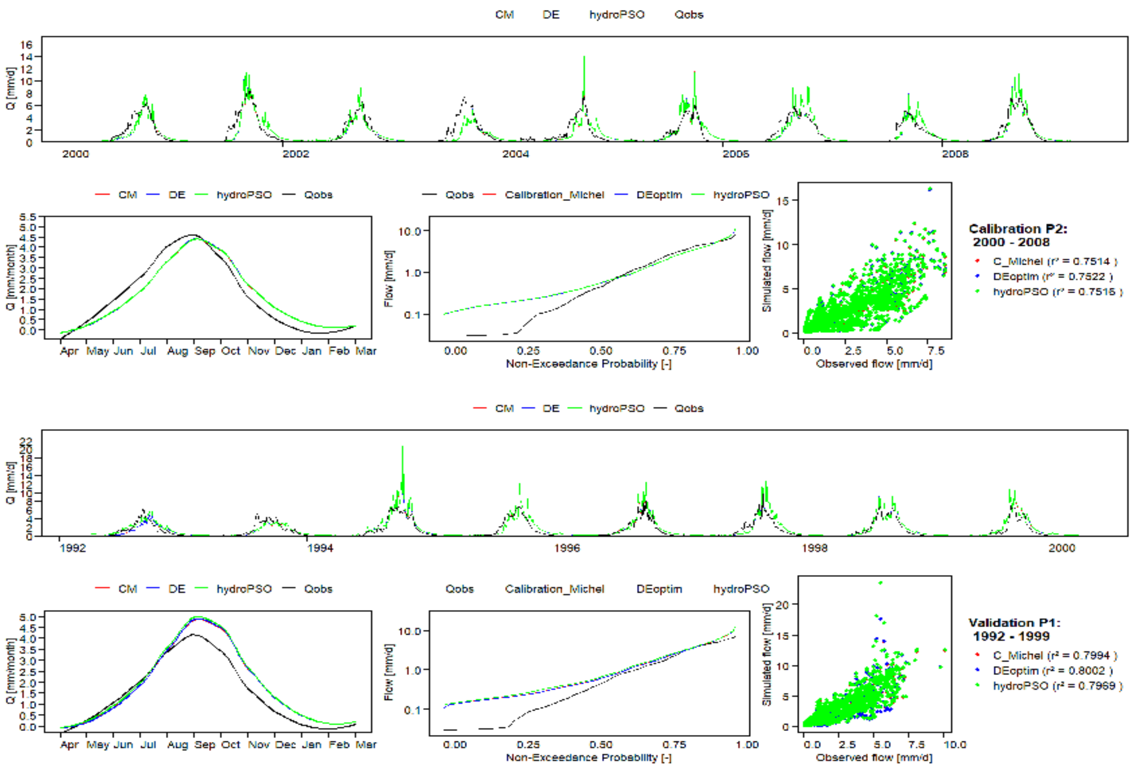

Figure 4.12. *Milo à Kankan watershed P2 Calibration – P1 Validation with Calibration Michel, DEoptim and hydroPSO algorithms results.*

- ***Bafing à Sokotoro watershed***

The parameters of the GR4J model for the Bafing à Sokotoro watershed are presented in Table 4.9.

Table 4.9. *Parameters of GR4J calibrated using Calibration Michel, DEoptim and hydroPSO on the Bafing à Sokotoro watershed for both calibration periods*

Parameter	**Calibration Michel (CM)**		**DEoptim**		**hydroPSO**	
	2008 – 2013	**2014 - 2019**	**2008 – 2013**	**2014 - 2019**	**2008 – 2013**	**2014 - 2019**
X1 (mm)	1382.326	1327.495	1381.542	1307.212	1277.718	1265.330
X2 (mm)	-1.649	-3.626	-1.684	-3.889	-0.486	-1.690
X3 (mm)	170.912	239.699	176.583	269.176	180.095	249.513
X4 (d)	3.553	4.328	3.544	3.414	3.537	4.350

The GR4J model parameters for the Bafing à Sokotoro watershed showed distinct variations across two calibration periods (2008-2013 and 2014-2019) for three optimization algorithms. X1 was consistently higher in the first period for all algorithms, with CM and DEoptim values slightly above 1380 mm, while hydroPSO had a lower value of around 1277.718 mm. In the second period, X1 decreased for all algorithms, with CM and DEoptim values above 1300 mm and hydroPSO at 1265.330 mm. Parameter X2 exhibited a noticeable decrease, with CM and DEoptim showing more negative values in the second period, indicating increased groundwater exchanges. HydroPSO displayed less negative X2 values compared to the other algorithms. On the other hand, the parameter X3 showed an increase in the second period for all algorithms, particularly in DEoptim, where it rose from 176.583 mm to 269.176 mm. Additionally, the parameter X4 remained relatively stable for all algorithms, with minor fluctuations; it was slightly higher in the second period for CM and hydroPSO, indicating a slight increase in the time constant. These parameter shifts suggested that the watershed's hydrological response characteristics have evolved over time, with significant changes in groundwater exchanges and storage capacities.

Since each technique yielded slightly different values for the parameters, this fact led to a variation in model performance. The performance metrics for both the calibration and validation phases are summarized in Table 4.10.

Table 4.10. *GR4J performance metrics with modified KGE as objective function on Bafing à Sokotoro watershed for calibration and validation periods using split sample test for each algorithm*

Algorithm	Period	Calibration				Validation			
		KGE	NSE	RMSE	Dv	KGE	NSE	RMSE	Dv
CM	P1	0.9032	0.8061	0.8292	0.4090	0.8695	0.7968	0.8488	-7.556
	P2	0.9018	0.8057	0.9110	-0.064	0.8663	0.7628	1.0065	8.4715
DEoptim	P1	0.9031	0.8068	0.8277	0.4258	0.8712	0.7940	0.8546	-6.875
	P2	0.9019	0.8067	0.9086	0.6017	0.8670	0.7660	0.9998	8.4848
hydroPSO	P1	0.9076	0.8063	0.8293	3.4907	0.8640	0.7839	0.9340	11.458
	P2	0.9037	0.8055	1.0204	3.6354	0.8503	0.7717	1.1624	17.693

The GR4J model metrics for the Bafing à Sokotoro watershed indicated strong calibration and validation performance across two periods (P1 and P2) for three optimization algorithms. During the calibration periods, all algorithms achieved high Kling-Gupta Efficiency (KGE) values around 0.90, with hydroPSO slightly higher at 0.9076 for P1 and 0.9037 for P2. The Nash-Sutcliffe Efficiency (NSE) values were consistently above 0.80 during calibration for all algorithms, indicating good model accuracy. RMSE values were also comparable across algorithms, with slight increases from P1 to P2, and all showed minimal bias (Dv%) except for hydroPSO in P1, which exhibited a higher positive bias. In the validation periods, KGE values slightly decreased but remained robust, particularly for CM and DEoptim, with values around 0.87 and 0.86, respectively. NSE values showed minor declines but are still acceptable, which reflects reliable model performance. RMSE values increased in validation, especially for hydroPSO, which also showed substantial positive bias (Dv) in both periods. Overall, while all algorithms performed well, DEoptim and CM exhibited slightly more consistent and balanced metrics across both calibration and validation periods compared to hydroPSO. This highlighted the parsimony and reliability of the GR4J.

Figures 4.13 and 4.14 present the GR4J model's calibration and validation results for three algorithms on the Bafing à Sokotoro watershed. All algorithms effectively captured seasonal patterns and major flood events, though hydroPSO overestimated peak flows in both periods. CM and DE showed closer alignment with observed data, especially in non-peak months and low flow conditions. The flow duration curves and scatter plots indicated good agreement across all algorithms, with hydroPSO showing more scatter for higher flows.

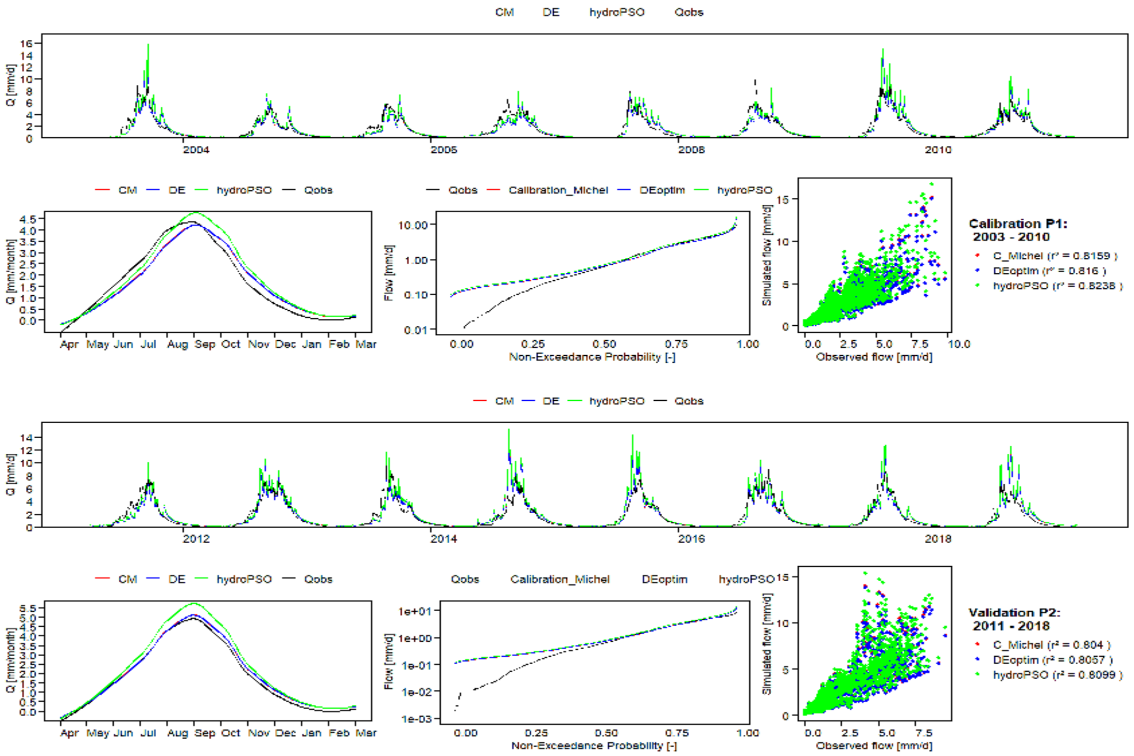

Figure 4.13. *Bafing à Sokotoro watershed P1 Calibration – P2 Validation with Calibration Michel, DEoptim and hydroPSO algorithms results.*

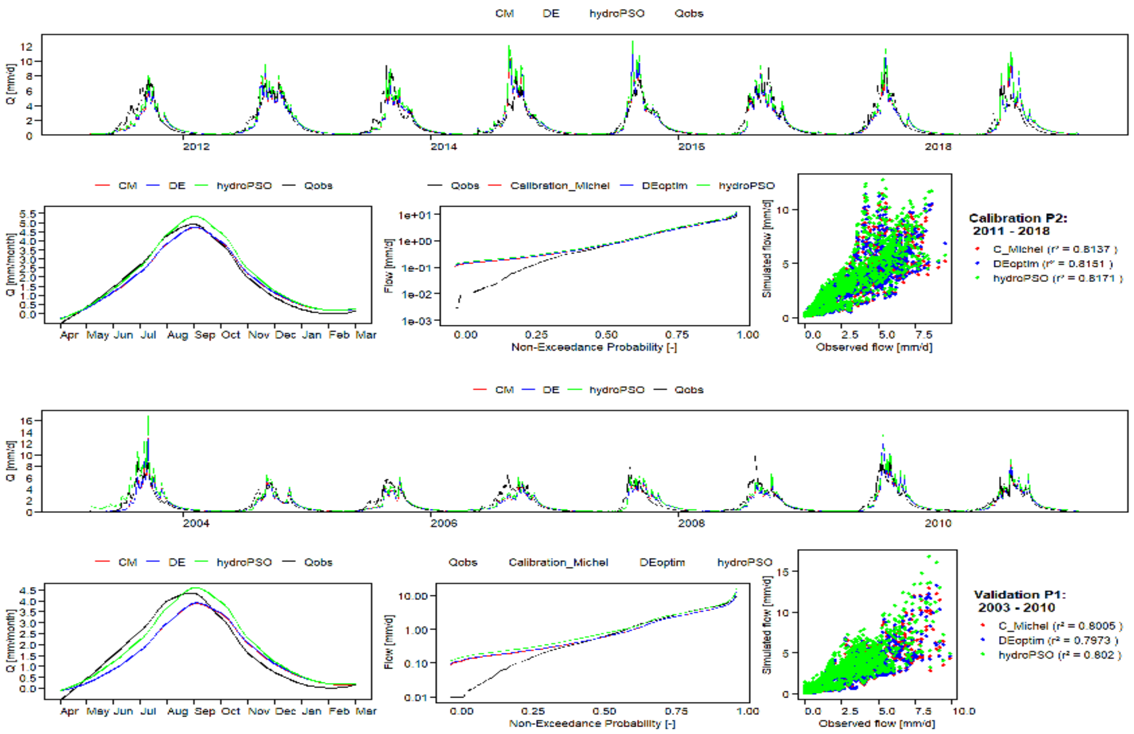

Figure 4.14. *Bafing à Sokotoro watershed P2 Calibration – P1 Validation with Calibration Michel, DEoptim and hydroPSO algorithms results.*

4.1.2. Monthly time scale results

The GR2M model was used to model the five watersheds at monthly time steps. The calibration parameters, determined using the Michel Calibration algorithm and the split sample test, are presented in Table 4.11.

Table 4.11. *Parameters of GR2M calibrated using Calibration Michel on Çukurkışla, Kayabaşı, Niger, Milo, and Sokotoro watersheds for both calibration periods*

Basin Name	Warm-up Period	Calibration Period	Parameters	
			X1 [140 – 2640] (mm)	X2 [0.21 – 1.31] (-)
Çukurkışla	10/1999 – 09/2000	10/2000 – 09/2009	992.275	1.050
	10/2008 – 09/2009	10/2009 – 09/2019	1067.546	1.072
Kayabaşı	10/2006 – 09/2007	10/2007 – 09/2013	317.348	1.170
	10/2012 – 09/2013	10/2013 – 09/2019	354.249	1.112
Niger	04/1991 – 03/1992	04/1992 – 03/2003	871.312	0.740
	04/2003 – 03/2004	04/2004 – 03/2017	1312.908	0.760
Milo	04/1991 – 03/1992	04/1992 – 03/1999	874.117	0.783
	04/1999 – 03/2000	04/2000 – 03/2009	760.766	0.864
Sokotoro	04/2002 – 03/2003	04/2003 –03/ 2011	1450.988	0.770
	04/2010 – 03/2010	04/2011 –03/ 2019	1540.712	0.752

The GR2M model parameters of the Çukurkışla and Kayabaşı watersheds in Türkiye, as well as the Niger, Milo, and Sokotoro watersheds in Guinea, revealed significant variations in catchment characteristics and hydrological responses.

For the Turkish basins, Çukurkışla had a moderate soil water capacity (X1) and an exchange coefficient (X2) value greater than 1, indicating a net gain in water due to groundwater recharge. Over time, both X1 and X2 values slightly increased, suggesting changes in land use or climatic conditions that affected soil moisture storage and groundwater dynamics. On the other hand, Kayabaşı had a much lower X1 value, indicating a smaller soil water storage capacity. However, its higher X2 values showed substantial groundwater recharge. Changes in X1 and X2 between calibration periods reflected minor shifts in soil water capacity and groundwater exchange, possibly due to management practices or environmental changes.

In contrast, the Guinean watersheds generally exhibited higher X1 values, implying significant soil water storage capacities. The Niger and Milo basins, with X2 values less than 1, indicate a net water loss due to groundwater discharge. Over time, the Niger basin showed a significant increase in X1, suggesting an increased soil water capacity, likely influenced by changing rainfall patterns or vegetation cover. Similarly, Milo exhibited a decrease in X1 and an increase in X2, indicating reduced soil water storage and increased groundwater exchange. That could be due to more evapotranspiration in the Milo basin. The Sokotoro basin, with the highest X1 values among all basins, showed an extremely high soil water storage capacity. Although its X2 values slightly decreased over time, they still reflect moderate groundwater exchange, indicating stable yet slightly changing subsurface water flow dynamics.

These variations in parameters across the basins highlight the diverse hydrological and geological conditions influenced by regional climate, soil properties, land use, and vegetation cover. Due to that, in every basin, model metrics were different from one basin to another. The performance metrics for both the calibration and validation phases are summarized in Table 4.12.

Table 4.12. *GR2M performance metrics with modified KGE as objective function on Çukurkışla, Kayabaşı, Niger, Milo, and Sokotoro watersheds for calibration and validation periods using split sample test*

Basin Name	Period	Calibration				Validation			
		KGE	**NSE**	**RMSE**	**Dv**	**KGE**	**NSE**	**RMSE**	**Dv**
Çukurkışla	P1	0.840	0.674	6.936	0.727	0.820	0.666	7.011	6.347
	P2	0.864	0.722	7.349	1.088	0.844	0.725	7.313	-3.986
Kayabaşı	P1	0.604	0.469	18.804	-8.332	0.582	0.461	18.950	-21.65
	P2	0.427	0.313	20.921	-10.58	0.409	0.2881	21.292	4.049
Niger	P1	0.898	0.815	15.802	-0.430	0.847	0.851	14.175	-1.669
	P2	0.901	0.804	15.421	-0.040	0.849	0.724	18.326	2.199
Milo	P1	0.951	0.904	16.421	-0.218	0.811	0.833	21.604	18.12
	P2	0.944	0.890	19.114	-0.261	0.831	0.871	20.748	-16.02
Sokotoro	P1	0.966	0.933	14.144	-0.018	0.948	0.934	14.073	-3.756
	P2	0.924	0.850	23.291	-0.359	0.914	0.834	24.470	3.384

The GR2M model metrics for the five watersheds, Çukurkışla and Kayabaşı (Turkish), and Niger, Milo, and Sokotoro (Guinean), revealed varying performances across calibration and validation periods.

For Çukurkışla, the Kling-Gupta Efficiency (KGE) values were high for both periods, with slight improvements in P2 calibration and validation, indicating good overall model performance. The Nash-Sutcliffe Efficiency (NSE) values were consistent, showing reliable prediction accuracy. RMSE values were relatively low, and Dv% indicated minor deviations, with some improvement in P2 validation. The increase in soil water capacity (X1) and consistent groundwater gain (X2) could reflect the stable hydrological performance captured in the metrics. However, the metrics could have been further improved if snow dynamics were included because a shift of one month between observed and modeled discharge was obvious (see Figure 4.15).

Kayabaşı exhibited lower model performance compared to Çukurkışla, with KGE and NSE values below 0.6, indicating less accurate predictions. RMSE values were notably higher, reflecting larger errors in simulation. The significant deviations (Dv%) reflected substantial errors, likely due to snow processes which are not in GR2M. On the other hand, the metrics were correlated with the lower X1 value, indicating less soil water storage, and high X2 values, suggesting substantial but perhaps unstable groundwater recharge, impacting model accuracy. Additionally, one potential reason for this discrepancy could be the presence of snow in the Turkish basins (especially dominant in Kayabaşı), which was not accounted for in the GR2M model (Figure 4.16).

In the Guinean watersheds, the Niger basin demonstrated strong model performance, with high KGE (around 0.9) and NSE values consistent across both P1 and P2 periods, low RMSE, and minimal Dv%, indicating accurate simulations. Milo also showed high KGE (more than 0.94) and NSE values, especially in P1, though it exhibited higher RMSE and Dv% in validation, indicating some variability in predictions. The changes in X1 and X2 values between P1 and P2 suggest reduced soil water storage but increased groundwater exchange, impacting validation metrics. Sokotoro exhibited the highest KGE (0.966 in P1 calibration) and NSE values, reflecting excellent model performance, with the lowest RMSE values and minimal Dv%, indicating highly accurate simulations. The high X1 values for Sokotoro indicated substantial soil water storage capacity, and consistent X2 values supported stable groundwater exchange, resulting in robust model metrics across periods. In contrast, the GR2M model metrics for the Turkish basins were lower, potentially due to the absence of snow which was not considered. Thus, incorporating snow dynamics could be beneficial for improving model performance in watersheds where snow exists, even when modeling on a monthly basis.

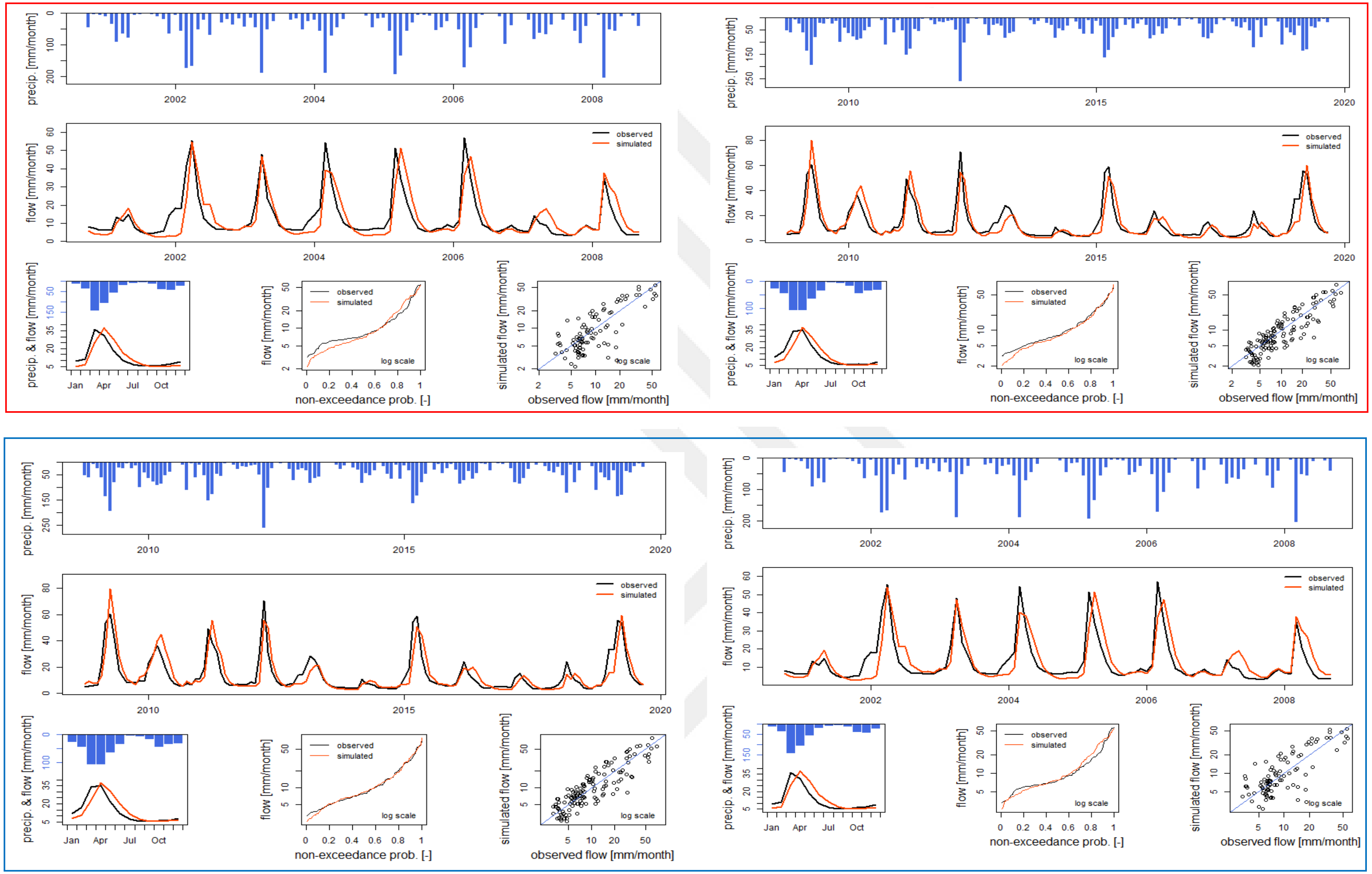

Figure 4.15. *Çukurkışla watershed monthly modeling with GR2M model (red frame P1Calibration -P2 Validation; blue frame P2Calibration – P1 Validation)*

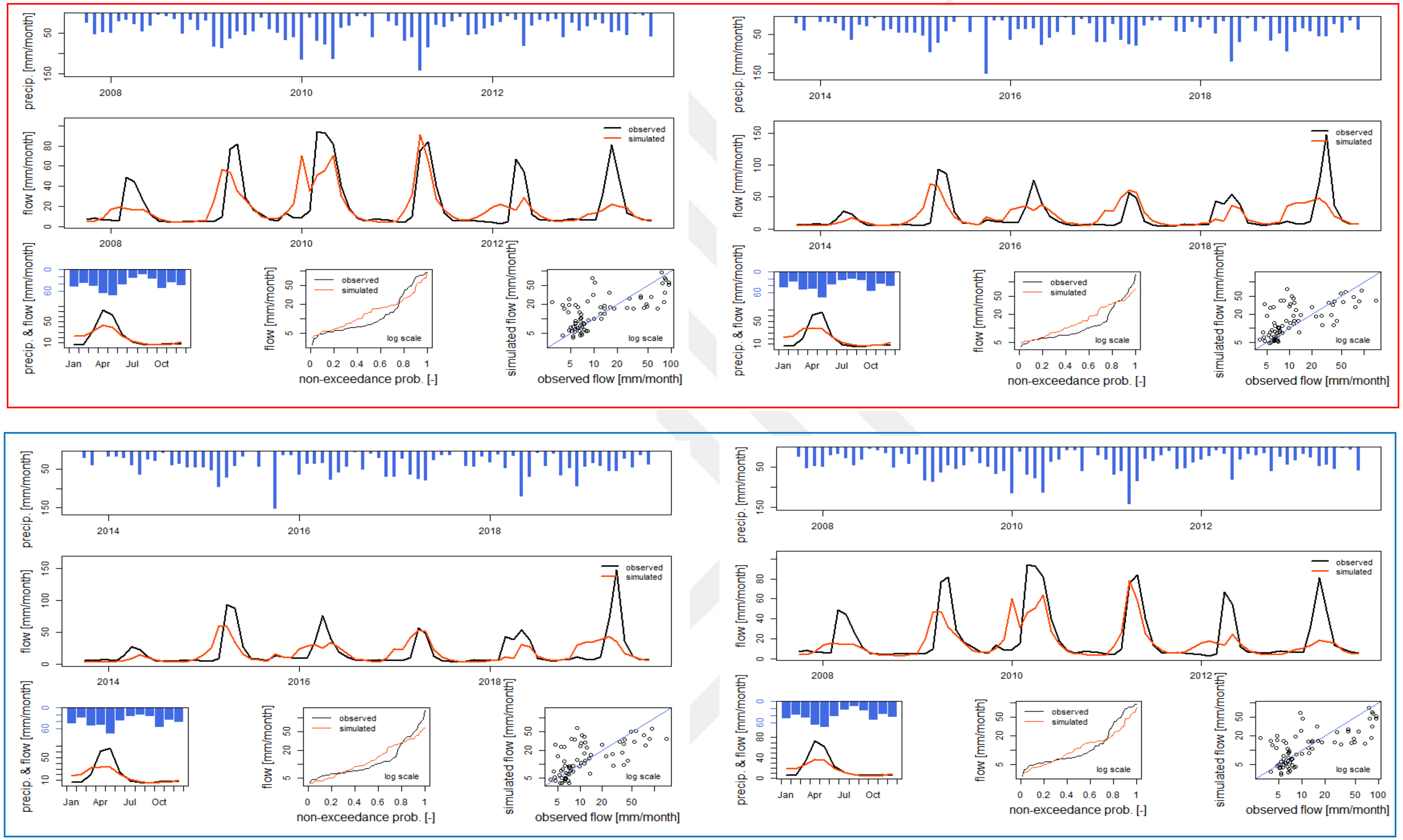

Figure 4.16. *Kayabaşı watershed monthly modeling with GR2M model (red frame P1Calibration – P2 Validation; blue frame P2 Calibration – P1 Validation)*

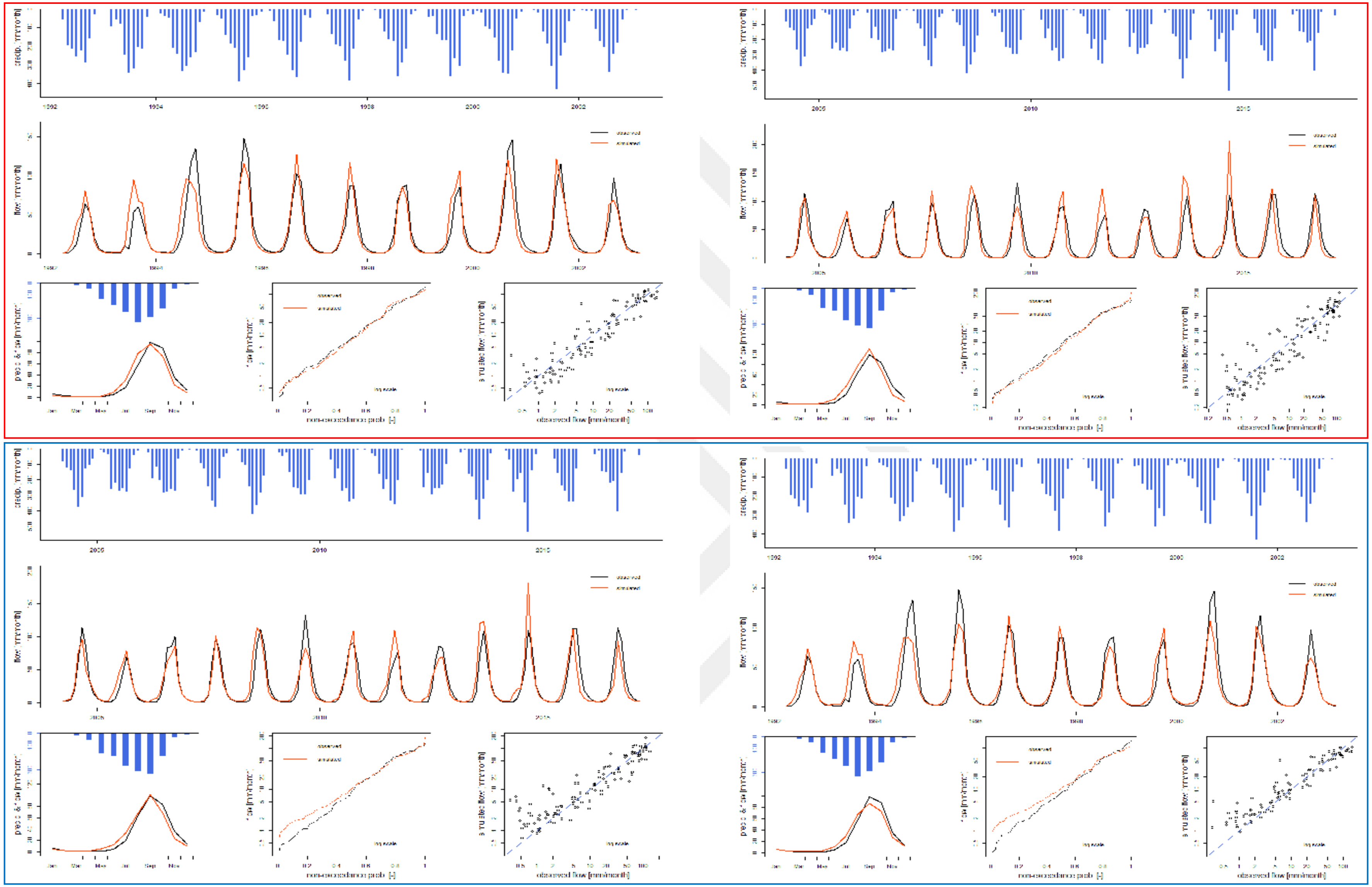

Figure 4.17. *Niger à Kouroussa watershed monthly modeling with GR2M model (red frame P1Calibration – P2 Validation; blue frame P2 Calibration – P1 Validation)*

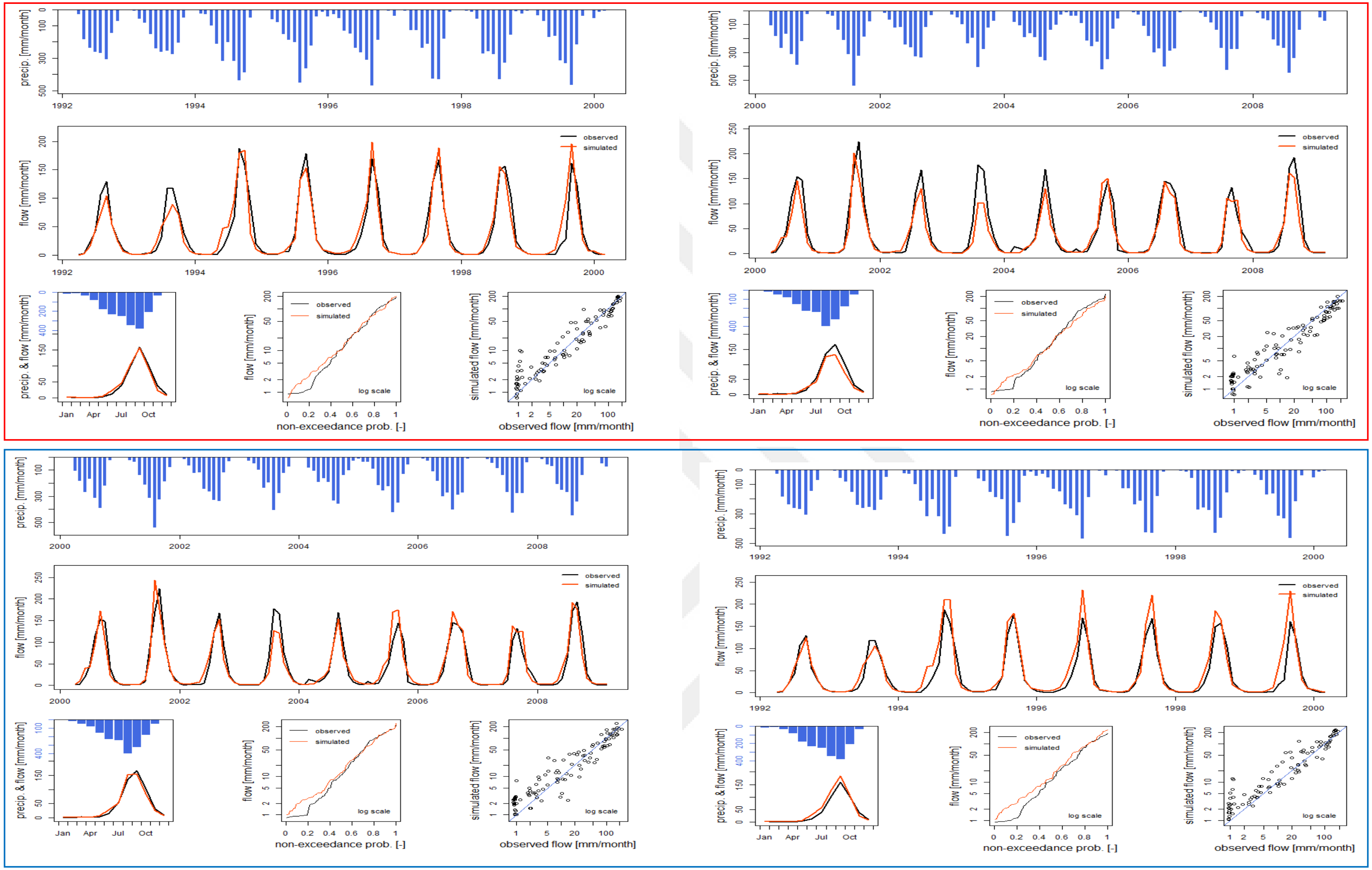

Figure 4.18. *Milo à Kankan watershed monthly modeling with GR2M model (red frame P1Calibration – P2 Validation; blue frame P2 Calibration – P1 Validation)*

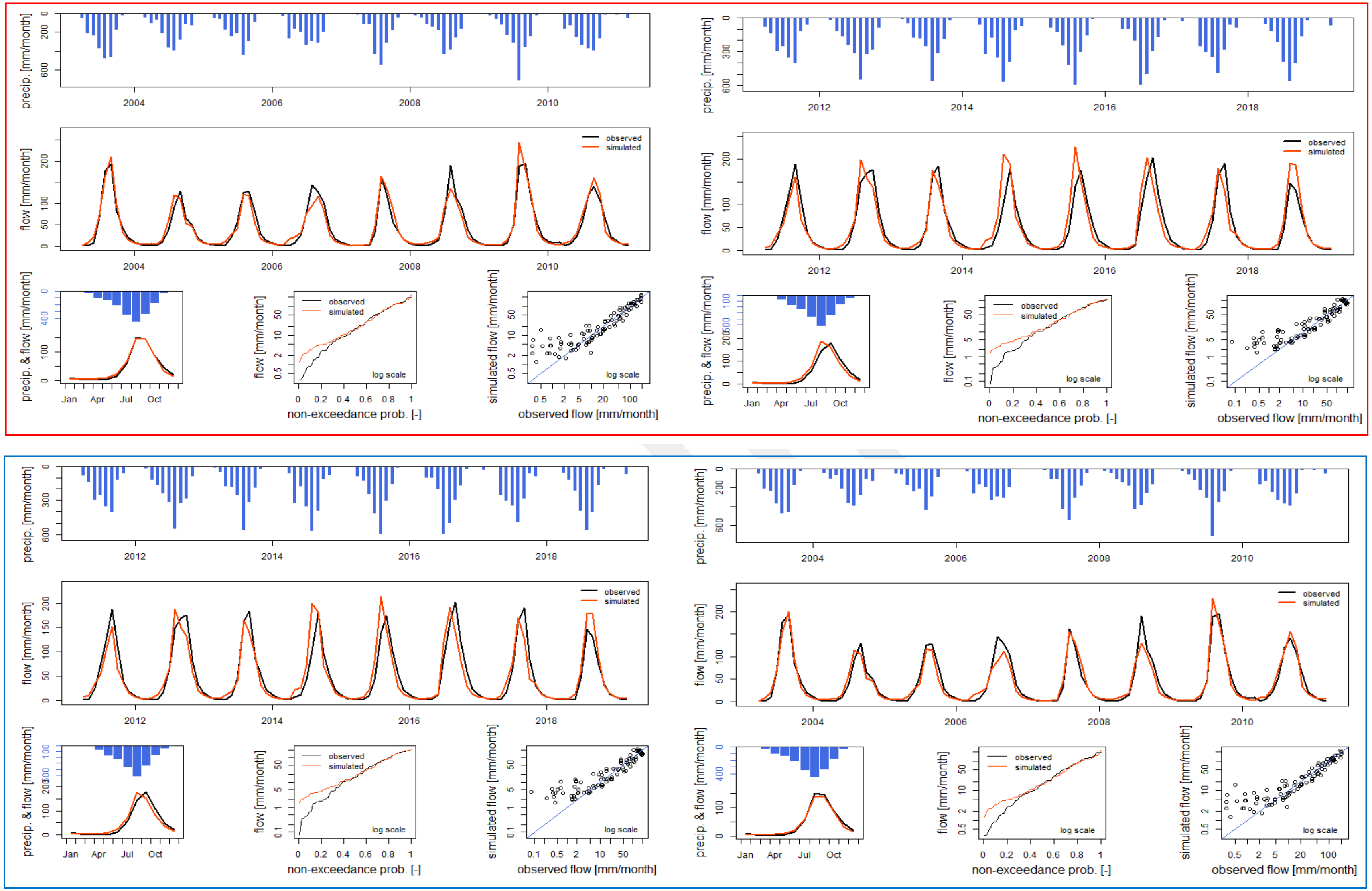

Figure 4.19. *Bafing à Sokotoro watershed monthly modeling with GR2M model (red frame P1Calibration – P2 Validation; blue frame P2 Calibration – P1 Validation)*

4.1.3. Yearly time scale results

The GR1A hydrological model was used to simulate the five watersheds at annual time steps. The calibration parameters, determined using the Calibration Michel algorithm and the split sample test, are presented in Table 4.13.

Table 4.13. *Parameters of GR1A calibrated using Calibration Michel on Çukurkışla, Kayabaşı, Niger, Milo, and Sokotoro watersheds for both calibration periods*

Basin Name	Calibration Warm-up	Calibration period	Parameter X [0.13 – 3.5] (-)
Çukurkışla	2000	P1: 2001 – 2008	0.757
	2008	P2: 2009 – 2019	0.706
Kayabaşı	2007	P1: 2008 – 2013	0.421
	2013	P2: 2014 – 2019	0.509
Niger	1991	P1: 1992 – 2002	1.277
	2003	P2: 2004 – 2016	1.261
Milo	1991	P1: 1992 – 1999	1.092
	1999	P2: 2000 – 2008	1.044
Sokotoro	2002	P1: 2003 – 2010	1.186
	2010	P2: 2011 – 2018	1.338

In the Turkish basins, the X parameter values were below 1, indicating water gains. For Çukurkışla, X decreased slightly from 0.757 in P1 to 0.706 in P2, suggesting a slight increase in water gain over time. Kayabaşı showed a more substantial increase in X from 0.421 in P1 to 0.509 in P2, indicating a reduction in water gain, which could be attributed to variations in climatic conditions.

In contrast, the Guinean watersheds, characterized by high evapotranspiration due to their tropical location, showed X parameter values above 1, indicating water losses. For the Niger basin, X remained relatively stable with a slight decrease from 1.277 in P1 to 1.261 in P2, suggesting consistent water loss over time. Milo also exhibited stable parameters, with X decreasing slightly from 1.092 in P1 to 1.044 in P2, reflecting a consistent water loss. Sokotoro, however, showed an increase in X from 1.186 in P1 to 1.338 in P2, indicating an increase in water loss. This could be due to changes in precipitation patterns and evapotranspiration rates over the calibration periods.

Overall, Turkish and Guinean watershed parameter changes highlighted the climatic and hydrological differences. The Turkish basins, influenced by snow processes and less potential evapotranspiration, showed water gains, while the tropical Guinean watersheds consistently lost water due to high evapotranspiration. Additionally, the consistent water gain observed in the Turkish watersheds and the consistent water loss observed in the Guinean watersheds were also evident in the results from the GR4J and GR2M models, reinforcing the observed hydrological behaviors across different modeling approaches. The performance metrics for both the calibration and validation phases are summarized in Table 4.14.

Table 4.14. *GR2M performance metrics with modified KGE as objective function on Çukurkışla, Kayabaşı, Niger, Milo, and Sokotoro watersheds for calibration and validation periods using split sample test*

Basin Name	Period	Calibration				Validation			
		KGE	NSE	RMSE	Dv	KGE	NSE	RMSE	Dv
Çukurkışla	P1	0.783	0.551	31.093	0.505	0.766	0.423	35.267	8.933
	P2	0.838	0.802	30.092	4.446	0.818	0.835	27.514	-3.357
Kayabaşı	P1	0.837	0.660	42.017	4.448	0.775	0.598	45.636	-9.566
	P2	0.774	0.591	43.753	-1.146	0.726	0.381	53.827	13.294
Niger	P1	0.406	0.412	70.737	-5.112	0.406	0.434	69.392	-3.350
	P2	0.090	-0.548	61.964	-3.884	0.0897	-0.605	63.087	-5.644
Milo	P1	0.615	-0.281	72.125	8.639	0.610	-1.143	93.270	14.709
	P2	0.553	0.220	69.486	-3.557	0.549	-0.054	80.776	-8.783
Sokotoro	P1	0.585	0.050	76.777	3.306	0.559	-0.369	92.161	-11.04
	P2	0.289	-0.419	91.113	-8.040	0.275	-0.351	88.885	6.170

The GR1A hydrological model metrics for the five watersheds, including Çukurkışla and Kayabaşı in Turkey and Niger, Milo, and Sokotoro in Guinea, showed varied performance. Çukurkışla demonstrated relatively high model performance with KGE values of 0.783 and 0.838 for the P1 and P2 calibration periods, respectively, and validation values slightly lower but still robust. Similarly, Kayabaşı had a strong model performance during the calibration periods with KGE values of 0.837 and 0.774. However, validation metrics showed a drop, particularly in RMSE and Dv%.

In contrast, the Guinean watersheds had lower model performance compared to the Turkish watersheds. The KGE values were significantly lower in the Guinean watersheds.

The Niger basin had particularly poor model fit, with KGE values as low as 0.090 and negative NSE values during the P2 period. The Milo basin also had low KGE and NSE values, with high RMSE and Dv values indicating large discrepancies between observed and simulated flows. Sokotoro showed similarly low model performance, with KGE values of 0.585 and 0.289 for the calibration periods and negative NSE values. This reflects significant difficulties in accurately modeling runoff at annual time step in regions with high evapotranspiration rates.

The differences in model performance can be attributed to the climatic conditions that affect each basin. The Turkish watersheds still showed relatively better performance likely due to less potential evapotranspiration patterns compared to the Guinean watersheds. Thus, the high evapotranspiration in the tropical Guinean watersheds consistently led to poorer model performance. Thus, while the parameter X of the GR1A model confirms water loss in the Guinean watersheds to their immediate environment, similar to observations in the GR2M and GR4J models, it produces poor results in these watersheds. Therefore, for operations requiring annual hydrological modeling results, aggregating the outcomes of the GR4J or GR2M models on an annual basis might be more effective.

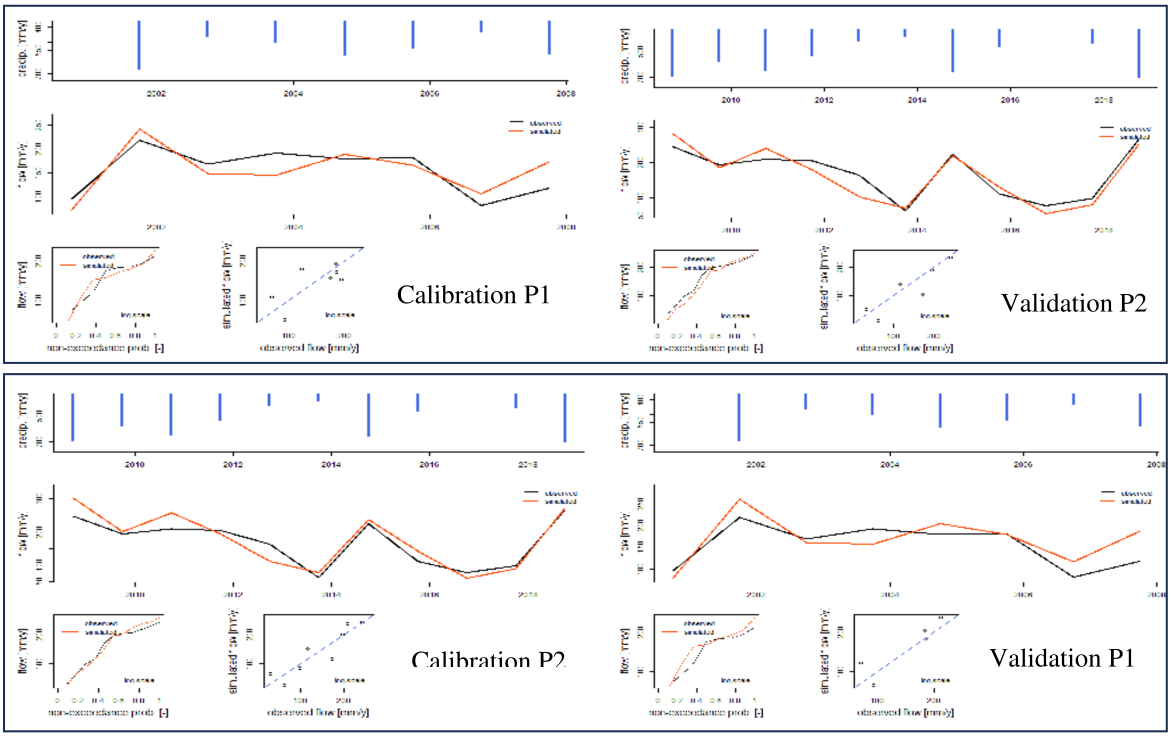

Figure 4.20. *Çukurkışla watershed P1 Calibration – P2 Validation and P2 Calibration – P1 Validation with GR1A using Calibration Michel*

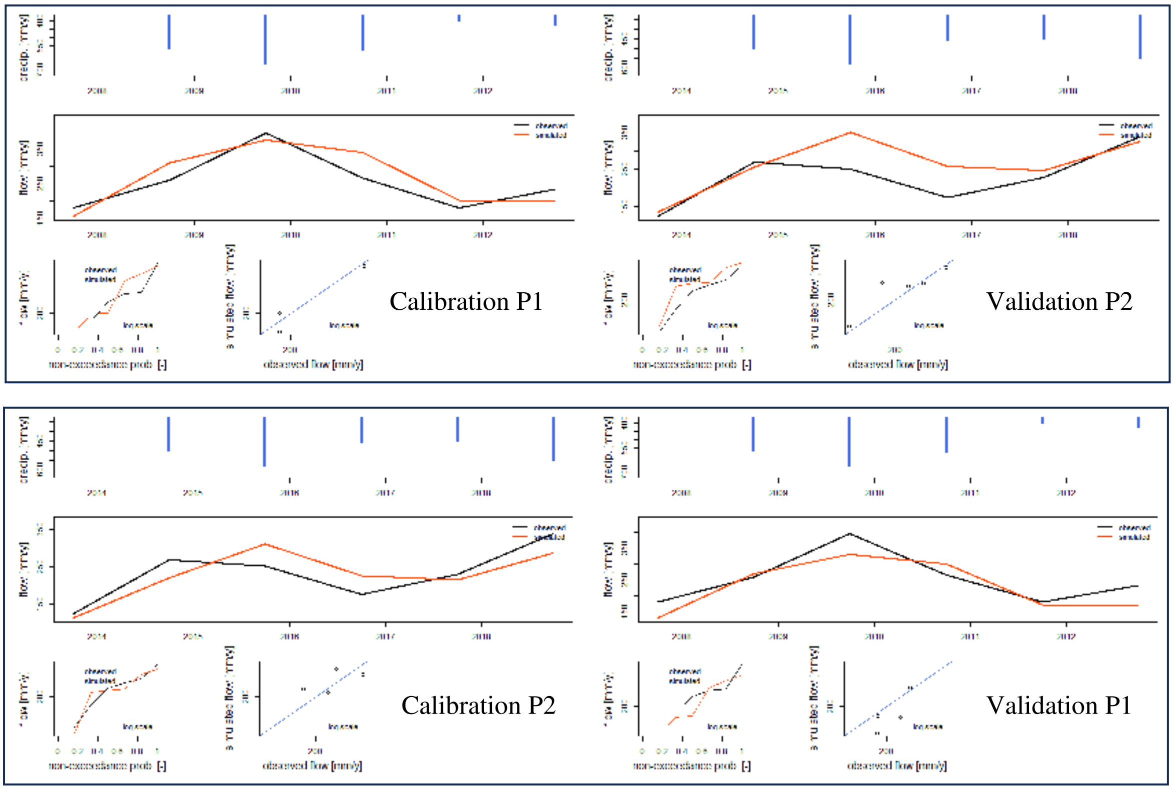

Figure 4.21. *Kayabaşı watershed P1 Calibration – P2 Validation and P2 Calibration – P1 Validation with GR1A using Calibration Michel*

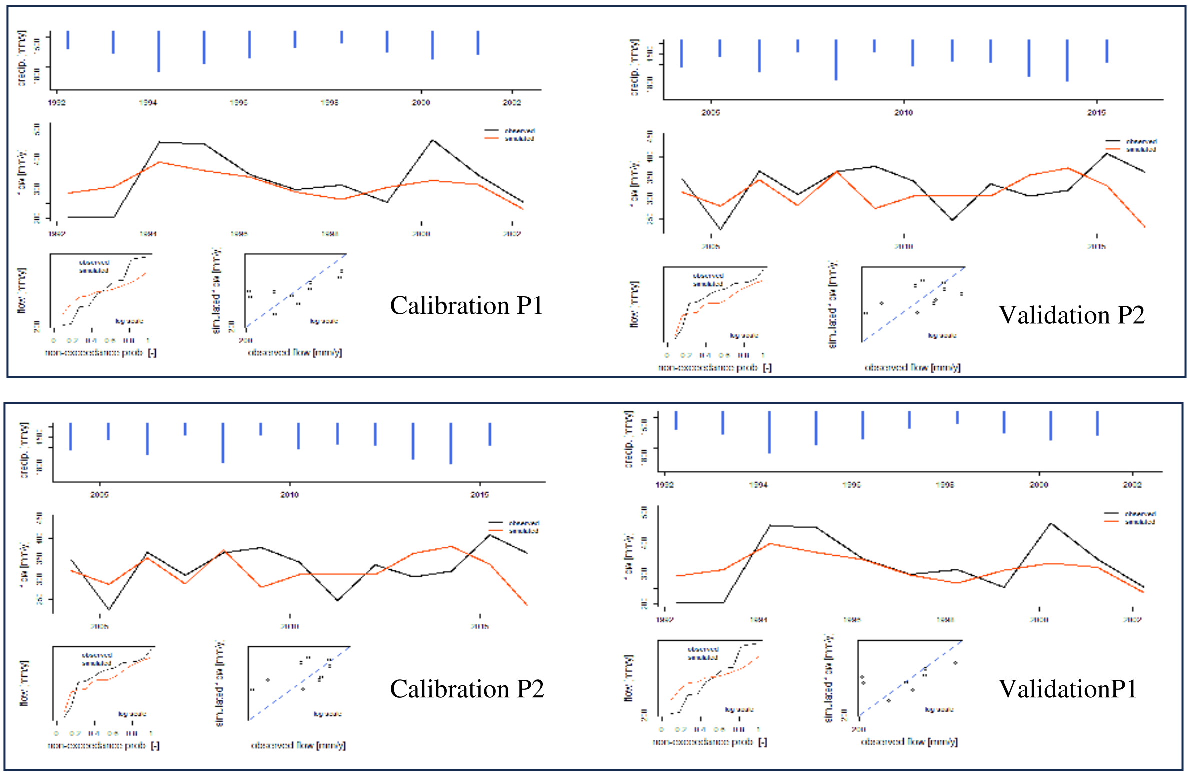

Figure 4.22. *Niger à Kouroussa watershed P1 Calibration – P2 Validation and P2 Calibration – P1 Validation with GR1A using Calibration Michel*

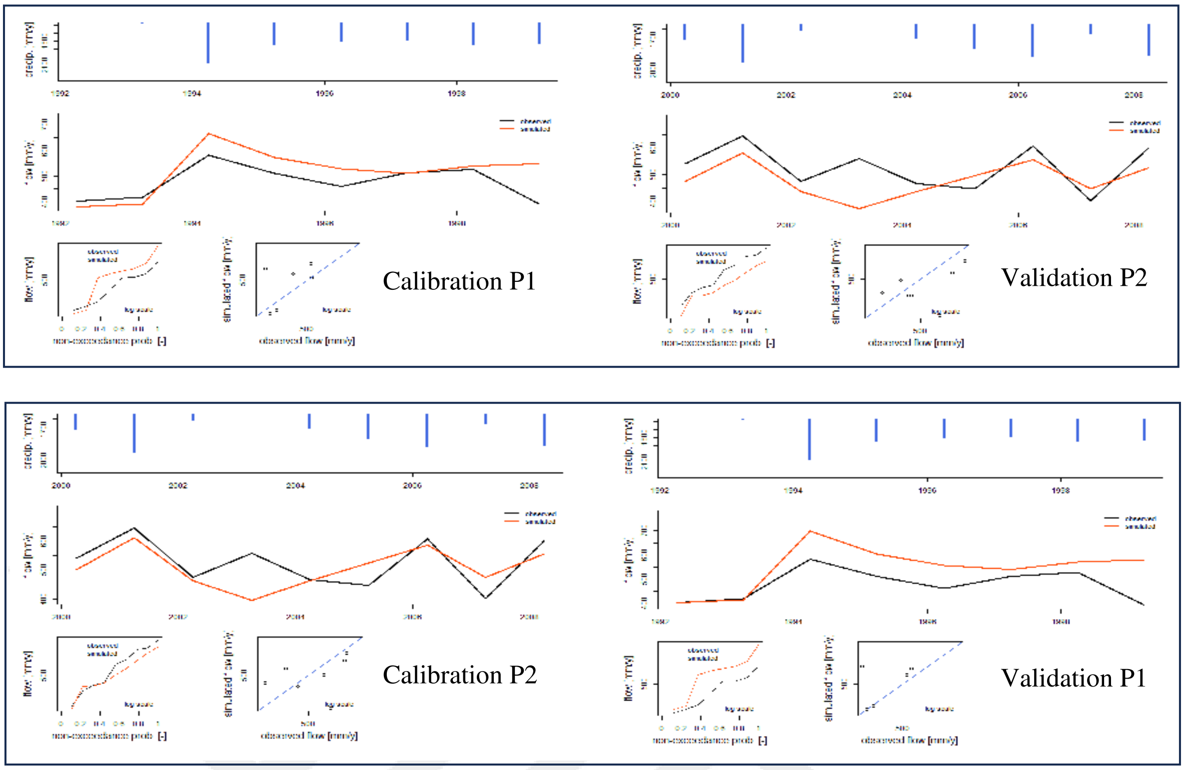

Figure 4.23. *Milo à Kankan watershed P1 Calibration – P2 Validation and P2 Calibration – P1 Validation with GR1A using Calibration Michel*

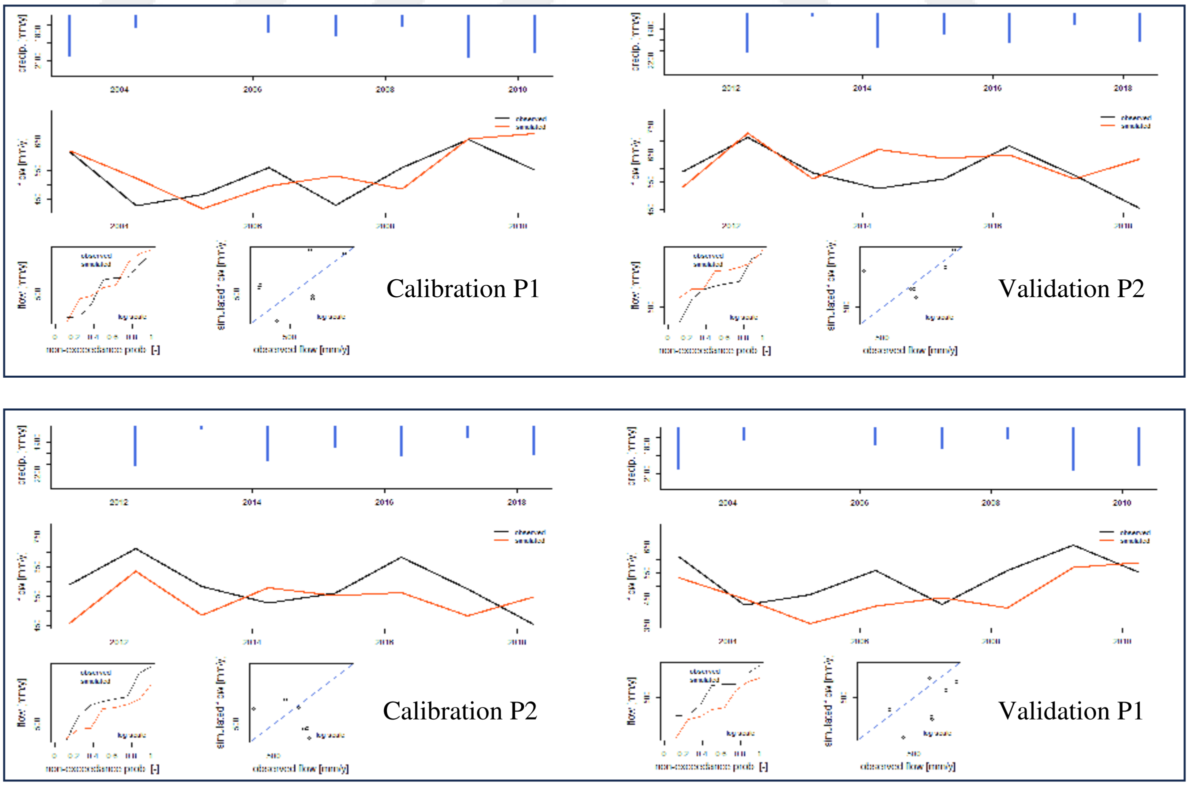

Figure 4.24. *Bafing à Sokotoro watershed P1 Calibration – P2 Validation and P2 Calibration – P1 Validation with GR2M using Calibration Michel*

4.2. Multi Objective Calibration Results

This section presents the results of multi-objective optimization applied to GR4J coupled with CemaNeige using hysteresis parameters across Çukurkışla and Kayabaşı basins. The first part focuses on the snow cover area and discharge within Turkish basins, highlighting the complex relationship between snow dynamics and hydrological responses. The second part examines soil moisture and discharge in Guinean basins, emphasizing the influence of soil moisture on streamflow patterns.

4.2.1. Discharge and snow cover area calibration for Turkish basins

Multi-objective calibration was conducted on the two watersheds by varying the weighting for streamflow and snow cover criteria in each optimization. Initially, the weighting was fully assigned to streamflow (wSN = 0). The basins were divided into five equal-surface zones to capture the spatial variability of snow cover. An increment of 1% was applied to each altitude zone, totaling 5% for the entire basin. This increment was increased until the snow cover criterion reached 100%, leaving 0% for streamflow. Considering hysteresis, the number of CemaNeige parameters increased from two to four, resulting in a total of eight parameters to be calibrated. The multi-criteria objective function (MEsn) included the KGE for both streamflow and snow criteria, where CM and DE algorithms were used to optimize this objective function.

- ***Çukurkışla watershed***

For the Çukurkışla basin, the calibration period was P2 (2009-2019), with 2008 water year used as warm-up. The validation period was P1 (2001-2008). The GR4J coupled with CemaNeige using hysteresis calibration parameters are shown in Figure 4.25.

As it can be seen on this Figure, the parameter X1 for CM remained relatively stable across different weights from 0 to 0.65, ranging from 906.781 mm to 955.176 mm. It then increased significantly, reaching 1043.150 mm when wSN = 0.95. In contrast, for DE, X1 decreased as wSN increased, with values fluctuating between 1238.449 mm and 821.923 mm for wSN values of 0 and 1, respectively. This indicates that DE tends to decrease the production store capacity when the focus shifts more towards optimizing for snow cover area (SCA), while CM behaved differently and more stably.

The two algorithms also showed different trends for X2. CM exhibited a decreasing trend, while DE increased it with wSN. At a weight of 1, DE dropped from its highest value of 2.200 mm to the lowest value of -1.534 mm.

The X3 parameter showed a marked increase for DE, particularly at higher wSN values, indicating sensitivity to snow cover area criterion. CM, on the other hand, kept X3 values relatively stable, decreasing as wSN increased.

For X4, DE showed a gradual increase as wSN increased, while CM maintained a consistent and lower value. This suggests that DE adjusts the time constant significantly as the optimization criterion shifts, responding more dynamically to changes in objective function weighting compared to the stable response seen with CM.

Overall, for GR4J parameters, CM seemed to provide parameters more accurate and less sensitive to variations in weighting compared to DE.

The CNX1 parameter remained stable for DE while CM showed a consistent then clear increasing trend as wSN increased. DE's insensitivity to CNX1 with changes in wSN was unexpected. On the other hand, taking into account hysteresis in CemaNeige allowed the algorithm CM to adjust the weighting coefficient more sensitively to optimize for snow cover area, indicating a more dynamic response to changes in weighting. As wSN increased, it made the snowpack more inert and less sensitive to daily air temperature variations, allowing the snowpack to stay on the ground longer.

For CNX2, the degree-day factor, both DE and CM showed a decreasing trend with increasing wSN. However, CM started with a higher initial value (21.149 mm/°C/d) and experienced a steeper decline, indicating a more aggressive adjustment to optimize snow cover area efficiency. DE's more gradual decline suggested a steadier approach to adjusting the degree-day factor, and it remained lower because the upper boundary was set to 10 mm/°C/d. When wSN = 0.45, Kf (= 4.765 mm/°C/d) became less than the highest value suggested by WMO (1989) and continued to decrease till 3.787 mm/°C/d.

The CNHX1 parameter increased for both algorithms as wSN increased. However, the increase was more pronounced for CM, suggesting a higher sensitivity to snow cover area optimization. DE showed a more moderate and stable increase, indicating less sensitivity to weighting changes. For CM, CNHX1 values at wSN = 0.20 and 0.25 were 10.017 mm and 12.988 mm respectively, similar to values recommended by Riboust et al. (2019), who suggested fixing it at 10 mm.

The CNHX2 parameter remained relatively stable for DE across all wSN values but showed a clear increasing trend for CM. This indicates that CM adjusts the hysteresis factor more dynamically in response to optimizing for snow cover area, while DE maintains a consistent value, suggesting a more static response to changes in objective function weighting.

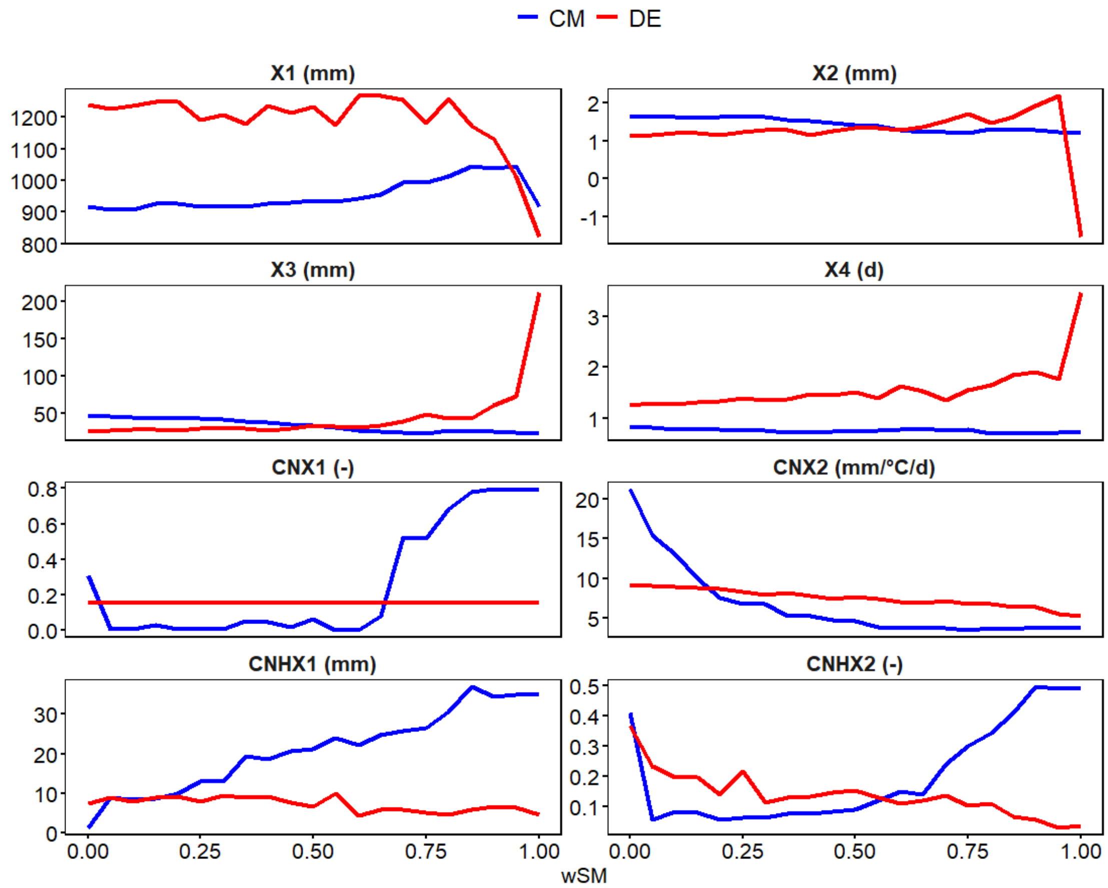

Figure 4.25. *GR4J coupled with CemaNeige using hysteresis parameters on Çukurkışla watershed*

Overall, the CM algorithm provided a more stable and consistent parameter set for GR4J across varying weights and for CemaNeige with hysteresis parameters were more sensitive to weight variation, indicating robustness in the calibration process. That was what we expected because a higher wSN means more magnitude on snow. On the other hand, DE showed greater sensitivity to GR4J parameter but less to CemaNeige with hysteresis parameters which seemed to be wrong.

Since each execution of DE resulted in a new set of parameters, it was run 20 times for each value of wSN, changing the seed each time to ensure reproducibility. The average of these 20 executions was taken for comparison. This approach might partly explain the results obtained from DE. However, DE still showed less performance compared to CM. The parameter results from the multiple runs are presented in Figure 4.26.

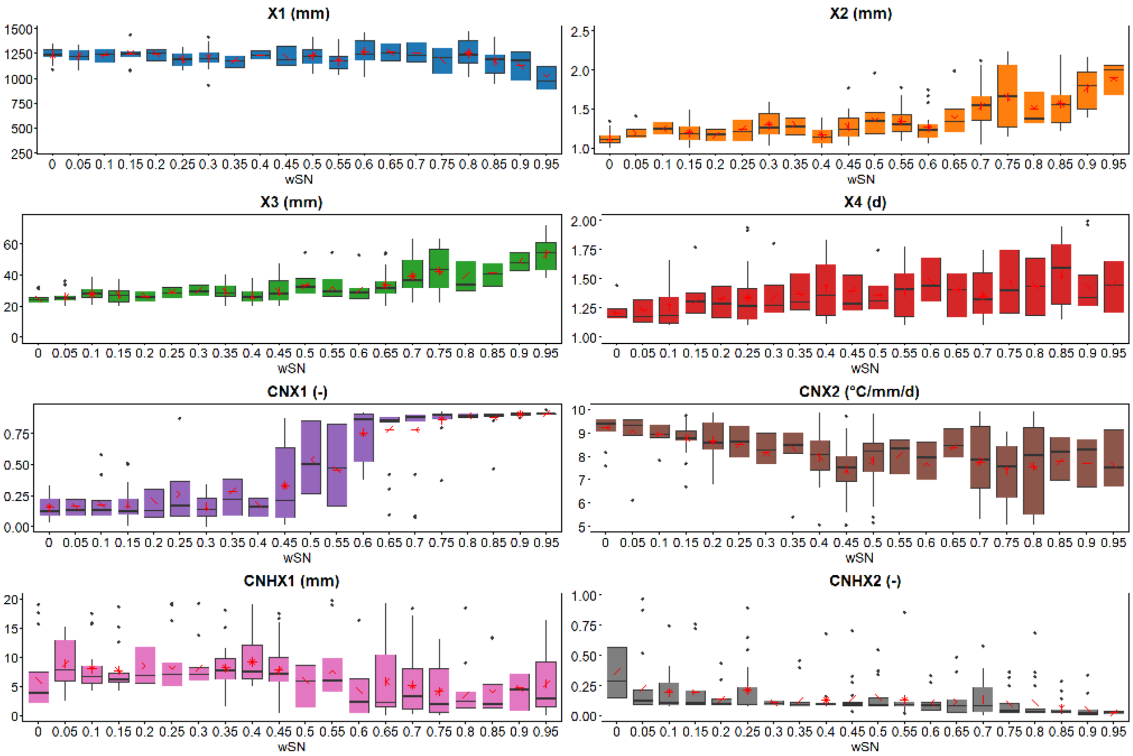

Figure 4.26. *GR4J coupled with CemaNeige using hysteresis parameters generated by DE in 20 runs on Çukurkışla watershed*

The CM algorithm in GR4J coupled using CemaNeige with hysteresis provides a more stable and balanced performance across different weights of wSN, demonstrating robustness in handling both discharge and snow cover area simulations. The DE algorithm, on the other hand, shows greater sensitivity and variability, with a noticeable trade-off between optimizing for discharge and snow cover area. The multi-objective criterion MEsn for the calibration period (Figure 4.27) was relatively stable, showing a slight U-shaped trend with the lowest values around wSN of 0.5 and higher values at the extremes (0 and 1 for 0.895 and 0.934 respectively). This indicated a balanced performance between Q and SCA in both algorithms. In the validation period (Figure 4.28), the U-shaped was slightly attenuated but with variation throughout wSN values.

For both algorithms, KGE(Q) showed a decreasing trend as wSN increased, indicating that prioritizing snow cover area (SCA) negatively impacts discharge performance. This trend was more pronounced for DE than for CM. Similarly, NSE(Q) also decreased with higher wSN for both algorithms, reinforcing that emphasizing SCA reduces discharge accuracy. However, the decline in discharge performance was relatively modest, with CM's KGE(Q) decreasing by 12.71% from weight 0 to 1 in calibration and by 3.68% in validation from 0 to 0.95.

As expected, KGE(SCA) increased with higher wSN, indicating improved snow cover simulation as more weight is given to SCA. The total improvements in calibration and validation were 79.92% and 36.27%, respectively. Additionally, in calibration, when wSN was set to 0.05 for the entire basin, KGE(SCA) improved by 43.18% while discharge decay was only 0.75%, suggesting that it is not beneficial to give more weight to SCA. This fact was also fund by (Riboust et al., 2019, and Ruelland, 2024) where it was suggested to set wSN to 0.25.

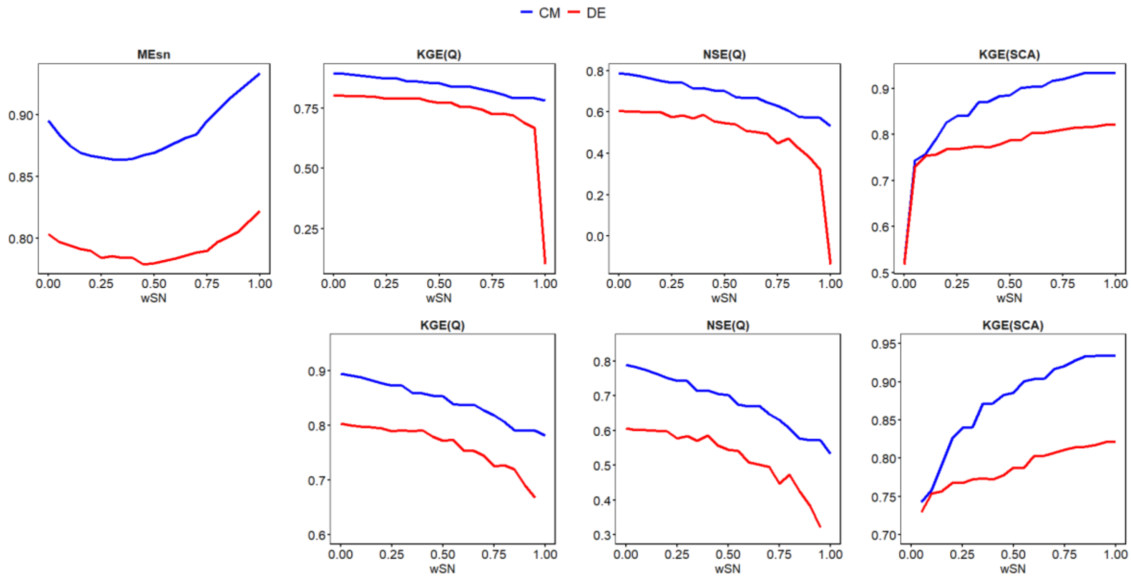

Figure 4.27. *GR4J coupled with CemaNeige using hysteresis calibration metrics for Çukurkışla watershed: bottom panels are upper panels zoomed to see variation more obviously*

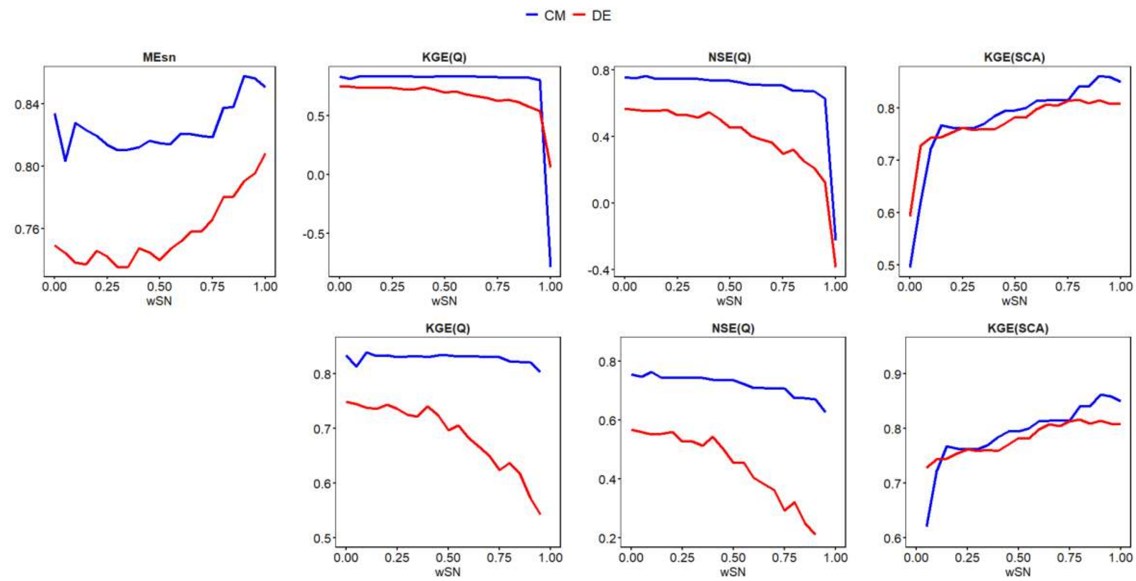

Figure 4.28. *GR4J coupled with CemaNeige using hysteresis validation metrics for Çukurkışla watershed: bottom panels are upper panels zoomed to see variation more obviously*

As mentioned above, calibration was conducted from 10/01/2008 to 09/31/2019, and validation on the period from 10/01/2000 to 09/31/2008. Figure 4.29 zooms in on one year within these periods to highlight variations in hydrographs, snowpacks, and SCA due to changes in wSN. For clarity, only selected weights were used in the graphics, with the full calibration and validation periods detailed in the appendix.

The figure shows that observed flow and simulated flows under different weighting schemes (wSN ranging from 0.05 to 0.95) aligned well during peak flow periods but deteriorated as wSN increased. For these years, the SWE of the standard CemaNeige model without hysteresis was generally lower than that of the model with hysteresis, which indicated that incorporating hysteresis resulted in higher snow accumulation estimates. Different wSN values produced varying SWE amounts, with higher weights on snow leading to greater SWE values. During calibration and validation, Snow Cover Area (SCA) aligned well with MODIS observations for most of the period, particularly in early accumulation phases. However, deviations appeared during the melt period, where the standard CemaNeige model (SCA_std) showed quicker melting compared to simulations with hysteresis. This could be due to the higher CNX2 value leading to quicker melting. Additionally, the standard CemaNeige model was unable to reach the maximum SCA value (1), a finding also reported by Riboust et al. (2019). All included, including hysteresis delayed snowmelt, provided a better fit to observed SCA patterns, and suggested improved model performance in representing snow processes, resulting in a more accurate representation of SWE and SCA dynamics.

Figures 4.30 and 4.31 show the scatter plots from weight 0 to 1 respectively for calibration and validation. When wSN was 0.00, the highest r^2 value of 0.8043 was observed in calibration and 0.7487 in validation, indicating a strong correlation between simulated and observed flows when the model focused exclusively on discharge without considering snow cover area (SCA). As wSN increased, the r^2 values gradually decreased, showing that the model's ability to simulate flow diminished as more weight was placed on SCA. At wSN values ranging from 0.05 to 0.65 for calibration, the r^2 values remained relatively high, around 0.70 to 0.79. However, as wSN continued to rise from 0.70 to 1.00, the r^2 values dropped significantly, reaching as low as 0.6254 at a wSN of 0.95 in calibration and 0.5022 at a wSN of 1 in validation. This trend suggested that while the model could balance the objectives of discharge and SCA to some extent, prioritizing SCA too heavily led to a less accurate representation of flow.

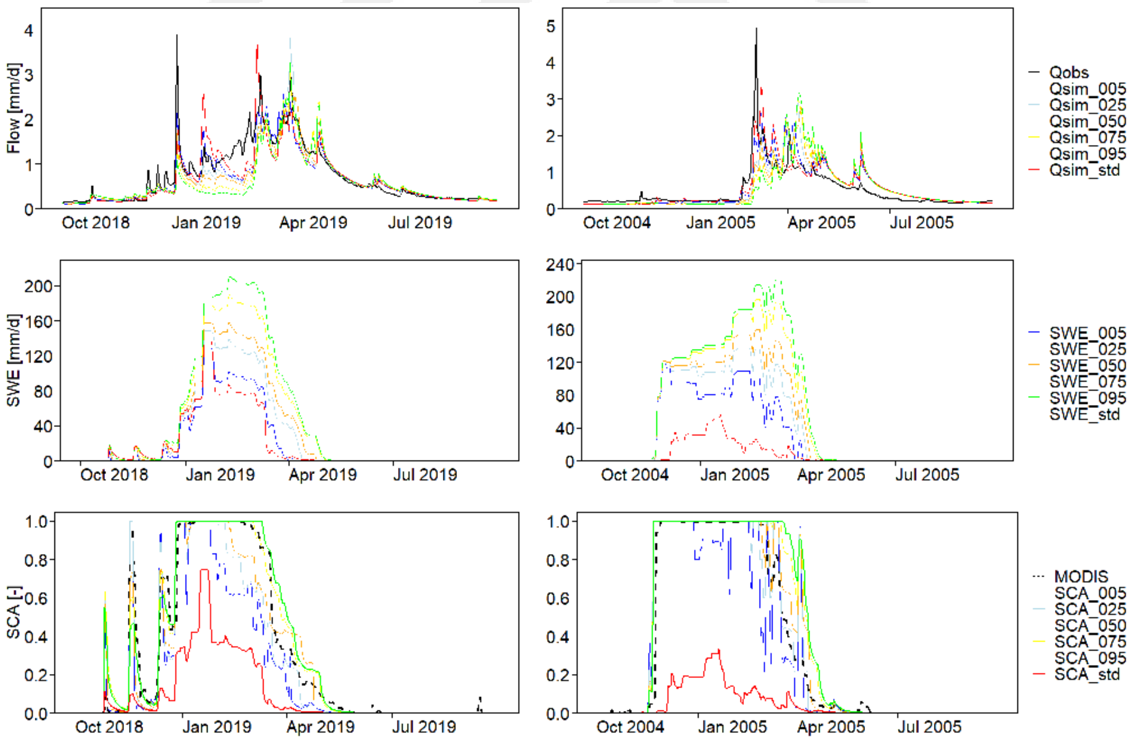

Figure 4.29. *GR4J coupled with CemaNeige using hysteresis on Çukurkışla hydrograph, snowpack and snow cover area for some weight and standard CemaNeige SWE and SCA: calibration on left and validation on right. Read SCA_std: standard CemaNeige without hysteresis SCA*

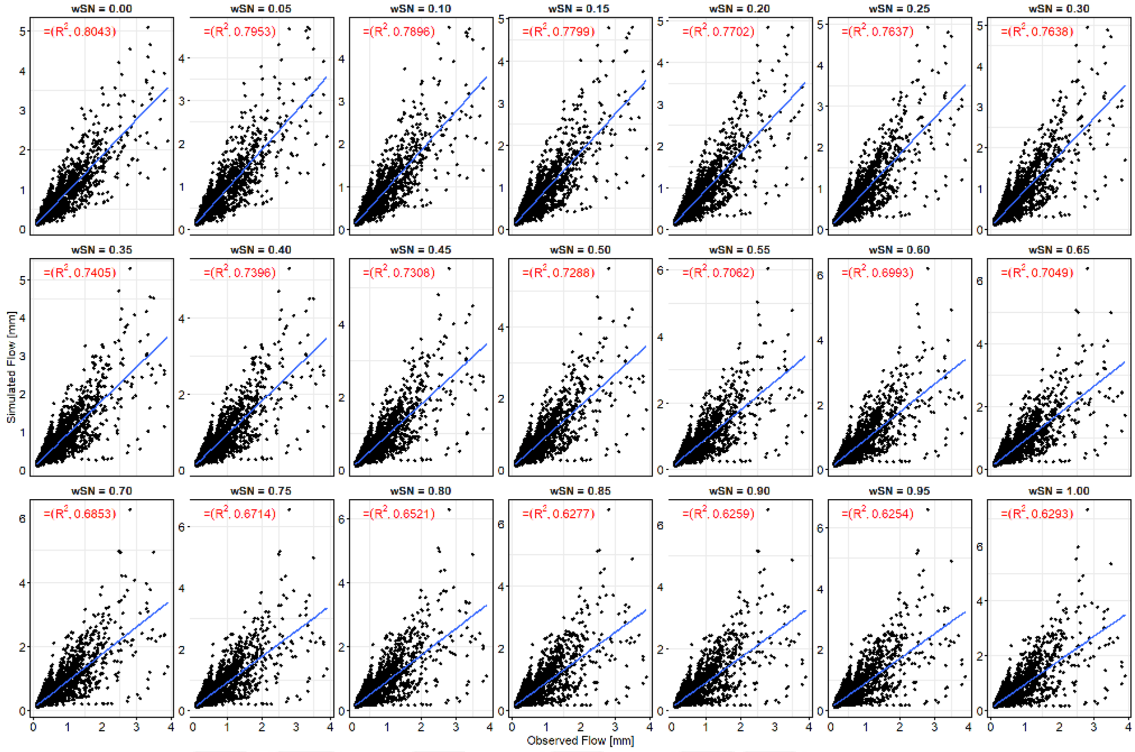

Figure 4.30. *Çukurkışla watershed using CM calibration observed and simulated discharges with wSN from 0 to 1 scatter plots*

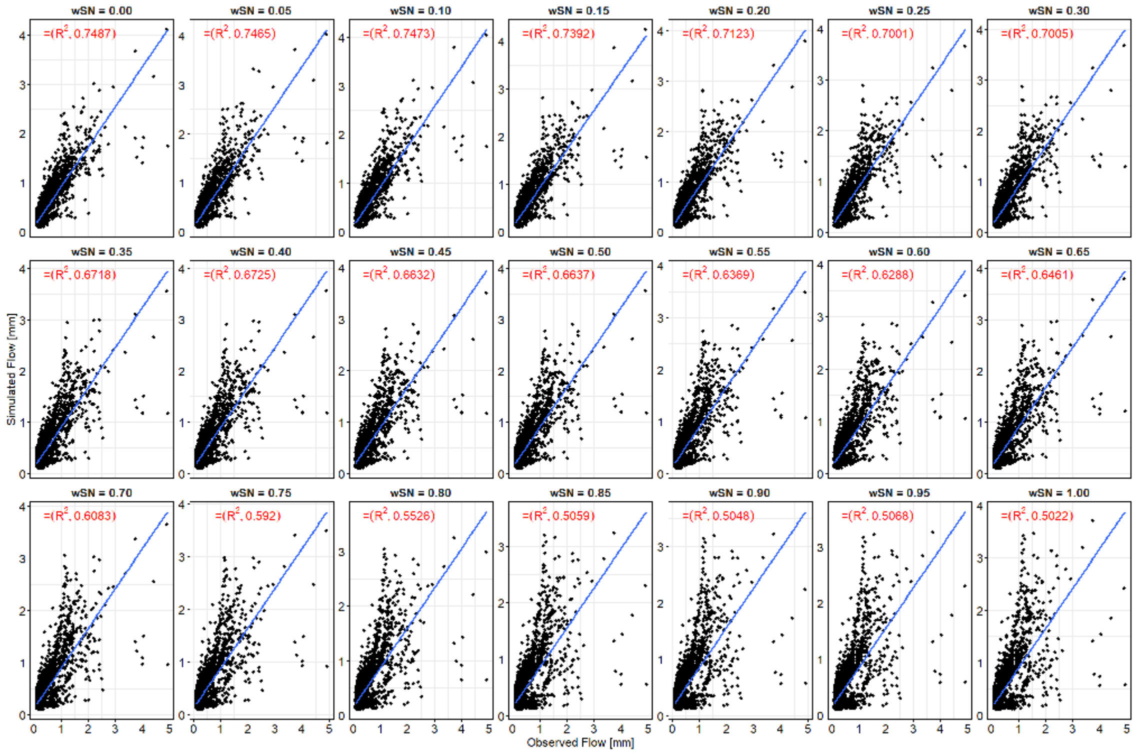

Figure 4.31. *Çukurkışla watershed validation observed and simulated discharges with wSN from 0 to 1 scatter plots*

Figure 4.32 plots depicted the variation in discharge across different weights on snow (wSN) for each month, derived by subtracting the simulated discharges at other wSN values (Qsim_***) from the simulated discharge at wSN = 0.00 (Qsim_000). During the winter months of January and February, a clear decreasing trend was observed which indicated that the discharge was consistently lower when more weight was given to snow cover area (SCA) in the model, suggesting a higher retention of snow and delayed meltwater contribution to the discharge.

Conversely, from April through October, an increasing trend was evident. In April, May, and June, the differences grew larger as wSN increased, highlighting that more weight on SCA led to higher discharges during these months. This trend suggested that the snow accumulated during winter started to melt, contributing significantly to the discharge. The summer months of July and August also showed an increasing trend, although with some fluctuations, indicating the impact of snowmelt on discharge continued into these months. Additionally, spring rainfall likely contributed to the increasing runoff observed in the summer. In September and October, the trend remained positive, and might be due to eventual rainfall or residual snowmelt. November and December showed a slight increase in differences as wSN increased, suggesting the beginning of snow accumulation and its initial effects on discharge patterns. For the validation period, the same trend was observable, making model calibration more accurate (Figure 4.33).

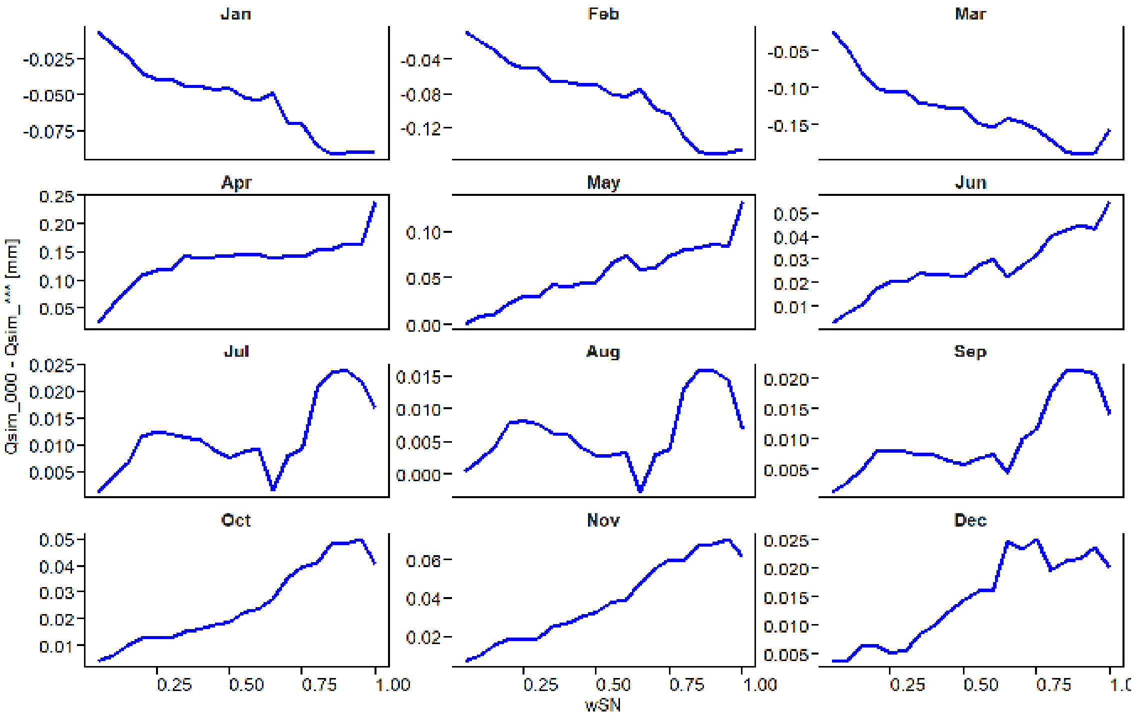

Figure 4.32. *Çukurkışla watershed calibration monthly discharge variation as wSN increased*

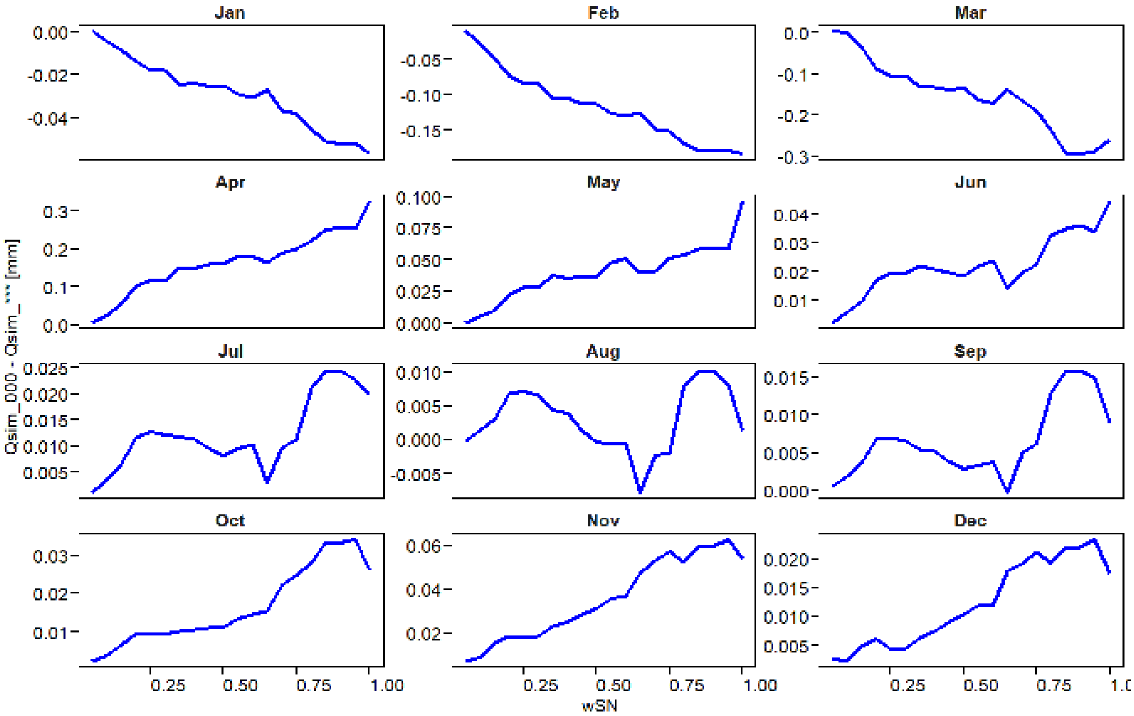

Figure 4.33. *Çukurkışla watershed validation monthly discharge variation as wSN increased*

- ***Kayabaşı watershed***

For the Kayabaşı basin, the calibration period was P2 (2014-2019), with 2013 water year as a warm-up. The validation period was P1 (2008-2013). The parameters for this period are shown in Figure 4.34.

The GR4J X1 parameter showed a relatively stable trend across different weights (wSN) for both the Calibration Michel (CM) and Differential Evolution (DE) algorithms. The CM algorithm maintained a steady value from 342.681 to 362.435 mm, while the DE algorithm exhibited slightly higher values, fluctuating around 360.423-404.425 mm. However, DE algorithm indicated a sharp increase at wSN =1.0 with X1 = 607.936 mm. On the other hand, at the same weight CM showed a slight decrease probably because of the value that was set as the start seed for global search algorithm in Calibration Michel. Somehow, both algorithms indicated an increase towards the higher end of wSN which meant an increased storage capacity when more weight was given to snow cover area (SCA).

The X2 parameter remained relatively constant for both algorithms, with CM generally producing slightly higher values compared to DE. The values for DE fluctuated around 2.0 mm, while CM showed a slight decline from approximately 3.0 mm to values close to zero and got negative at wSN = 1.0. Despite this decline, but not much, indicated that the groundwater exchange was not significantly affected by the varying weights of discharge and SCA in the multi-objective criterion.

The X3 parameter exhibited low values for both CM and DE across the range of wSN. CM maintained a more stable trend around 30-80 mm, and DE showed the same trend but with more variability, particularly towards higher weights for SCA, where it reached values up to 200 mm. The stability when wSN is less than 0.5 suggested that GR4J was less sensitive to the inclusion of hysteresis that involved minor adjustments in flow routing delays.

The X4 parameter, which represents the unit hydrograph time base, demonstrated a slight upward trend for both algorithms as wSN increased. CM produced stable values around 1.0-1.5 days, while DE showed a gradual increase, particularly noticeable beyond wSN of 0.5, reaching up to 2.5 days. This indicated that higher weights on SCA led to longer response times in the model, particularly more pronounced by DE.

All included the parameters of GR4J were less sensitive to the variation of wSN, which seemed to be perfect for inclusion in CemaNeige hysteresis.

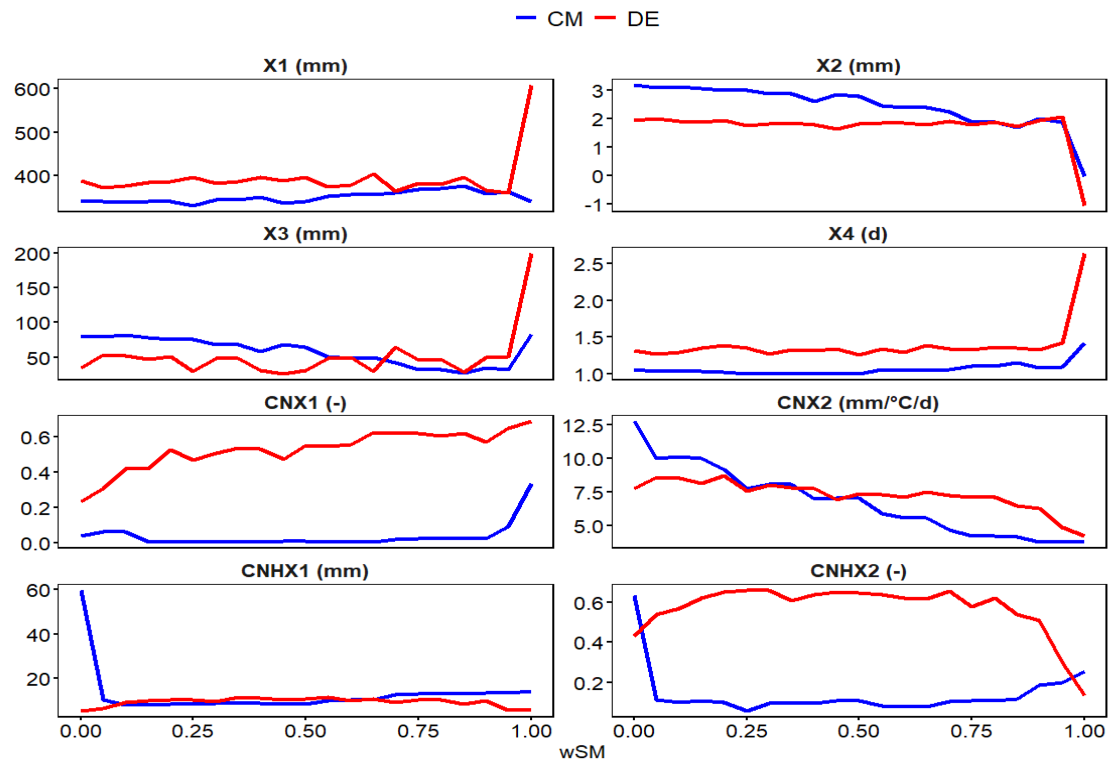

Figure 4.34. *GR4J coupled with CemaNeige using hysteresis parameter on Kayabaşı watershed*

The CNX1 parameter showed distinct trends between CM and DE. CM values were low and stable around 0.1-0.2, while DE displayed higher values around 0.3-0.6. This indicated that DE gave values that were more responsive to variations in snow cover, adjusting the thermal state of the mantle weighting coefficient more significantly compared to CM.

The CNX2 parameter, indicating the degree-day factor, showed a decreasing trend for both algorithms as wSN increased. CM started around 12.7 mm/°C/d and decreased to about 3.7 mm/°C/d, while DE followed a similar trend but with slightly lower initial values and a slower decline. This suggested that hysteresis inclusion adjust the temperature sensitivity to snow melting as more emphasis was placed on SCA.

The CNHX1 parameter remained relatively stable for both CM and DE across most of the wSN range. CM values hovered around 8-13 mm except wSN = 0.0 (CNHX1 = 59.8 mm), while DE values were slightly lower, around 5-11 mm. However, both algorithms showed a slight increase towards the higher end of wSN, indicating increased sensitivity to accumulation threshold when more weight was given to SCA.

The CNHX2 parameter exhibited a more stable and increasing trend for CM, maintaining values around 0.01-0.2 but when wSN = 0.0 then CNHX2= 0.637. DE, however, showed more variability, with values ranging from 0.2 to 0.65, particularly increasing and decreasing towards the higher end of wSN. The increasing trend in both algorithms suggested that CemaNeige with hysteresis was more adaptable to changes in snow cover.

Overall, the CM and DE algorithms provided a more stable parameter set for GR4J across varying weights and for CemaNeige with hysteresis parameters were more sensitive to weight variation, indicating robustness in the calibration process. That was what we expected because a higher wSN means more magnitude on snow. Additionally, the searched parameter space of both algorithms was quite similar in Kayabaşı compared to Çukurkışla which might indicate that in snow dominant watersheds, algorithms are likely able to provide accurate parameters.

Since each execution of DE resulted in a new set of parameters, it was run 20 times for each value of wSN, changing the seed each time to ensure reproducibility. The average of these 20 executions was taken for comparison. This approach might partly explain the results obtained from DE. However, DE still showed less performance compared to CM. The parameter results from the multiple runs are presented in Figure 4.35.

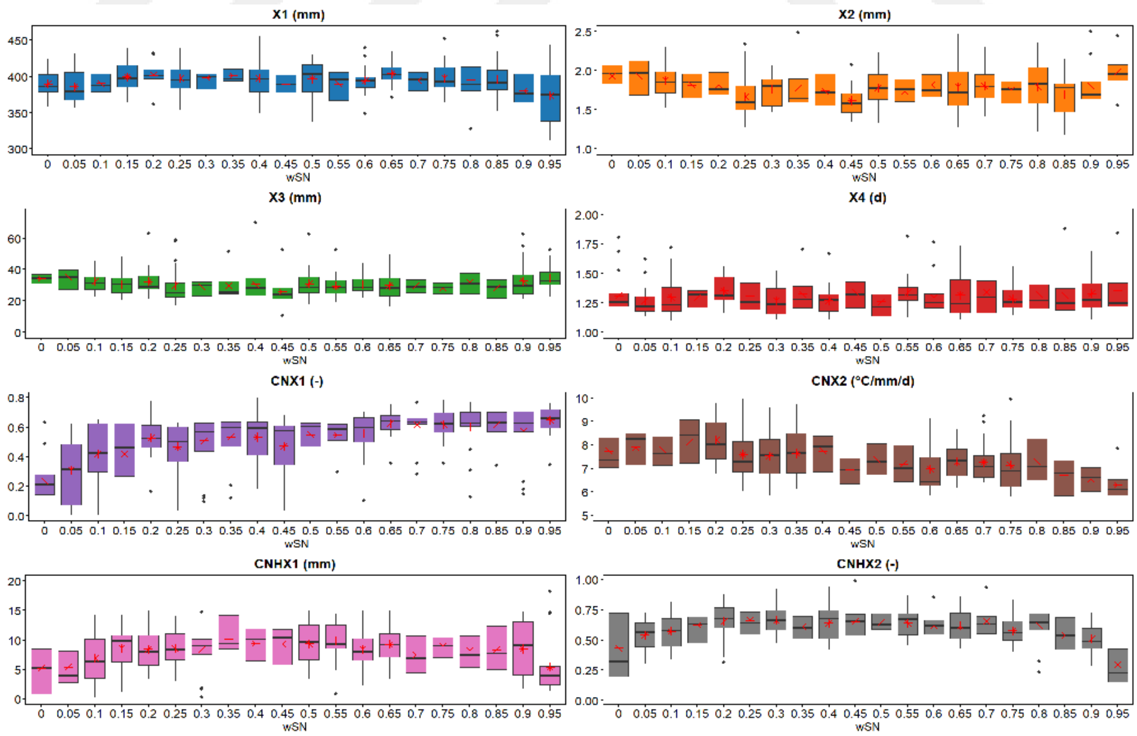

Figure 4.35. *GR4J coupled with CemaNeige using hysteresis parameters generated by DE in 20 runs on Kayabaşı watershed*

The multi-criteria objective function MEsn for Kayabaşı calibration across varying weights on discharge and snow showed an increase with higher wSN for both algorithms. That indicated that more weight on SCA improved the multi-criteria objective function regarding snow processes without deteriorating discharge performance (Figure 4.36).

The Kling-Gupta Efficiency for discharge showed high values for most wSN values but dropped sharply when wSN reached 1. This suggested that while the model performed well for discharge across a range of wSN values, extreme weighting on snow adversely affected performance. The Nash-Sutcliffe Efficiency for discharge also exhibited a stable trend, maintaining high values across most wSN values but decreasing significantly at wSN = 1. From wSN = 0 to wSN = 0.95, discharge performance decay was 3.00% and 7.95% for KGE(Q) and NSE(Q) respectively in CM, and 5.63% and 12.63% for KGE(Q) and NSE(Q) in DE. However, when wSN was set to 1.0 the decrease became absolutely higher (72.89% and 46.35% for KGE(Q) and NSE(Q) respectively in CM, and 86.12% and 87.65% for KGE(Q) and NSE(Q) respectively in DE). This indicated that the model's predictive power for discharge was reliable across different snow weightings until it became fully effective.

As expected, KGE(SCA) increased with higher wSN, indicating improved snow cover simulation as more weight is given to SCA. The total improvement in calibration was 62.28% in CM. Additionally, in calibration, when wSN was set to 0.05 for the entire basin, KGE(SCA) improved by 51.28% while discharge decay was only 0.32%, suggesting that it is not beneficial to give more weight to SCA. This fact was also fund by (Riboust et al., 2019, and (Ruelland D. , 2024)) where it was suggested to set wSN to 0.25.

Figure 4.37 illustrates the performance metrics for the Kayabaşı validation period (10/01/2007 - 09/31/2013) across varying weights on snow. MEsn is the multi-criteria objective function and showed a slight decrease for both CM and DE as wSN increased, with the DE model exhibiting a more consistent downward trend. This indicated that increasing the weight on the snow cover area (SCA) did not improve and, in fact, slightly deteriorated the model's efficiency in capturing discharge and snow processes during the validation period.

The KGE(Q) and NSE(Q) demonstrated high values across a broad range of wSN values for both models but dropped sharply at wSN = 1. This pattern in the validation was not what was expected and could be due to climatic conditions changes from calibration to validation. On the other hand, the KGE for SCA exhibited an overall improvement with increasing wSN values, particularly when CM was applied. However, snow cover metric improvement was not as much as in calibration. The total improvement from wSN =0.05 to 1 was 14.59% and 8.39% in CM and DE respectively. Besides this improvement, interestingly, in the validation period, KGE(Q) and NSE(Q) metrics displayed increasing trends at higher wSN values, indicating enhanced performance in discharge simulation with increased emphasis on snow cover area.

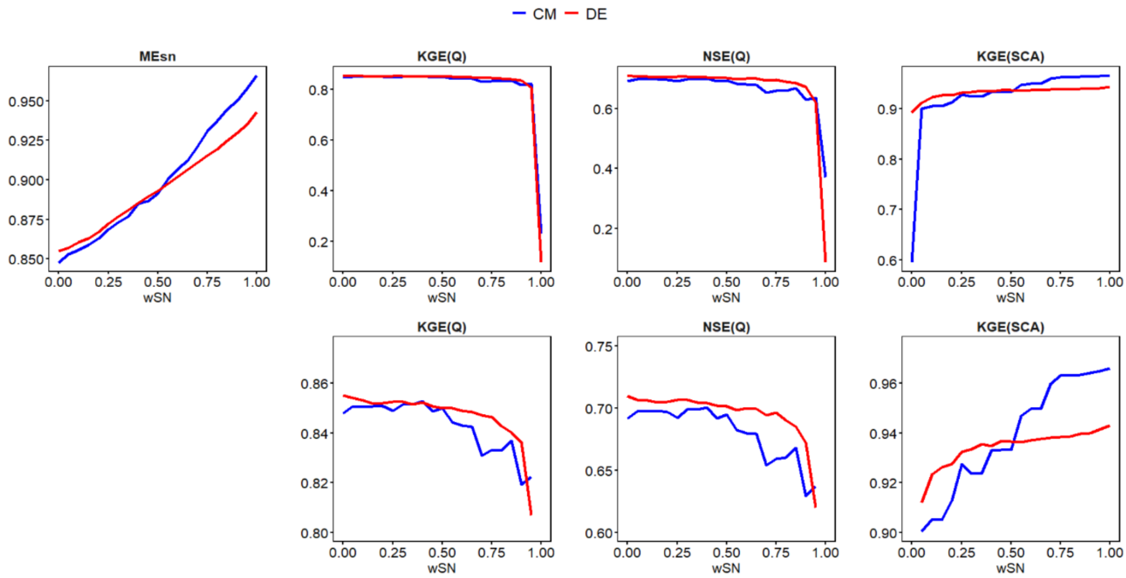

Figure 4.36. *GR4J coupled with CemaNeige using hysteresis calibration metrics for Kayabaşı watershed: bottom panels are upper panels zoomed to see variation more obviously*

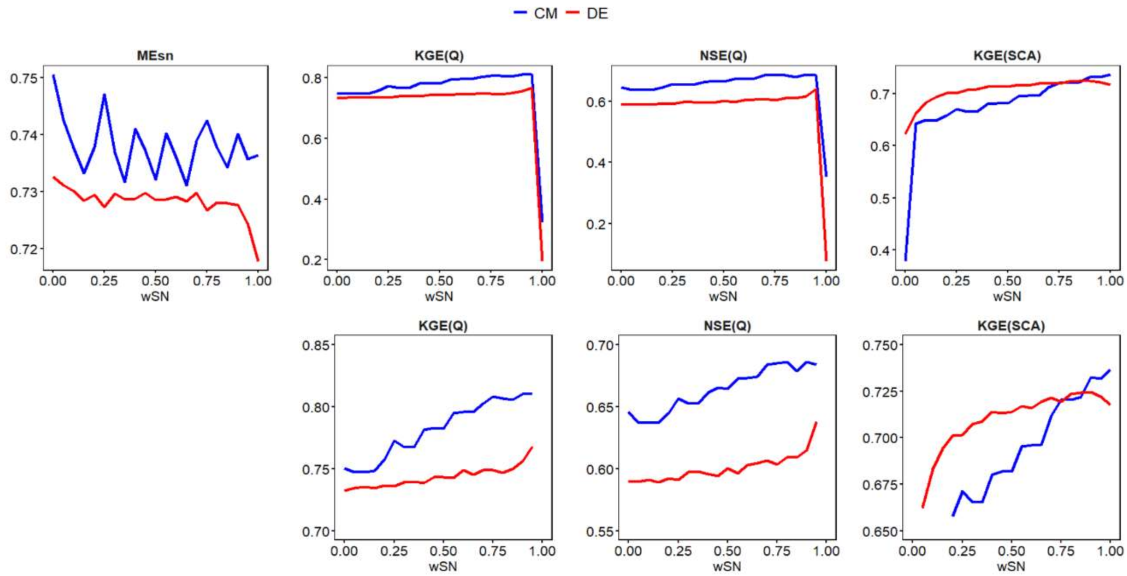

Figure 4.37. *GR4J coupled with CemaNeige using hysteresis validation metrics for Kayabaşı watershed: bottom panels are upper panels zoomed to see variation more obviously*

As mentioned above, calibration was conducted from 10/01/2013 to 09/31/2019, and validation on the period from 10/01/2007 to 09/31/2013. Figure 4.38 zooms in on one year within these periods to highlight variations in hydrographs, snowpacks, and SCA due to changes in wSN. For clarity, only selected weights were used in the graphics, with the full calibration and validation periods detailed in the appendix.

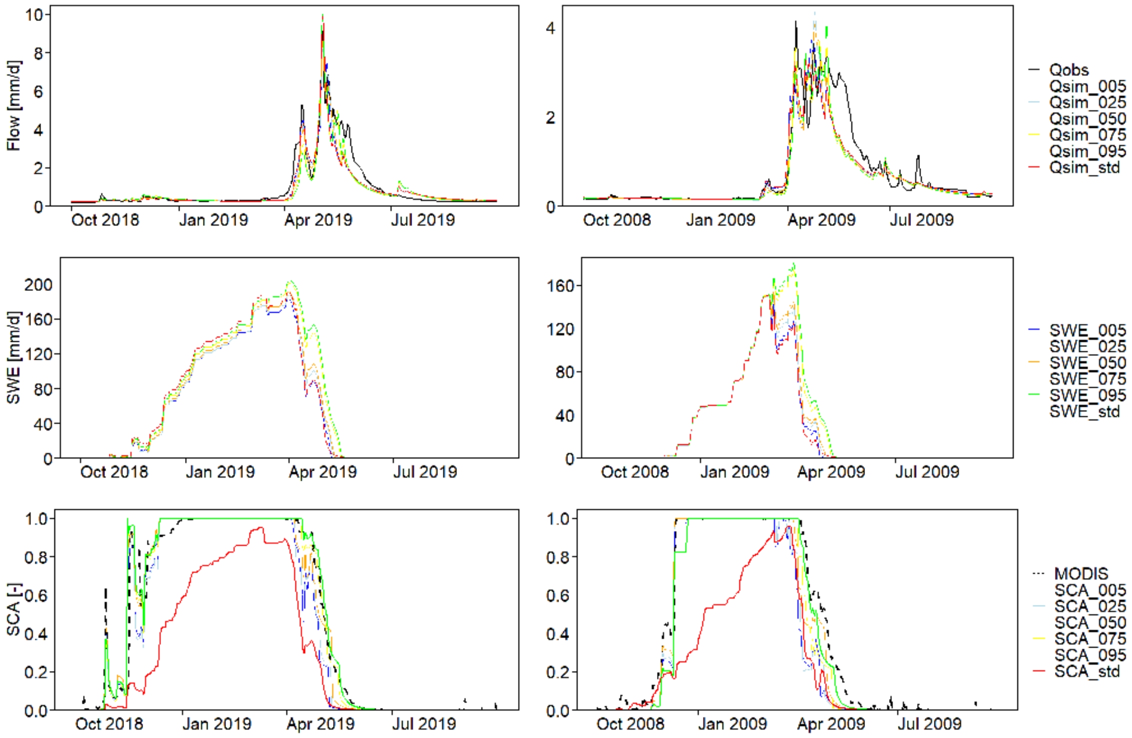

Figure 4.38. *GR4J coupled with CemaNeige using hysteresis on Kayabaşı hydrograph, snowpack and snow cover area for some weight and standard CemaNeige SWE and SCA: calibration on left and validation on right. Read SCA_std: standard CemaNeige without hysteresis SCA*

During the calibration and validation periods, the simulated discharge aligned well with observed discharge. However, there were slight discrepancies in the magnitude of peak flows, with simulations underestimating or overestimating the peaks depending on the wSN value.

For these years, the SWE of the standard CemaNeige model (CemaNeige without hysteresis) was generally lower than that of the model with hysteresis, which indicated that incorporating hysteresis resulted in higher snow accumulation estimates. Different wSN values produced varying SWE amounts, with higher weights on snow leading to greater SWE values. During calibration and validation, Snow Cover Area aligned well with MODIS observations, particularly wSN = 0.95 matched perfectly. However, the standard CemaNeige showed slower accumulation compared to simulations with hysteresis. This fact highlighted the effect of taking hysteresis on snow accumulation phase in CemaNeige. Additionally, melting occurred earlier in standard CemaNeige than CemaNeige with hysteresis. The more the wSN increased, the delay in melting was pronounced. The earlier snow melting in standard CemaNeige could be due to the higher CNX2 value. Additionally, the standard CemaNeige model was unable to reach the maximum SCA value (1), a finding also reported by Riboust et al. (2019).

All included, including hysteresis made faster snow accumulation and delayed snowmelt, provided a better fit to observed SCA patterns, and suggested improved model performance in representing snow processes, resulting in a more accurate representation of SWE and SCA dynamics.

Figures 4.39 and 4.40 show the scatter plots from weight 0 to 1 respectively for calibration and validation. When wSN was 0.00, the highest r^2 value of 0.7197 was observed in calibration, indicating a strong correlation between simulated and observed flows when the model focused exclusively on discharge without considering snow cover area. As wSN increased, the r^2 values gradually decreased, showing that the model's ability to simulate flow diminished as more weight was placed on SCA. At wSN values ranging from 0.05 to 0.85 for calibration, the r^2 values remained relatively high, around 0.70 to 0.72. However, as wSN continued to rise from 0.90 to 1.00, the r^2 values dropped significantly, reaching as low as 0.5567 at a wSN of 1.0. This trend suggested that while the model could balance the objectives of discharge and SCA to some extent, prioritizing SCA too heavily led to a less accurate representation of flow.

On the other hand, validation exhibited a fluctuated trend since at wSN = 0.0 r^2 was 0.5924 and slightly decrease from weight 0.05 to 0.15 before starting to increase to the highest value 0.6478 at wSN = 0.80. The fall followed this trend to 0.5694 at wSN =1 (Figure 4.40).

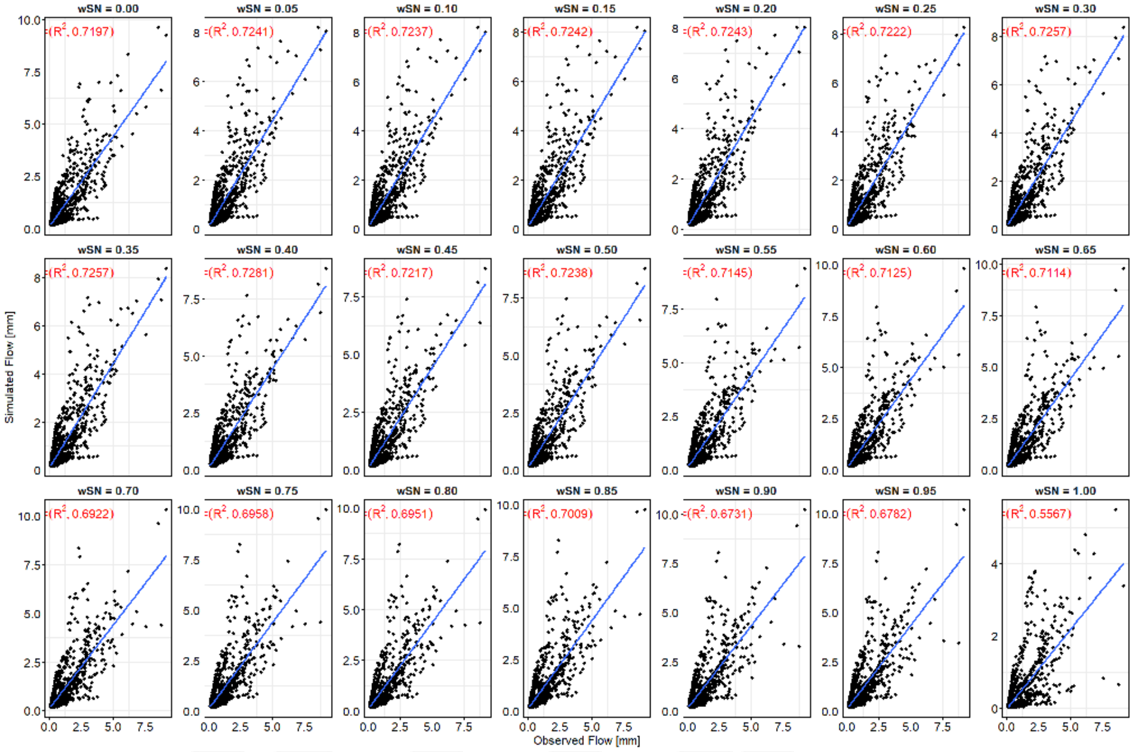

Figure 4.39. *Kayabaşı watershed using CM calibration observed and simulated discharges with wSN from 0 to 1 scatter plots*

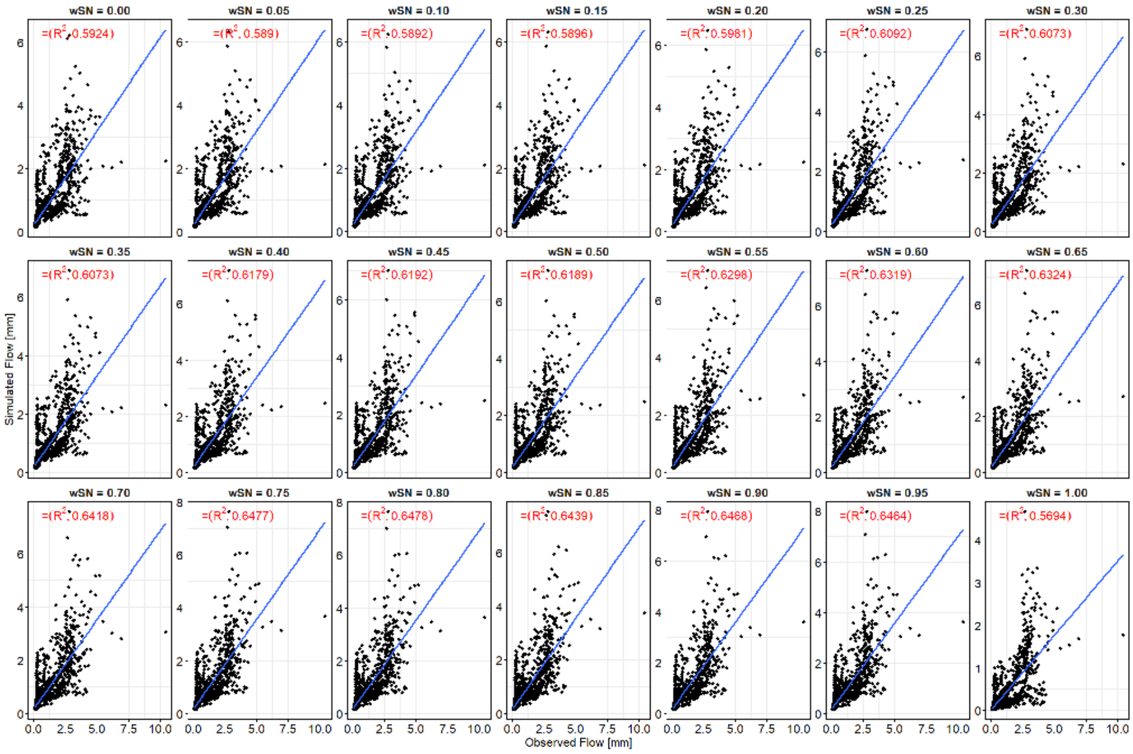

Figure 4.40. *Kayabaşı watershed validation observed and simulated discharges with wSN from 0 to 1 scatter plots*

Figure 4.41 plots depicted the variation in simulated discharges across different weights on snow for each month, derived by subtracting the simulated discharges at other wSN values (Qsim_***) from the simulated discharge at wSN = 0.00 (Qsim_000). During months from October to February a slight increasing trend was observed which indicated that the discharge was consistently higher when more weight was given to snow cover area (SCA) in the model, suggesting a lower retention of earlier snow that contributed to the discharge. During the winter months of January, February, and March, a clear decreasing trend was observed which indicated that the discharge was consistently lower when more weight was given to snow cover area in the model, suggesting a higher retention of snow and delayed meltwater contribution to the discharge.

Conversely, from March to April, a decreasing trend was evident and more pronounced in April. In these months, a clear decreasing trend indicated that the discharge was consistently lower when more weight was given to snow cover area in the model, suggesting a higher retention of snow and delayed meltwater contribution to the discharge. In May and June, the differences grew larger as wSN increased, highlighting that more weight on SCA led to higher discharges during these months. This trend suggested that the snow accumulated during winter started to melt, contributing to the discharge. The summer months of July, August and September showed a slight decrease trend, indicating the impact of snowmelt on discharge had diminished into these months. For the validation period, the same trend was observable, but with a shift of a month (Figure 4.33). For instance, in calibration the snow melting affected the discharge (increase) in May, but it occurred in validation from March to May and more pronounced in April. This fact may be due to the climatic conditions and also validation metrics were not as good as calibration period's.

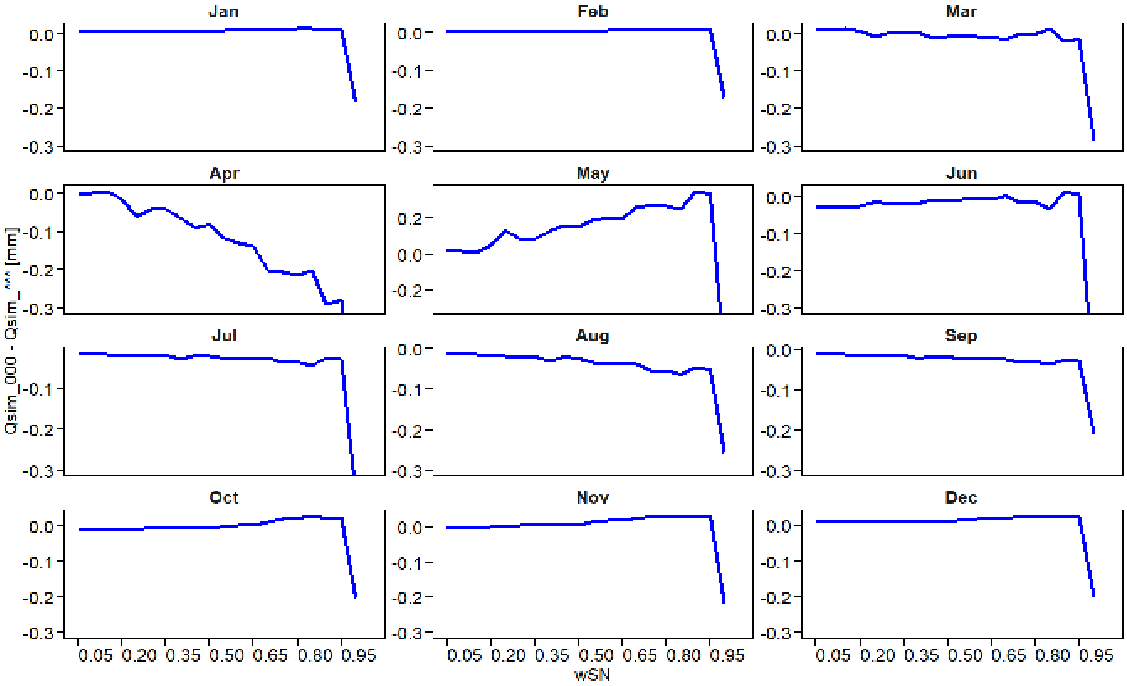

Figure 4.41. *Kayabaşı watershed calibration monthly discharge variation as wSN increased*

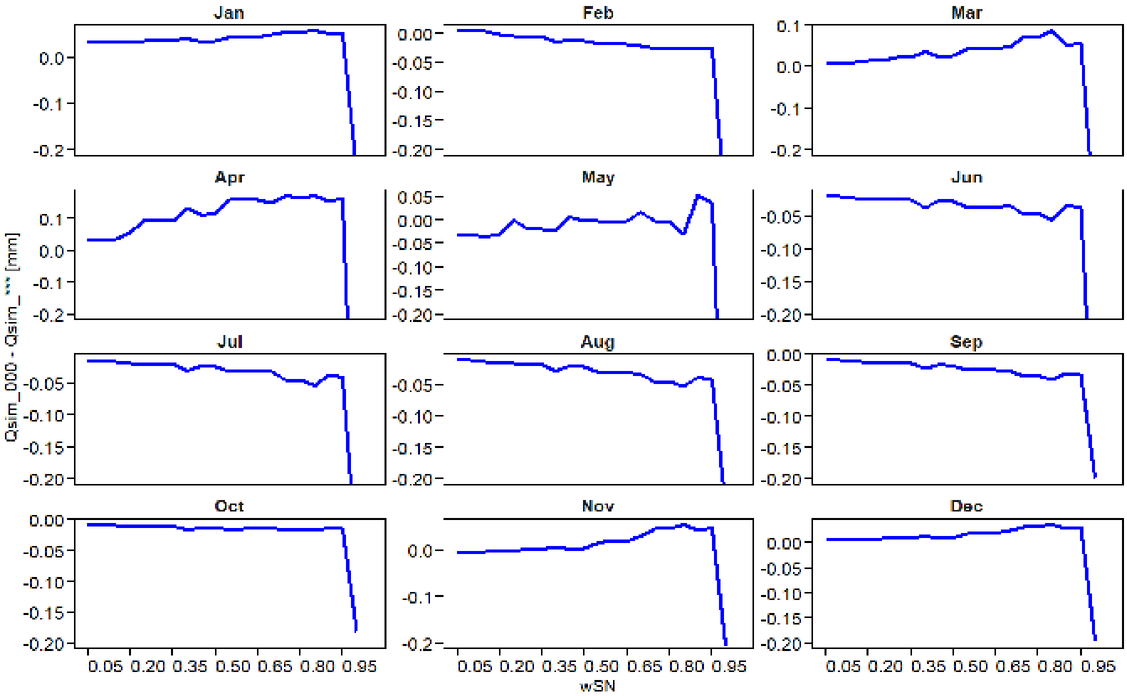

Figure 4.42. *Kayabaşı watershed validation monthly discharge variation as wSN increased*

4.2.2. Discharge and soil moisture calibration for Guinea basins

Multi-objective calibration was conducted on the three watersheds by varying the weighting for streamflow and soil moisture. Initially, the weighting was fully assigned to streamflow (wSM = 0). The basins were taken in lumped mode and an increment of 5% was applied for each step until the soil moisture criterion reached 100%, leaving 0% for streamflow. The multi-criteria objective function (MEsm) included the combined NSE for streamflow and Pearson correlation for soil moisture criteria, and CM algorithms was used to optimize this objective function.

- ***<u>Niger à Kouroussa watershed</u>***

The multi-objective calibration of the GR4J model applied to the Niger à Kouroussa watershed, considering both discharge (Q) and soil moisture (SM) was performed for one year. The parameters and the model's performance metrics are given in Figure 4.43.

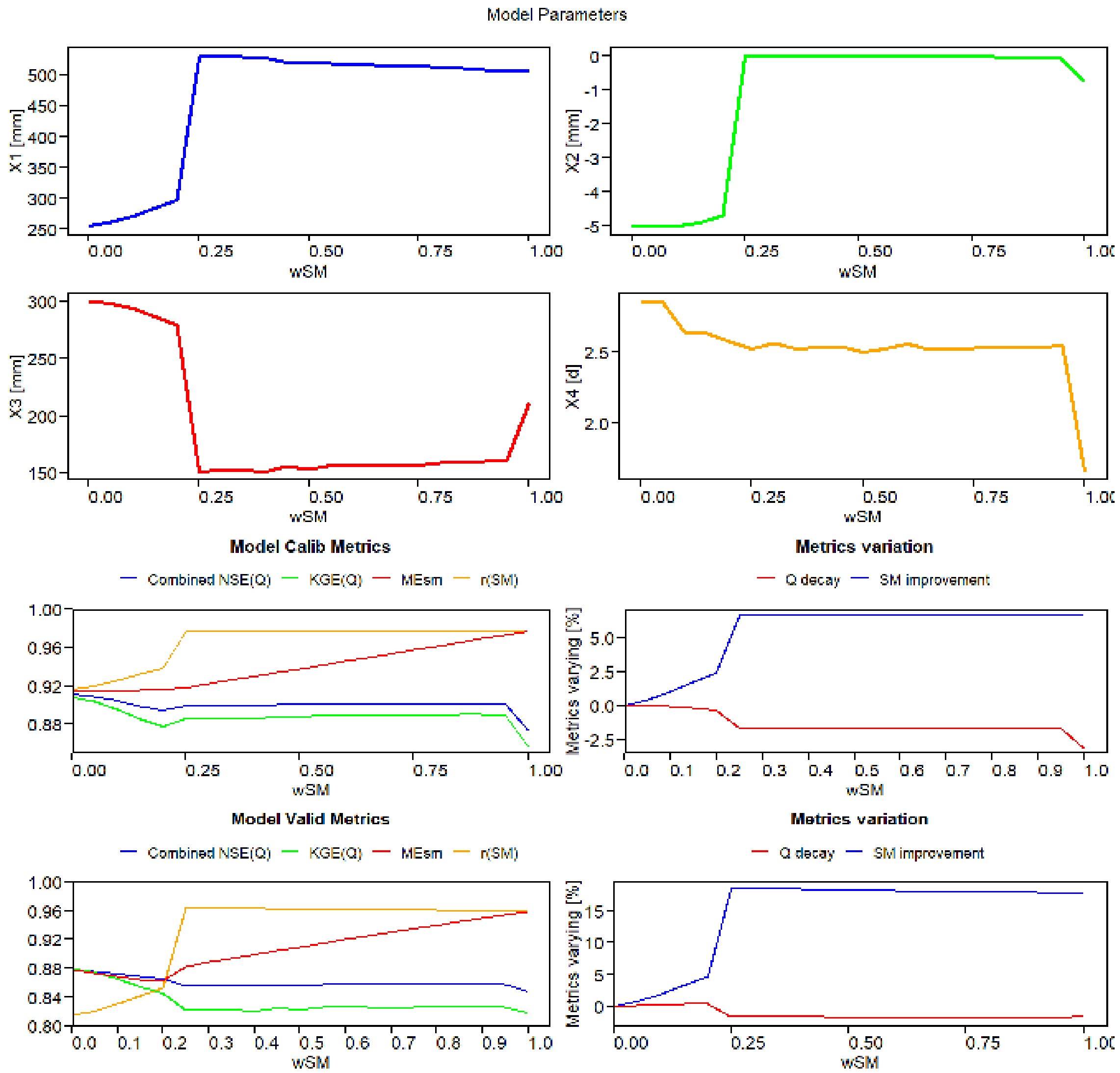

Figure 4.43. *Niger à Kouroussa watershed parameters and metrics*

The X1 parameter showed a significant increase as wSM increased from 0 to 0.25, after which it remained stable at a higher value and slightly decreased. Its values ranged between 254.925 mm and 531.022 mm with the maximum occurring at wSN = 0.30.

The X2 indicated a steep increase when wSM reached 0.25, followed by a slight decrease at wSM = 1.0. As X2 is the groundwater exchange, its variation implies that the model adjusted its subsurface flow to balance the weight given to soil moisture.

The third parameter X3 was inversely correlated to X1. Thus, when X1 increased that led to a decrease for X3. As wSM increased, X3 reached a minimum at wSM = 0.25 and then increased slightly to balance X1 decreasing.

Finally, the fourth parameter X4 decreased steadily as wSM increased, showing the model's adaptation in terms of the time lag between rainfall and runoff when soil moisture is prioritized.

To sum up, the trend of parameters as wSM increased were comprehensible since X1 and X2 (relate to the production function: soil content) increased and X3 and X4 (relate to the transfer function: flow routing) decreased.

The model performance metrics followed the expected trend. The multi-criteria objective function (MEsm) increased, while the combined NSE(Q) (NSE and logNSE) slightly decreased as wSM increased in both calibration and validation. The Pearson correlation coefficient also increased as wSM increased.

The decrease in discharge performance indicated a minor decline in discharge simulation accuracy when soil moisture was given priority. Furthermore, KGE(Q) showed consistent performance across different wSM values, suggesting a balanced trade-off between bias, correlation, and variability. In contrast, the increase in Pearson correlation with increase wSM emphasized the improvement in soil moisture simulation when its weighting was increased.

The variation in metrics displayed the rate at which discharge performance decayed and soil moisture performance improved. During calibration, the decay in Q was relatively low until wSM reached 0.20, then it declined at 0.25 before stabilizing around -1.6% and then reached -3.10% at wSM = 1.0. However, during validation, it initially increased to wSM = 0.25 and then decreased again before remaining stable. On the other hand, soil moisture (SM) improved by 6.64% during calibration at wSM = 1.0 and 18.46% at wSM = 0.30 before slightly decreasing to 17.74% at wSM = 1.0.

Figure 4.44 shows hydrographs with some wSM that were selected.

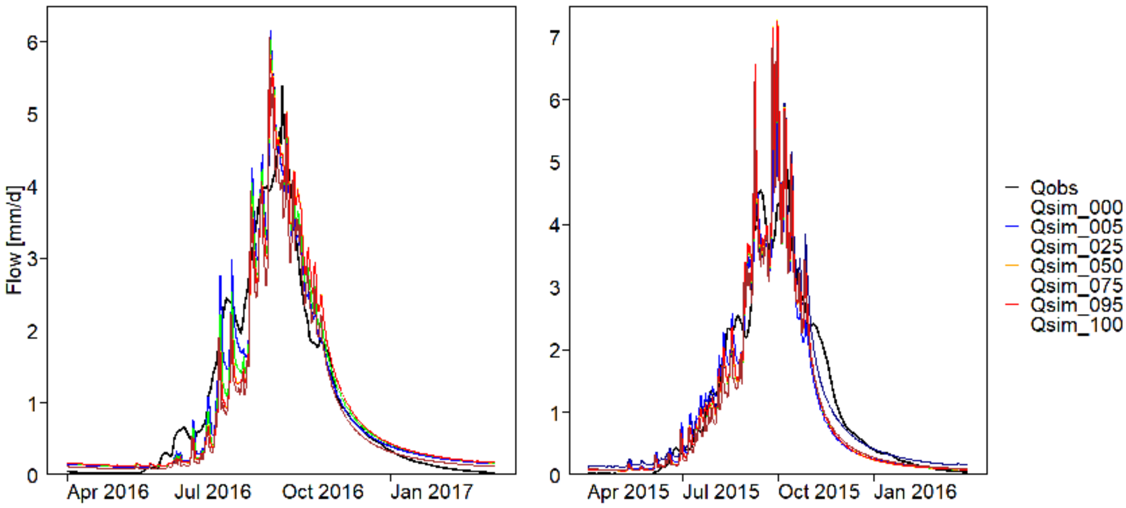

Figure 4.44. *Niger à Kouroussa watershed hydrographs with varying wSM: left calibration and right validation*

Figures 4.45 and 4.46 show discharge scatter plots from weight 0 to 1 respectively for calibration and validation. When wSM was 0.00, the highest r^2 value of 0.9329 was observed in calibration and 0.8933 in validation, indicating a strong correlation between simulated and observed flows when the model focused exclusively on discharge without considering soil moisture (SM). As wSM increased, the r^2 values gradually decreased, showing that the model's ability to simulate flow diminished as more weight was placed on SM. At wSM values ranging from 0.05 to 0.30 for calibration, the r^2 values remained relatively high, around 0.90 to 0.93. However, as wSM continued to rise from 0.35 to 1.00, the r^2 values dropped slightly, reaching 0.8875 at a wSM of 1.0 for calibration and 0.8724 at a wSM of 1 for validation. This trend suggested that while the model could balance the objectives of discharge and SM to some extent, prioritizing SM too heavily led to a less accurate representation of flow.

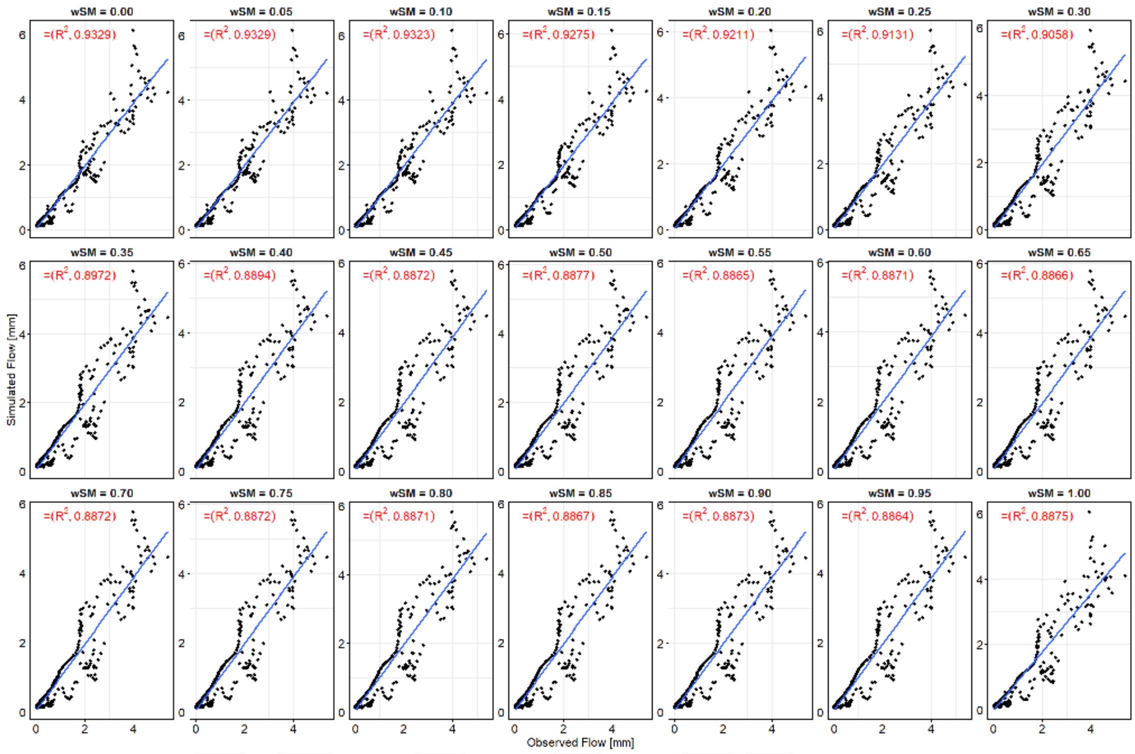

Figure 4.45. *Niger à Kouroussa watershed calibration observed and simulated discharges with wSM from 0 to 1 scatter plots*

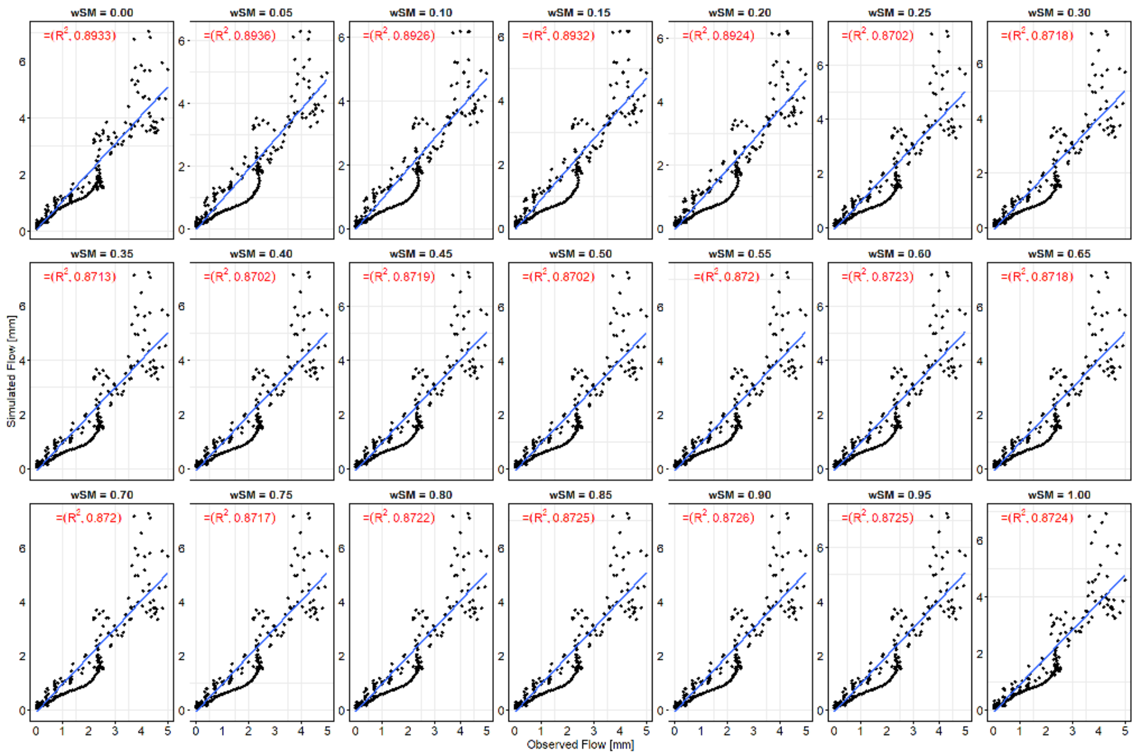

Figure 4.46. *Niger à Kouroussa watershed validation observed and simulated discharges with wSM from 0 to 1 scatter plots*

Figure 4.47 plots depicted the variation in discharge across different weights on soil moisture (wSM) for each month, derived by subtracting the simulated discharges at other wSM values (Qsim_***) from the simulated discharge at wSN = 0.00 (Qsim_000). During the rainfall months of July, August, and September, a clear decreasing trend was observed which indicated that the discharge was consistently lower when more weight was given to soil moisture (SM) in the model. This may be attributed to the fact that during the rainy season, as wSM increased, the model soil layer expanded, resulting in a greater capacity for the soil to retain water. As a result, surface flow decreased compared to wSM = 0.

Conversely, from October through June, an increasing trend was evident. In these months, the differences grew larger as wSM increased, highlighting that more weight on SM led to higher discharges during these months. This trend suggested that the soil held moisture during rainy season started to be released, contributing to the discharge. For the validation period, the same trend was observable, making model calibration more accurate (Figure 4.48). However, for both calibration and validation periods, at wSM = 1.0, a sharp decrease was noticeable for each month indicating that full weighting on soil moisture adversely impacted discharge simulation accuracy.

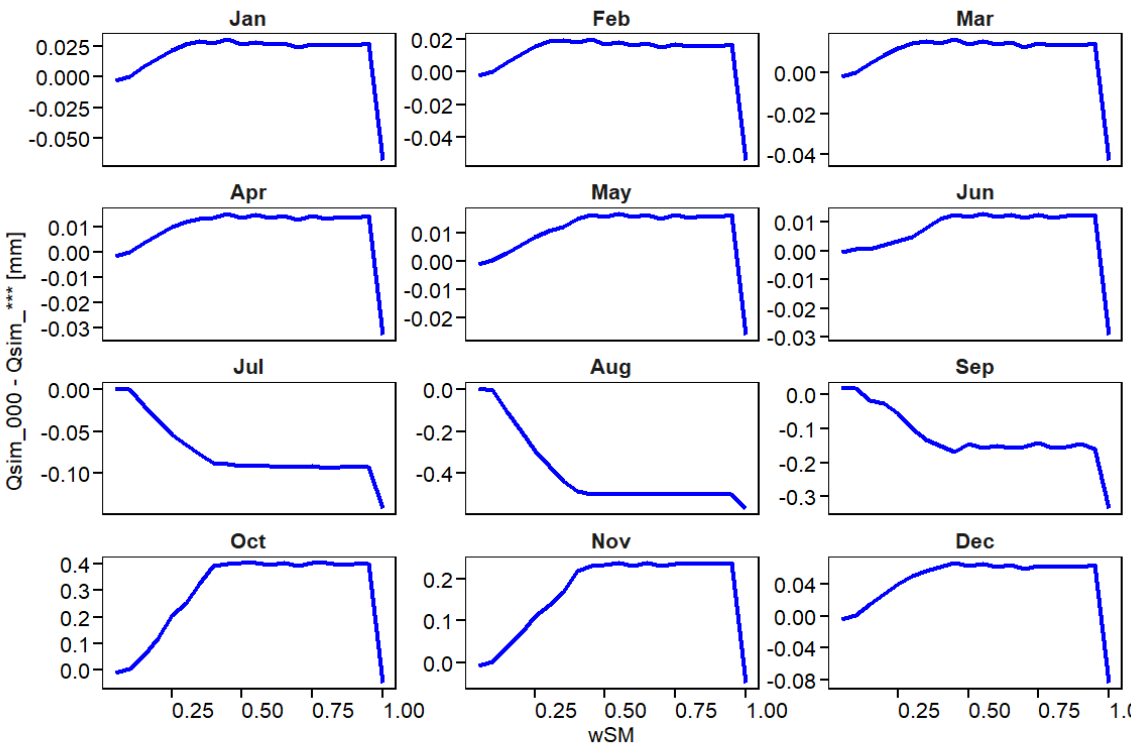

Figure 4.47. *Niger à Kouroussa watershed calibration monthly discharge variation as wSM increased*

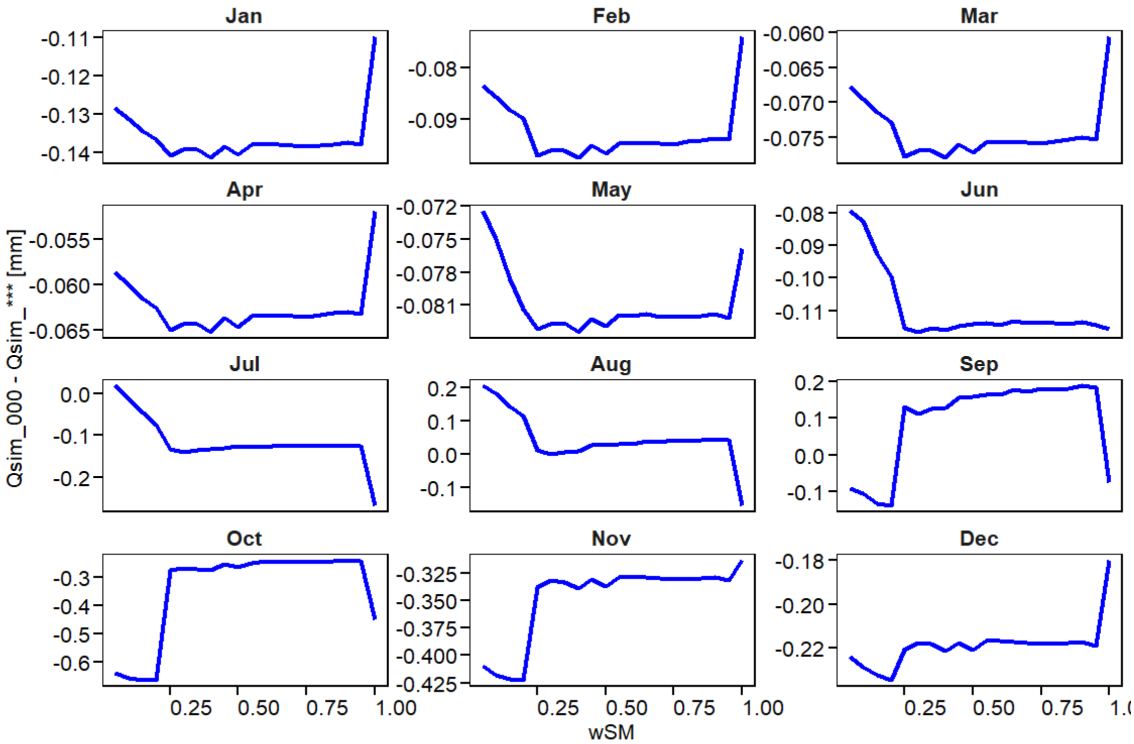

Figure 4.48. *Niger à Kouroussa watershed validation monthly discharge variation as wSM increased*

Figure 4.49 shows the comparison between SMAP soil moisture data and the model's soil moisture (SM) simulations using different wSM values. The left graph represents the calibration period (04/01/2016 to 03/31/2017), while the right graph represents the validation period (04/01/2015 to 03/31/2016).

During the calibration period, the model's SM simulations aligned well with the SMAP data during the rainy season, particularly when the weighting on soil moisture was increased. However, in the dry season, even with the highest weighting (wSM = 1.0), the model struggled to match the SMAP data. The same patterns observed during calibration were consistent in the validation period. This consistency between the calibration and validation periods indicates the model's reliability in capturing soil moisture dynamics during wet conditions when calibrated with appropriate weights on soil moisture. However, the model's accuracy is compromised during the dry season. This suggests that the model's soil water content layer may not extend deep enough to fully capture the moisture dynamics of the root zone as represented by SMAP. Additionally, fluctuations in the model's soil water content layer to simulate discharge pattern may contribute to difficulties in simulating soil moisture patterns during dry season. These findings highlight the need to refine the model's soil moisture parameterization or include additional processes to better represent soil moisture dynamics throughout all seasons.

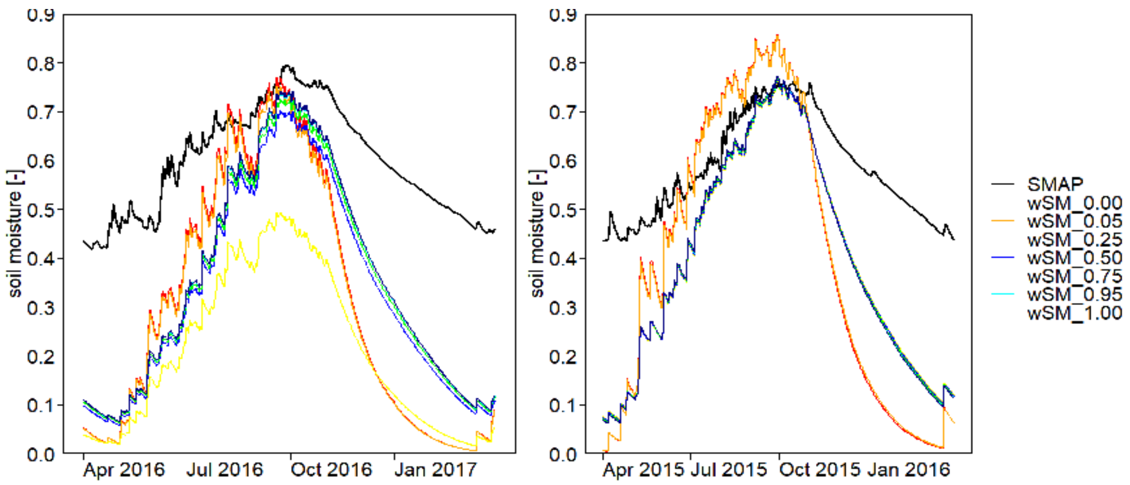

Figure 4.49. *Niger à Kouroussa watershed soil moisture with varying wSM: left calibration and right validation*

Figures 4.50 and 4.51 show model soil moisture versus SMAP soil moisture scatter plots from weight 0 to 1 respectively for calibration and validation. When wSM was 1.00, the highest r^2 value of 0.9543 was observed in calibration and 0.9198 in validation, indicating a strong correlation between simulated and observed soil moisture when the model focused exclusively on soil water content without considering discharge. As wSM decreased, the r^2 values gradually decreased, showing that the model's ability to simulate soil water content diminished as less weight was placed on SM.

As it can be seen in Figure 4.49, like hydrograph, soil moisture has rising and falling limbs. It was remarked that the increase of wSM improved the falling limb than rising limb. The scatter plots of these two parts are presented in the appendix.

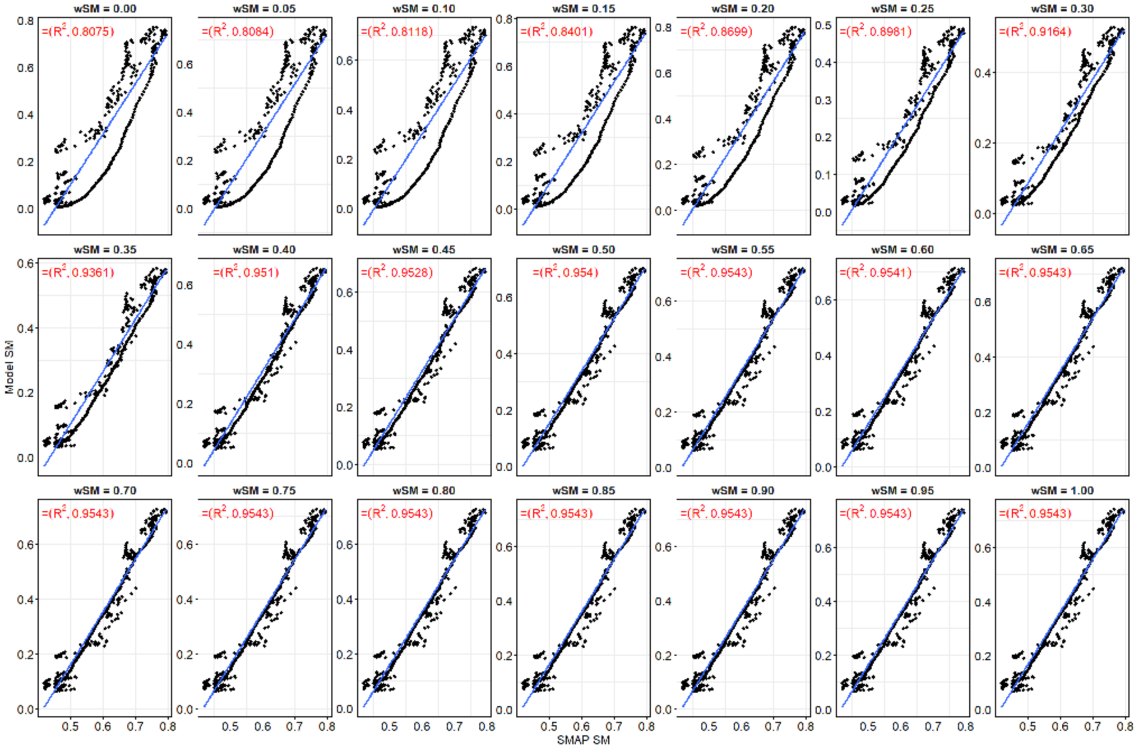

Figure 4.50. *Niger à Kouroussa watershed calibration observed and simulated soil moisture with wSM from 0 to 1 scatter plots*

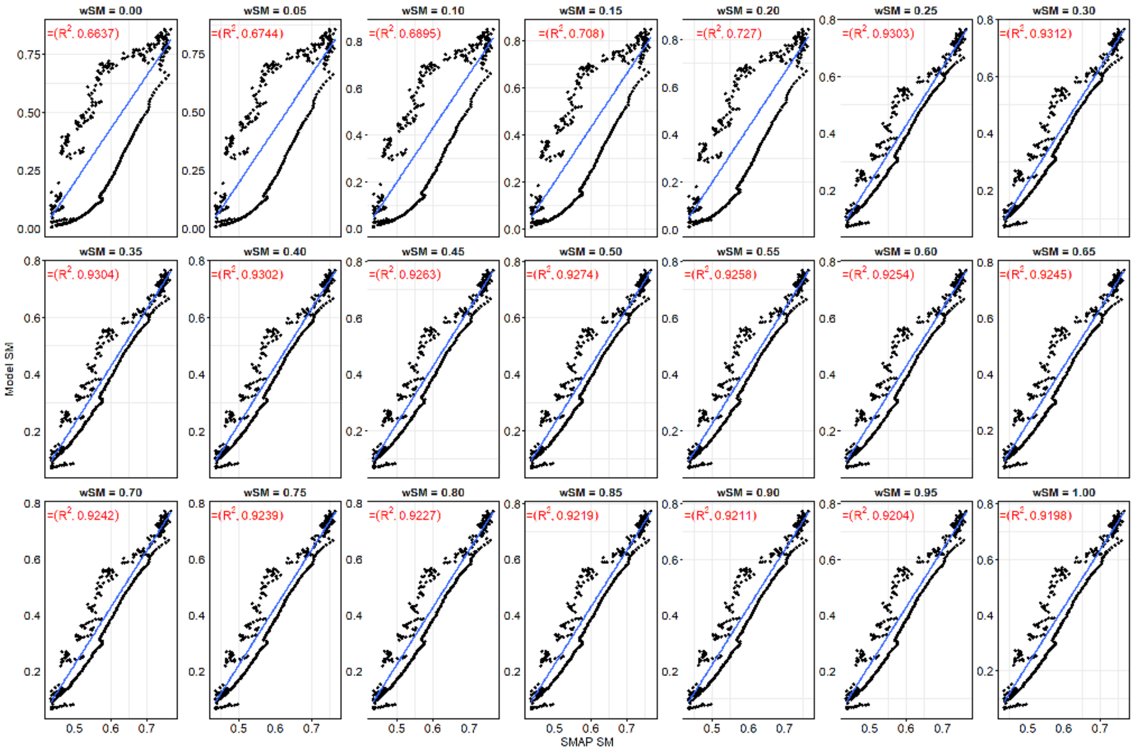

Figure 4.51. *Niger à Kouroussa watershed validation observed and simulated soil moisture with wSM from 0 to 1 scatter plots*

- ***Milo à Kankan watershed***

The multi-objective calibration of the GR4J model applied to the Milo à Kankan watershed, considering both discharge (Q) and soil moisture (SM) was performed for one year. The parameters and the model's performance metrics are given in Figure 4.52.

The parameter X1 showed a significant increase as wSM increased from 0 to 1.0, indicating that more weight on SM leads to a high capacity of soil to hold more water. Its values ranged between 100.324 mm and 372.528 mm for weight 0.0 and 1.0 respectively.

The X2 indicated a gradual increase as wSM increased followed by a sharp decrease at wSM = 1.0. As X2 is the groundwater exchange, its variation implies that the model adjusted its subsurface flow to balance the weight given to soil moisture.

The third parameter X3 showed a decreasing trend as wSM increased. It was inversely correlated to X1 and ranged between 309.027 mm (wSM = 0.0) and 155.562 mm (wSM = 0.95). At wSM = 1.0, a sharp decrease happened and got the value as small as 27.382 mm.

Finally, the fourth parameter X4 decreased steadily as wSM increased, showing the model's adaptation in terms of the time lag between rainfall and runoff when soil moisture is prioritized. Again, at wSM = 1.0, a plummet occurred.

To sum up, like in Milo à Kankan, the trend of parameters as wSM increased were comprehensible since X1 and X2 (relate to the production function: soil content) increased and X3 and X4 (relate to the transfer function: flow routing) decreased.

The model performance metrics followed the expected trend. The multi-criteria objective function (MEsm) increased, while the combined NSE(Q) slightly decreased as wSM increased in both calibration and validation. The Pearson correlation coefficient also increased as wSM increased.

The decrease in discharge performance indicated a minor decline in discharge simulation accuracy when soil moisture was given priority. Furthermore, KGE(Q) showed consistent performance across different wSM values, suggesting a balanced trade-off between bias, correlation, and variability. In contrast, the increase in Pearson correlation with increased wSM emphasized the improvement in soil moisture simulation when its weighting was increased.

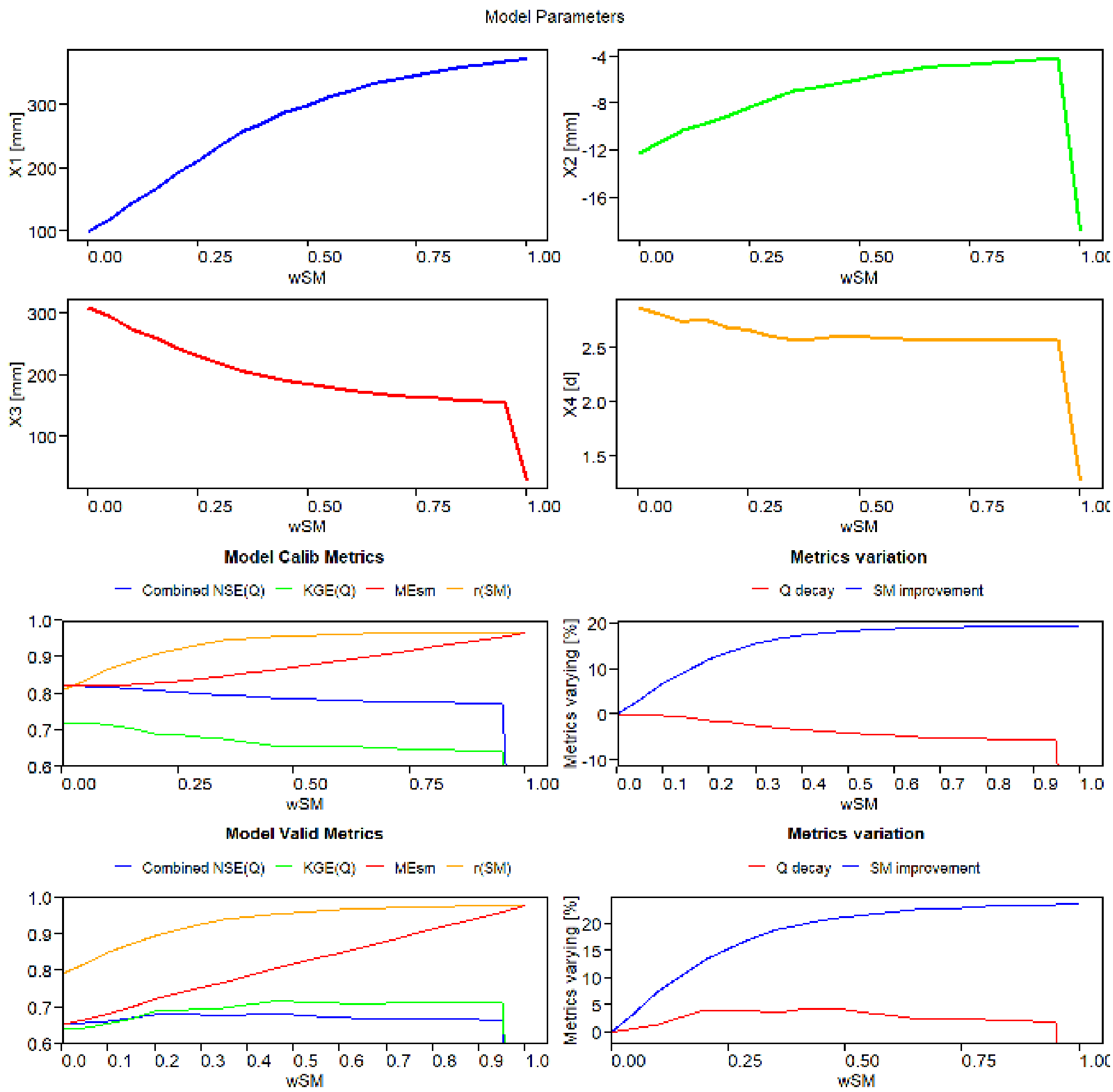

Figure 4.52. *Milo à Kankan watershed parameters and metrics*

The variation in metrics displayed the rate at which discharge performance decayed and soil moisture performance improved. During calibration, the decay in Q was relatively low until wSM reached 0.25 (1.81%). The total decay before the crash was 5.78%, while at wSM = 1.0, it was 147.47%. However, during validation, it initially increased to wSM = 0.20 (4.09%) and then decreased to 1.7% at wSM = 0.95 (wSM = 1.0 was 166.75%). On the other hand, soil moisture (SM) improved by 19.16% during calibration at wSM = 1.0 and while validation improved by 23.56% at wSM = 1.0.

Figure 4.53 shows hydrographs with some wSM that were selected.

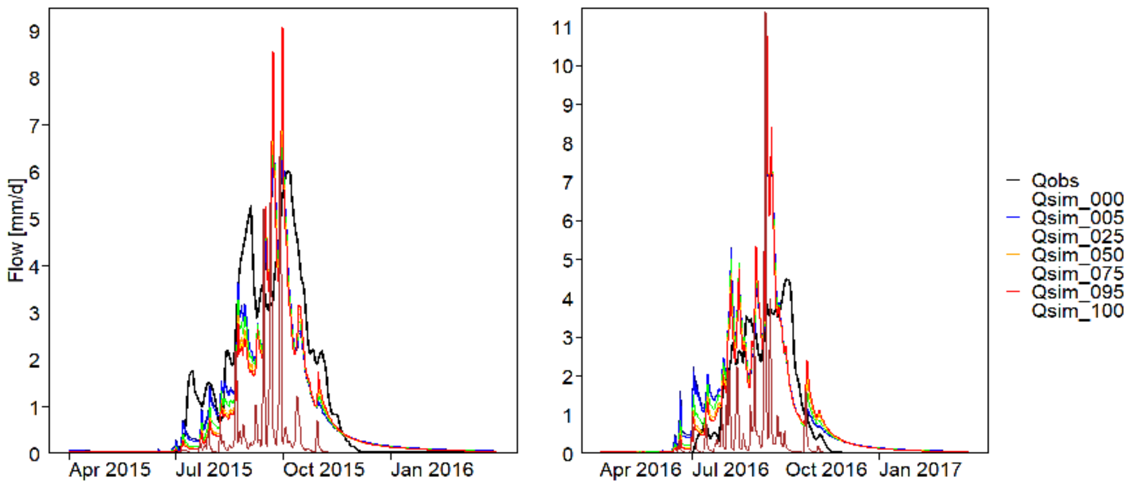

Figure 4.53. *Milo à Kankan watershed hydrographs with varying wSM: left calibration and right validation*

Figures 4.54 and 4.55 show discharge scatter plots from weight 0 to 1 respectively for calibration and validation. When wSM was 0.00, the highest r^2 value of 0.7639 was observed in calibration and 0.6919 for validation, indicating a good correlation between simulated and observed flows when the model focused exclusively on discharge without considering SM. As wSM increased, the r^2 values gradually decreased, showing that the model's ability to simulate flow diminished as more weight was placed on SM. At wSM values ranging from 0.05 to 0.60 for calibration, the r^2 values remained relatively high, around 0.70 to 0.76. However, as wSM continued to rise from 0.65 to 1.00, the r^2 values dropped slightly, reaching 0.1787 at a wSM of 1.0 for calibration and 0.1542 at a wSM of 1 for validation. This trend suggested that while the model could balance the objectives of discharge and SM to some extent, prioritizing SM too heavily led to a less accurate representation of flow.

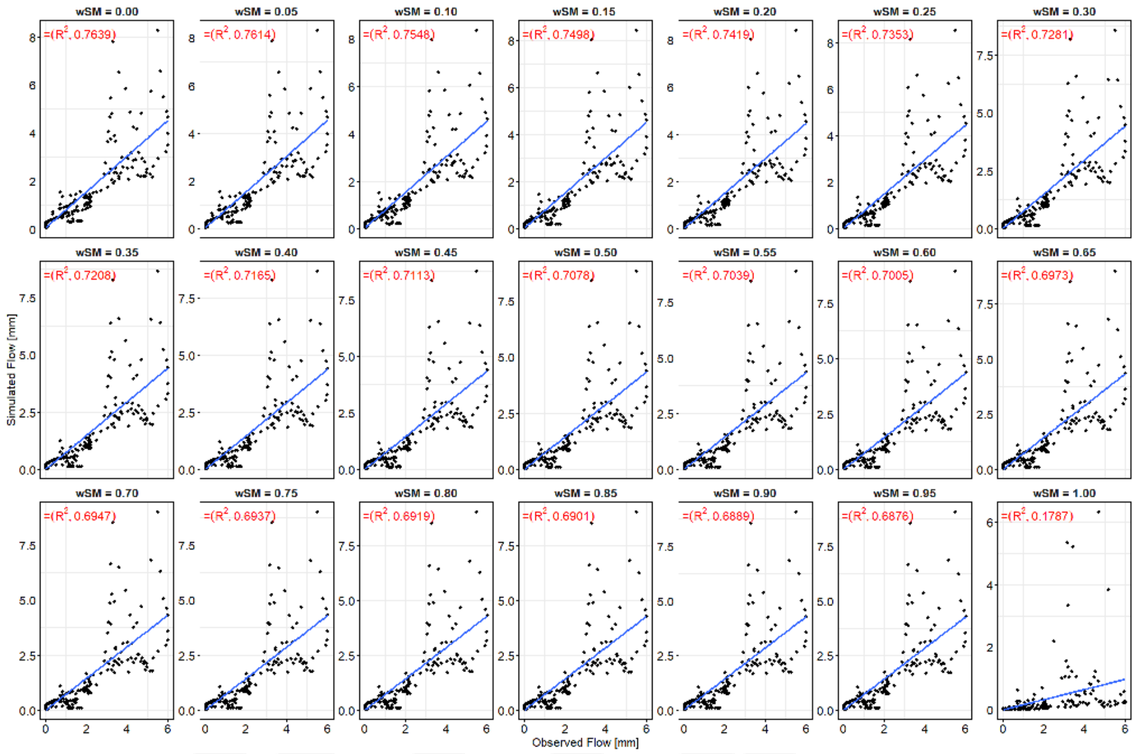

Figure 4.54. *Milo à Kankan watershed calibration observed and simulated discharges with wSM from 0 to 1 scatter plots*

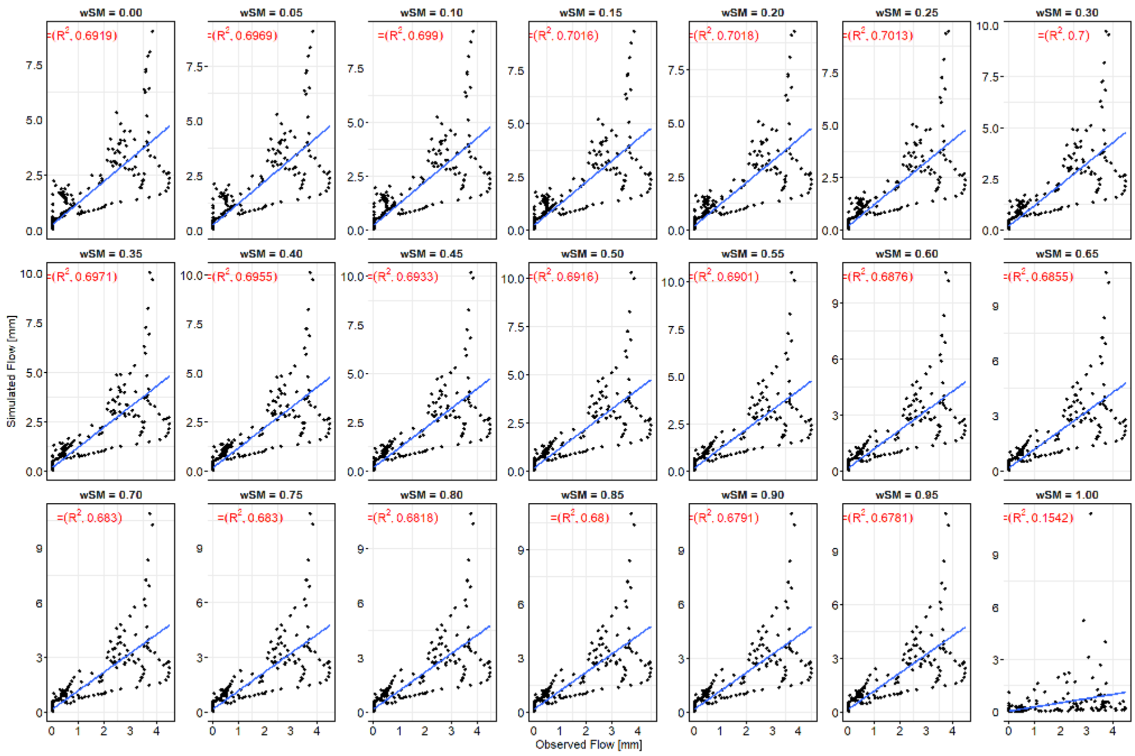

Figure 4.55. *Milo à Kankan watershed validation observed and simulated discharges with wSM from 0 to 1 scatter plots*

Figure 4.56 plots depicted the variation in discharge across different weights on soil moisture (wSM) for each month, derived by subtracting the simulated discharges at other wSM values (Qsim_***) from the simulated discharge at wSN = 0.00 (Qsim_000). During all months of the year expect November, a clear decreasing trend was observed which indicated that the discharge was consistently lower when more weight was given to SM in the model. This may be attributed to the fact that during these months, as wSM increased, the model soil layer expanded, resulting in a greater capacity for the soil to retain water (high X1). As a result, surface flow decreased compared to wSM = 0.

Conversely, for November, which corresponds to the end of rainy season, an increasing trend was evident. In this month, the differences grew larger as wSM increased, highlighting that more weight on SM led to higher discharges. This trend suggested that the held soil moisture during rainy season started to be released, contributing significantly to the discharge in November. For the validation period, the same trend was observable, making model calibration more accurate (Figure 4.57). However, for both calibration and validation periods, at wSM = 1.0, a sharp decrease was noticeable for each month indicating that excessive weighting (especially wSM = 1.0) on soil moisture adversely impacted discharge simulation accuracy.

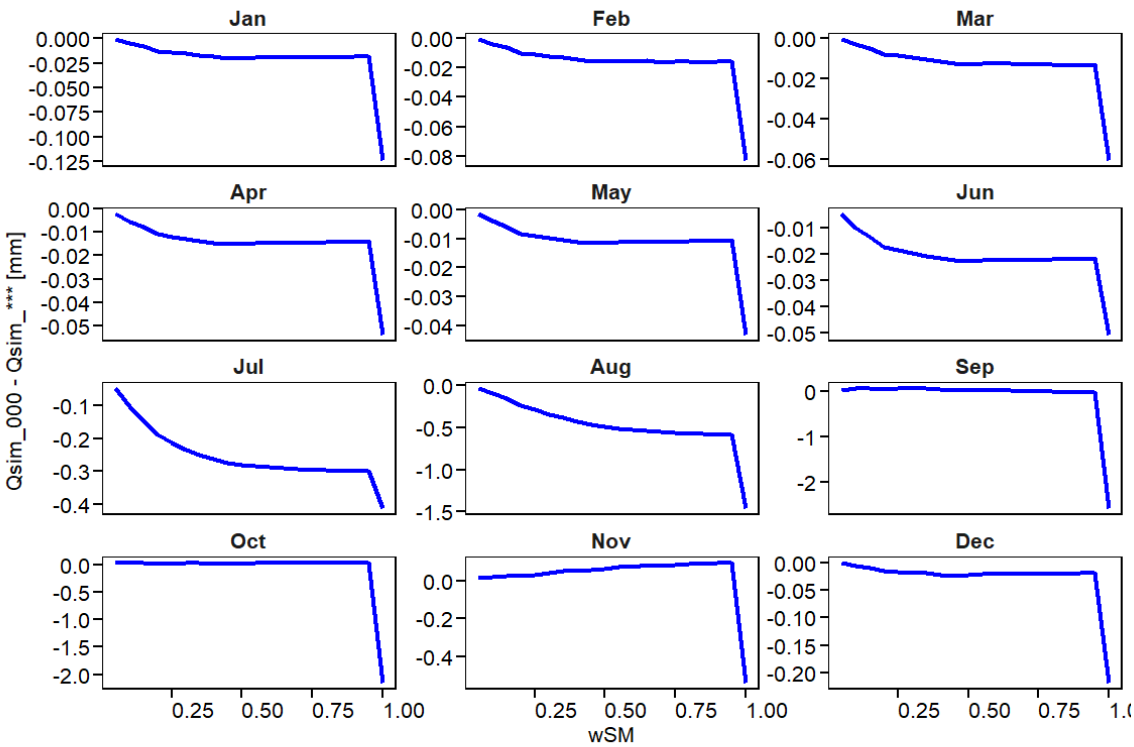

Figure 4.56. *Milo à Kankan watershed calibration monthly discharge variation as wSM increased*

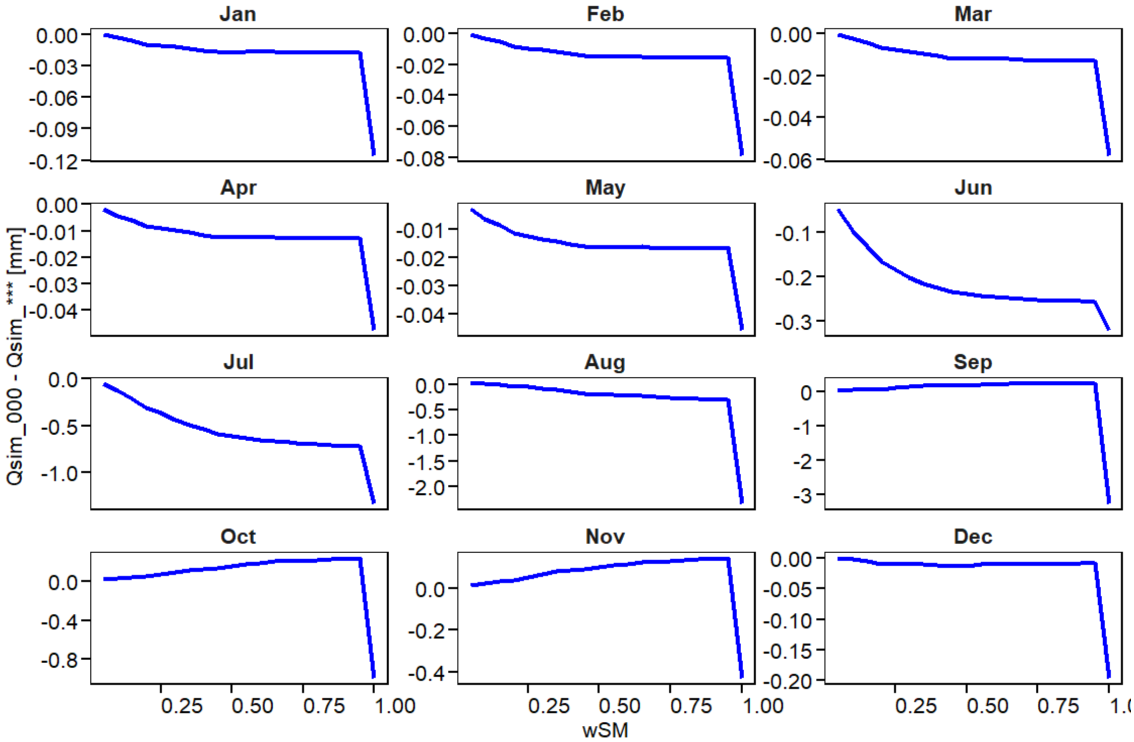

Figure 4.57. *Milo à Kankan watershed validation monthly discharge variation as wSM increased*

Figure 4.58 shows the comparison between SMAP soil moisture data and the model's soil moisture (SM) simulations using different wSM values. The left graph represents the calibration period (04/01/2015 to 03/31/2016), while the right graph represents the validation period (04/01/2016 to 03/31/2017).

During the calibration period, the model's SM simulations aligned well with the SMAP data during the rainy season, particularly when the weighting on soil moisture (wSM) was increased. However, in the dry season, even with the highest weighting (wSM = 1.0), the model struggled to match the SMAP data. The same patterns observed during calibration were consistent in the validation period. This consistency between the calibration and validation periods indicates the model's reliability in capturing soil moisture dynamics during wet conditions when calibrated with appropriate weights on soil moisture. However, the model's accuracy is compromised during the dry season. This suggests that the model's soil water content layer may not extend deep enough to fully capture the moisture dynamics of the root zone as represented by SMAP. Additionally, fluctuations in the model's soil water content layer to simulate discharge pattern may contribute to difficulties in simulating soil moisture patterns during dry season. These findings highlight the need to refine the model's soil moisture parameterization or include additional processes to better represent soil moisture dynamics throughout all seasons.

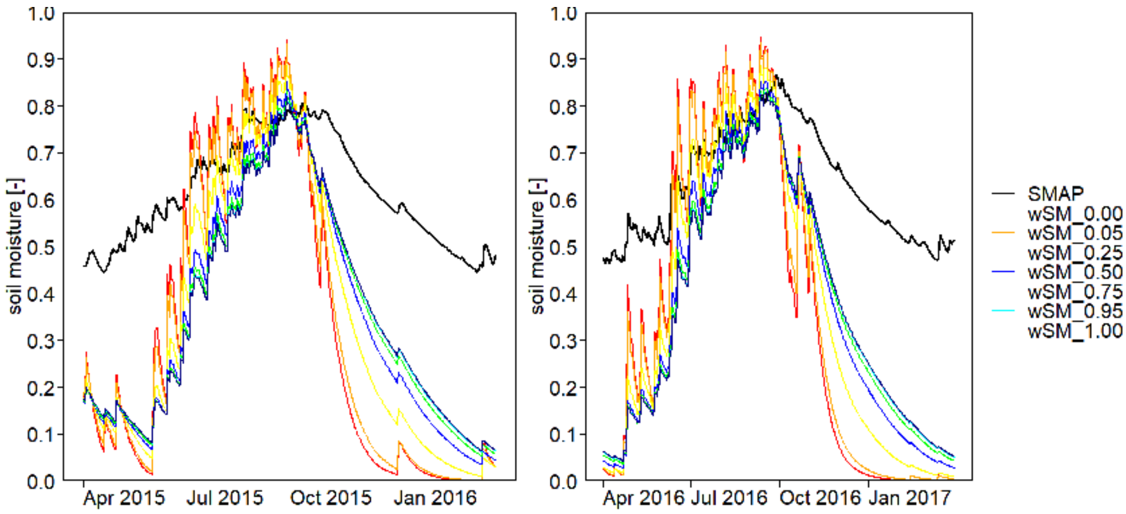

Figure 4.58. *Milo à Kankan watershed soil moisture with varying wSM: left calibration and right validation*

Figures 4.59 and 4.60 show model soil moisture versus SMAP soil moisture scatter plots from weight 0 to 1 respectively for calibration and validation. When wSM was 1.00, the highest r^2 value of 0.9306 was observed for calibration and 0.9551 for validation, indicating a strong correlation between simulated and observed soil moisture when the model focused exclusively on soil water content without considering discharge. As wSM decreased, the r^2 values gradually decreased, showing that the model's ability to simulate soil water content diminished as less weight was placed on SM.

As it can be seen in Figure 4.58, like hydrograph, soil moisture has rising and falling limbs. It was remarked that the increase of wSM improved the falling limb than rising limb. The scatter plots of these two parts are presented in the appendix.

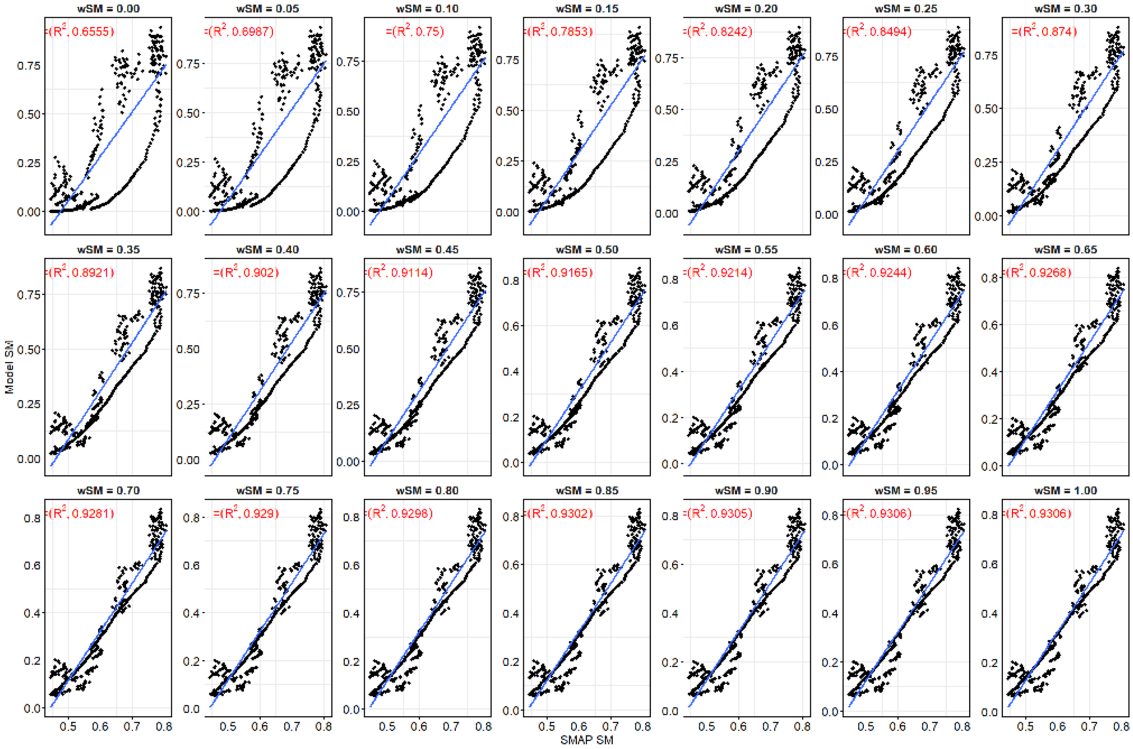

Figure 4.59. *Milo à Kankan watershed calibration observed and simulated soil moisture with wSM from 0 to 1 scatter plots*

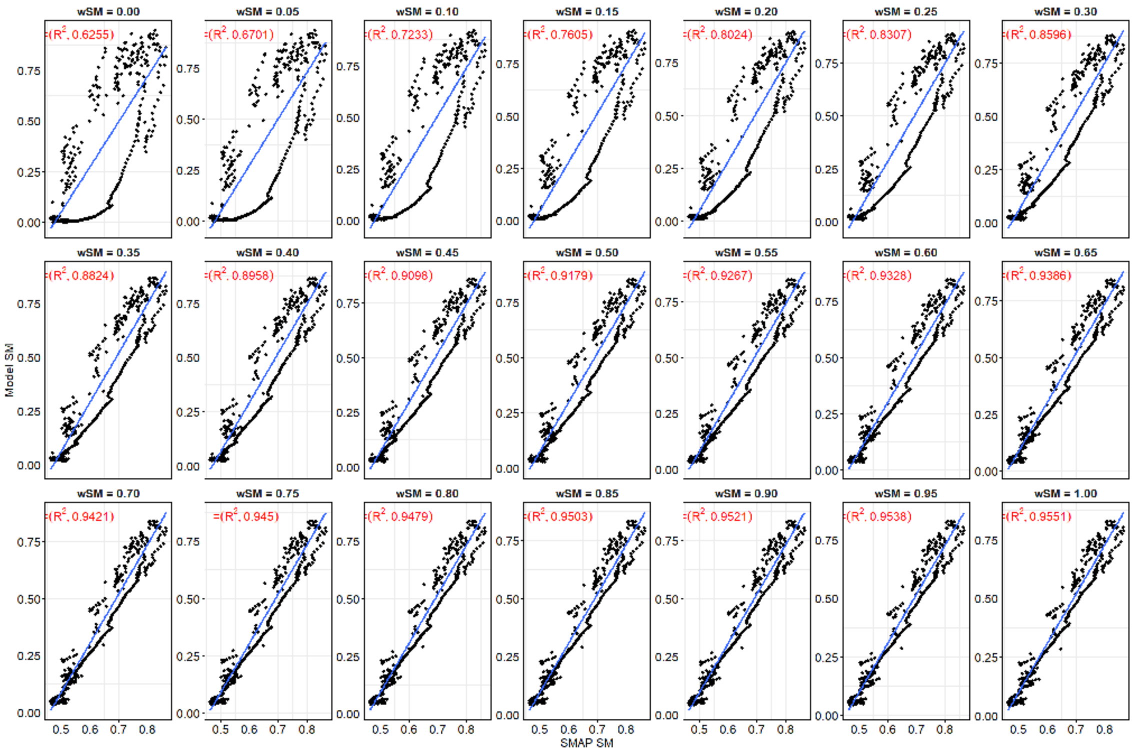

Figure 4.60. *Milo à Kankan watershed validation observed and simulated soil moisture with wSM from 0 to 1 scatter plots*

- ***Bafing à Sokotoro watershed***

The multi-objective calibration of the GR4J model applied to the Niger à Kouroussa watershed, considering both discharge (Q) and soil moisture (SM) was performed for two years. The parameters and the model's performance metrics are given in Figure 4.61.

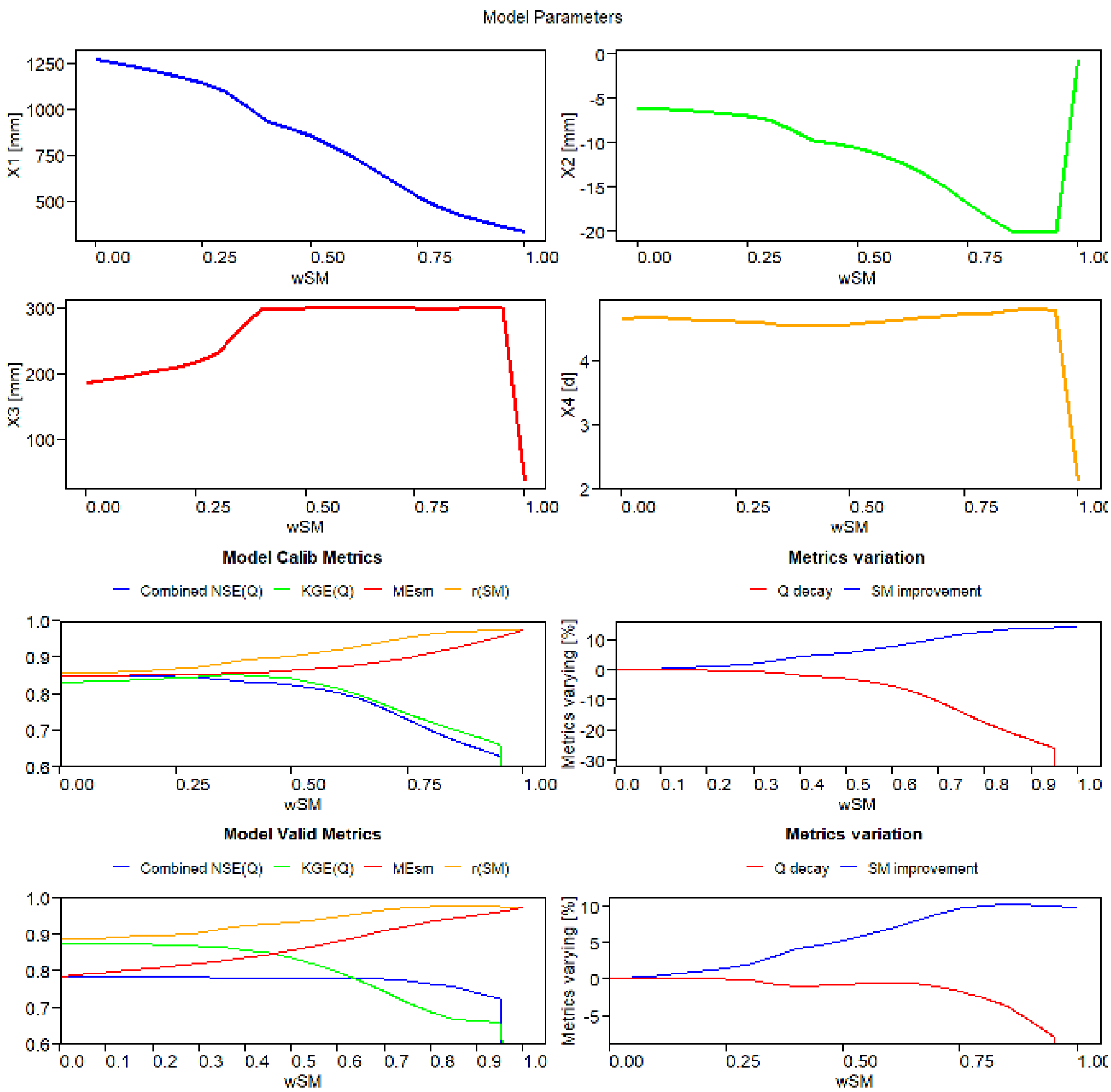

Figure 4.61. *Bafing à Sokotoro watershed parameters and metrics*

The parameter X1 showed a decreasing trend as wSM increased from 0 to 1.0. Its values ranged between 1273.961 mm and 336.400 mm for wSM = 0.0 and wSM = 1.0 respectively.

The X2 also showed a decreasing trend when wSM increased from -6.011 mm (wSM = 0.0) to -19.98 mm (wSM = 0.95), followed by a sharp increase at wSM = 1.0.

As X2 is the groundwater exchange, its variation implies that the model adjusted its subsurface flow to balance the weight given to soil moisture.

The third parameter X3 was inversely correlated to X1. Thus, when X1 decreased that led to an increase for X3. As wSM increased, X3 smoothly increased from 186.444 mm to 231.656 mm at wSM = 0.30 and then soared to 299.773 mm at wSM = 0.40 before maintaining a stably position then crash at wSM = 1.0.

Finally, the fourth parameter X4 increased steadily as wSM increased, showing the model's adaptation in terms of the time lag between rainfall and runoff when soil moisture is prioritized.

To sum up, the trend of parameters as wSM increased in Bafing à Sokotoro was not similar to the Niger à Kouroussa and Milo à Kankan. This difference may be due to the high value of X1 at wSM = 0.0 and X2 much decreasing. Furthermore, soil type and hydrogeologic characteristic may be a reason.

The model performance metrics followed the expected trend. The multi-criteria objective function (MEsm) increased, while the combined NSE(Q) slightly decreased as wSM increased in both calibration and validation. The Pearson correlation coefficient also increased as wSM increased.

The decrease in discharge performance indicated a minor decline in discharge simulation accuracy when soil moisture was given priority. Furthermore, KGE(Q) showed consistent performance across different wSM values from 0.0 to 0.5, suggesting a balanced trade-off between bias, correlation, and variability. In contrast, the increase in Pearson correlation with increased wSM emphasized the improvement in soil moisture simulation when its weighting was increased.

The variation in metrics displayed the rate at which discharge performance decayed and soil moisture performance improved. During calibration, the decay in Q was relatively low until wSM reached 0.30 (0.48%), then it declined in second phase to 5.31% at 0.60 before plummeting to 26.02% then crashed at 1.0. However, during validation, it showed initially a very small increase to wSM = 0.25 and then decreased before increasing and decreasing again. On the other hand, soil moisture (SM) improved by 14.14% during calibration at wSM = 1.0 and during validation (9.74% at wSM = 1.0).

Figure 4.62 shows hydrographs with some wSM that was selected.

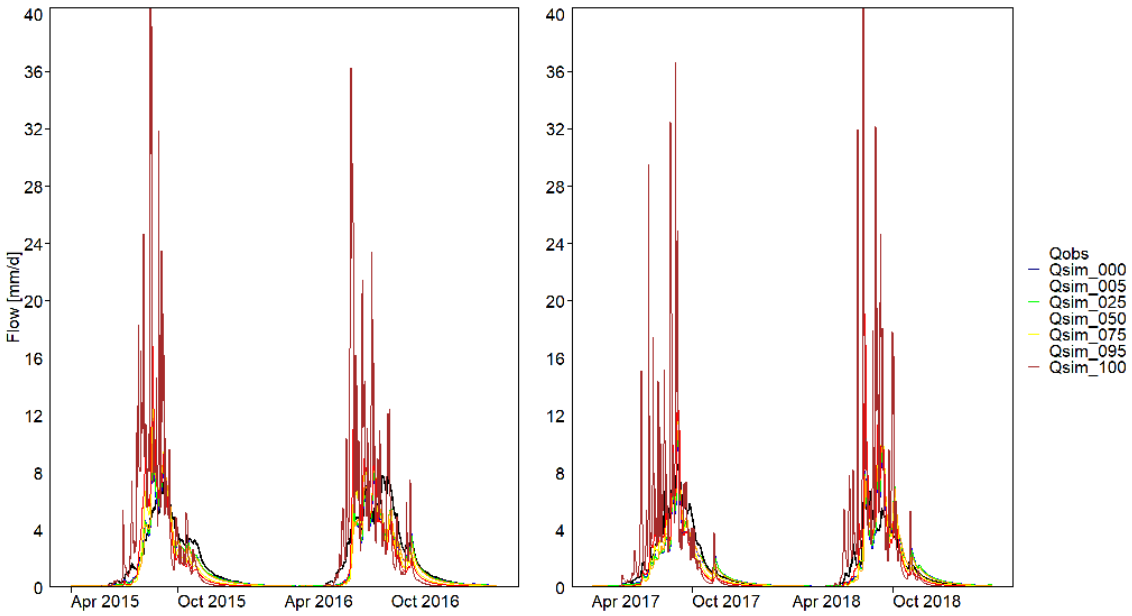

Figure 4.62. *Bafing à Sokotoro watershed hydrographs with varying wSM: left calibration and right validation*

Figures 4.63 and 4.64 show discharge scatter plots from weight 0 to 1 respectively for calibration and validation. When wSM was 0.00, the highest r^2 value of 0.8454 was observed for calibration and 0.8933 indicating a strong correlation between simulated and observed flows when the model focused exclusively on discharge without considering SM. As wSM increased, the r^2 values gradually decreased, showing that the model's ability to simulate flow diminished as more weight was placed on SM. At wSM values ranging from 0.05 to 0.60 for calibration, the r^2 values remained relatively high, around 0.80 to 0.84. However, as wSM continued to rise from 0.65 to 1.00, the r^2 values dropped, reaching 0.6547 at a wSM of 0.95, then 0.3810 at wSM = 1.0 for calibration. During validation, r^2 showed a fluctuating trend since it improved for some high value of wSM and the worst was in wSM = 1.0 (0.3869). This trend suggested that while the model could balance the objectives of discharge and SM to some extent, prioritizing SM too heavily led to a less accurate representation of flow.

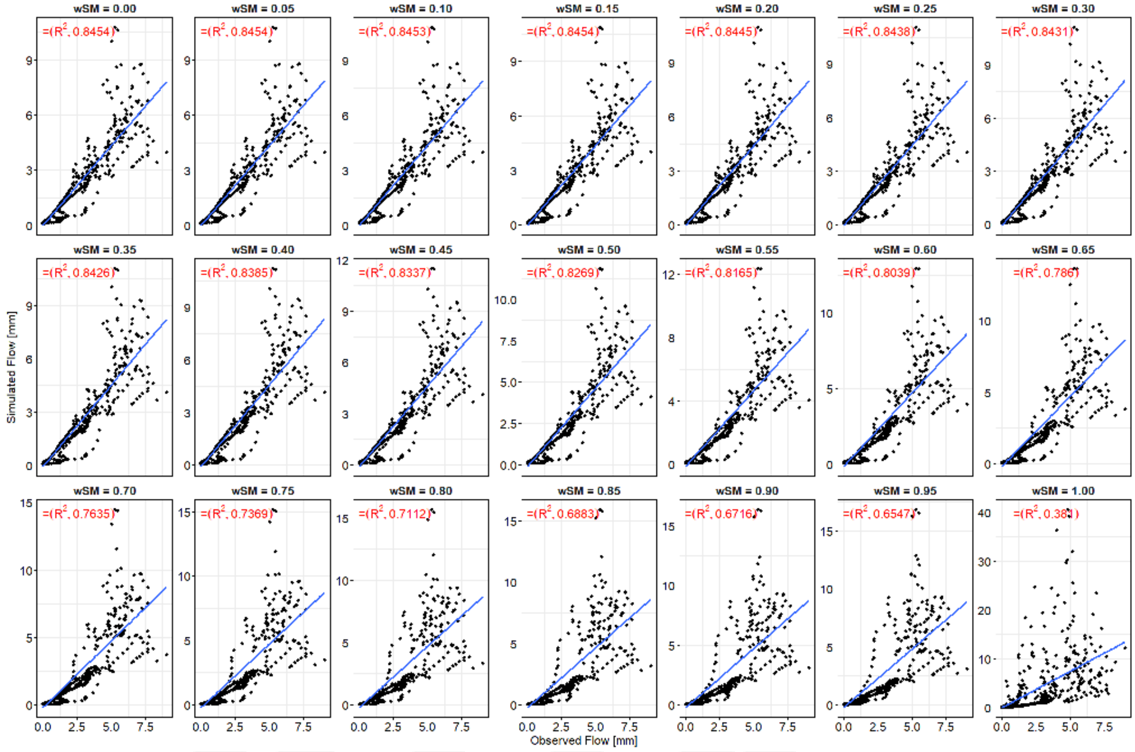

Figure 4.63. *Bafing à Sokotoro watershed calibration observed and simulated discharges with wSM from 0 to 1 scatter plots*

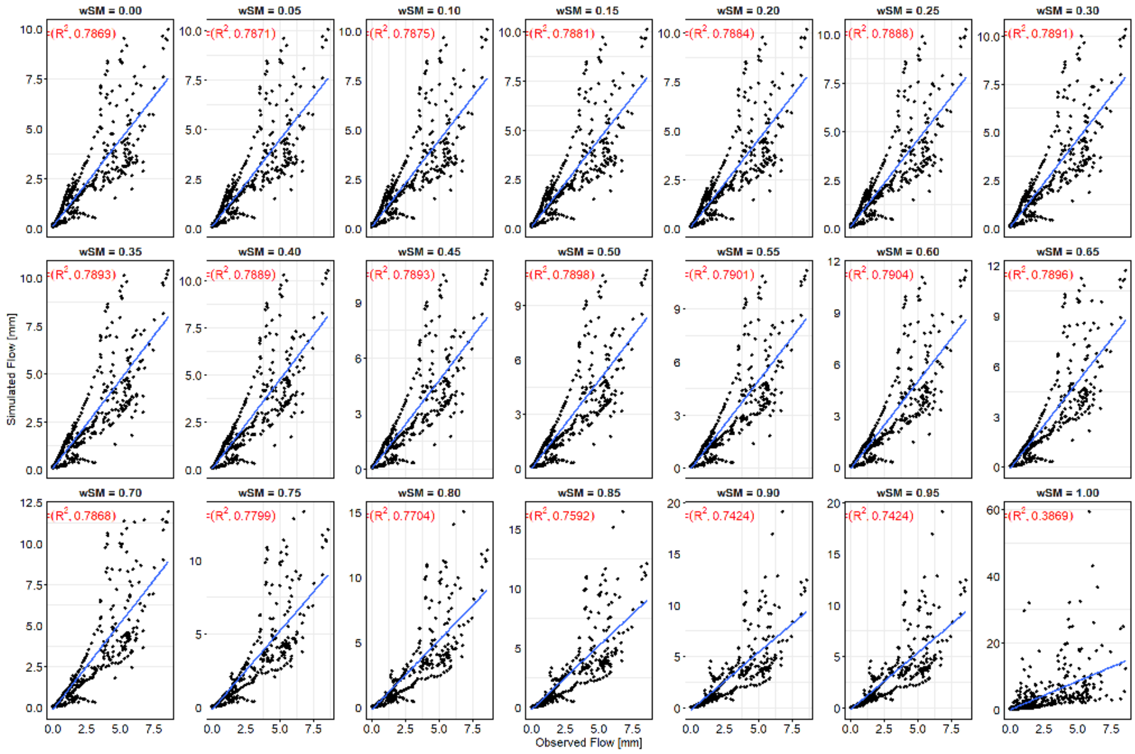

Figure 4.64. *Bafing à Sokotoro watershed validation observed and simulated discharges with wSM from 0 to 1 scatter plots*

Figure 4.65 plots depicted the variation in discharge across different weights on soil moisture (wSM) for each month, derived by subtracting the simulated discharges at other wSM values (Qsim_***) from the simulated discharge at wSN = 0.00 (Qsim_000). During all months of a year expect July, August and September, a clear decreasing trend was observed which indicated that the discharge was consistently lower when more weight was given to SM in the model. This may be attributed to the fact that during these months, as wSM increased, the model soil layer expanded, resulting in a greater capacity for the soil to retain water (high X1). As a result, surface flow decreased compared to wSM = 0.

Conversely, for July to September, which correspond to the rainy season, an increasing trend was evident. In these months, the differences grew larger as wSM increased, highlighting that more weight on SM led to higher discharges. This trend suggested that the soil was saturated in the rainy season and the overflow contributed significantly to the discharge in these months. For the validation period, the same trend was observable, making model calibration more accurate (Figure 4.66). However, for both calibration and validation periods, at wSM = 1.0, a sharp decrease was noticeable for each month indicating that excessive weighting (especially wSM = 1.0) on soil moisture adversely impacted discharge simulation accuracy.

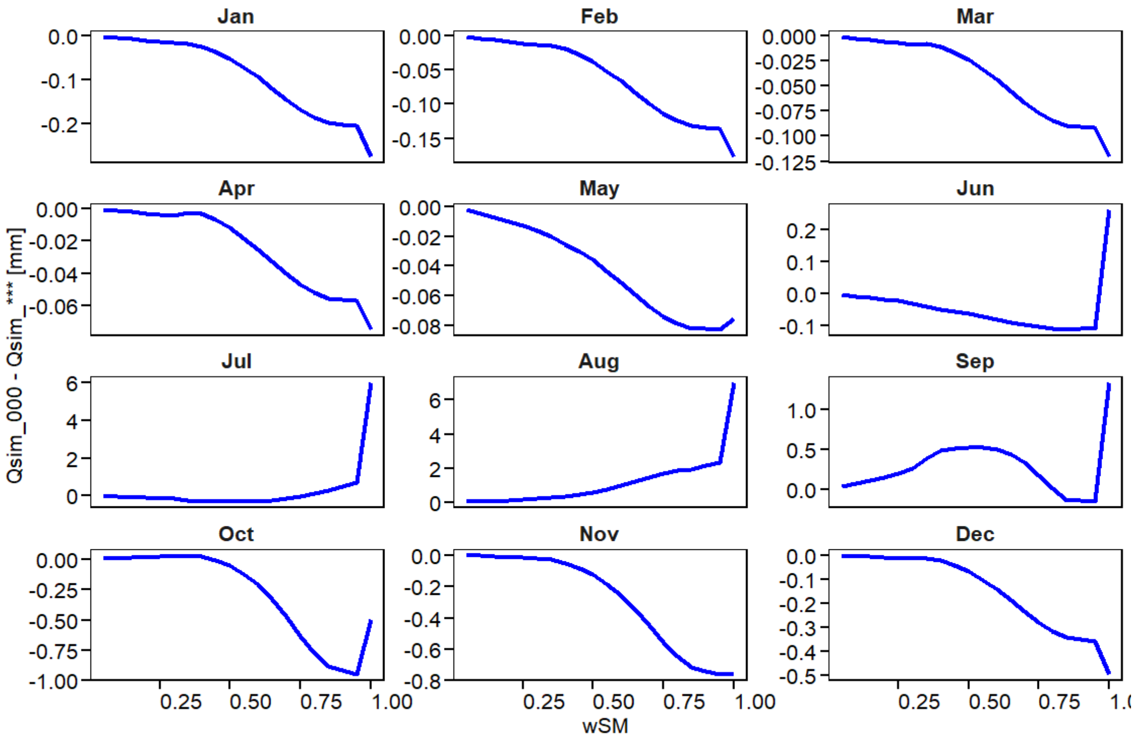

Figure 4.65. *Bafing à Sokotoro watershed calibration monthly discharge variation as wSM increased*

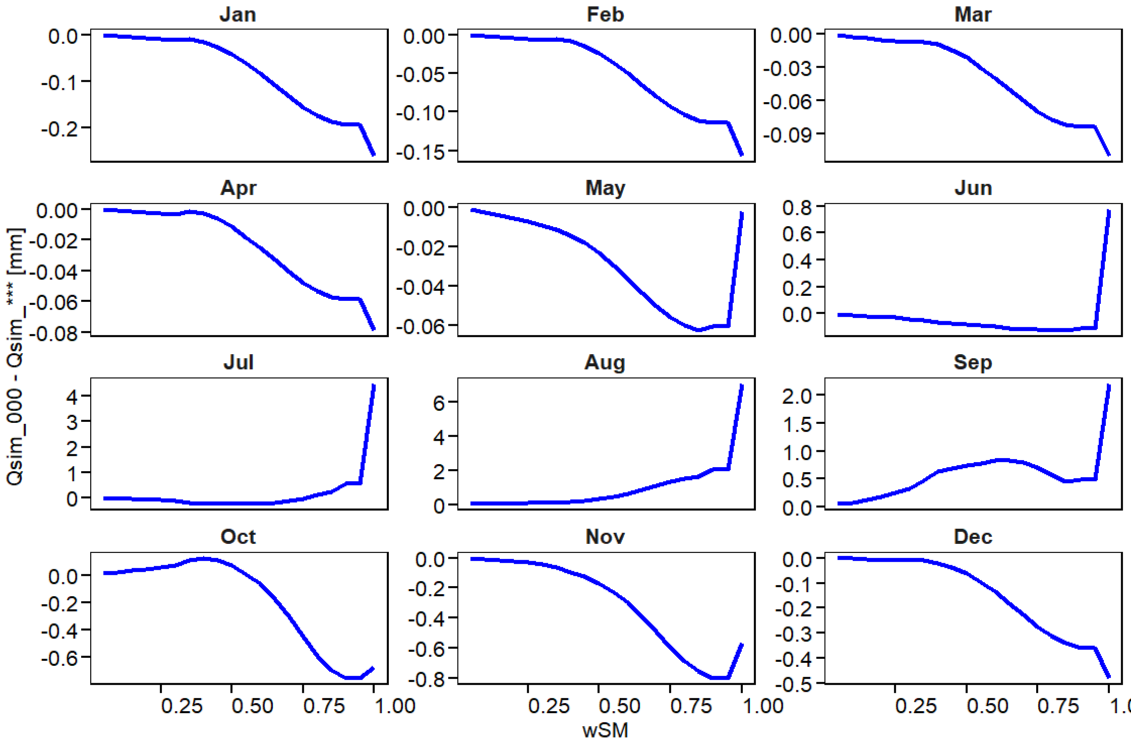

Figure 4.66. *Bafing à Sokotoro watershed validation monthly discharge variation as wSM increased*

Figure 4.67 shows the comparison between SMAP soil moisture data and the model's soil moisture (SM) simulations using different wSM values. The left graph represents the calibration period (04/01/2015 to 03/31/2017), while the right graph represents the validation period (04/01/2017 to 03/31/2019).

During the calibration period, the model's SM simulations aligned well with the SMAP data during the rainy season, particularly when the weighting on soil moisture (wSM) was increased. However, in the dry season, even with the highest weighting (wSM = 1.0), the model struggled to match the SMAP data and present soil state drier as wSM increased. The same patterns observed during calibration were consistent in the validation period. This consistency between the calibration and validation periods indicates the model's reliability in capturing soil moisture dynamics during wet conditions when calibrated with appropriate weights on soil moisture. However, the model's accuracy is compromised during the dry season. This suggests that the model's soil water content layer may not extend deep enough to fully capture the moisture dynamics of the root zone as represented by SMAP. Additionally, fluctuations in the model's soil water content layer to simulate discharge pattern may contribute to difficulties in simulating soil moisture patterns during dry season. These findings highlight the need to refine the model's soil moisture parameterization or include additional processes to better represent soil moisture dynamics throughout all seasons.

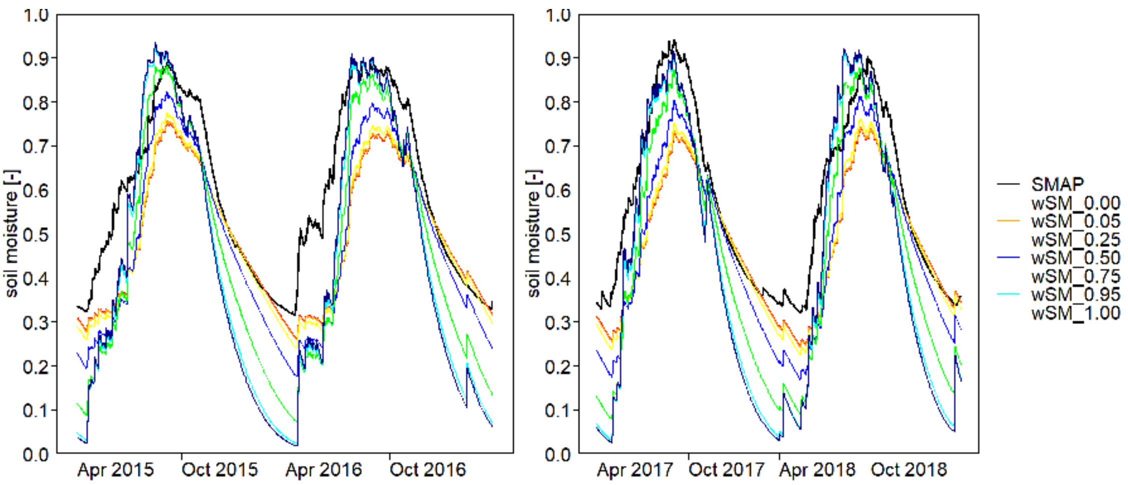

Figure 4.67. *Bafing à Sokotoro watershed soil moisture with varying wSM: left calibration and right validation*

Figures 4.68 and 4.69 show model soil moisture versus SMAP soil moisture scatter plots from weight 0 to 1 respectively for calibration and validation. When wSM was 1.00, the highest r^2 value of 0.9519 was observed for calibration and 0.9472 for validation, indicating a strong correlation between simulated and observed soil moisture when the model focused exclusively on soil water content without considering discharge. As wSM decreased, the r^2 values gradually decreased, showing that the model's ability to simulate soil water content diminished as less weight was placed on SM.

As it can be seen in Figure 4.67, like hydrograph, soil moisture has rising and falling limbs. It was remarked that the increase of wSM improved the falling limb than rising limb. The scatter plots of these two parts are presented in the appendix.

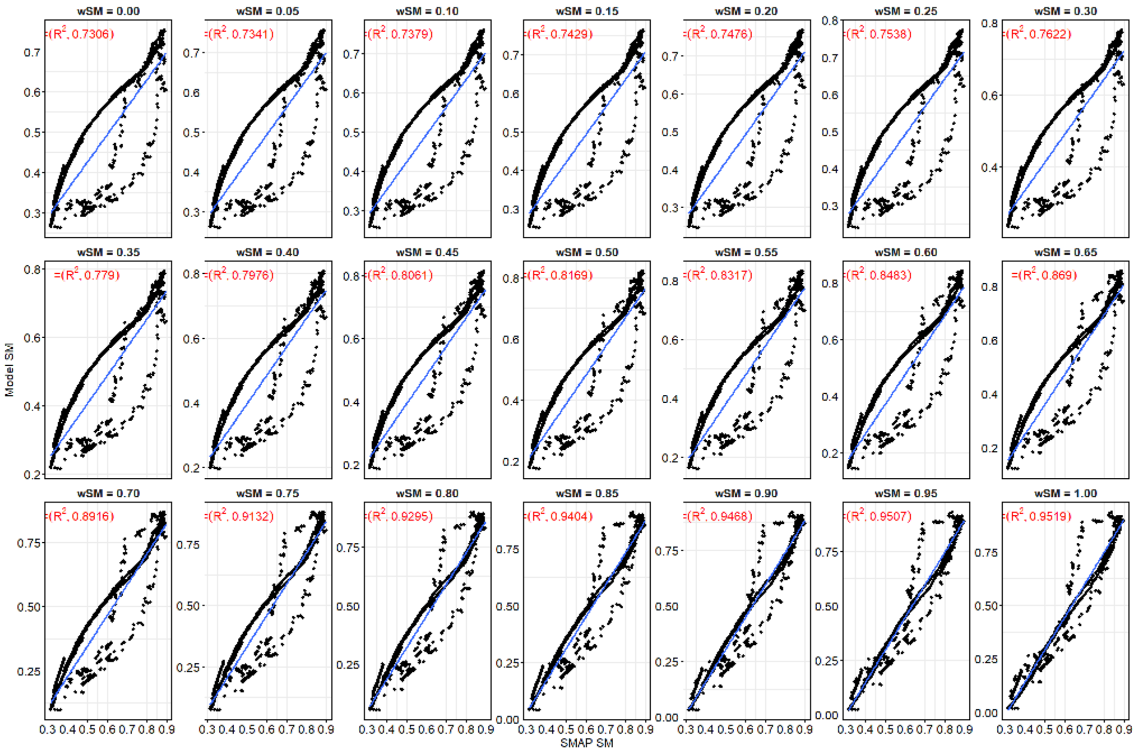

Figure 4.68. *Bafing à Sokotoro watershed calibration observed and simulated soil moisture with wSM from 0 to 1 scatter plots*

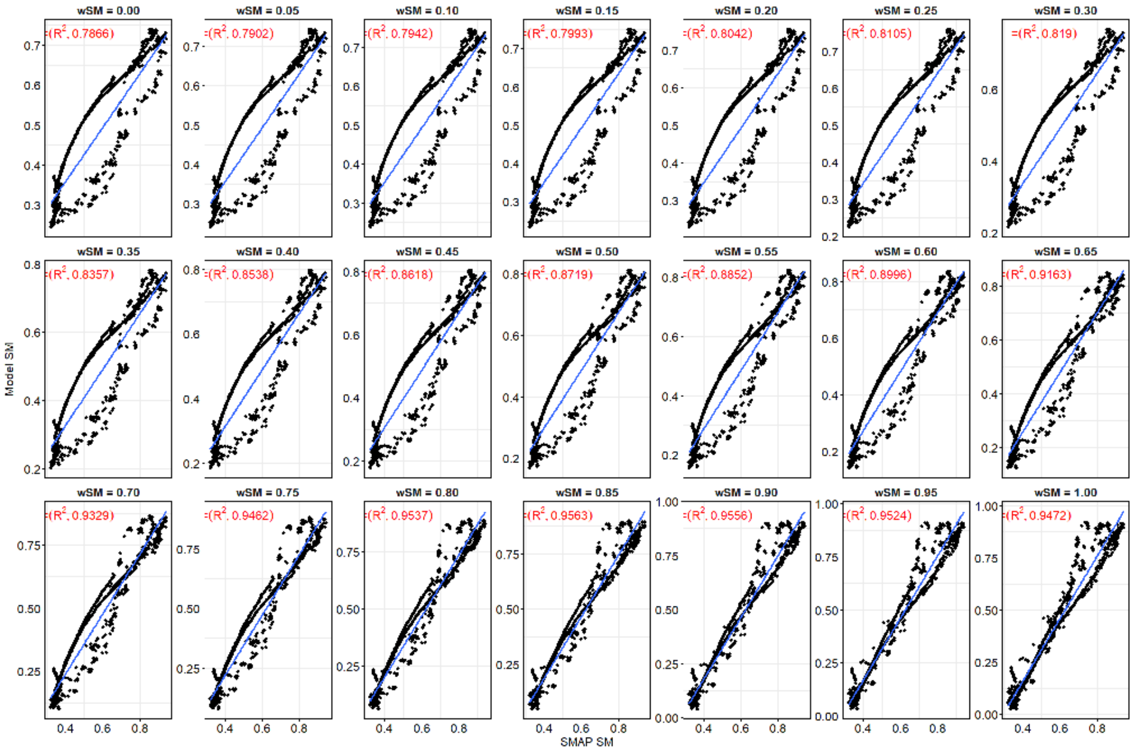

Figure 4.69. *Bafing à Sokotoro watershed validation observed and simulated soil moisture with wSM from 0 to 1 scatter plots*

5. CONCLUSION AND RECOMMANDATIONS

In this study, we analyzed two regions with different hydroclimatic conditions: Türkiye, characterized by a temperate climate where snowmelt significantly contributes to streamflow, and Guinea, characterized by a humid tropical climate with monsoon rains. Rainfall-runoff modeling was conducted at daily, monthly, and annual time steps using split-sample test method and single objective calibration. To explore the parameter space more effectively, at daily time step, three algorithms were used namely Calibration Michel (CM), DEoptim, and hydroPSO to optimize the objective function (KGE).

At the daily time step, the GR4J coupled with the CemaNeige snow module (Valéry et al. 2014b) was applied to the two Turkish watersheds, while the GR4J model was used for the three Guinean watersheds. Satisfactory results were achieved for both regions, evidenced by KGE values around 0.9. Additionally, the split-sample test method showed that the model's performance and parameters were consistent across each algorithm, indicating reliable results. Nonetheless, it was observed that the degree-day factor parameter of the snow module in the Turkish basins, particularly for Çukurkışla, assumed excessively high and physically unrealistic values.

At the monthly time step, the performance metrics of the GR2M model in the Turkish basins were not as satisfactory as those obtained for Guinea, where KGE values were approximately 0.9. Notably, the metrics for Kayabaşı were weaker compared to other basins, which was attributed to the impact of snow not being accounted for in the monthly GR2M model. The performance metrics for Çukurkışla and Kayabaşı could have been further improved if snow dynamics were included because a shift of one month between observed and modeled discharge was clearly detectable.

Regarding annual time step modeling with the GR1A model, satisfactory results were obtained for the Turkish watersheds. However, the results for the Guinean watersheds were generally less favorable. It was found that aggregating the results of GR4J or GR2M on an annual basis was more suitable for the Guinean basins, contrary to the conclusions drawn by Mouelhi et al. (2013).

Following this initial analysis, a multi-objective calibration was conducted to further refine the daily models by taking into account the hysteresis that exist between snow accumulation and melting phases in snowy basins and soil moisture in others. This multi-objective approach aimed to enhance the accuracy and robustness of the models by incorporating multiple hydrological variables, thereby providing a more comprehensive understanding of the water balance in these two regions.

For the Turkish basins, both discharge and MODIS snow cover data were used as calibration criteria. The results obtained from this multi-criteria optimization show that the CemaNeige with hysteresis parameters are more sensitive to weight variation than GR4J parameters which indicate robustness in the calibration process because a higher wSN means more magnitude on snow. As wSN increases, the discharge performance gradually decreased, showing that the model's ability to simulate flow diminished as more weight was placed on SCA. However, the decline in discharge performance is relatively modest when wSN is low and varies from one basin to another. Conversely, snow cover simulation improves significantly as more weight is given to SCA, resulting in a closer match between MODIS SCA and model's snow cover area. Furthermore, the impact of different wSN values on discharge varies by month. In winter, increasing weight leads to a decrease in discharge, indicating the dominant role of snow accumulation. Conversely, during spring, increasing wSN results in an increase in discharge, aligning with contributions of snowmelt.

On the other hand, the standard CemaNeige cannot accurately model snow cover dynamics without hysteresis. This is because its simulation in the accumulation phase is slower and faster in the melting phase due to the high degree-day factor value. Additionally, it barely fully covers the basin with snow during winter, which contradicts MODIS observations and slightly underestimates the snowpack compared to hysteresis simulations. Therefore, by considering hysteresis in the CemaNeige snow module, it is possible to accurately simulate snow cover dynamics without compromising discharge performance.

The calibration criteria for the Guinean basins were chosen to be discharge and soil moisture, as soil moisture plays a crucial role in the hydrological processes of the humid tropical climate. The key findings indicate that the model's simulations of soil moisture closely matched the SMAP data during the rainy season, especially when the weighting on soil moisture was increased. However, in the dry season, the model faced challenges in accurately reproducing the SMAP soil moisture data, even with a strong emphasis on soil moisture. This suggests that the model's soil water content layer may not extend deep enough during the dry season to fully capture the moisture dynamics of the root zone as represented by SMAP. Furthermore, fluctuations in the model's soil water content layer, used to simulate discharge patterns, may contribute to difficulties in accurately representing soil moisture patterns during the dry season. These findings emphasize the need to refine the model's soil moisture parameterization or incorporate additional processes to better represent soil moisture dynamics throughout all seasons.

The parameters of the model vary with wSM, and their variation depends on basins. X1 and X2, which relate to the production function, are correlated, as are X3 and X4, which relate to the transfer function. However, the first two parameters are inversely correlated with the last two. When the first two parameters increase, the model simulates a slight increase in SM during the dry season. Conversely, if they decrease, the dry season becomes even drier as wSM increases. On the other hand, when priority is given to soil moisture, discharge performance decreases while soil water content improves. This trend suggests that while the model can balance the objectives of discharge and SM to some extent, prioritizing SM too heavily leads to a less accurate representation of the flow. Additionally, as wSM increases, the falling limb of simulated SM is more correlated to SMAP SM than the rising limb. Furthermore, the impact of different wSM values on discharge varies by month. Generally, the months that correspond to the end of the rainy season show an increasing trend as wSM increases, while others show a decreasing trend.

Overall, the use of remote sensing data in hydrological modeling plays a crucial role in enhancing our understanding and management of hydrological processes. However, when applying multi calibration approach in hydrological modeling, it is essential to consider discharge and balance the weights assigned to snow (wSN) and soil moisture (wSM). Based on the observed performance of the model, it is recommended that these weights should not exceed 0.5. Assigning excessively high weights to wSN and wSM can cause the model to prioritize snow and soil moisture simulations at the expense of discharge accuracy, potentially leading to simulation failures. Thus, maintaining weights below this threshold ensures more stable and reliable discharge simulations.

In snow-dominant basins, it is recommended to consider the impact of snow in the GR2M model in order to more accurately simulate discharge. Furthermore, when performing multi-criteria calibration using both discharge and soil moisture, it is vital to accurately define the soil water content layer to represent soil moisture patterns throughout all seasons.

Future studies should explore integrating snow cover data and soil moisture data alongside discharge to enhance the accuracy and reliability of hydrological models.

Utilizing a broader range of soil moisture data, including surface soil moisture and other satellite-based products, will provide a more comprehensive understanding of soil moisture dynamics and their impact on hydrological processes. Additionally, applying this approach to different study areas will help verify the robustness and generalizability of the model, ensuring its effectiveness under different hydroclimatic conditions. This will improve model performance and offer valuable insights for water resource management in diverse environments.

REFERENCES

Adeyeri, O. E., Laux, P., Arnault, J., Lawin, A. E., & Kunstmann, H. (2020). Conceptual hydrological model calibration using multi-objective optimization techniques over the transboundary Komadugu-Yobe basin, Lake Chad Area, West Africa. *Journal of Hydrology: Regional Studies, 27*, 100655. doi:10.1016/j.ejrh.2019.100655

AGUE, A. I. (2014). Etude comparative d'un modèle conceptuel global (GR4J) et d'un modèle semi-distribué (GeoSFM) sur le bassin versant de l'Ouémé à Save (Bénin, Afrique de l'Ouest). *Revue Scientifique Technique*.

Andersson, J. C., Arheimer, B., Traoré, F., Gustafsson, D., & Ali, A. (2017). Process refinements improve a hydrological model concept applied to the Niger River basin. *Hydrol. Process., 31*, 4540–4554. doi:10.1002/hyp.11376

Andrade, J. M., Neto, A. R., Nobrega, R. L., Rico-Ramirez, M. A., & Montenegro, S. M. (2024). Efficiency of global precipitation datasets in tropical and subtropical catchments revealed by large sampling hydrological modelling. *Journal of Hydrology, 633*, 131016. doi:10.1016/j.jhydrol.2024.131016

Ardia, D., & Mullen, K. (2010). DEoptim: Differential Evolution Optimization in R. R package version 2.0-4. Retrieved from http://CRAN.R-project.org/package=DEoptim

Arnold, J. G., Srinivasan, R., Muttiah, R. S., & Williams, J. R. (1998). Large area hydrologic modeling and assessment part I: Model development. *Journal of the American Water Resources Association, 34(1)*, 73-89.

Bajracharya, A. R., Ahmed, M. I., & Stadnyk, T. (2023). Process based calibration of a continental-scale hydrological model using soil moisture and streamflow data. *Journal of Hydrology: Regional Studies, 47*, 101391. doi:10.1016/j.ejrh.2023.101391

Beven, K. J., & Kirkby, M. J. (1979). A physically based, variable contributing area model of basin hydrology. *Hydrological Sciences Bulletin, 24(1)*, 43-69.

Bodian, A., Dezetter, A., & Dacosta, H. (2012). Apport de la modélisation pluie-débit pour la connaissance de la ressource en eau : Application au haut bassin du fleuve Sénégal. *Climatologie, 9*, 109-125.

Bouanani, R., Hamed, K. B., & Bouanani, A. (2012). Utilisation d'un modèle global pour la modélisation pluie-débit : cas du bassin d'Oued Sikkak. *Nature & Technologie*.

Coron, L., Delaigue, O., Thirel, G., Dorchies, D., Perrin, C., & Michel, C. (2023). airGR: Suite of GR Hydrological Models for Precipitation-Runoff Modelling. Manual of the R package version 1.7.6. *HAL Open Science*, 102p. doi:10.15454/EX11NA

Coron, L., Thirel, G., Delaigue, O., Perrin, C., & V., A. (2017). The Suite of Lumped GR Hydrological Models in an R package. *Environ. Model. Softw.*, 166–171. Retrieved from https://doi.org/10.1016/j.envsoft.2017.05.002

Delaigue, O., Brigode, P., Thirel, G., & Coron, L. (2023). airGRteaching: an open-source tool for teaching hydrological modeling with R. *Hydrol. Earth Syst. Sci., 27*, 3293–3327. doi:10.5194/hess-27-3293-2023

Duethmann, D., Peters, J., Blume, T., Vorogushyn, S., & Guntner, A. (2014). The value of satellite-derived snow cover images for calibrating a hydrological model in snow-dominated catchments in Central Asia. *Water Resour., 50*, 2002–2021. doi:10.1002/2013WR014382

Edijatno. (1991). Mise au point d'un modèle élémentaire pluie-débit au pas de temps journalier. *PhD. Université Louis Pasteur/ENGEES*, 242 pp.

Edijatno, & Michel, C. (1989). Un modèle pluie-débit journalier à trois paramètres. *La Houille Blanche*, 113-121.

Eini, M. R., Massari, C., & Piniewski, M. (2023). Satellite-based soil moisture enhances the reliability of agro-hydrological modeling in large transboundary river basins. *Science of the Total Environment, 873*, 162396. doi:10.1016/j.scitotenv.2023.162396

Eylen, A. (2024). Kar ve toprak nemi uydu görüntüleri kullanarak çok kriterli hidrolojik modelleme. *MSc Thesis ESTÜ*, 223pp.

Feldman, A. D. (2000). *Hydrologic Modeling System HEC-HMS: Technical Reference Manual.* US Army Corps of Engineers, Hydrologic Engineering Center.

Gosset, C. (2014). Quel apport des données satellite d'enneigement pour le calage d'un modèle hydrologique sur des bassins de montagne ? *Science de la Terre et de l'Univers HHS*, 55 pp.

Gupta, H., Kling, H., Yilmaz, K., & Martinez, G. (2009). Decomposition of the mean squared error and NSE performance criteria: Implications for improving hydrological modelling. *Journal of hydrology, 377(1-2)*, 80-91. doi:10.1016/j.jhydrol.2009.08.003

Harlan, D., Wangsadipura, M., & Munajat, C. M. (2010). Rainfall-Runoff Modeling of Citarum Hulu River Basin by Using GR4J. *World Congress on Engineering.* London, U.K.

Kabouya, M. (1990). Modélisation pluie-débit aux pas de temps mensuel et annuel en Algérie septentrionale. Thèse de Doctorat. *Université Paris Sud Orsay*, 347pp.

Kabouya, M., & Michel, C. (1991). Estimation des ressources en eau superficielle aux pas de temps mensuel et annuel, application à un pays semi-aride. *Revue des Sciences de l'Eau*, 569-587.

Karaosmanoglu, F. (2021). Determination of ecological conditions and geographical distribution of vegetation in the Goksu basin. *International Journal of Multidisciplinary Research and Growth Evaluation, 2*, 51-61. doi:10.54669/anfo.2021.3.1.5

Karcı, A. (2017). Differential Evolution Algorithm and Its Variants. *Anatolian Journal of Computer Sciences, 2*, 10-14.

Keller, E. A., & Pinter, N. (1996). *Active Tectonics, Earthquake Uplift and Landscape, Upper Saddle River* (2nd ed.). Prentice Hall.

Kennedy, J., & Eberhart, R. (1995). Particle Swarm Optimization. Proceedings of the IEEE . *International Conference on Neural Networks, 4*, 1942-1948. doi:10.1109/ICNN.1995.488968

Kim, S., Lee, J., Jeon, S., Lee, M., An, H., Jung, K., . . . Park, D. (2021). Correlation Analysis between Hydrologic Flow Metrics and Benthic Macroinvertebrates Index (BMI) in the Han River Basin, South KoreaMacroinvertebrates Index (BMI) in the Han River Basin, South Korea. *Sustainability, 13*, 11477. doi:10.3390/su132011477

Klemeš, V. (1986). Operational testing of hydrological simulation models. *Hydrol. Sci. J., 1*, 13-24.

Kling, H., Fuchs, M., & Paulin, M. (2012). Runoff conditions in the upper Danube basin under an ensemble of climate change scenarios. *Journal of Hydrology, 424-425*, 264-277. doi:10.1016/j.jhydrol.2012.01.011

Koster, R. D., Liu, Q., Mahanama, S. P., & Reichle, R. H. (2018). Improved Hydrological Simulation Using SMAP Data: Relative Impacts of Model Calibration and Data Assimilation. *Journal of Hydrometeorology*, 44. doi:10.1175/JHM-D-17-0228.1

Kubáň, M., Parajka, J., Tong, R., Greimeister-Pfeil, I., Vreugdenhil, M., Szolgay, J., . . . Brziak, A. (2022). The effects of satellite soil moisture data on the parametrization of topsoil and root zone soil moisture in a conceptual hydrological model. *Journal of Hydrology and Hydromechanics, 70, 3*, 295–307.

Le Moine, N., Andréassian, V., Perrin, C., & Michel, C. (2007). How can rainfall-runoff models handle intercatchment groundwater flow? Theoretical study based on 1040 French catchments. *Water Resour. Res., 43*, W06428. doi:10.1029/2006WR005608

Legates, D. R., & McCabe, G. J. (1999). Evaluating the use of "goodness-of-fit" measures in hydrologic and hydroclimatic model validation. *Water Resources Res.*, 233-241.

Li, Y., Grimaldi, S., Pauwels, V. R., & Walker, J. P. (2018). Hydrologic model calibration using remotely sensed soil moisture and discharge measurements: The impact on predictions at gauged and ungauged locations. *Journal of Hydrology*, 557, 897-909. doi:10.1016/j.jhydrol.2018.01.013

Liu, E., Zhu, Y., Calvet, J.-C., Lü, H., Bonan, B., Zheng, J., . . . Chen, T. (2024). Evaluation of root zone soil moistureproducts over the Huai River basin. *Hydrology and Earth System Sciences, 28*, 2375-2400. doi:10.5194/hess-28-2375-2024

Magand, C. (2014). Influence de la représentation des processus nivaux sur l'hydrologie de la Durance et sa réponse au changement climatique. *Hydrologie. Université Pierre et Marie Curie - Paris VI*, 333pp.

Magand, C. D. (2014). Introducing hysteresis in snow depletion curves to improve the water budget of a land surface model in an Alpine Catchment. *J. Hydrometeorol.*, 631-649.

Maidment, D. R. (1993). *Handbook of Hydrology.* McGraw-Hill.

Makhlouf, Z. (1994). Compléments sur le modèle pluie-débit GR4J et essai d'estimation de ses paramètres. *PhD thesis, University Paris XI Orsay*, 426pp.

Makhlouf, Z., & Michel, C. (1994). A two-parameter monthly water balance model for French watersheds. *Journal of Hydrology, 162*, 299-318.

Mathevet, T. (2005). Quels modèles pluie-débit globaux pour le pas de temps horaire ? Développement empirique et comparaison de modèles sur un large échantillon de bassins versants. *Thèse de Doctorat, ENGREF (Paris), Cemagref (Antony), France*, 463pp.

Michel, C. (1983). Que peut-on faire en hydrologie avec un modèle conceptuel à un seul paramètre ? *La Houille Blanche*, 39-44.

Moriasi, D. N., Arnold, J. G., Van Liew, M. W., Bingner, R. L., Harmel, R. D., & Veith, T. L. (2007). Model Evaluation Guidelines For Systematic Quantification Of Accuracy In Watershed. *American Society of Agricultural and Biological Engineers*, 885−900.

Morid, S., Gosain, A. K., & Keshari, A. K. (2000). An algorithm for monitoring snow water equivalent in ungauged catchments. *International Conference of Integreted Water Resource Management.*

Mouelhi, S. (2003). Vers une chaîne cohérente de modèles pluie-débit conceptuels globaux aux pas de temps pluriannuel, annuel, mensuel et journalier. *Thèse de Doctorat, ENGREF, Cemagref Antony, France*, 323 pp.

Mouelhi, S., Madani, K., & Lebdi, F. (2013). A Structural Overview through GR(s) Models Characteristics for Better Yearly Runoff Simulation. *Open Journal of Modern Hydrology*, 179-187. doi:10.4236/ojmh.2013.34022

Mouelhi, S., Michel, C., Perrin, C., & Andréassian, V. (2006b). Stepwise development of a two-parameter monthly water balance model. *Journal of Hydrology, 318(1-4)*, 200-214. doi:10.1016/j.jhydrol.2005.06.014

Mouelhi, S., Michel, C., Perrin, C., & mAndreassian, V. (2006a). Linking stream flow to rainfall at the annual time step: the Manabe bucket model revisited. *Journal of Hydrology, 328*, 283-296. doi:10.1016/j.jhydrol.2005.12.022

Mullen, K. M., Ardia, D., Gil, D. L., Windover, D., & Cline, J. (2011). DEoptim: An R Package for Global Optimization by Differential Evolution. *Journal of Statistical Software, 40*, Issue 6. doi:10.18637/jss.v040.i06

Nan, Y., & Tian, F. (2024). Isotope data-constrained hydrological model improves soil moisture simulation and runoff source apportionment. *Journal of Hydrology*, (633) 131006. doi:10.1016/j.jhydrol.2024.131006

Nash, J., & Sutcliffe, J. (1970). River flow forecasting through conceptual models – Part I: A discussion of principles. *J. Hydrol.*, 282-290.

Nemri, S., & Kinnard, C. (2020). Comparing calibration strategies of a conceptual snow hydrology model and their impact on model performance and parameter identifiabilityhydrology model and their impact on model performance and parameter identifiability. *Journal of hydrology, 582*, 124474. doi:10.1016/j.jhydrol.2019.124474

Nonguierma, A., & Niang, A. (2006). *Etude cartographique de la partie guinéenne du bassin du fleuve Sénégal. Identification des besoins cartographiques et élaboration des TDR pour la cartographie et l'interprétation.* Dakar: OMVS.

Parajka, J., & Blöschl, G. (2008). The value of MODIS snow cover data in validating and calibrating conceptual hydrologic models. *Journal of Hydrology*, 358, 240– 258. doi:10.1016/j.jhydrol.2008.06.006

Parajka, J., Naeimi, V., Blöschl, G., & Komma, J. (2009). Matching ERS scatterometer based soil moisture patterns with simulations of a conceptual dual layer hydrologic model over Austria. *Hydrology and Earth System Sciences, 13(2)*, 259-271. doi:10.5194/hess-13-

Peker, İ., & Şorman, A. A. (2021). Application of SWAT using snow data and detecting climate change impacts in the mountainous eastern regions of Turkey. *Water, 13(14)*, 1982. doi:10.3390/w13141982

Perrin, C. (2000). Vers une amélioration d'un modèle global pluie-débit au travers d'une approche comparative. *Thèse de Doctorat, INPG (Grenoble) / Cemagref (Antony)*, 530pp.

Perrin, C., Michel, C., & Andréassian, V. (2003). Improvement of a parsimonious model for streamflow simulation. *Journal of Hydrology*, 275-289.

Perrin, C., Michel, C., & Andréassian, V. (2007). Modèles hydrologiques du Génie Rural (GR). *rap. CEMAGREF*, 1-16. Retrieved from http://www.cemagref.fr/webgr

Perrin, C., Michel, C., & Andréassian, V. (2010). A Set of Hydrological Models. In J.-M. Tanguy, *Mathematical Models, Volume 2* (pp. 493-509). Wiley. doi:10.1002/9781118557853.ch16

Ponce, V. M., & Hawkins, R. H. (1996). Runoff curve number: Has it reached maturity? *Journal of Hydrologic Engineering, 1(1)*, 1-19.

Rajib, M. A., Merwade, V., & Yu, Z. (2016). Multi-objective calibration of a hydrologic model using spatially distributed remotely sensed/in-situ soil moisture. *Journal of Hydrology, 536*, 192-207. doi:10.1016/j.jhydrol.2016.02.037

Rezaie, H., Jabbari, A., Behmanesh, J., Jarihani, B., & Hessari, B. (2014). Evaluation of SURM and GR4J rainfall runoff models, for the Nazloo River catchment in northwest of Iran. *World Journal of Environmental Biosciences*.

Riboust, P. (2018). De la neige au débit : de l'intérêt d'une meilleure contrainte et représentation de la neige dans les modèles. *Hydrologie. Sorbonne Université*, 323P.

Riboust, P., Thirel, G., Le Moine, N., & Ribstein, P. (2019). Revisiting a simple degree-day model for integrating satellite data: implementation of SWE-SCA hystereses. *J. Hydrol. Hydromech*, 70–81. Retrieved from https://doi.org/10.2478/johh-2018-0004

Ruelland, D. (2023). Development of the snow- and ice-accounting routine (SIAR). *Journal of Hydrology, 624*, 129867. doi:10.1016/j.jhydrol.2023.129867

Ruelland, D. (2024). Potential of snow data to improve the consistency and robustness of a semi-distributed hydrological model using the SAFRAN input dataset. *Journal of Hydrology, 631*, 130820. doi:10.1016/j.jhydrol.2024.130820

Schönfelder, L. H., Bakken, T. H., Alfredsen, K., & Adera, A. G. (2017). *Application of HYPE in Norway: Assessment of the hydrological model HYPE as a tool to support the implementation of EU Water Framework Directive in Norway.* SINTEF.

Simonneaux, V., Hanich, L., Boulet, G., & Thomas, S. (n.d.). Modelling runoff in the Rheraya Catchment (High Atlas, Morocco) using the simple daily model GR4J. Trends over the last decades.

Singh, V. P. (1995). *Computer Models of Watershed Hydrology.* Water Resources Publications.

Sleziak, P., Holko, L., Danko, M., & Parajka, J. (2020). Uncertainty in the number of calibration repetitions of a hydrologic model in varying climatic conditions. *Water, 12(9)*, 2362. doi:10.3390/w12092362

Şorman, A. A., Uysal, G., & Şensoy, A. (2019). Probabilistic Snow Cover and Ensemble Streamflow Estimations in the Upper Euphrates Basin. *Journal of hydrology and hydromechanics, 67*, 82–92. doi:10.2478/johh-2018-0025

Storn, R., & Price, K. (1995). Heuristic for global optimization over continuous spaces. *Journal of Global Optimization*, 341-359.

Taia, S., Erraioui, L., Arjdal, Y., Chao, J., El Mansouri, B., & Scozzari, A. (2023). TheApplication of SWAT Model and Remotely Sensed Products to Characterize the Dynamic of Streamflow and Snow in a Mountainous Watershed in the High Atlas. *Sensors, 23*, 1246. doi:10.3390/s23031246

Thirel, G., Salamon, P., Burek, P., & Kalas, M. (2013). Assimilation of MODIS Snow Cover Area Data in a Distributed Hydrological Model Using the Particle Filter. *Remote Sensing, 5*, 5825-5850. doi:10.3390/rs5115825

Thornton, J. M., Brauchli, T., Mariethoz, G., & Brunner, P. (2021). Efficient multi-objective calibration and uncertainty analysis of distributed snow simulations in rugged alpine terrain. *Journal of hydrology, 598*, 126241. doi:10.1016/j.jhydrol.2021.126241

Tong, R., Parajka, J., Széles, B., Greimeister-Pfeil, I., Vreugdenhil, M., Komma, J., . . . Blöschl, G. (2022). The value of satellite soil moisture and snow cover data for the transfer of hydrological model parameters to ungauged sites. *Hydrology and Earth System Sciences, 26*, 1779–1799. doi: 10.5194/hess-26-1779-2022

Traoré, V. B., Sambou, S., Tamba, S., Fall, S., Diaw, A. T., & Cissé, M. T. (2014). Calibrating the rainfall-runoff model GR4J and GR2M on the Koulountou river basin, a tributary of the Gambia river. *American Journal of Environmental Protection*, 36-44. doi:10.11648/j.ajep.20140301.15

Troin, M., Arsenault, R., & Brissette, F. (2015). Performance and Uncertainty Evaluation of Snow Models on Snowmelt Flow Simulations over a Nordic Catchment (Mistassibi, Canada). *Hydrology*, 2, 289-317. doi:10.3390/hydrology2040289

Turcotte, R., Fortin, L. G., Fortin, V., Fortin, J. P., & Villeneuve, J. P. (2007). Operational analysis of the spatial distribution and the temporal evolution of the snowpack water equivalent in southern Québec, Canada. *Nordic Hydrol., 38(3),* , 211–234.

UN-Water. (2021). *Summary Progress Update 2021: SDG 6 - water and sanitation for all.* UN Water.

USACE. (1956). *Annual report of the Chief of Engineers, U.S. Army on Civil Works activities.* U.S. Government Printing Office.

Uysal, G., Dogan, Y. O., Civelek, H. S., Sorman, A. A., & Sensoy, A. (2024). Analyzing the Effects of Climate Change for the Water Tower of Mesopotamia, Türkiye. *Proc. IAHS, 385*, 465–470. doi:10.5194/piahs-385-465-2024

Valéry, A. (2010). Modélisation précipitations - débit sous influence nivale - élaboration d'un module neige et évaluation sur 380 bassins versants. *PhD Agro Paris Tech*, 405 pp.

Valéry, A., Andréassian, V., & Perrin, C. (2014a). "As simple as possible but not simpler" What is useful in a temperature-based snow-accounting routine? Part 1 – Comparison of six snow accounting routines on 380 catchments. *Journal of Hydrology, 517*, 1166-1175. doi:10.1016/j.jhydrol.2014.04.059

Valéry, A., Andréassian, V., & Perrin, C. (2014b). As simple as possible but not simpler: What is useful in a temperature-based snow-accounting routine? Part 2 – Sensitivity analysis of the Cemaneige snow accounting routine on 380 catchments. *J. Hydrol*, 517, 1176–1187. doi:10.1016/j.jhydrol.2014.04.058

Vaze, J., Chiew, F. H., Perraud, J. M., Viney, N., Post, D., & Teng, J. (2011). Rainfall-runoff modelling across southeast Australia: Datasets, models and results. *Australian Journal of Water Resources*, 101-116.

WMO. (1986). *Annual Report of the World Meteorological Organization 1986.* Geneva: WMO.

WMO. (2021). *World Meteorological Organization (WMO): The State of Climate Services 2021: Water.* WMO.

Xiong, L., & Zeng, L. (2019). Impacts of introducing remote sensing soil moisture in calibrating a distributed hydrological model for streamflow simulation. *Water, 11(4)*, 666. doi:10.3390/w11040666

Yi, L., Zhang, W., & Li, X. (2018). Assessing Hydrological Modelling Driven by Different Precipitation Datasets via the SMAP Soil Moisture Product and Gauged Streamflow Data. *Remote Sensing, 10*, 1872. doi:10.3390/rs10121872

Zambrano-Bigiarini, Z., & Rojas, R. (2013). A model-independent Particle Swarm Optimisation software for model calibration. *Environmental Modelling & Software, 43*, 5-25. doi:10.1016/j.envsoft.2013.01.004

APPENDIX

A-I: Türkiye basins

- **Çukurkışla watershed**

GR4J coupled with CemaNeige using hysteresis on Çukurkışla hydrograph, snowpack and snow cover area for some weight (wSN) and standard CemaNeige SWE and SCA: calibration on left and validation on right. Read SCA_std: standard CemaNeige without hysteresis

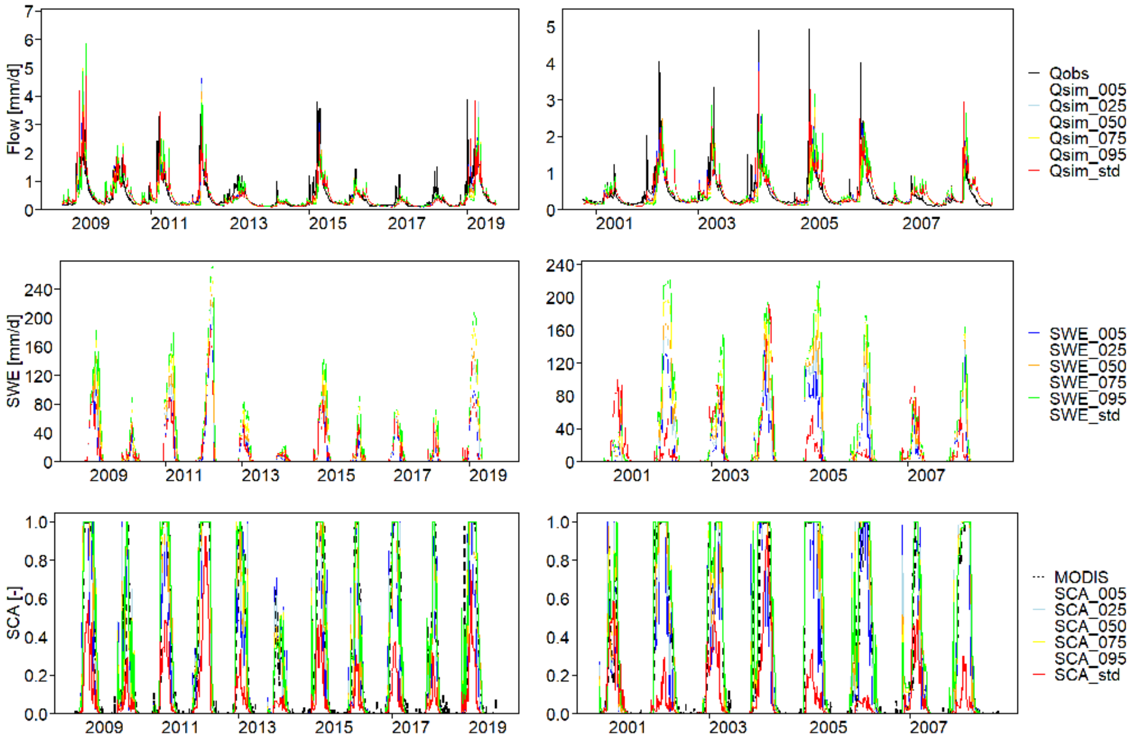

- **Kayabaşı watershed**

GR4J coupled with CemaNeige using hysteresis on Kayabaşı hydrograph, snowpack and snow cover area for some weight (wSN) and standard CemaNeige SWE and SCA: calibration on left and validation on right. Read SCA_std: standard CemaNeige without hysteresis

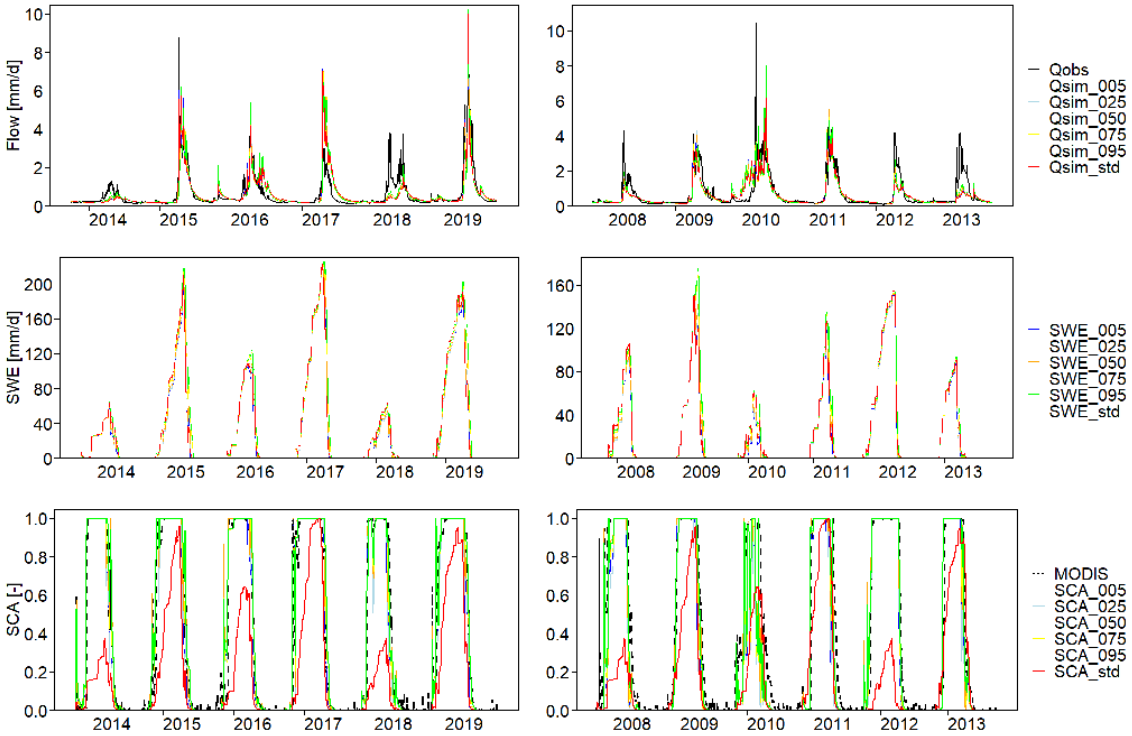

A-II: Guinean basins

- **Niger à Kouroussa watershed**

SMAP observed SM and GR4J simulated SM with wSM from 0 to 1 scatter plots

- Rising limb for calibration period

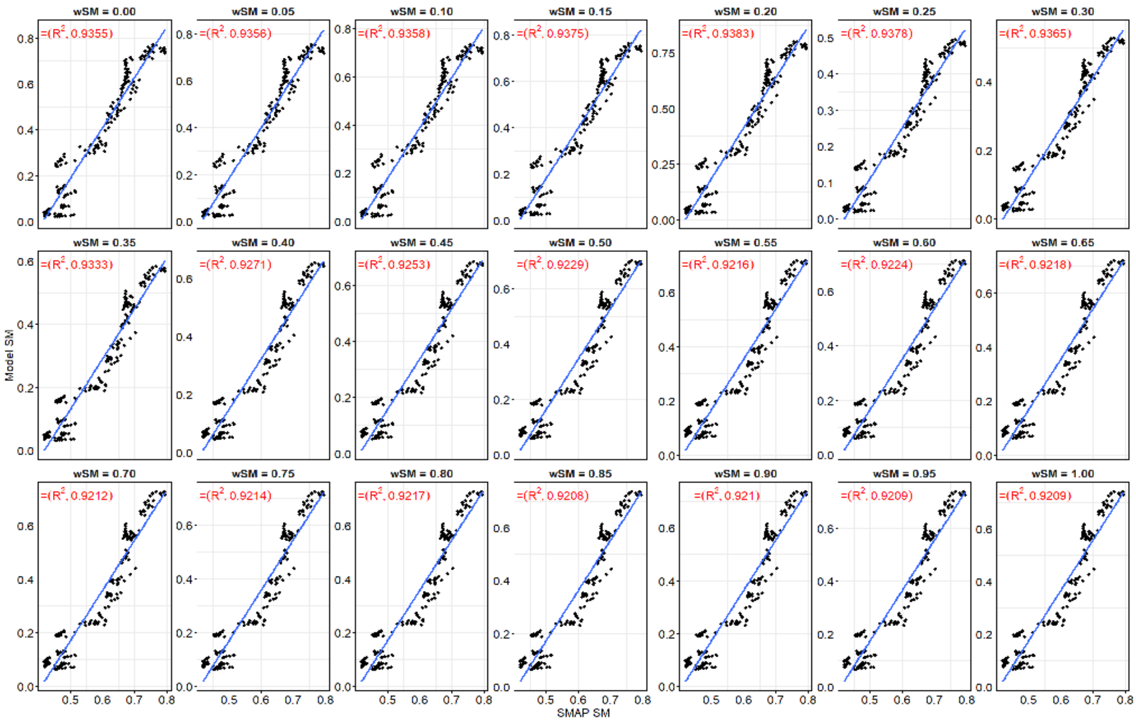

- Falling limb for calibration period

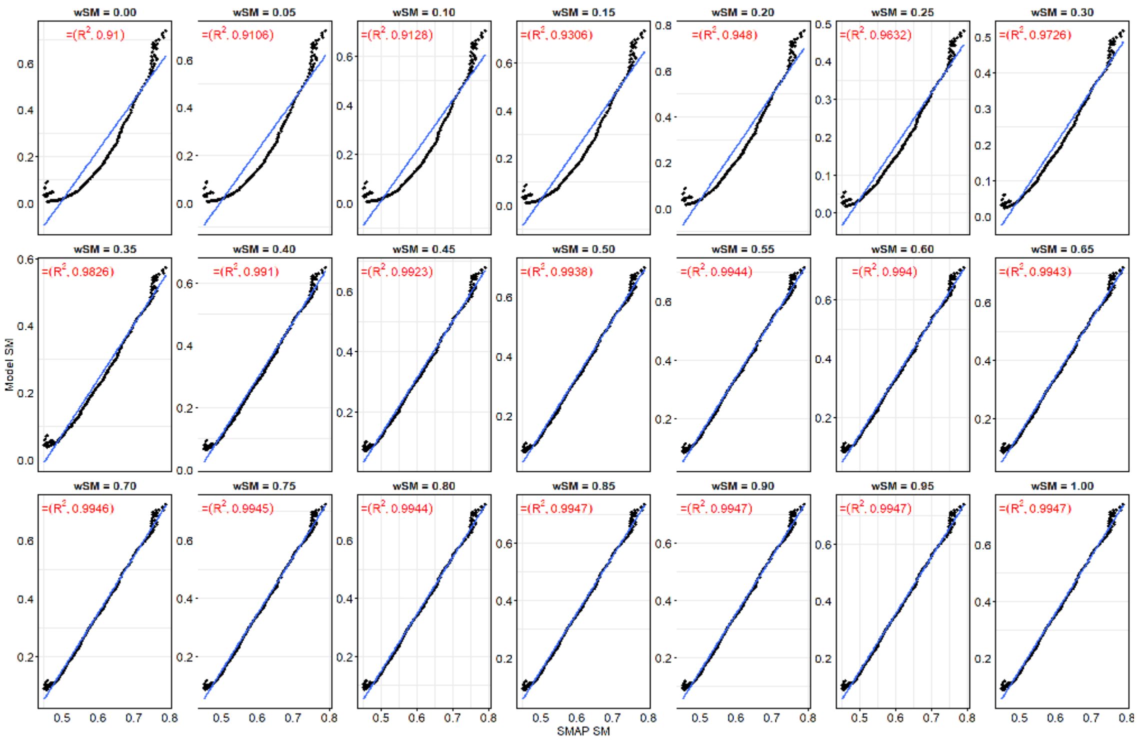

- Rising limb for validation period

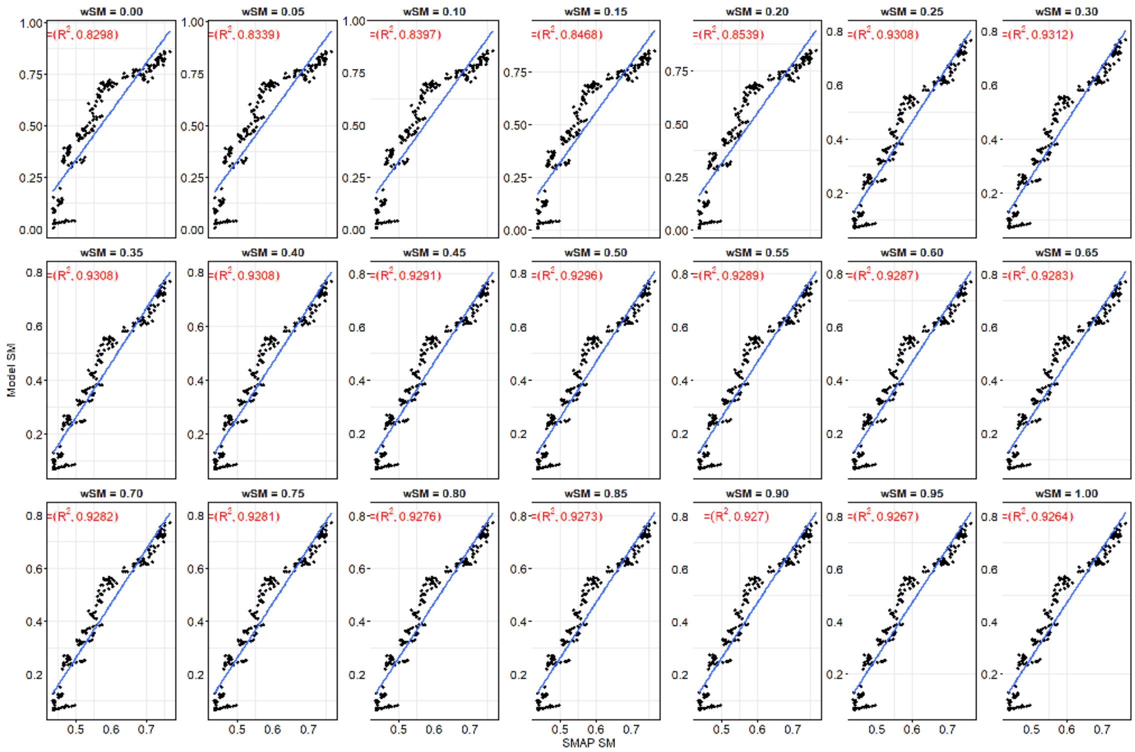

- Falling limb for validation period

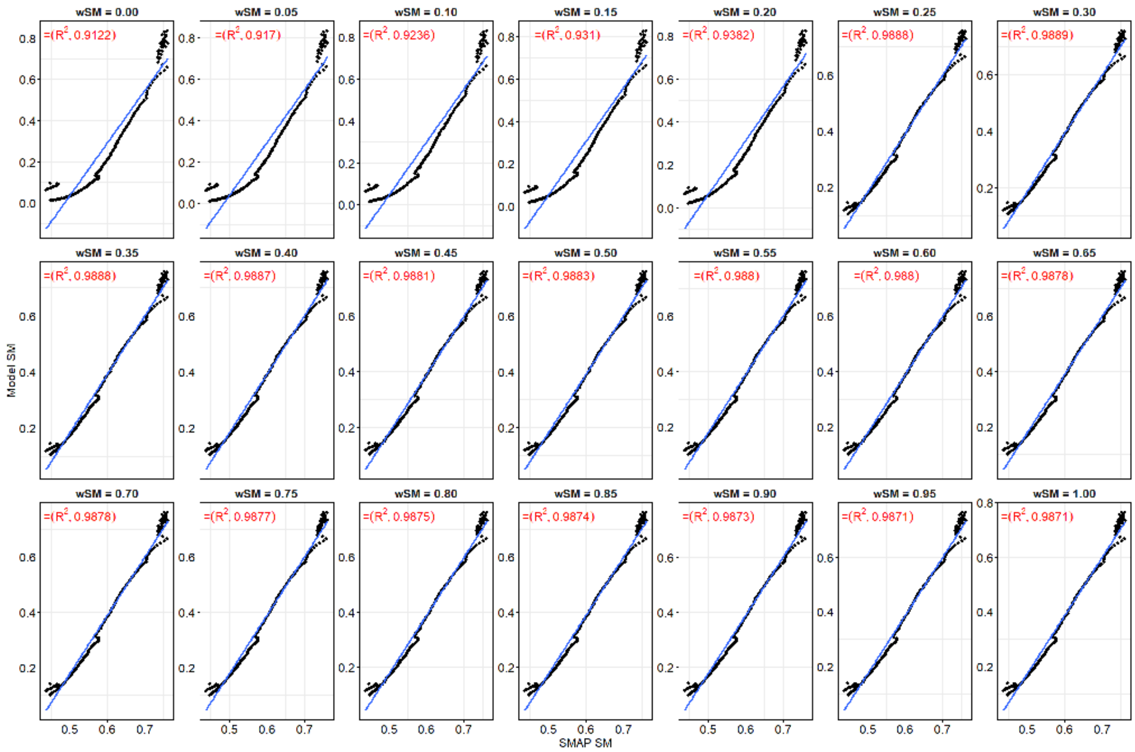

- **Milo à Kankan watershed**

SMAP observed SM and GR4J simulated SM with wSM from 0 to 1 scatter plots

- Rising limb for calibration period

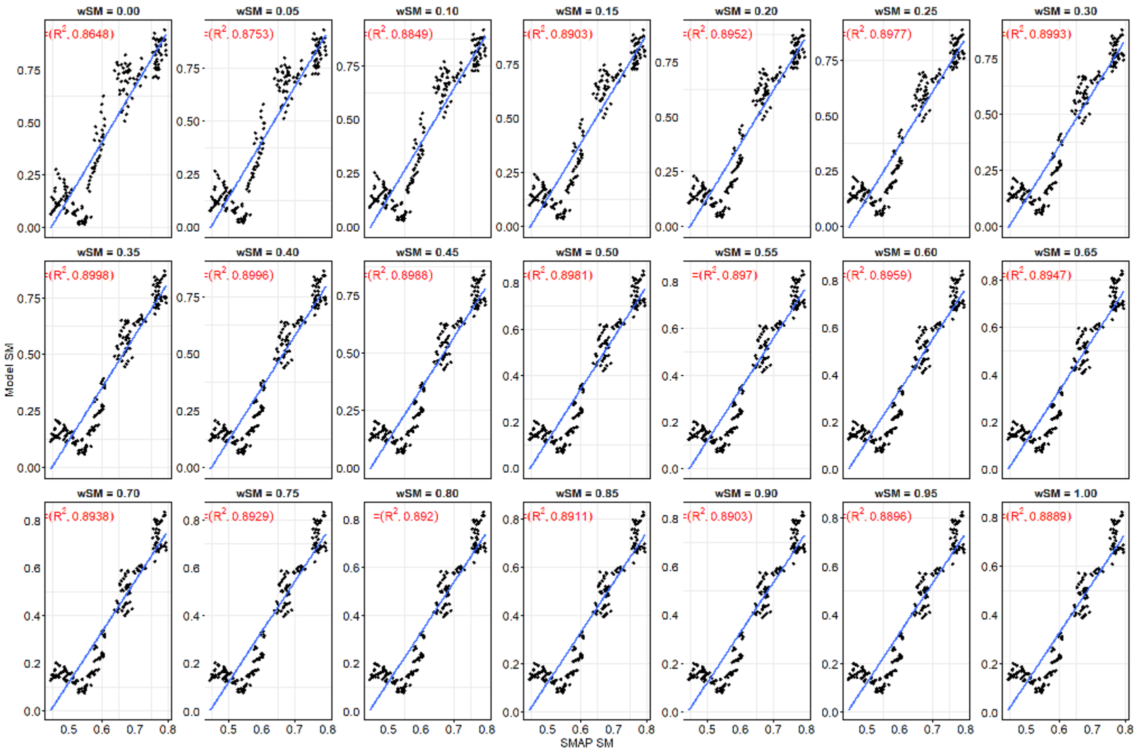

- Falling limb for calibration period

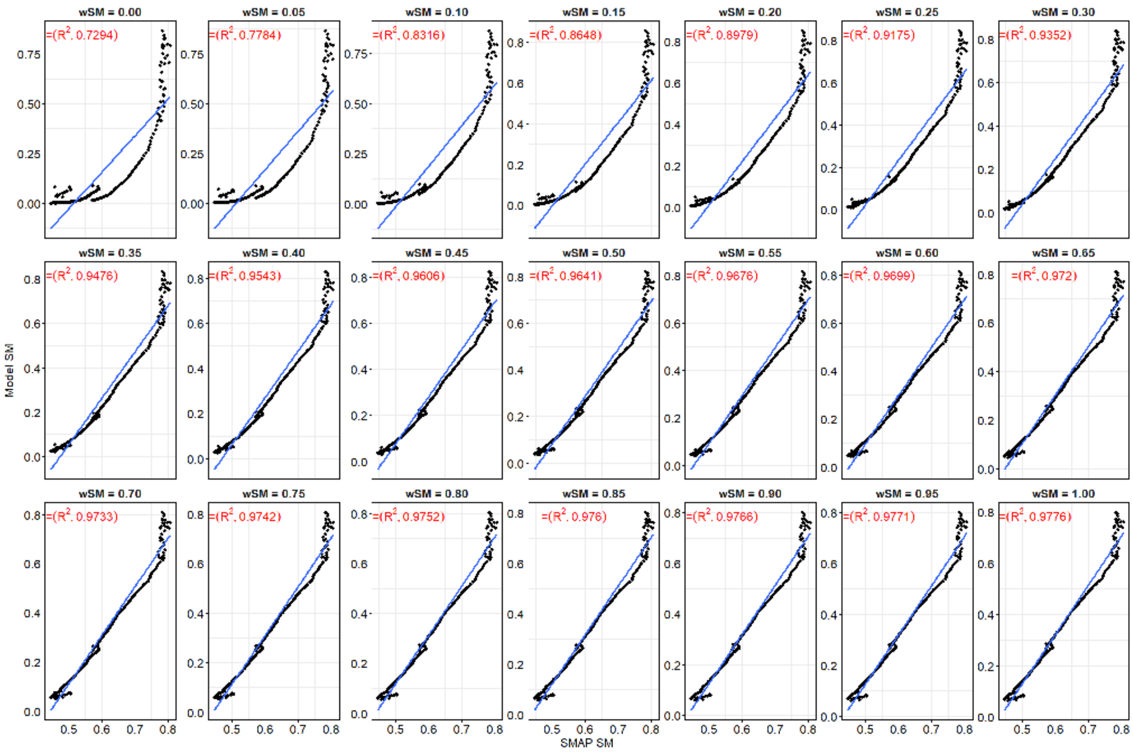

- Rising limb for validation period

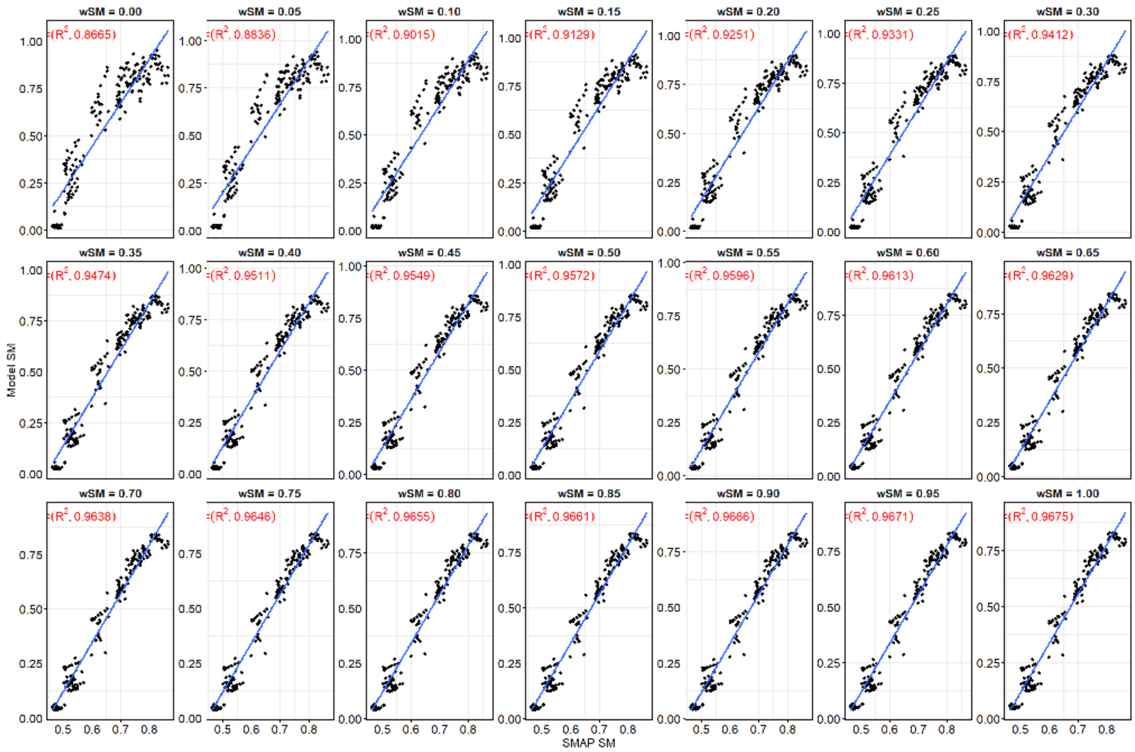

- Falling limb for validation period

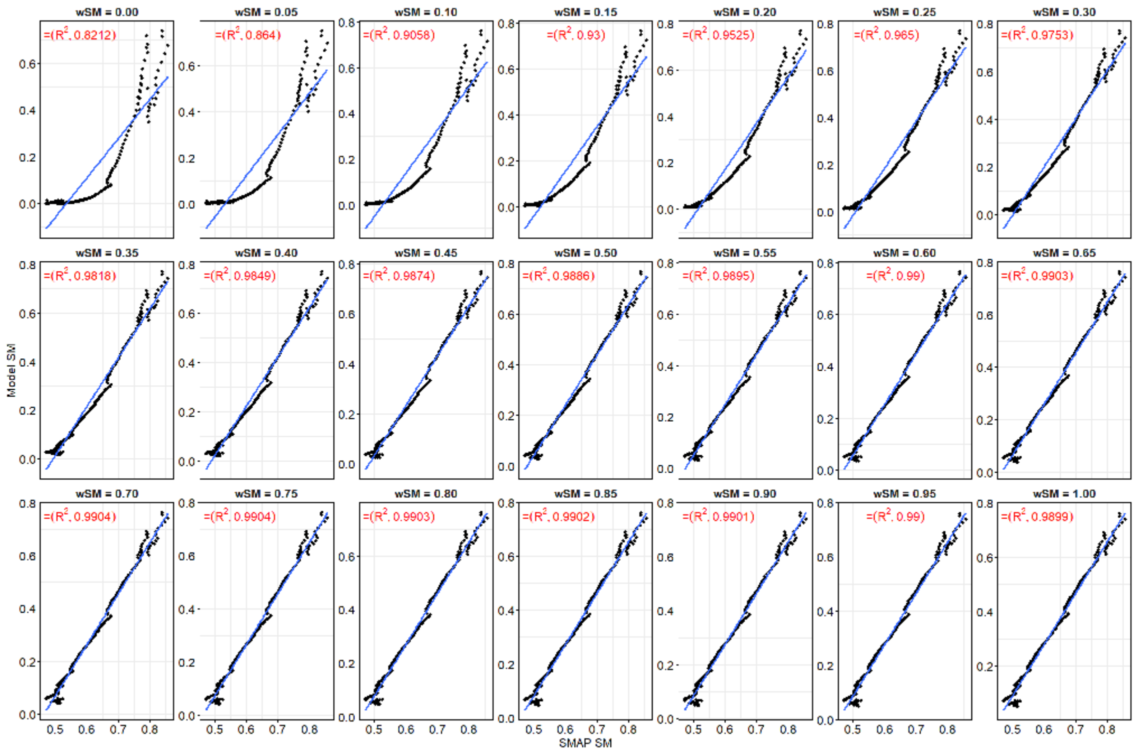

- **Bafing à Sokotoro watershed**

SMAP observed SM and GR4J simulated SM with wSM from 0 to 1 scatter plots

- Rising limb for calibration period

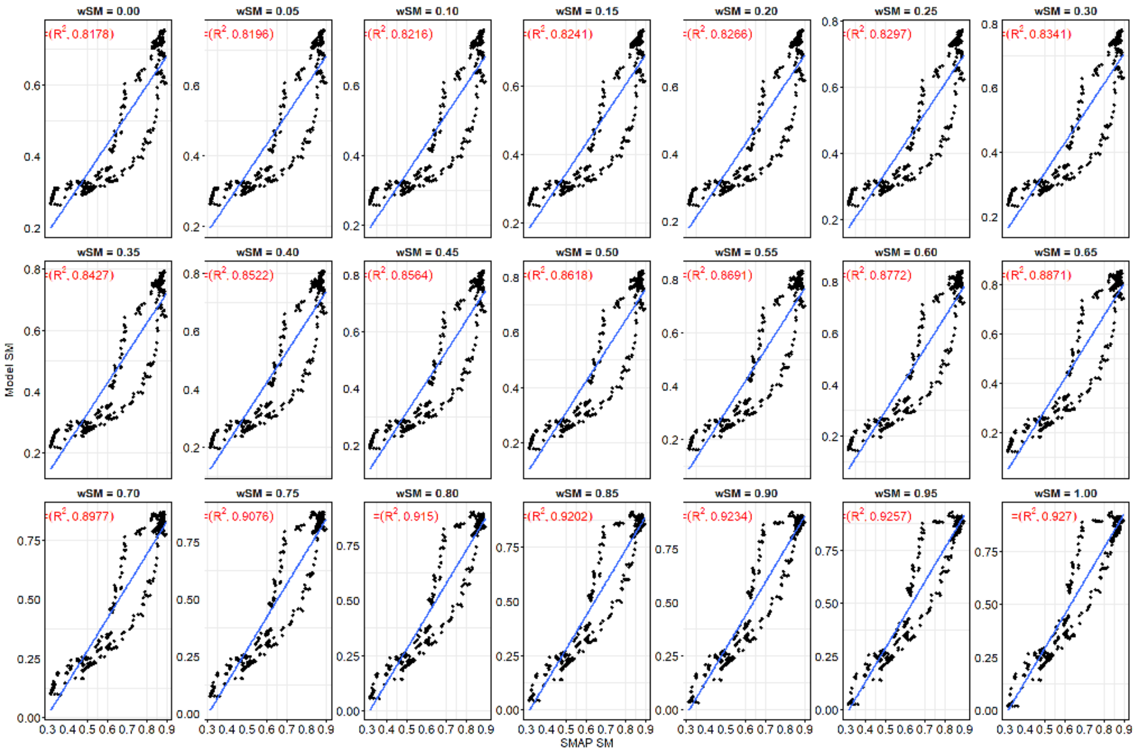

- Falling limb for calibration period

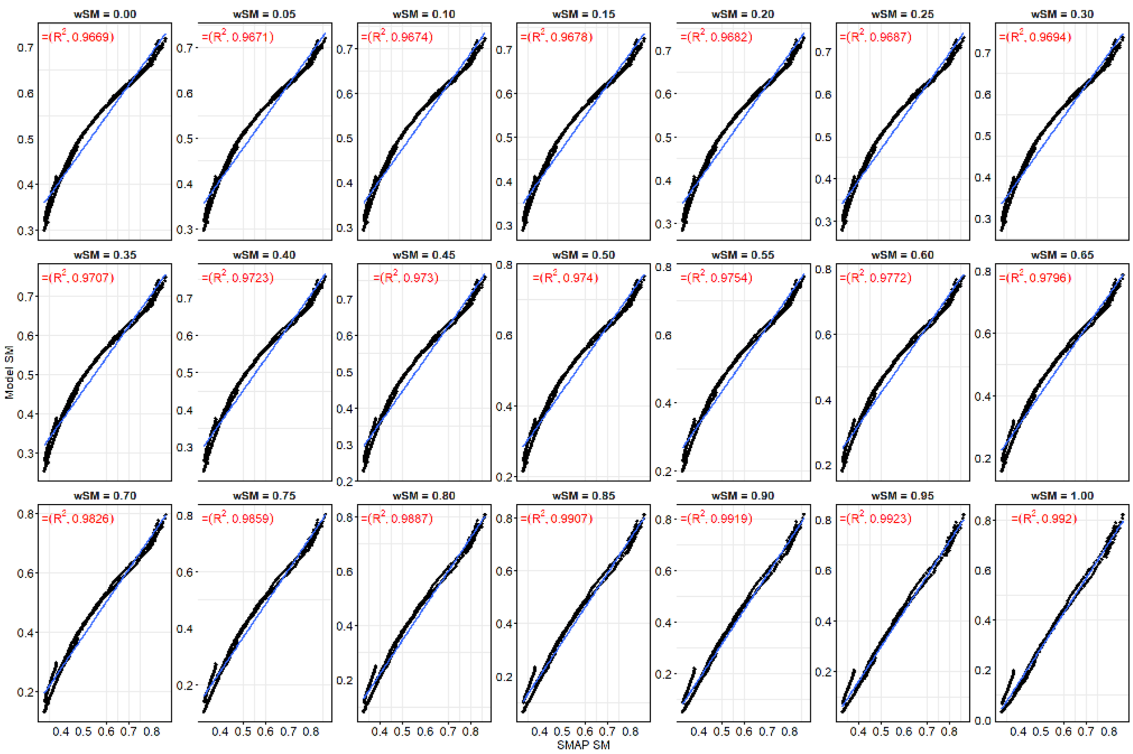

- Rising limb for validation period

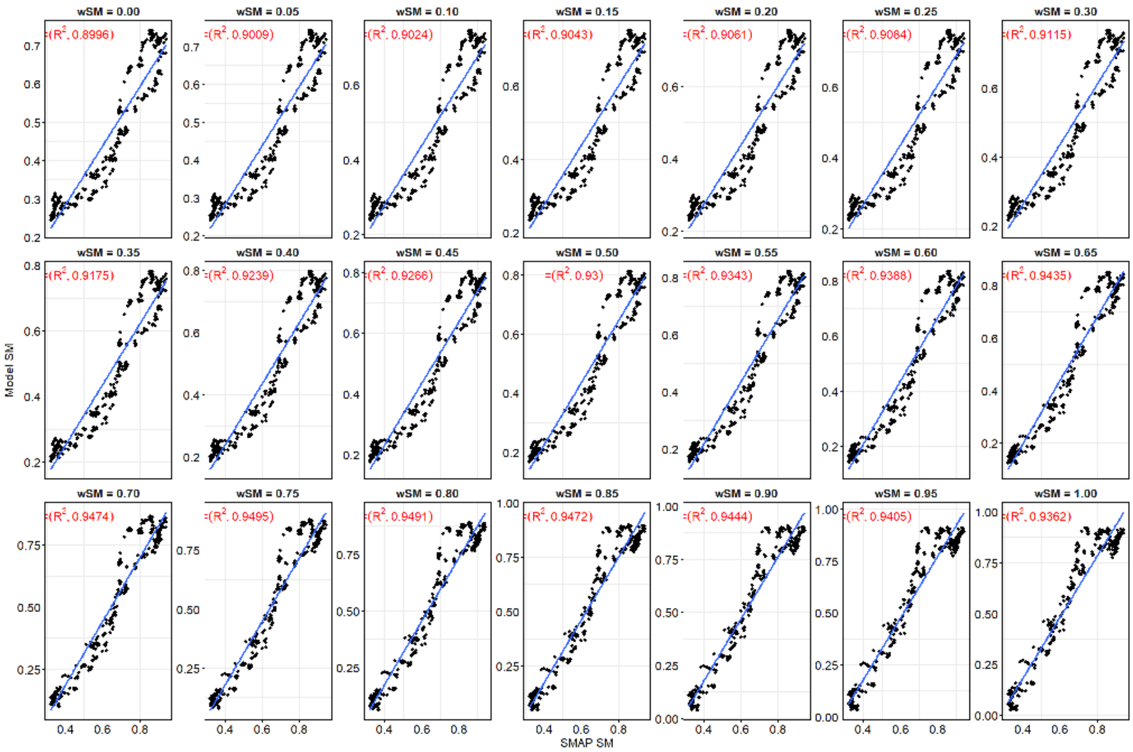

- Falling limb for validation period

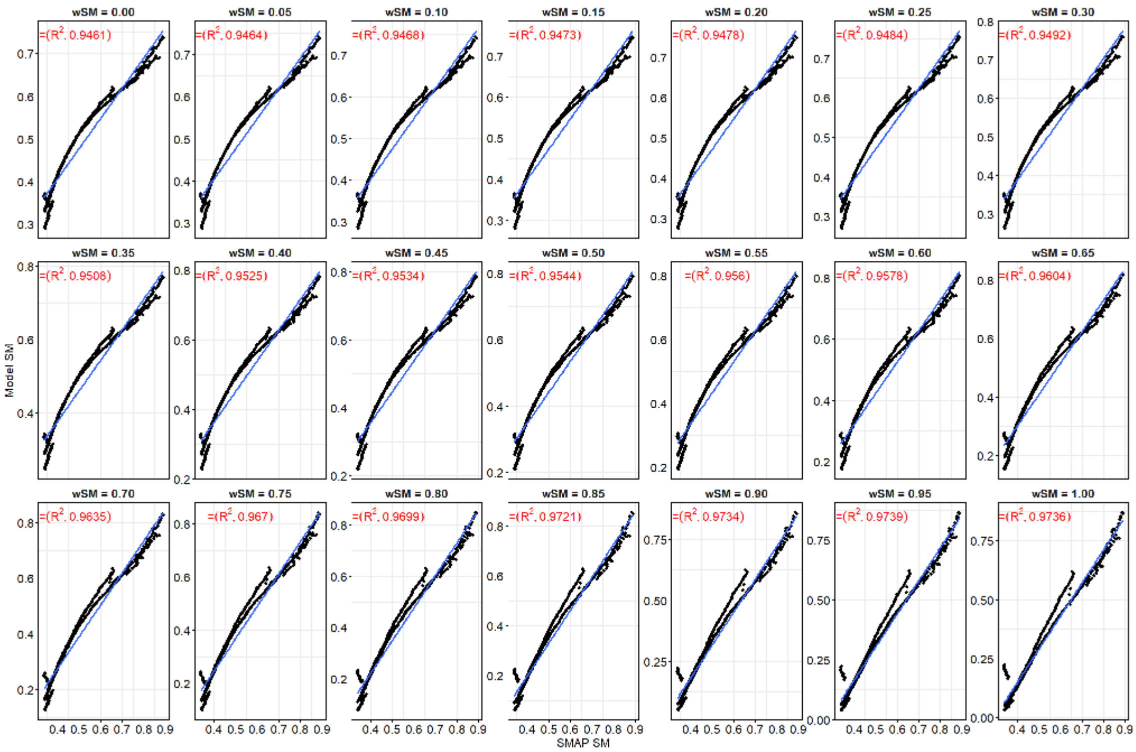

CURRICULUM VITAE

ORCID ID: 0009-0009-4723-3251

Name Surname : **Mamadi TRAORE**

Foreign Language : **English, French, Turkish**

Education and Professional Background:

- 2019, Conakry Gamal Abdel Nasser University, Polytechnic Institute, Department of Civil Engineering,
- March 2020 - Present, Project Engineer, Administration et Contrôle des Grands Projets (ACGP-Guinea), Engineering Studies Department (Département d'Etudes Techniques – DET/DEBAT),
- 2020, Graduate Teaching Assistant, Conakry Gamal Abdel Nasser University, Polytechnic Institute, Department of Civil Engineering, Water Supply for Urban and Industrial Areas.

Publications and/or Scientific/Artistic Activities:

- Şorman, A. A., Eylen, A., Traoré, M., Taç, E., Rahimi, A. (2022) Yukari Seyhan Havzasında farklı hidrolojik modellerin karşılaştırması, 11. Ulusal Hidroloji Kongresi, s. 618-626, Gaziantep, Türkiye.